Vascular cell migration and force generation under tailored geometrical constraints

Aude Sagnimorte

To cite this version:

Aude Sagnimorte. Vascular cell migration and force generation under tailored geometrical constraints. Fluid mechanics [physics.class-ph]. Institut Polytechnique de Paris, 2023. English. NNT : 2023IPPAX148 . tel-04505507

NNT : 2023IPPAX148

Thèse de doctorat

Vascular cell migration and force generation under tailored geometrical constraints

Thèse de doctorat de l'Institut Polytechnique de Paris
préparée à l'École polytechnique

École doctorale n°626 École doctorale de l'Institut Polytechnique de Paris (ED IP Paris)
Spécialité de doctorat : Mécanique des fluides et des solides, acoustique

Thèse présentée et soutenue à Palaiseau, le 11 Décembre 2023, par

AUDE SAGNIMORTE

Composition du Jury :

Karine Anselme Directrice de recherche, CNRS (IS2M)	Présidente
Karine Anselme Directrice de recherche, CNRS (IS2M)	Rapportrice
Hélène Delanoë-Ayari Maître de conférences, Université Lyon 1 (iLM)	Rapportrice
Anke Lindner Professeure, Université Paris Cité (PMMH-ESPCI)	Examinatrice
Pablo J Sáez Professeur, University Medical Center Hamburg- Eppendorf (CellComM)	Examinateur
Camille Duprat Professeure, École polytechnique (LadHyX)	Directrice de thèse
Avin Babataheri Ingénieure de recherche, École polytechnique (LadHyX)	Co-encadrante de thèse
David Gonzalez-Rodriguez Maître de conférences, Université de Lorraine (LCP-A2MC)	Co-directeur de thèse
Janine Nunes Lecturer and Research Scholar, Princeton University (MAE)	Invitée

À tous ceux qui m’ont tendu la main.

Remerciements

La recherche ne se fait pas toute seule et sans toutes les personnes qui ne m'auraient pas aidée, je n'aurais pas pu aller si loin. Je suis très reconnaissante pour toutes ces rencontres et je m'excuse par avance si j'oublie des noms.

Je souhaite tout d'abord remercier les membres de mon jury pour avoir accepté de lire mon manuscrit et d'évaluer mon travail. J'ai beaucoup apprécié vos remarques constructives et nos échanges lors de ma soutenance. Dommage que certains étaient à distance, Pablo et Janine j'espère un jour pouvoir vous rencontrer en personne.

Merci ensuite à mes encadrants de thèse Avin Babataheri, David Gonzalez-Rodriguez et depuis peu Camille Duprat de m'avoir accompagnée chacun à leur façon dans cette thèse et m'avoir permis d'aller jusqu'au bout.

Je souhaite ensuite remercier tous les gens qui ont contribué à la réalisation de cette thèse, avec qui j'ai eu la chance de collaborer. Merci à Sandrine Mariot et Laura Wallon de m'avoir permis de faire des mesures de tension d'interfaces au LPS. Merci à Joni Frederick pour toutes ces journées de mesures à l'AFM, et de m'avoir autant soutenue au long de ma thèse. Merci à Guillaume Lamour et Clément Campillo du LAMBE d'avoir accepté juste avant la soutenance de faire quelques mesures supplémentaires à l'AFM pour me permettre d'interpréter mes résultats. Merci à Pablo Sáez d'avoir accepté de collaborer avec nous sur le projet de la migration et pour ton aide avec la détection des cellules et tes retours constructifs. Merci à Julien Husson pour les mesures de microindentation et pour tes nombreux conseils et ton soutien lors de ma dernière année. Merci à Gaspard de Tournemire d'être venu en stage sur le projet de la migration, j'ai beaucoup appris sur le travail d'équipe et j'espère m'améliorer dans le futur. Merci à Caroline Frot, dès le premier jour de mon stage de master tu as été là pour m'apprendre à faire des fibres d'hydrogel, et tout au long de ma thèse tu m'as non seulement aidée à chaque fois que j'avais un problème technique, mais tu as aussi été un énorme soutien moral qui m'a permis d'avancer. Je te souhaite le meilleur pour la suite.

Je tiens ensuite à remercier toute l'équipe des permanents du LadHyX. Merci à Sandrine, Magdalena et Mélanie pour assurer la logistique du labo, merci à ToaÏ et Daniel pour la gestion informatique et d'être toujours aussi réactifs. Merci à Antoine et Caroline pour tout ce qui est mise en place des manips et sécurité du labo. Merci à Lutz et Christophe d'avoir dirigé le labo pendant ces trois années et pour votre disponibilité. Merci Arezki pour les discussions sur la migration et sur un tout autre domaine, d'avoir donné l'opportunité aux membres du labo de faire de la voile. J'ai adoré apprendre à en faire et cela m'a motivée à continuer. Merci à Abdul de m'avoir incluse comme si je faisais partie de ton équipe, de m'avoir incluse dans les Group meetings, les Journal clubs, les Christmas dinners, les sorties d'équipe et pour tes retours. Un grand merci à tous les autres permanents pour ces trois années passées au LadHyX, je pense notamment à Stéphanie, Julien, Gabriel et Pascal.

Je m'attaque enfin aux doctorants et postdoctorants passés et présents qui m'ont accompagnée tout au long de mon stage de master puis de ma thèse. Il y a d'abord toute l'équipe d'Abdul : Claire D qui a participé à mon recrutement en stage, m'a encouragée à faire cette thèse et m'a appris énormément sur les péricytes. Claire L et Alessia qui sont devenues un peu les deux mamans de l'équipe, merci Alessia pour ton soutien et ta bonne humeur. Merci Claire pour tous tes retours sur la migration, d'avoir relu un bout de ma thèse et tes conseils et soutien en général. Merci Bettina, avec ton énergie communicative tu étais la personne à aller voir pour se remotiver et toujours présente pour aider, merci aussi pour ta franchise, j'ai hâte de me retrouver pas loin de ton labo pour te croiser plus souvent. Merci à Clara et Sara, vous m'avez soutenue pendant ces trois années, j'ai adoré notre summer school en Belgique, vous êtes devenues des amies qui me sont chères et j'espère pouvoir maintenir cela. Merci aussi à Thevy, Manuel et Giulia pour votre bonne humeur et les petites pauses-café ou déjeuner. Je souhaite aussi remercier mes co-bureaux, au début Paul, Mahdi et Claire, puis ensuite Taha, Hassan et Anis. Vous avez toujours été partants pour que ce soit discuter science, me donner un retour, aller skier pour certains ou simplement papoter. Merci à Pierre-Antoine, Pierre, Olivier, Taha, Valentin, Julien B, Elise, Paul, Hassan, Rodolphe, Maxime (du LOB) d'avoir accepté de rejoindre le groupe de microfluidique, nos discussions m'ont énormément aidée pendant la première année de ma thèse et encore une semaine avant ma soutenance vous avez répondu présent pour me faire répéter donc merci ! Enfin, merci à tous les non-permanents du bâtiment 67 que j'ai croisés moins souvent mais avec qui j'ai beaucoup aimé échanger, faire des BBQ (merci Alice, Antoine et Hector pour l'organisation), faire des Thursday cakes fut un temps où avoir des discussions dans le RER.

Je tiens ensuite à remercier les personnes avec qui j'ai eu la chance d'enseigner et par le même biais apprendre beaucoup. Merci Gabriel, tu as été le premier avec qui j'ai enseigné le modal, j'ai beaucoup appris et merci d'avoir toujours pris 5 min pour discuter de mon projet. Merci à Riwal et Julie pour l'enseignement sur les 'Waves in fluids, with illustrations from geophysics', je maîtrisais moins bien ce cours mais j'ai adoré l'enseigner et le préparer malgré le temps que cela demandait.

Au cours de ma troisième année de thèse, j'ai eu la chance de pouvoir partir faire un échange à Manchester au sein de l'équipe de 'Physics of Fluids and Soft Matter' sous l'encadrement de Anne. Sylvia, merci pour la logistique et pour ta disponibilité, et je souhaite remercier Engineering for Health (E4H) interdisciplinary center qui m'a octroyée une bourse pour partir. Je vais maintenant passer en anglais pour remercier l'équipe de Manchester. Thank you Anne for having me in your team for three months, for taking the time to discuss with me every week. I keep saying it but I have learned a lot in those three months and it has motivated me to do a postdoc. Thank you Valeria for including me in your PhD project, it was a pleasure to work with you every day and I am really glad that we managed to keep in touch. Thank you Qi for teaching me how to make capsules and for all your help with the experiments. Thank you Alice for welcoming me on my first day in Manchester, introducing me to the lab, and including me in the cross-country team. Thank you Schresht for all the small talk and for helping me prepare for my lessons! Thanks to Sammy, Jack, Elliott, Chenyang, Haolin and Martin for helping me, showing me your work, and taking me into the team. I would also like to thank Finn Box and Draga Pihler-Puzovic, even though I did not work with you directly, I would like to thank you for your feedback and help. All in all, it was a great stay and I hope the team will keep up the same spirit!

Avant de remercier mes proches je souhaite remercier Mme Coussot, vous m'avez accompagnée pendant ma dernière année, vous avez toujours répondu disponible et essayé de trouver des solutions. Pour cela merci!

Enfin, je souhaite remercier tous mes amis, et ma famille d'avoir été là pour m'écouter parler de ma thèse ou me changer les idées pendant ces trois années. En particulier, merci à mes parents qui m'ont toujours soutenue peu importe mes choix et ce depuis petite et qui ont toujours cru en moi.

Bien entendu, merci Alexandre. Merci d'avoir été là pendant ces trois années d'émotions intenses qu'est la thèse. Merci d'avoir pris le temps de comprendre ma thèse, de m'écouter, de me soutenir, de me remotiver et d'essayer de me faire relativiser. J'ai hâte de partager la suite avec toi!

Résumé substantiel

Les vaisseaux sanguins se composent de différents types de cellules, dont les cellules endothéliales et les cellules murales. Les cellules endothéliales tapissent la paroi interne des vaisseaux, tandis que les cellules murales se situent à l'extérieur des vaisseaux sanguins. Le terme " cellules murales " englobe deux types de cellules : les cellules musculaires lisses vasculaires (CMLs), présentes autour des gros vaisseaux, des artères aux artérioles, et les péricytes (PCs), présentes autour des vaisseaux plus petits comme les capillaires. Les péricytes jouent un rôle essentiel dans notre santé, renforçant mécaniquement les microvaisseaux, contrôlant le flux sanguin et contribuant à l'angiogenèse par exemple. Leur dysfonctionnement est à l'origine de nombreuses maladies, telles que la maladie d'Alzheimer, la formation de tumeurs ou la rétinopathie diabétique. Malgré l'importance des péricytes, des aspects tels que l'hétérogénéité et les fonctions des PCs restent à clarifier, suscitant divers débats scientifiques. Dans cette thèse, nous nous concentrons sur l'étude de deux fonctions essentielles des péricytes : leur migration et leur capacité à exercer des forces contractiles. Pour ce faire, nous développons deux outils in vitro reproduisant les contraintes géométriques rencontrées in vivo par les péricytes.

Dans la première partie de la thèse, nous abordons la caractérisation de la migration des péricytes en utilisant des micropatterns en forme de ligne imitant le confinement des péricytes sur les microvaisseaux. Notre configuration $1\mathrm{D}$ nous permet de retrouver certains paramètres morphologiques des PCs in vivo, comme la longueur des péricytes ou le recouvrement moyen des microvaisseaux, contrairement aux surfaces $2\mathrm{D}$. En suivant les trajectoires des péricytes en fonction du temps, nous observons une population hétérogène, avec certaines cellules qui ont tendance à s'étaler et à être moins motiles, tandis que d'autres sont plus courtes et dynamiques. Ces observations nous amènent à quantifier la vitesse des cellules en fonction de leur longueur. L'analyse révèle une relation inverse entre la vitesse et la longueur des péricytes, avec une distribution de probabilité des vitesses instantanées décroissante de manière exponentielle. Nous démontrons ensuite que la migration des péricytes peut être modélisée comme un mouvement brownien $1\mathrm{D}$ avec friction sèche. In vivo, les péricytes forment des chaînes cellulaires où chacune est confinée à un territoire sans chevauchement avec ses voisines. Nous introduisons donc ensuite des espaces non-adhérents aux lignes, créant des micropatterns contraignant à la fois latéralement et longitudinalement les péricytes. Sur ces micropatterns de différentes longueurs, nous observons des distributions de vitesses instantanées et des relations longueur-vitesses similaires aux péricytes sur les lignes. Nos observations montrent que les péricytes sur des micropatterns contraints longitudinalement peuvent aussi être décrits comme un mouvement brownien avec friction sèche, sauf pour les cellules complètement étalées qui sont pratiquement immobiles, en particulier sur les micropatterns très contraignants. Pour caractériser biologiquement la friction sèche des cellules avec le substrat, nous analysons l'impact de la largeur du micropattern sur la vitesse des cellules. Contrairement à notre hypothèse initiale, nos résultats préliminaires montrent que la vitesse des cellules ne dépend pas de l'aire de contact avec le substrat mais de l'aire totale des adhésions focales. Une autre caractéristique de la migration des péricytes in vivo est leur capacité à migrer sur des substrats non homogènes avec des discontinuités ou à créer des ponts entre deux capillaires. Pour analyser cet aspect, nous étudions la probabilité de franchissement des péricytes d'espaces non adhérents de différentes tailles. Nous observons une diminution exponentielle de la probabilité de franchissement avec la taille de l'espace non-adhérent, indépendamment de la longueur et de la largeur des micropatterns. Nous démontrons que cette probabilité peut être décrite par la probabilité pour un système agité de franchir une barrière énergétique.

La deuxième partie de cette thèse vise à mesurer les forces contractiles exercées par les cellules murales. Pour cela, nous fabriquons des microfibres d'hydrogel suffisamment molles pour mesurer les forces des cellules murales et suffisamment fines pour imiter la courbure des microvaisseaux. Les fibres d'hydrogel sont produites dans des microcanaux de focalisation de flux à deux phases et solidifiées par photopolymérisation. Nous établissons d'abord des lignes directrices pour produire les fibres souhaitées en nous basant sur l'impact du nombre capillaire sur la formation et la stabilité d'un jet. Pour cela nous faisons varier, les dimensions du canal, les viscosités et la tension d'interface des solutions ou encore les débits des phases. Puis, nous caractérisons quantitativement les propriétés mécaniques des fibres obtenues, telles que leur module de Young, à l'aide de la microscopie à force atomique. Nos résultats montrent une augmentation exponentielle du module de

Young avec le temps d'exposition aux UV. En parallèle, les mesures du module de Young des microbilles produites avec la même solution, un temps d'exposition aux UV similaire et un diamètre comparable à celui des fibres, étonnamment nous donnent des valeurs de module de Young plus de dix fois plus élevées que pour les fibres correspondantes. Ces observations, ainsi que des mesures de rétrécissements, montrent que les microbilles et les microfibres produites dans des conditions similaires ont des rigidités différentes, suggérant que le flux et la forme du pré-gel ont un impact sur les propriétés mécaniques de l'hydrogel. Après avoir obtenu des microfibres fines d'une rigidité de quelques kilopascals nous devons les fonctionnaliser, car elles ne favorisent pas naturellement l'adhésion cellulaire. Nous étudions ensuite l'effet de la courbure sur l'organisation des CMLs et observons que, comme montré dans la littérature sur les fibres rigides de verre, elles s'alignent longitudinalement avec la fibre et non orthogonalement comme observé en in vivo. En raison de cette organisation, nous n'observons pas de déformation radiale des fibres larges. Cependant, sur des fibres encore plus fines, les cellules murales (PCs et CMLs) sont capables de fléchir les fibres, ce qui nous permet d'estimer les forces de traction exercées par les cellules. Ces quantifications préliminaires montrent des valeurs similaires à celles obtenues dans la littérature à l'aide d'autres techniques.

Dans l'ensemble, cette thèse apporte des informations sur la migration des cellules murales ainsi que sur leur comportement sur des substrats courbés et mous. De plus, la caractérisation mécanique des fibres d'hydrogel peut servir à d'autres applications en biologie ou en interactions fluide-structure.

Outline

List of Figures

Chapter 1

Introduction

Blood vessels are constituted of different types of cells, including endothelial cells and mural cells. Endothelial cells form the vessel's inner wall, while mural cells line the outer endothelial tube. The term mural cells refers to two types of cells, vascular smooth muscle cells (smcs) and pericytes (PCs) [1, 2]. Both cell types are crucial to our health for instance, they are known to regulate blood flow, provide structural support and integrity to blood vessel walls, and are involved in several diseases [1].

SMCs, which under normal conditions mainly contribute to the homeostasis of large vessels, are also key players in the progression of several cardiovascular diseases, including atherosclerosis [1], aortic aneurysms, and vascular calcification, but also in cancerous growth [1, 3]. For example, in atherosclerosis SMCs contribute to plaque formation by switching from their normal contractile phenotype to a synthetic phenotype that allows them to migrate into the plaque, where they form a fibrous cap [1, 4]. Severe atherosclerosis can lead to ischaemia [2], which in turn can lead to ischaemic stroke [3][1].

Pericytes are located on smaller vessels such as capillaries and their main functions are to maintain the blood-brain barrier (BBB), form new blood vessels (angiogenesis), regulate blood flow within the microcirculation and they are even able to perform immune cell function [5, 6, 7]. Pericyte dysfunction has been implicated in the progression of vascular and neurodegenerative diseases, tumours and diabetes. For example, in Alzheimer's disease, pericyte loss is observed, leading to a decrease in amyloid beta (Ab) clearance, causing Ab accumulation, which in turn increases PC death and increase of the BBB permeability [1, 7]. After an ischaemic stroke, pericytes contribute to the no-reflow phenomenon by constricting capillaries and dying; their death contributes to BBB leakage and, therefore neuronal damage [5, 7]. In diabetic retinopathy, the leading cause of blindness worldwide, hyperglycaemia has been observed to cause pericyte migration from the capillaries into the interstitial tissue, or pericyte apoptosis, both might cause blood vessel leakage [8, 9, 10, 11].

The majority of these pathologies constitute the leading causes of death across the world, and a better understanding of mural cells' functions would allow the creation of more efficient targeted therapeutic treatments against those diseases [6, 7]. In this thesis, we mainly focus on the study of pericytes. Pericytes were first discovered in the 19th century, and it has been just over 100 years since they were first described in detail by Zimmermann [12]. In the last 20 years, the number of studies on pericytes has increased dramatically, focusing on defining pericyte subtypes and understanding their functions and roles in health and diseases, with a particular interest in brain pericytes [7]. Despite this increased interest, several aspects, such as the heterogeneity and functions of pericytes, remain to be fully understood. In this thesis, we focus our work on studying two essential pericyte functions, migration and contractility. For that purpose, we create two in vitro tools that mimic the geometrical constraints pericytes experience in vivo.

---

[1] Atherosclerosis is the buildup of fats, cholesterol, cells and other substances in and on the artery walls. This build-up forms atherosclerotic plaque [1].

[2] Ischaemia is the reduction in blood flow.

[3] Ischaemic stroke corresponds to the loss of blood flow to the brain.

Outline

The first chapter of this thesis provides a description of pericyte morphologies, functions and the interactions of pericytes with their environment. Additionally, it discusses the ongoing debates regarding the nomenclature and functions of pericytes.

The two chapters of this thesis are structured as follows, with an introduction detailing the major concepts of the chapter as well as the existing in vitro tools used to study the function of interest. The second section of each chapter consists of a detailed description of the methods we used for our experiments and analyses, followed by a presentation of the results obtained, and concludes with a discussion and conclusion.

In chapter 2, we introduce micropatterned lines as a platform to study pericyte migration under similar confinement as in vivo. In parallel, we develop a minimal theoretical model to rationalise cell behaviour. We observe that using micropatterned lines, we are able to reproduce morphological parameters as in vivo pericytes, such as cell length and vessel coverage. The quantification of PC migration shows that cell speed is inversely proportional to cell length and that PC migration can be modelled as a particle undergoing $1\mathrm{D}$ Brownian motion with dry friction. Pericyte motility in confined micropatterns of different lengths is then investigated, as is the ability of pericytes to migrate on nonhomogeneous substrates. For this purpose, non-adhesive gaps of different sizes are inserted into the micropattern lines and gap crossing is quantified. We observe that pericyte crossing ability exponentially decreases with gap size and we can predict a systematic gap length that PCs can cross.

In chapter 3, we aim to measure the contractile forces exerted by mural cells. To do this, hydrogel microfibres that are soft enough to measure cell forces and thin enough to mimic the curvature of small blood vessels are fabricated. The first half of the results section focuses on microfibre fabrication and mechanical characterisation. To fabricate the microfibres, we use a two-phase flow flow-focusing channel and photopolymerisation. We investigate the impact of several parameters such as channel geometry, solution composition and flow rates, to produce thin fibres and then use atomic force microscopy to quantify the rigidity of these fibres. Our measurements show that Young's modulus of our microfibres exponentially increases with light exposure time. Once microfibres of diameter close to the microvasculature diameter and of a few kilopascals are produced, in the second half of this chapter, we explore the effect of curvature on SMC organisation and the buckling of microfibres due to mural cell forces.

Chapter 4 summarises this thesis and suggests future experiments and analysis for pericyte migration, measure of mural cell forces and hydrogel mechanical characterisation. Appendices A and B provide detailed protocols, as well as analytical calculations and supplementary graphs and images. Appendix C gives an overview of the project I had the opportunity to join during my 3-month stay in the group of Prof. Anne Juel, Physics of Fluids and Soft Matter Group, in Manchester. The project focuses on the study of clogging of deformable capsules using constricted microfluidic channels.

Collaborations

The theoretical model in chapter 2 was developed by my co-adviser, Dr. David Gonzalez-Rodriguez (LCP-A2MC, University of Lorraine). Prof. Pablo J. Sáez (Cell Communication and Migration Lab, University Medical Center Hamburg-Eppendorf) contributed to the segmentation of cell shapes in bright-field movies by developing a code utilising *Trainable Weka Segmentation* Fiji plugin. Part of the migration experiments was performed by one of the interns Mr. Gaspard de Tournemire who stayed four months at the LadHyX. The setup used in chapter 3 is adapted from a microfluidic platform already implemented at the LadHyX by Prof. Camille Duprat. Ms. Caroline Frot (research engineer at LadhyX) helped to run the first experiments for fibre fabrication. The Atomic force microscopy measurements were done with Dr. Joni Frederick (LadHyX) and microindentation measurements by Prof. Julien Husson (LadHyX). Interfacial tension measurements from chapter 3 were performed at the Solid States Physic Laboratory (LPS, University of Paris Saclay). Finally, I spent three months with Prof. Anne Juel's group (Physics of Fluids and Soft Matter Group, University of Manchester) working with one of her PhD students Ms. Valeria Ciccone.

1.1 Theoretical background

1.1.1 Mural cells description and identification

SMCs can be found on large vessels such as arteries or veins (a few millimetres diameter) down to smaller vessels such as arterioles or venules $(\sim 30\ \mu m)$ [13]. However, in capillaries, the smallest vessels $(\sim 8\ \mu m)$, SMCs leave their place to pericytes [2]. Although we can easily distinguish SMCs on arterioles from PCs on capillaries (Figure 1.1.b), the boundary between the two cell types is blurred and not easy to define. In fact, between SMCs on large vessels and PCs on capillaries, there are transitional phenotypes at the interface between pre-capillary arterioles and capillaries and at the interface between post-capillary and venules that have characteristics of both SMCs and PCs [2]. In addition, the population of PCs is quite heterogeneous, with different characteristics for each subtype. All of this leads to the lack of a consensual definition for pericytes, leading to debate within the scientific community.

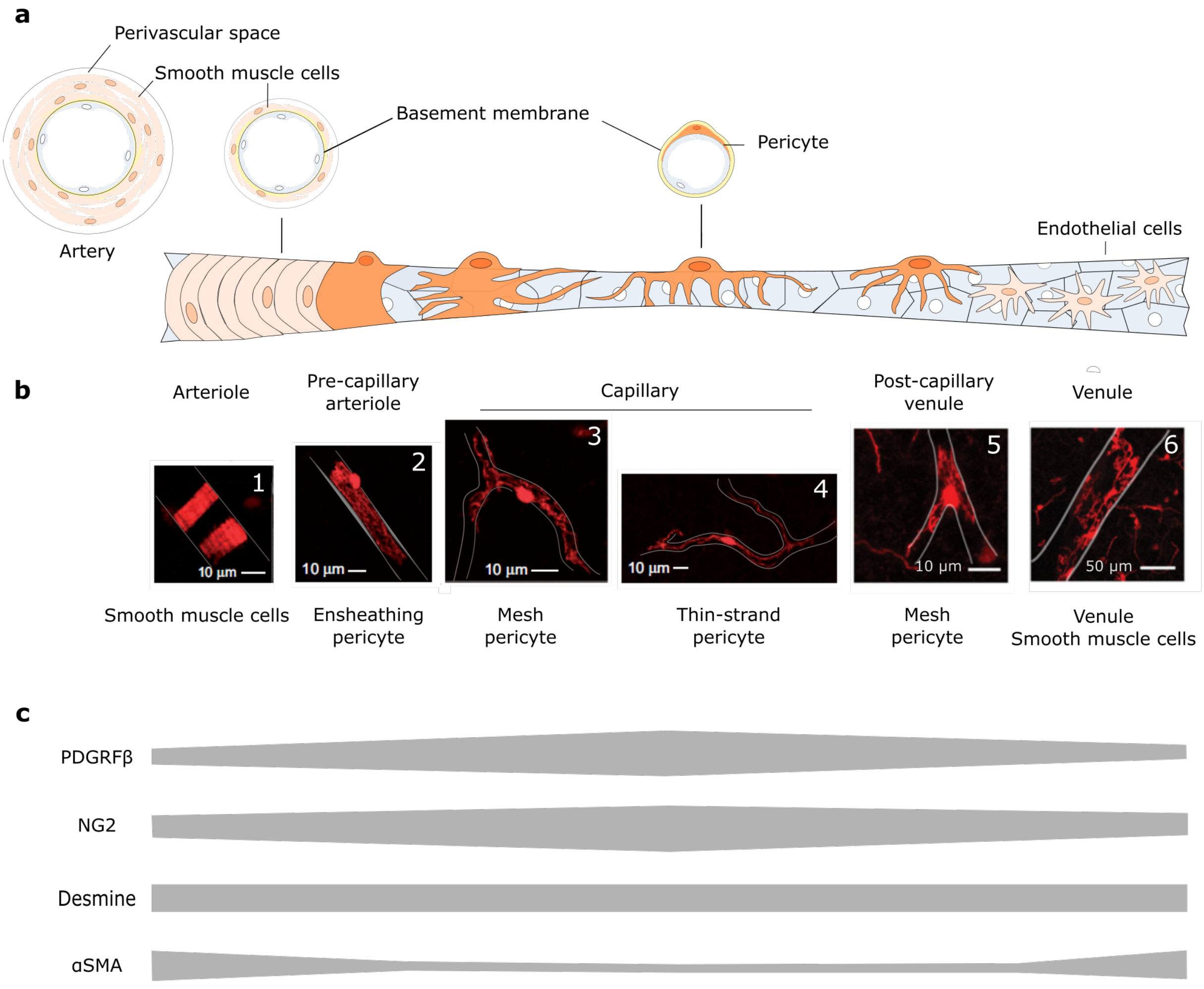

Figure 1.1: Mural cell classification along the vascular tree. **a**, Schematic representing the diversity of mural cell phenotypes with pericytes in orange and SMCs in beige. Adapted from Hartmaan et al. 2015 and Lendahl et al. [14, 15]. **b**, Representative imaging of the different mural cell subtypes in NG2-tdTomato mice brain. Grey lines delimit the vessels. Adapted from Berthiaume et al. 2018 (review) and Grant et al. [2, 16]. **c**, Levels of expression of mural cell markers as a function of localisation in the vascular tree. Adapted from Holm et al. [17]

1.1.1.1 Different location and morphologies

In large vessels such as arteries and veins, SMCs are arranged circumferentially and form multiple layers. In contrast, on arterioles and venules, there is only one layer of SMCs (Figure 1.1.a). SMCs are defined as short cells ($\sim 18\ \mu$m) with broad circumferential processes that wrap around the vessel, they are densely packed and may encircle the vessel several times (Figure 1.1.b.1) [2, 5, 18]. Note that this definition differs for venules, where SMCs are more stellate in shape and do not fully cover the endothelial cells (Figure 1.1.b.6) [16, 18]. As shown in Figure 1.1.a pericytes can be found, from pre-capillary arterioles to post-capillary venules. They constitute a heterogeneous population of cells, as we will discuss in the following section 1.1.1.2. However, PCs are usually described as solitary cells embedded within the basement membrane (BM) with a protruding cell body. They extend longitudinal processes along the vessel wall, usually longer than SMCs, and do not entirely cover the vessel [19].

1.1.1.2 Pericyte classification

Pericytes were first discovered by Eberth and Rouget [20] at the end of the 19^{th} century, then described in detail by Zimmerman in 1923 [12] who named them "pericytes". According to Zimmerman's classification, pericytes are divided into three main subtypes: pre-capillary, capillary and post-capillary pericytes [12, 21]. In addition to the classification from Zimmerman, we will use here the detailed classification from Grant et al. [2].

Pre-capillary pericytes, referred to as ensheathing PCs by Grant et al. [2] (Figure 1.1.b.2) are located at the distal end of penetrating arterioles, which are surrounded by SMCs. Pre-capillary pericytes are the transitional mural cells and depending on the study, they may be referred to as PCs, SMCs or both. Indeed, they have been variously referred to as pericytes (Hall et al. [22]), transitional mural cells (Holm et al. [17]), smooth muscle cell-pericyte hybrids (Attwell et al. [5]), pre-capillary SMCs (Hill et al. [18]), or arteriolar SMCs (Vanlandewijck et al. [23]). They differ from SMCs by their length (L), which is two times longer $L \sim 42\ \mu$m compared to $L \sim 17\ \mu$m for SMCs and the fact that they do not wrap around vessel multiple times as SMCs do [2]. However, they are much smaller than capillary PCs and their vessel coverage is similar to that of SMCs, up to 95% with numerous secondary processes that are large and fully wrap the vessel [5, 24, 25]. In addition, as we will see in section 1.1.1.3 they are rich in alpha smooth muscle actin (αSMA), a contractile protein that SMCs also express in large quantities [2].

Capillary PCs can be divided into two subtypes: mesh pericytes and thin-strand pericytes [2]. Thin-strand (Figure 1.1.b.4) pericytes have two thin processes of a few hundred microns that run longitudinally along the vessel on both sides of their protruding cell body. They also have shorter processes that are orthogonal to the primary ones and partially wrap the capillaries [2, 26]. Note that compared to Pre-capillary pericytes, they have fewer circumferential processes [5]. They have an average length, $L \sim 150\ \mu$m and a low vessel coverage ($\sim 50\%$). Mesh pericytes ((Figure 1.1.b.3) have an intermediate phenotype with a large vessel coverage $\sim 70\%$ that is more apparent to pre-capillary pericytes and thin processes and long cell length ($L \sim 100\ \mu$m) that are similar to thin-strand PCs. Note that in the majority of the articles, there is no distinction between mesh and thin-strand pericytes, and they are categorised as capillary pericytes [5, 17, 19, 25].

Finally, post-capillary pericytes, referred as mesh pericytes by Grant et al. [2] are very little studied and have a different organisation than the two other types, they have a stellate shape and are shorter in length than capillary PCs ((Figure 1.1.b.5). However, they still display a protruding cell body [2, 16, 17].

Morphological features and localisation of PCs are not always sufficient to distinguish SMCs from PCs, especially in the transition between the two cell types.

1.1.1.3 Molecular markers of microvasculature mural cells

Common markers that are currently used for PCs are neural/glial antigen 2 (NG2), platelet-derived growth factor receptor β (PDGFRβ), Desmin, alanyl (membrane) aminopeptidase (CD13) and αSMA [7, 17, 21]. However, it is important to note that none of these markers is PC specific as all of them are also expressed by SMCs and some are even expressed by cells different from mural cells [11]. As we can see in Figure 1.1.c, PDGFRβ and NG2 are both present on SMCs and PCs. However, the level of expression is more important for PCs [17, 21]. Desmin is an intermediate and contractile filament also found in PCs and SMCs, it can be used to distinguish mural cells from endothelial cells (ECs) that do not express it [11]. Figure 1.1.c shows that αSMA, a contractile filament like Desmin, is not found in the same quantity across all mural cells. Indeed, thin-strand PCs, mesh pericytes on capillaries and PCs on post-capillary venules express very little to no αSMA whereas, PCs on pre-capillary arterioles (ensheating pericytes) do express it [2, 17, 21]. The fact that ensheathing PCs have similar morphology and expression as SMCs has led certain studies to classify them as SMCs [5, 18]. Therefore, to confirm pericyte identity, location on the microvascular tree, morphological aspects (protruding cell body), and at least two pericyte markers are commonly used [7].

Other recent and promising techniques, such as single-cell sequencing, have been used to distinguish mural cells [7]. For instance, Vanlandewijck et al. [23] used single-cell RNA sequencing on brain cells. They observed differences between pericytes on capillaries and SMCs on arterioles in gene expression. However, no difference was observed among PC subtypes, although different gene expressions were observed between PCs from the brain and lungs.

1.1.2 Pericyte mechanobiology

1.1.2.1 Pericyte migration

In addition to being a heterogeneous population of cells depending on location in the vascular tree and tissue, pericytes exhibit two different states: quiescent and active [25]. The main difference between these two states, apart from morphology, is their migration.

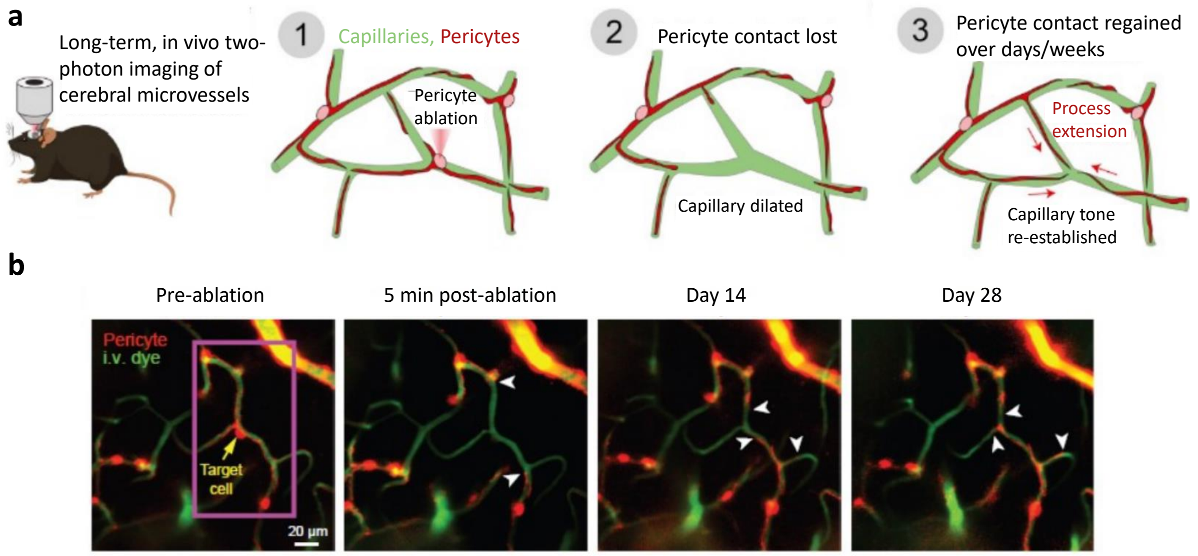

Figure 1.2: Pericyte remodelling following laser ablation of an adjacent pericyte. **a**, Schematic of pericyte remodeling. **b**, Representative images of pericyte ablation in mouse brain, followed by extension of neighbouring PC processes to cover the vessel wall. The white arrowheads indicate the invading processes. Adapted from Berthiaume et al. 2018 [27].

The quiescent state corresponds to PC morphologies described in section 1.1.1.2. A pericyte that is encased within the basement membrane in contact with endothelial cells with a protruding cell body and processes. It has been observed for capillary PCs that their soma is immobile, whereas their processes' length slightly fluctuates (0.5 μ m/day), probing their environment [27]. Organised in a cellular chain along the microvasculature, they each have their own territory and exert contact inhibition, meaning that they do not touch each other, as we can see in Figure 1.2.a [27]. Berthiaume et al. 2018 [27] observed in mice brains that following PC ablation with high-power laser radiation, the adjacent pericytes drastically extended their processes ($6-8$ μm/day) to cover the microvessel wall (Figure 1.2). Note that this phenomenon is referred to as process extension rather than migration as the cell's soma does not move [28].

During angiogenesis, quiescent pericytes can perform a 2D migration along the blood vessel, referred to as "crawling or sliding". Indeed, it has been observed that PCs in the vicinity of endothelial sprouts exhibit persistent and directional migration along newly formed vessels [28]. It is suggested that chemotactic cues from sprouting endothelial cells, such as platelet-derived growth factor-BB (PDGF-BB), may trigger PC migration. As we can see in Figure 1.3, crawling corresponds to a two-step migration, with first a slow extension of PC processes along the EC junctions and then a translocation of the rest of the cell [29].

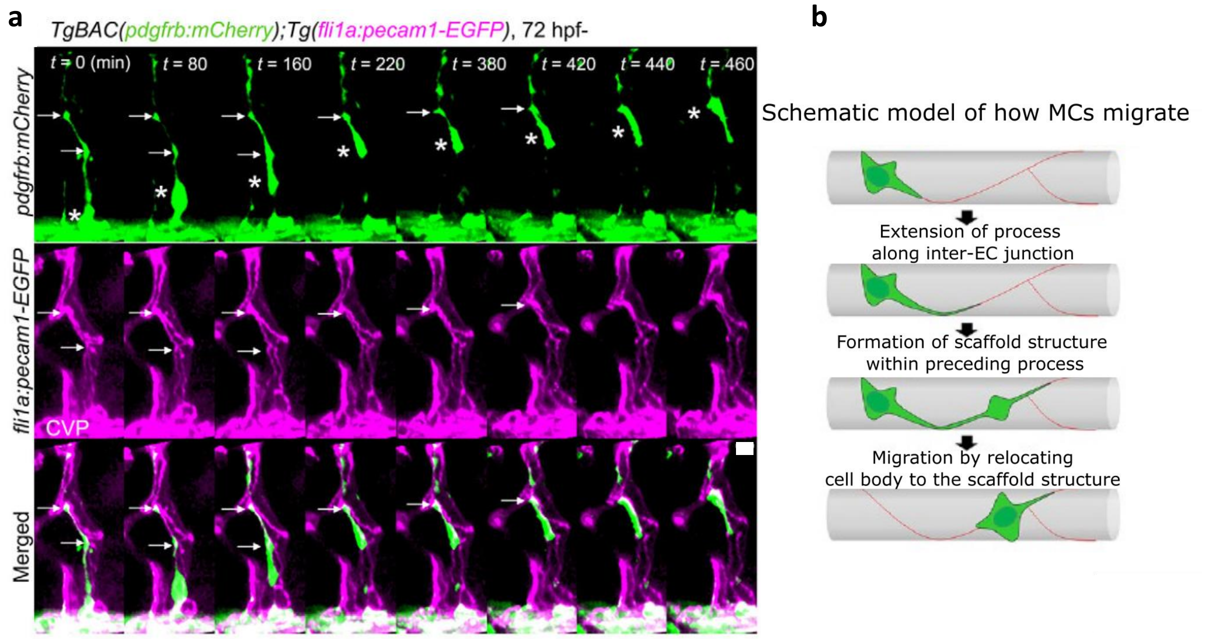

Figure 1.3: Crawling of a pericyte along a blood vessel. a, Time-lapse confocal images of a mural cell migrating along the blood vessel in a zebrafish embryo. Asterisks indicate the mural cell soma and arrows the processes. Mural cells (MCs) are in green and endothelial cells (ECs) in magenta. Scale bar = $10\ \mu$m. **b**, Schematic of the different steps of mural cell migration along a blood vessel (crawling). The red lines represent the EC junctions. Adapted from Ando et al. [29].

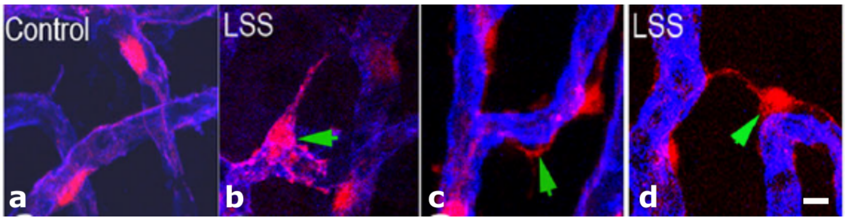

Figure 1.4: Active pericyte migration: escaping. Confocal images from cochlear blood vessels of transgenic mice under normal conditions (**a**) or loud sound-stimulated conditions (LSS) (**b,c,d**). Pericytes are in magenta and capillaries in blue. Under LSS, pericytes can form a protrusion at its soma (antenna) (**b**), have processes that detach from the vessel wall (green arrowhead, **c**) or form bridges with other vessels (**d**). Scale bar = $10\ \mu$m. Adapted from Hou et al. [30].

The mechanisms that control the switch from quiescent to active state are still unknown [25]. Briefly, in their active state, pericytes first retract their processes and then extend a new process at the tip of their soma, like an antenna (Figure 1.4.b). After this step, they detach from the microvessel wall (Figure 1.4.c) and migrate into the surrounding tissue. They can also extend their processes into the neighbouring vessel to form bridges, as shown in Figure 1.4.d. This type of migration is referred to as 'escaping' and can occur as crawling does during angiogenesis but also under stress conditions, such as hyperglycemia in diabetes retinopathy or exposure to loud sounds in acoustic trauma [9, 30].

1.1.2.2 Pericyte interactions with their environment

Pericytes are in direct contact with ECs, they form peg-and-socket, gap junctions and adherens junctions with ECs (Figure 1.5.a). Peg-and-socket are protrusions usually arising from PCs that insert themselves into ECs [31]. Gap junctions correspond to channels made of connexin proteins allowing the direct connection between the cytoplasm of PCs and ECs [25, 31]. Finally, adherens junctions are areas that connect the cytoskeleton of both cells through transmembrane proteins as VE-cadherin or N-cadherin [25, 31].

Pericytes are located within a layered BM between collagen type IV on the outer side and laminin on the pericyte-EC interstitium [32]. It has been shown that the laminin layer of the BM contains small fibronectin spots that colocalise with focal adhesion of both cell types [32, 33]. The binding to fibronectin spots and, thus to the BM is made with integrins. In a recent study, it was observed that in vitro, pericytes prefer to adhere to fibronectin over laminin (Figure 1.5.b) [32]. From these observations, we can hypothesise that crawling pericytes migrate on nonhomogeneous substrates by creating anchors to fibronectin patches.

Finally, PCs as we saw in the section 1.1.2.1 do not interact with their neighbouring PCs as they exert contact inhibition. All these interactions are necessary for communication, signalling and force transduction.

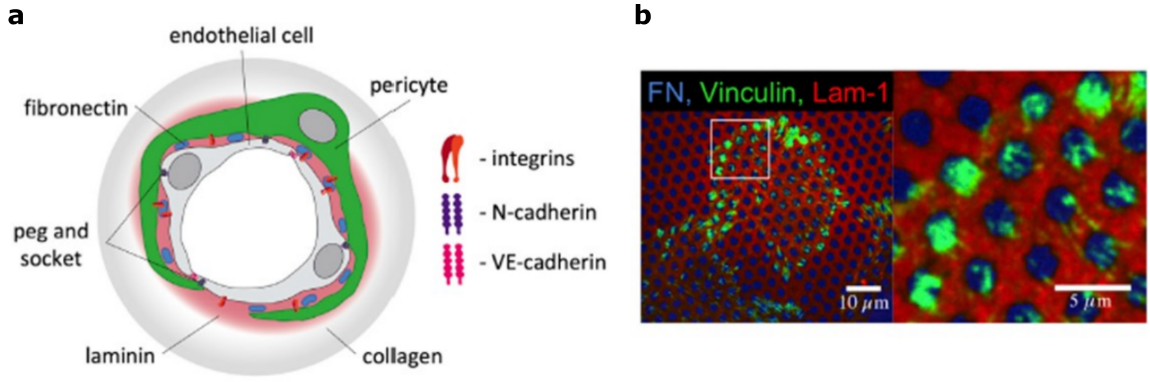

Figure 1.5: Pericyte interactions with endothelial cells and the basement membrane. a, Schematic of the BM surrounding PCs and the interactions between PCs and ECs. **b**, Pericytes are seeded on a PDMS surface coated with laminin (red) and fibronectin spots (blue). Confocal immunofluorescent images show that the pericyte adhesions (green) are on fibronectin spots rather than on the laminin layer. Adapted from Iendaltseva et al. [32].

1.1.2.3 Pericyte functions

Pericytes have been reported to play crucial roles in blood vessel formation (angiogenesis) and the maintenance of the BBB, they are also important in the regulation of the immune system. For example, they have been observed to regulate the migration of immune cells (neutrophils) across the BBB [6, 7]. Pericytes also have stem cell-like properties, for example, they can differentiate into different cell types and finally, a more controversial function is their role in the control of cerebral blood flow [7, 22]. In this section, we will focus on the ability of pericytes to control blood flow.

It is important to recall that there is a lack of consensus in the scientific community on the definition and common nomenclature of pericytes, which has led to mixed opinions, with some studies reporting that pericytes control cerebral blood flow and others supporting that only SMCs play a role [5, 18, 19].

For example, in their study, Hill et al. [18] showed that capillary diameter at pericyte sites does not change in response to different stimuli and that it is actually SMCs on arterioles that are responsible for vasomotion. It is important to note that in this study, PCs were defined only as αSMA negative cells. In this study, ensheathing pericytes, which are located on pre-capillary arterioles close to SMCs, and which express contractile proteins such as αSMA and, like SMCs, have processes that completely surround the vessels, were considered to be SMCs rather than pericytes, despite their protruding cell body and thinner processes, that are typical of PCs. Other studies by Hall et al. [22] demonstrated that pericytes respond to neuronal activity and ischemia. Indeed, they observed that capillary pericytes dilate in response to neuronal activity and that they are the first element to relax before arterioles, showing the active and not passive role of PCs. They also observed capillary constriction during ischemia due to the death of PCs. Note that in this study, we do not know if capillary pericyte is a general term for all the PC subtypes or refers only to thin-strand pericytes. Despite the confusion in nomenclature, it seems that there is a consensus on ensheathing PCs (transitional SMCs) being contractile and controlling blood flow as SMCs do [5].

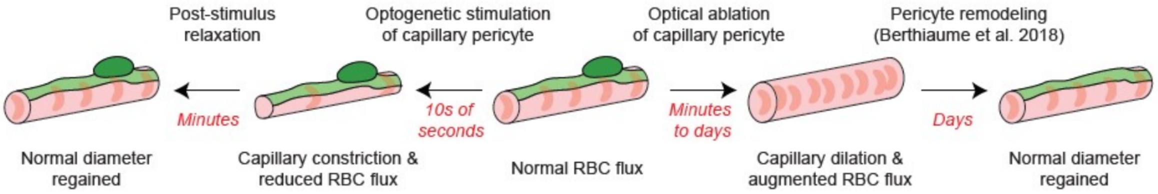

Figure 1.6: Summary of capillary pericyte influence on capillary diameter. In basal conditions, capillary PCs maintain a normal RBC flux. On the left, vasoconstriction of the capillary can be observed using optogenetic stimulation, this process happens in a few seconds compared to the restoration of normal diameter, which takes a few minutes. On the right, ablation of PCs can lead to vasodilatation of the capillary and thus increased RBC flux, it can take days before the normal diameter of the capillary is recovered due to the extension of processes from neighbouring PCs (section 1.1.2.1). Adapted from Hartmann et al. 2021 [34].

The ability to control blood flow is less clear for true capillary pericytes (mesh and thin-strand PCs) and venous pericytes, which express very little or no contractile proteins such as αSMA and do not completely cover the blood vessel. Indeed, the contractility of capillary pericytes has been more elusive in various reviews and communications [5, 19, 25]. In a recent study, Hartmann et al. 2021 [34] showed that capillary pericytes can influence blood flow (Figure 1.6). To do this, they used αSMA as well as morphological and localisation features to distinguish the different subtypes of pericytes. Then, they used optogenetic tools [4] to stimulate capillary pericytes and observed a constriction of the capillaries, followed by a reduction in red blood cell velocity and thus a decrease in blood flow. However, they observed that compared to arterioles or pre-capillary arterioles, capillary constriction is slower, as is post-stimulus relaxation, which takes minutes for capillaries compared to seconds for pre-capillary vessels. Finally, they performed pre-capillary ablation to quantify vasodilation. They observed 20 % capillary dilation compared to the baseline three days after cell ablation. All these experiments show that capillary pericytes exert a tone on capillaries, but it is smaller than that of SMCs and ensheathing PCs and can have a slower effect.

To our knowledge, very few to no studies have investigated the contractility of venous PCs and SMCs [25]. Hartmann et al. 2021 [34] looked at the change in diameter of venules under venous SMCs, but no significant difference was observed between controlled and stimulated areas. Further studies are required to draw conclusions. It has been suggested that venous pericytes are more important for the immune system by regulating the entry of immune cells to the surrounding tissue [5].

---

[4] Optogenetic tools allow to control the activity of cells using light. For instance, this is achieved by the excitation of ion channels in the targeted cell.

Chapter 2

Probing pericyte dynamics: investigating lateral and longitudinal confinement

2.1 Introduction

2.1.1 In vitro tools to study pericyte migration

Although pericytes (PCs) were discovered 150 years ago, many questions about their mechanobiology remain unanswered. As discussed in chapter 1, the main difference between the quiescent and active states is their mode of migration. In vivo studies have investigated how pericytes migrate in different situations (pathology, angiogenesis, etc.) [9, 28, 29]. However, a limitation of in vivo studies is the difficulty in decorrelating the effect of different parameters. In vitro systems are simplified versions of the in vivo environment in which a few parameters of interest can be manipulated in a controlled way to better understand and characterise the observed phenomenon. In the following paragraph, we review the different in vitro platforms used in the literature to study pericyte migration and their applications.

In the literature, in vitro PC migration is mainly studied under pathological scenarios. For instance, 2D wound healing assays are used to investigate the effect of different culture media on PC motility or the role of specific proteins involved in different diseases [35, 36]. The 2D wound healing assay consists of seeding cells on a glass slide. Once the cells have formed a monolayer, a wound is created and migration is tracked (Figure 2.1.a). It is important to note that in vivo, pericytes do not usually form a monolayer, but rather form a chain-like arrangement along blood vessels and usually show contact inhibition [27]. In vitro, 2D assays are also used to study the migration of individual pericytes. For example, Graziuli et al. [37] investigated the role of $\alpha 4\beta 1$, a fibronectin receptor integrin, on PC migration; this molecule is known to be important in blood vessel development. Healthy and pericytes with altered $\alpha 4\beta 1$ migration are compared in a parallel flow chamber under shear flow. Parameters such as persistence time, time to initiate migration and average speed are quantified. Brown et al. [38] used single pericyte migration tracking, among other quantification approaches to characterise different pericyte morphologies on a 2D surface. They reported an average velocity of the cell nucleus between ~ 30 and ~ 240 μm/h (Figure 2.1.d) and a process velocity between ~ 120 and ~ 360 μm/h on glass coverslips. Another study used 2D migration assay to compare pericytes with fibroblasts and reported for PCs an average nuclear speed between 21 and 100 μm/h in similar conditions [39]. Note that these reported values cannot be compared with in vivo values as, to the best of our knowledge, there is no in vivo quantification of pericyte migration speed.

PC migration is also studied using 3D platforms such as transwell systems or more realistic ones such as organs-on-chip. As shown in Figure 2.1.b, in the transwell platform, cells are seeded on the top of a porous membrane and then migrate to the other side through the pores, where cells are counted to assess their motility. In the literature, as for 2D assays, transwell assays are mainly used to evaluate the effect of abnormal conditions on PC migration. For instance, in addition to the flow migration assay, Graziuli et al. [37] used the transwell assay to compare healthy pericytes and pericytes with altered $\alpha 4\beta 1$ integrin by measuring their migration rate under a fibronectin gradient. In another study, Hou et al. [30] used the transwell assay in addition to in vivo experiments to demonstrate that platelet-derived growth factor-BB (PDGF-BB), which is upregulated after long-time exposure to loud sound, triggers pericyte migration. Note that with transwell assays, cells cannot be imaged during migration [25].

More recently, organs-on-chip and more precisely vessels-on-chip have been developed and can be used to study PC migration [40, 41]. For example, Kim et al. 2015 [40] used a microfluidic platform to engineer a vascular network. As we can see in Figure 2.1.c they co-culture endothelial cells (ECs) with pericytes in fibrin gel and they used fibroblasts to trigger vessel formation (angiogenesis). This study demonstrates that PCs migrate along the nascent sprouts as in vivo [28]. To obtain quantitative values, complex imaging techniques and live dies are required.

Although there is a growing interest in PC migration, very few studies have characterised PC migration dynamics. Indeed, most published work only quantifies the number of cells that can migrate in different situations. To our knowledge, only three studies, Zhao et al., Brown et al., and Graziuli et al. have quantified cell speed or persistence [37, 38, 39]. Note that all these assays are in 2D and are not fully representative of in vivo conditions. For example, substrate topography, stiffness or curvature are not considered.

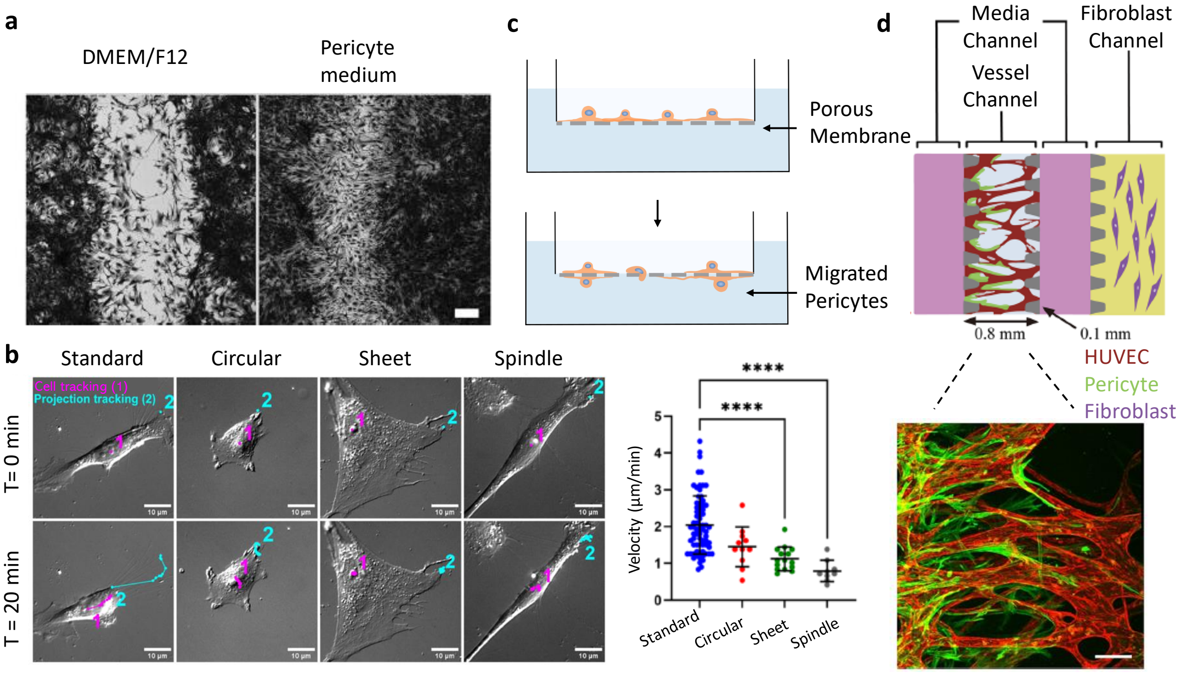

Figure 2.1: In vitro tools to study pericyte migration. **a**, Wound healing: pericyte migration after a scratch. The left image with Dulbecco's Modified Eagle Medium (DMEM), and the right image with pericyte medium. Scale bar = $50\ \mu$m. Adapted from Rustenhoven et al. [35]. **b**, 2D migration assay: DIC images of different pericyte subtypes on a 2D surface (left images). Nucleus tracking is shown in pink and protrusion tracking is shown in cyan. On the right is mean cell velocity (nucleus) for the different pericyte subtypes. Scale bar = $15\ \mu$m. Adapted from Brown et al. [38]. **c**, Transwell assay: migrating pericytes traverse the porous membrane and attach to the bottom side. The non-migratory pericytes that remain in the upper insert are removed and the other cells are stained and quantified [30]. **d**, Vessel-on-chip, angiogenesis assay: setup scheme showing the central vessel of the microfluidic device at day 6 after EC and pericyte seeding. Bellow is a confocal image of pericytes that migrate along EC sprouts. Scale bar = $100\ \mu$m. Adapted from Kim et al. 2015 [40].

2.1.2 Cell migration on 1D adhesive patterns

The 3D in vitro migration assay tends to better mimic physiological conditions, but it also renders it more complex to quantify cell migration. Conversely, unstructured 2D migration assays are simpler but differ significantly from the physiological environment. A halfway solution is offered by 1D migration assays that consider confinement. Micropatterns provide a simple tool to confine cells, using different surface coatings that correspond to areas to which cells can adhere, surrounded by cell-repellent regions. Micropatterns have been widely used to study cell migration, and in the following section, we present different studies using lines and non-adhesive gaps that we consider relevant for this work as they measure similar parameters to ours, such as cell speed and length and the ability to cross non-adhesive gaps for various other cell types.

Before presenting the various articles, here's a quick reminder of the migration cycle of the majority of the cells, except amoeboid cells (like immune cells). It follows four main steps: 1) front extension, with actin polymerising and pushing the membrane forward (formation of a protrusion); 2) the protrusion adheres to the extracellular matrix, forming nascent adhesions that mature at the back into focal adhesions (FA); 3) a local traction force is applied by the cell to the substrate to then generate a movement forward; 4) tail retraction, adhesion in the rear of the cell disassembles. The cycle is repeated with a new protrusion at the front [42, 43]. Depending on the cell type and conditions, this cycle might vary.

One of the simplest migration experiments using micropatterns is confinement on narrow lines. Despite its simplicity, it has been shown that studying single-cell migration on thin adhesive lines can mimic in vivo cell migration on collagen fibres [44]. It has also been demonstrated that cell morphology on 1D lines is close to that in 3D, where cells are elongated, compared to 2D, where they can spread widely [44]. An important study using 1D lines to quantify cell migration is the First World Cell Race [45]. In this study, the authors compared the motility of 54 different adherent cell types on fibronectin-coated lines. They showed that cell motility varies between cell types and that a higher average speed corresponds to more persistent cells. Using the race data, Hennig et al. [46] showed that there is a negative correlation between cell speed and length for the majority of the 54 cell types, which is consistent with the stick-slip behaviour they observed in the rest of their study. In stick-slip behaviour, when cells elongate, their speed decreases while their substrate interaction and contractile stress increase. This tendency is observed until maximum contractile stress is reached and a cell edge detaches from the substrate, leading to a shortening of the cell and, thus smaller cell-substrate interaction and contractile stress and higher cell velocity. Several other studies also use 1D micropatterned lines, for example, Mohammed et al. [47] used successive lines of different width to mimic the spatial confinement that follower cells experience within epithelial tissue. They demonstrated that epithelial cells (keratocytes) display leader behaviour on larger patterns, by increasing their velocity and exhibiting an aspect ratio of one, whereas on thinner lines they are more elongated and slower like follower cells. Note that depending on the type of cell that is used the contrary can be observed: Doyle et al. [44] observed for fibroblasts a decrease of cell velocity on wider lines.

In the context of pericytes, lines could reproduce the different confinements to which PC subtypes are subjected on the different microvessels (pre-capillary arterioles, capillaries, post-capillary venules), in contrast with 2D assays, which lack lateral confinement. However, in vivo, cells are not only confined, they can also encounter constraints or barriers as shown in Figure 2.2. For example, the extracellular matrix (ECM) is not homogeneous and contains non-adhesive regions [48]. In addition, the extracellular microenvironment contains confining pores through which cells must squeeze to migrate [49]. To reproduce these constraints, researchers have created more complex micropatterns, for example, by adding adhesion gradients or non-adhesive regions or by varying the level of confinement on micropatterns. We can cite several examples of studies using non-adhesive gaps. Garbett et al. [48] used successive micropatterned lines ($2\ \mu$m thick) with gaps of different sizes to study which proteins are involved in the mechanism of membrane protrusion and thus cell crossing (Figure 2.2.b). Another study by Caballero et al. [50] investigated how asymmetric adhesive patches can bias cell direction (Figure 2.2.d). The same assay is used to quantify how focal adhesion dynamics and distribution are related to the persistence of migration [51]. Another paper also investigated the adhesion-velocity relationship using micropatterns with variations in protein coating within the pattern (Figure 2.2.a) [52]. Zhou et al. [53]

used micropatterned lines of different length ranging from 70 to 270 μm to investigate the migration of cancer cells in a confined environment, they observed a quasi-periodic movement (Figure 2.2.f). Bruckner et al. [49] used micropatterns with two square adhesive islands connected by a thin bridge to study how cells overcome thin constrictions (Figure 2.2.e).

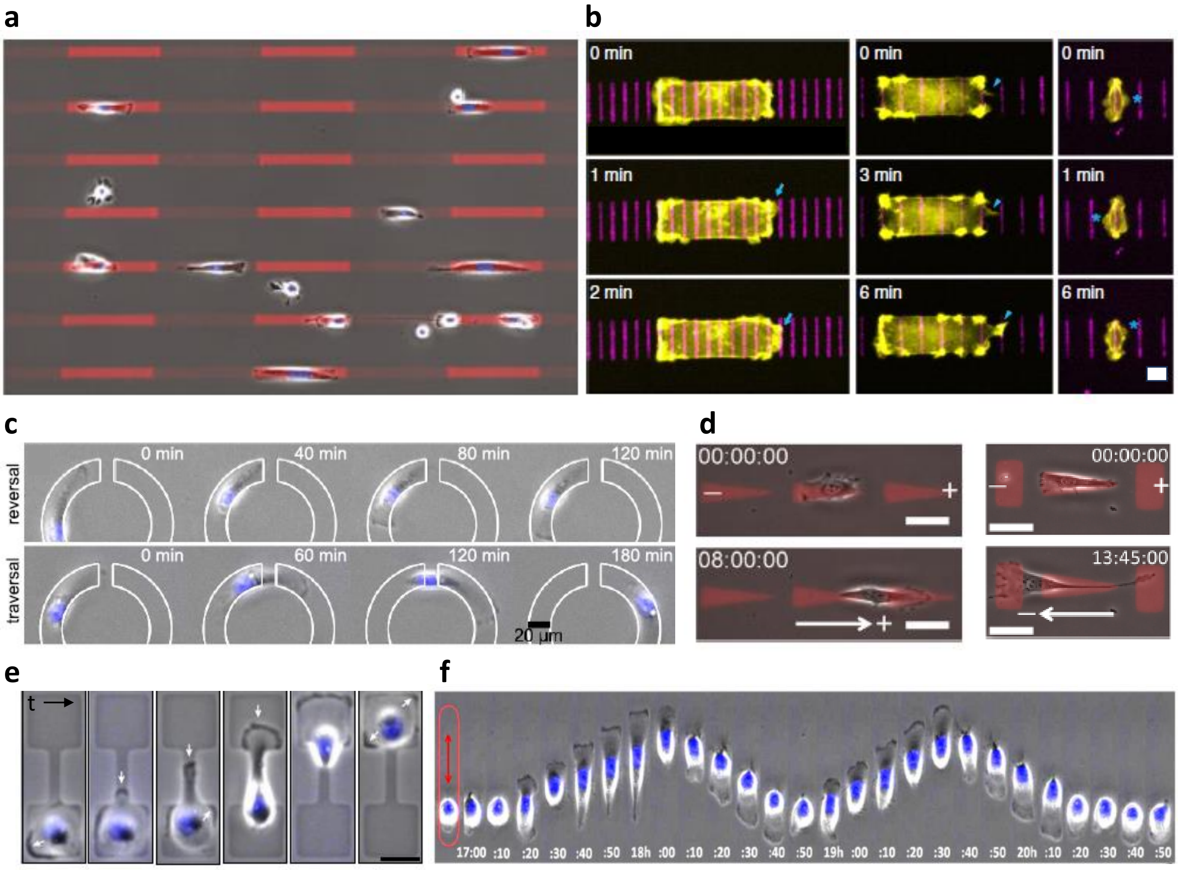

Figure 2.2: Cell migration on nonhomogeneous matrix and constrained micropatterns. In all the following examples, micropatterns are coated with fibronectin while the surrounding area is passivated with Pll-g-PEG (poly-L-lysine-grafted-poly(ethylene glycol)). **a**, Cancer cells on micropatterned lines with different concentrations of fibronectin. Red areas show higher concentrations than light areas. Areas are 150 μm long and 10 μm wide. Adapted from Schreiber et al. 2020 [52]. **b**, Human endothelial cells (yellow) on fibronectin strips (magenta) with gaps of 4 μm for the left column, 6 μm for the middle column and 10 μm for the right column. For a gap of 10 μm, the cells form blebs and cannot cross. Scale bar = 10 μm, adapted from Garbett et al. [48]. **c**, Human cancer cells migrating on ring-shaped micropatterns. The top panel shows a cell that does not cross the non-adhesive barrier and reverses its trajectory, while the bottom panel shows the cell crossing. Scale bar = 20 μm, adapted from Schreiber et al. 2016 [54]. **d**, On triangular micropatterns, cells cross at the top of triangles, whereas on triangle and rectangle micropatterns, cells cross at the base of triangles. Scale bar = 50 μm, adapted from Caballero et al. [50]. **e**, Human cancer cell migration on two-state micropatterns. White arrows indicate cell protrusions. Scale bar = 25 μm and the time-scale between images is 10 min. Adapted from Brückner et al. [49]. **f**, Human cancer cells oscillating on a rectangular micropattern shown in red, 120 μm long and 20 μm wide. Adapted from Zhou et al. [53].

In vivo, pericytes also encounter constraints and non-uniform substrates. In fact, as explained in chapter 1, pericytes are located along microvessels in a chain-like organisation. Each pericyte has its own territory and does not touch its neighbour. This situation could be compared to constrained migration along a certain length. In addition, PCs migrate on non-uniform substrates by anchoring to fibronectin patches [32]. They can also form bridges between two separated capillaries [9].

2.1.3 Mathematical description of cell trajectories on 1D patterns

There are a number of different models to describe the trajectory of a single cell. Here, we discuss some commonly used models to describe mesenchymal cell migration in 2D or 1D. In the past, the Ornstein-Uhlenbeck (OU) process, a simple model of persistent random motion, has been widely used to describe 2D cell migration [55, 56]. At short timescales, cells exhibit persistent motion, whereas at long timescales (longer than the persistence time), they exhibit random motility [57, 58]. Typically, the mean square displacement (MSD) and the probability distribution of velocities are used to determine whether cells are following an OU process. The MSD is proportional to t^2 for timescales shorter than the persistence time and proportional to 't' for long timescales. The probability distribution of velocities follows a normal Gaussian distribution as for Brownian motion [58]. As mentioned, the OU process is the simplest persistent random walk process, but there are many other versions. Taking the example of confined or restricted migration mentioned in the previous section 2.1.2 for example, Caballero et al. [50] proposed a model of persistent random walk to characterise cells migrating on asymmetric adhesive patches, using the experimentally measured biased probabilities of protrusion and adhesion as inputs. Note that a discrete model is used here, as it is the probability of observing a step in one direction that is calculated and not the MSD. Bruckner et al. [49] used a generalisation of the equations of the persistent random walk model to describe cell migration on structured micropatterns. In their generalisation, cell speed can depend on cell position, which is not the case for a simple persistent random walk.

Cells do not always exhibit persistent random motion properties, such as the Gaussian probability distribution of velocities, and other models are used to describe cell dynamics. For example, Alessandro et al. [59] studied single-cell migration on micropatterned lines and demonstrated the existence of spatial memory by using a self-interacting random walk model that takes into account the number of times a territory has been visited by a cell and interaction between the cell and that territory. In Schreider et al. 2016 [54] cells are first placed on ring-shaped micropatterns and then on ring-shaped micropatterns with a non-adhesive gap (Figure 2.2.c). Two-state motion is used to describe cell migration. In two-state motion, the cell alternates between ballistic motion (directional phase) and diffusive motion. Other models take forces exerted by the cell into account, as well as intracellular signalling or adhesion with the substrate [46, 53, 54].

2.1.4 Chapter outline

To characterise pericyte migration, in the first part of this chapter we use continuous micropatterned lines, which we will call 'infinite lines', to mimic the lateral confinement to which PCs are subjected in vivo. In the second part, we add non-adhesive gaps to the infinite lines to constrain PCs longitudinally, which we will refer to as 'constrained micropatterns'. As explained above, the latter can be compared to in vivo PCs arranged in a chain-like fashion that experience contact inhibition with their neighbours [27]. Cells are imaged with a bright-field microscope, and custom codes are developed to track the centroid and extremities of the cells. Based on these measurements, several parameters such as cell speed and length are quantified. A simple 1D model is developed to characterise cell motility. Finally, the phenomenon of gap crossing is analysed and quantified as a function of gap length and adhesive micropattern's length and width.

2.2 Materials and methods

2.2.1 Micropatterning

Patterns are created using PRIMO micropatterning system (Alvéole). The FluoroDish (WFD3523) is first activated with a Plasma cleaner (PDC-002-CE) for 45 seconds. A polydimethylsiloxane (PDMS) Stencil composed of 4 wells of each 4 μm diameter (Alvéole) is then placed on the bottom of the FluoroDish, where each well is treated with a blocking solution 0.1 mg/mL poly-L-lysine-grafted-poly(ethylene glycol) (PLL(20)-g[3.5]- PEG(2), SuSoS) for 1 hour and then washed out several times with Milli-Q water to avoid drying. The FluoroDish is then transferred to the microscope stage of an inverted microscope (Nikon EclipseTi) equipped with PRIMO system (Alvéole) and covered with a 7 μl drop per well of photosensitive reagent PLPP (Alvéole). It is important to avoid drying during the procedure to ensure the pattern quality. PRIMO (Alvéole) technology is a maskless photopatterning system. It projects an image of the desired pattern instead of a physical mask. Here, line motifs with gaps (designed in Inkscape) are projected. The PLPP is then degraded at the desired locations using a near-UV light (375 nm) through a 20x objective (Nikon, Plan fluor, $NA = 0.45$). After rinsing with Milli-Q water, fibronectin at 50 μg/ml (Sigma Aldrich) is incubated for 15 minutes to coat the burned area with adhesive proteins. To allow the visualisation of the micropattern, fibrinogen 647 (1.5 mg/ml, Invitrogen) is added to the fibronectin solution. The excess of fibronectin is then washed out with sterile phosphate-buffered saline (PBS). Patterned substrates are used immediately after preparation or up to 24 hours later (stored in PBS at 4℃). The quality of the micropatterns is assessed by visual inspection under the microscope and by measuring the image intensity profile along a line using ImageJ. Note that a step-by-step protocol of micropattern fabrication using Alvéole is detailed in appendix A.1.

2.2.2 Cell culture

Primary human brain vascular pericytes (PCs, SienCell) are cultured with pericyte growth medium (Pericyte Medium-phenol red free, 1201-PRF-SC, SienCell) in 5 ml culture flasks at 37℃ and 5 vol% CO_2, the medium is changed every two days. PC culture flasks are coated with Poly-L-Lysine (0.01%, Sigma Aldrich) to promote cell growth. Pericytes are cultured and used between passages 2 and 6 to maintain the cell phenotype. When they reach approximately 80% confluence, cells are detached using 10% (500 μl) trypsin (Tryple express, Gibco) for 3 minutes in the incubator and they are then seeded directly onto the patterned surface at a low density (6000 cells/ml) to avoid cell-cell interactions. Note that for PCs, approximately 80% confluency is used instead of full confluency to avoid influencing cell function or phenotype [38]. The samples are then incubated at 37℃ in 5% CO_2. After 1 hour, the non-adherent cells are washed with PBS (twice), and 2 ml fresh medium is added to the fluorodish.

Note that human umbilical vein endothelial cells (HUVECs, Lonza) are also used as preliminary test to compare with PCs. HUVECs are culture with EGM2-MV medium (Lonza) and are used at passage 5. The same experimental conditions are used as for PCs.

2.2.3 Microscopy

2.2.3.1 Live imaging

Live experiments are performed using an inverted microscope (Nikon Eclipse Ti) with temperature and CO_2 levels controlled by NIS software (Nikon). A 10x objective (Nikon, Plan fluor, $NA = 0.30$) is used. At least one fluorescence image of the patterns at each position is taken at the beginning of the experiment. Then the cells are imaged using phase contrast imaging with one image taken every 10 minutes for 24 hours. At the end of the experiment, the cells can be fixed and then stained. To visualise nuclei during live imaging, cells are incubated with Hoechst 33342 (Thermo Fisher Scientific, $1/10,000$ dilution) for 3 min and then seeded onto the micropatterns.

2.2.3.2 Cell fixation and staining

Cells are fixed with 4% paraformaldehyde (28908, Thermo Fisher) in PBS for 15 minutes, permeabilised with PBS + Triton-X-100 0.1% for a further 15 minutes and blocked with 3% bovine serum albumin (BSA) solution in PBS for 1 hour. The cells are then incubated with the primary antibody, mouse anti-paxillin ($1:200$, MA5-13356, Thermo Fisher) in PBS for 1 hour at room temperature. Cells are then washed three times with PBS and incubated for 1 hour at room temperature with Alexa Fluor 488-conjugated donkey anti-mouse antibody ($1:400$, ab150-0105, Abcam), DAPI ($1:1,000,000$, Sigma-Aldrich) and phalloidin Alexa Fluor 594 ($1:200$, A12379, Thermo Fisher) to detect focal adhesions (FAs), nuclei, and F-actin, respectively. Finally, samples are rinsed and incubated in PBS at 4° C overnight. Cells are then imaged using an inverted microscope (Nikon Eclipse Ti) with a 40x water immersion objective (N40XLWD-NIR, Nikon).

2.2.4 Image processing and data analysis

2.2.4.1 Cell crossing analysis

To study the percentage of cells that cross non-adhesive gaps, the time-lapse movies are analysed by eye, and strict criteria are applied to retain an experimental realisation for analysis:

- Cells should not undergo division during the 24 hours of tracking
- Cells dying before 24 hours are not considered
- Micropatterns should be well defined and fibronectin coating homogeneous
- No contamination should be detected
- If a cell crosses the gap and then collides with another cell, the cross is counted; however, a case where these two events happen in the opposite order is excluded from the analysis, as cell contact could alter cell behaviour.
- A cross is counted if the cell can move or extend from its initial adhesive area to at least the middle of the next one.

2.2.4.2 Cell segmentation and tracking

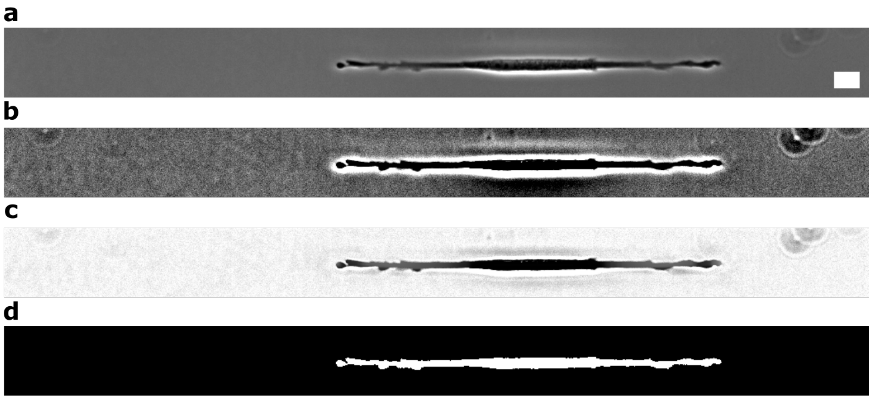

Figure 2.3: Steps to obtain pericyte mask using ImageJ a, Bright-field image using phase contrast of a pericyte on a $10\ \mu$m continuous line. **b**, First step: *unsharp mask*. **c**, Second step: *subtract bright background*. **d**, Final binary image of the pericyte mask obtained after *remove outliers*, *threshold* and then *particle analysis*. Scale bar = $20\ \mu$m .

First, a precise mask of the cell is generated using either an automatic code developed by Prof. Pablo J. Sáez (University Medical Center Hamburg-Eppendorf) or a custom written semi-automatic code. The automatic code uses a classifier previously trained with the *Trainable Weka Segmentation* plugin on a sample of our image dataset (PCs on constrained micropatterns of $10\ \mu$m width and $150\ \mu$m long) with different selected features [60]. It then performs *intensity thresholding* and *particle analysis* on the detected cell shape using ImageJ. The alternative image analysis technique is a macro that calls ImageJ functions in the following order: *unsharp mask* (Figure 2.3.b), *subtract background* (Figure 2.3.c), *remove outliers* before *intensity thresholding* and *particle analysis* (Figure2.3.d). The two procedures are equivalent, but the semi-automatic one allows more accurate detection of very thin processes and cells on micropatterns with a width of $20\ \mu$m. This difference is explained by the fact that the automatic code has only been trained on cells on $10\ \mu$m wide micropatterns and is, therefore, less robust for the detection of cells with different aspects, like brightness or shape.

2.2.4.3 Quantification of pericyte migration

Once a binary mask of the cell shape is created, we use custom written scripts in Matlab to determine the centroid and the extreme position of the cells, thus obtaining the cell position as a function of time. The centroid of the cell is calculated using Matlab's *centroid* function.

- The length of the cell, L is defined in Matlab as the distance between the two extremities (pixels) of the cell in the pattern direction. In our analysis, the mean cell length is usually used (L_{mean}).
- The instantaneous cell velocity of centroid is calculated as $\vec{v}(t) = (\vec{y}(t) - \vec{y}(t - \Delta t))/\Delta t$, with $\vec{y}$ the centroid position. From these data, the velocity autocorrelation function (VACF) is calculated. The following formula is used:

$$VACF(\tau) = \frac{\sum_{t=1}^{T-\tau}(v_t - \bar{v})(v_{t+\tau} - \bar{v})}{\sum_{t=1}^{T}(v_t - \bar{v})^2}, \tag{2.1}$$

  where $\tau = 0, 1, \ldots, T-1$, represents the time lag between two positions, given by $\tau\Delta t$, with $\Delta t = 10$ min the time interval between two consecutive images and $T = 145$.

- Cell average centroid speed is calculated as $V_{mean} = \frac{1}{N}\sum_{i=1}^{N}|v_i|$ with N the total number of analysed cells.
- Mean squared displacement (MSD) is calculated with the following formula:

$$MSD(\tau) =< \Delta y(\tau)^2 >=< (y(t_0 + \tau) - y(t_0))^2 > \tag{2.2}$$

  Where $< .. >$ denotes a combined average over all initial times t_0, τ represents the time lag between two positions (here 10 min), τ = 1,...,T-1, and $T = 145$, MSD($\tau = 0$) = 0 and N the total number of cell tracks.

- To determine the probability distribution of speed, the Matlab function *histcounts* is used to partition the instantaneous speed values into bins of fixed width: 5 μm/h.

2.2.4.4 Focal adhesion detection

The number of focal adhesions and the total focal adhesion area are automatically detected using an ImageJ macro developed by Natale et al. [61]. Only FAs whose area is between 1 and 10 μm^2 are considered (Figure 2.4).

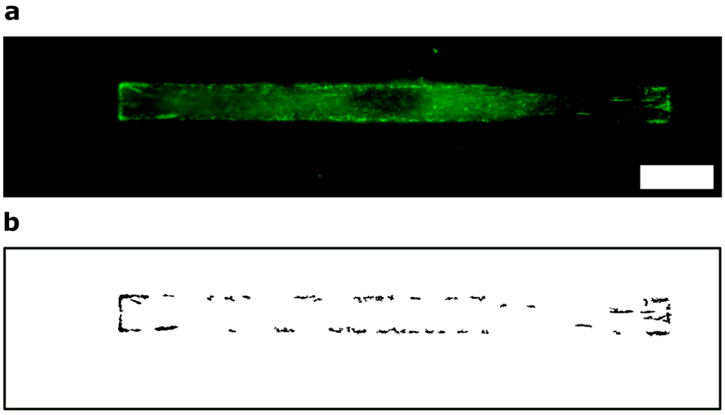

Figure 2.4: Focal adhesion analysis with ImageJ macro. **a**, Fluorescent image of a pericyte on a micropattern. Focal adhesions are stained with paxillin (green). **b**, Resulting mask of FA after ImageJ macro. Scale bar = 20 μm.

2.2.4.5 Statistical analysis

The statistical tests used in this chapter are non-parametric tests because our data sets are rather small and do not follow a normal distribution. When comparing a population with a given value, we use a signed test; when comparing two conditions, we use the Wilcoxon rank-sum test; and when comparing more than two conditions, we use the Kruskal-Wallis test. The Matlab functions *signrank*, *ranksum* and *kruskalwallis* functions are used respectively.

2.3 Results

2.3.1 1D pericyte migration on confined micropatterns

2.3.1.1 Micropatterned lines to mimic microvessel geometry: from fabrication to analysis

As explained in the introduction to this chapter (section 2.1), we choose to study pericyte (PC) migration on infinite lines [1] rather than on 2D surfaces. Indeed, thin lines confine pericytes in a similar way as they are on microvessels in vivo. Furthermore, it is shown in the literature that, despite their simplicity, many features of 1D substrates can mimic cell behaviour in 3D, such as cell morphology or speed [44]. Here, we produce narrow micropatterned lines to confine pericytes in a range of width similar to microvessels perimeter. In vivo, PCs are located on small blood vessels ranging from pre-capillary arterioles with diameters d = 15-20 μm and post-capillary venules; d = 10-30 μm to capillaries with d= 4-10 μm [2]. Therefore, to achieve similar confinement as on capillaries, the width (W_p) of the infinite lines should be between $W_p \sim 10$ μm and $W_p \sim 30$ μm. At the beginning of this project, we started with infinite lines of $W_p = 10$, 20 and 31 μm and even thinner W_p = 5 μm (section 4.2.1, Figure 4.1). Still, for simplicity, we decided to first focus on studying PCs on infinite lines of W_p = 10 μm for quantitative analysis.

Infinite lines are coated with fibronectin, which is known to be the preferred adhesive protein of PCs (Figure 2.5.a) [32]. The surrounding area is passivated with cell-repellent poly-L-lysine-grafted-poly(ethylene glycol) (Pll-g-PEG). Figure 2.5.b shows the quality of the micropatterns with adhesive areas that correspond to areas with higher grey values (fibronectin plus fibrinogen) and repulsive areas to areas with lower grey values (Pll-g-PEG). PCs are seeded onto these infinite lines at low density to avoid cell collision during imaging. PCs are imaged with bright-field microscopy for 24 hours with an acquisition every 10 minutes. To quantify cell dynamics, cell shape is obtained using either the segmentation algorithm developed by Prof. Pablo J. Sáez (Figure 2.5.c) or the semi-automatic code developed by us (section 2.2.4.2, Figure 2.3). These techniques allow us to obtain the precise shape of the cells, as shown in Figure 2.5.c and their position as a function of time by tracking both the centroid and the two extremities of the cells. Tracking the centroid provides information about the position of the cell as a whole. We wondered if the position of the centroid can be approximated by the nucleus position in our experiments. To verify this, PCs are cultured with Hoechst to visualise the nucleus, and both the position and speed of the centroid and the nucleus are compared. We can see in Figure 2.6.a that the position of the centroid of the cell and the trajectory of the nucleus are similar. However, when we compute the difference between the speeds of the centroid and the nucleus and then use the statistical sign test (Figure 2.6.b), we obtain a $p_{value} = 0.002$ showing that the test rejects the null hypothesis of a population with a median of 0 at the 5% significance level. Therefore, we cannot say that the centroid position corresponds to that of the nucleus based on this comparison. For this study, we decided to continue the analysis with the detection of the centroid, and avoid using dies which might have a non-negligible impact on cell behaviour by their toxicity. In the future, it will be interesting to track the cell nucleus, especially for the section 2.3.2 and see if it can bring more information.

---

[1] Infinite lines are quite long of at least 1.5 mm.

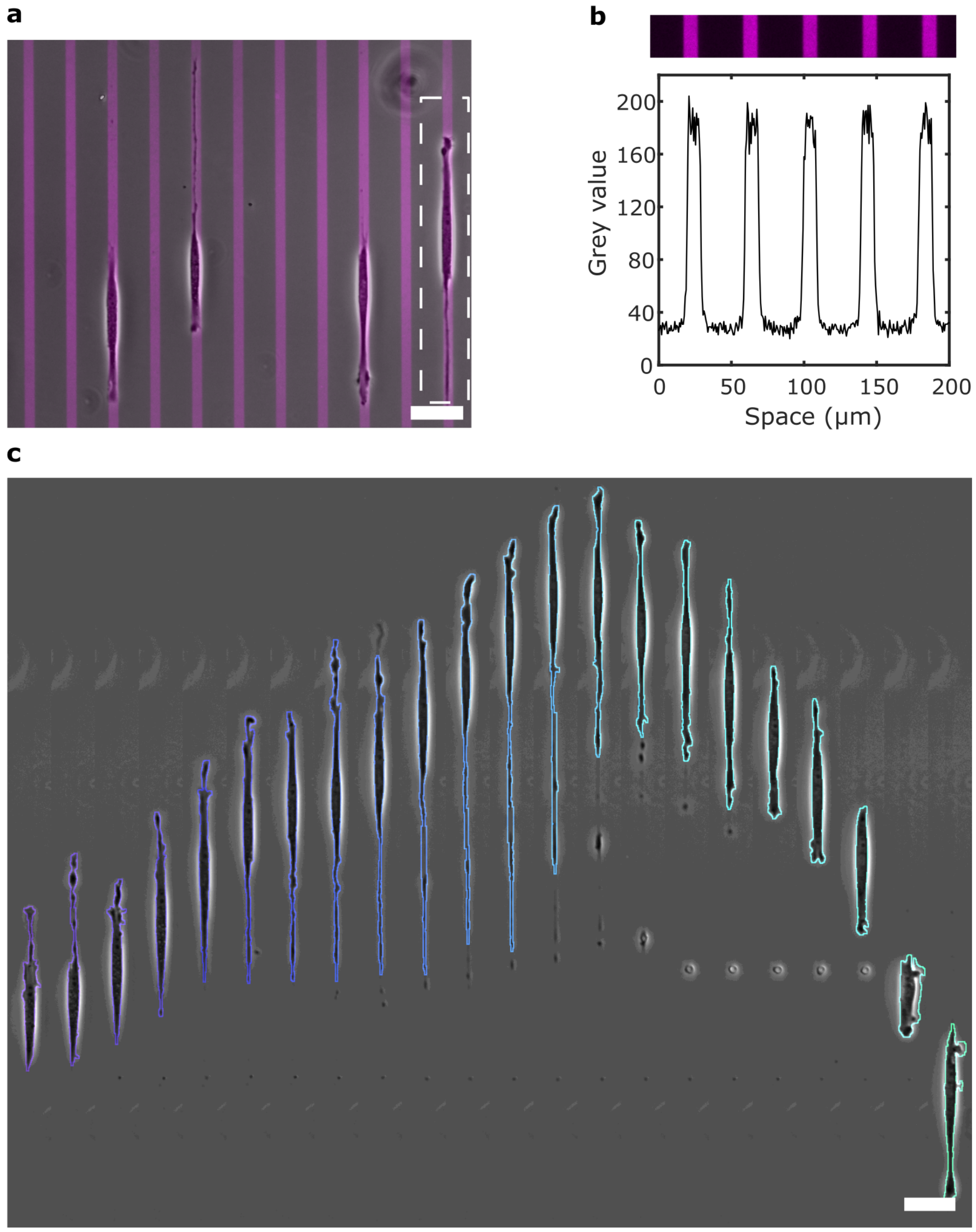

Figure 2.5: Experimental setup of pericytes confined on infinite lines. **a**, Pericytes seeded on fibronectin lines (magenta) of $W_p = 10$ μm width separated by non-adhesive areas coated with Pll-g-PEG. **b**, Cropped image of fibronectin-coated lines shown in (**a**) with intensity quantification along a horizontal line, showing the uniformity of the micropatterns. **c**, Detection of the pericyte shape using the segmentation algorithm developed by Prof. Pablo J. Sáez. The stack in time of the obtained mask of the pericyte framed in (**a**) is indicated in colour, showing a precise detection of the cell contour.The time scale is one hour between two consecutive positions. Scale bars = 50 μm.

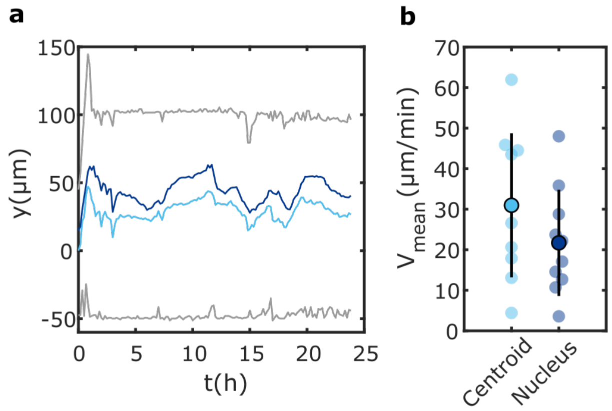

Figure 2.6: Pericyte centroid and nucleus trajectories. a, Kymograph of a pericyte on a micropattern for 24 hours. The cyan line corresponds to the centroid of the cell and dark blue to the nucleus, and grey lines to the extremities of the cells. The nucleus is tracked using Hoechst dye. **b**, Comparison of the average speed of the centroid and nucleus for 24 hours. For the statistical sign test we use the difference between centroid speed and nucleus speed for each cell. Error bars correspond to the standard deviation of the mean (STD). $n_{cell} = 10$ and data are extracted from one experiment.

2.3.1.2 Pericytes on confined infinite lines display morphologies similar to in vivo pericyte phenotypes

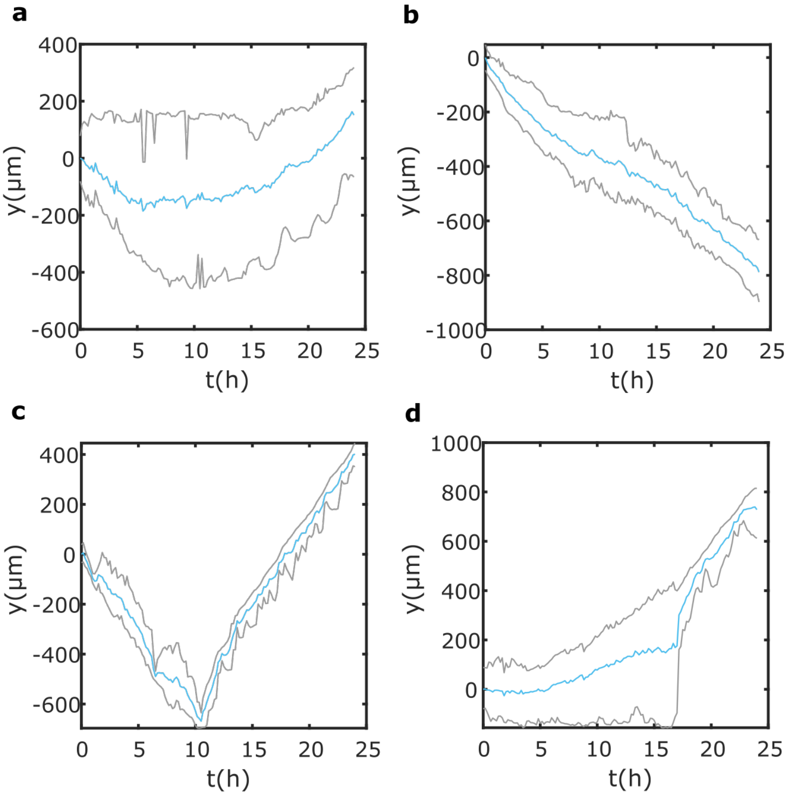

Figure 2.7: Representative kymographes of the different pericyte migration behaviours observed on infinite lines. Cyan lines correspond to the centroid of the cells, and grey lines to the extremities of the cells. **a,b**, Spreading pericytes that are either undecided (**a**) or persistent (**b**). **c**, Short pericytes with directed trajectories. **d**, Alternating pericytes that elongate and then retract as in stick and slip behaviour.

In Figure 2.7 we observe that pericytes display a large heterogeneity of migration behaviours across the population. In this paragraph, we propose a classification in three categories based on the kymographs and bright-field movies: spreading, short and alternating.

- The ’spreading’ category, which constitutes the majority of cells (48%) , is characterised by pericytes that tend to spread with a length that can reach $500\ \mu$m (Figure 2.7.a,b). In this category of spreading PCs, we can observe cells that are undecided with two lamellipodia (Figure 2.7.a and 2.8.a). Usually, these cells are less motile than the other two categories, however their centroid remains motile. Conversely, other spreading PCs have a persistent trajectory with a clear front and rear (Figure 2.7.b and 2.8.b).
- The ’short’ category consists of pericytes with an average length of less than $150\ \mu$m and a higher speed when compared to spreading ones, they display directed trajectories (25.9%) (Figure 2.7.c and 2.8.c).
- Finally, some cells are classified as ’alternating’ as they exhibit both behaviours (25.9%), with phases of extension followed by phases of retraction (Figure 2.7.d), such as stick and slip behaviour [46].

Note that, compared to other studies of cells on infinite lines, oscillatory behaviour is hardly observed [59]. The morphology we observe on infinite lines is closer to in vivo PCs with thin, elongated shape than PCs on 2D substrates. Indeed, as a control, PCs are seeded on glass slides coated with fibronectin and observed for 24 hours. As shown in Figure 2.8, in the absence of confinement, PCs can display a spread shape (Figure 2.8.d), a circular shape (Figure 2.8.e) or a short polarised shape (2.8.f). In both spread and circular morphologies, the cells appear less motile. Compared to 1D assays, most PCs are short, as in Figure 2.8.f, and very few are thin and elongated. Note that our observations on 2D substrates agree with the literature [38].

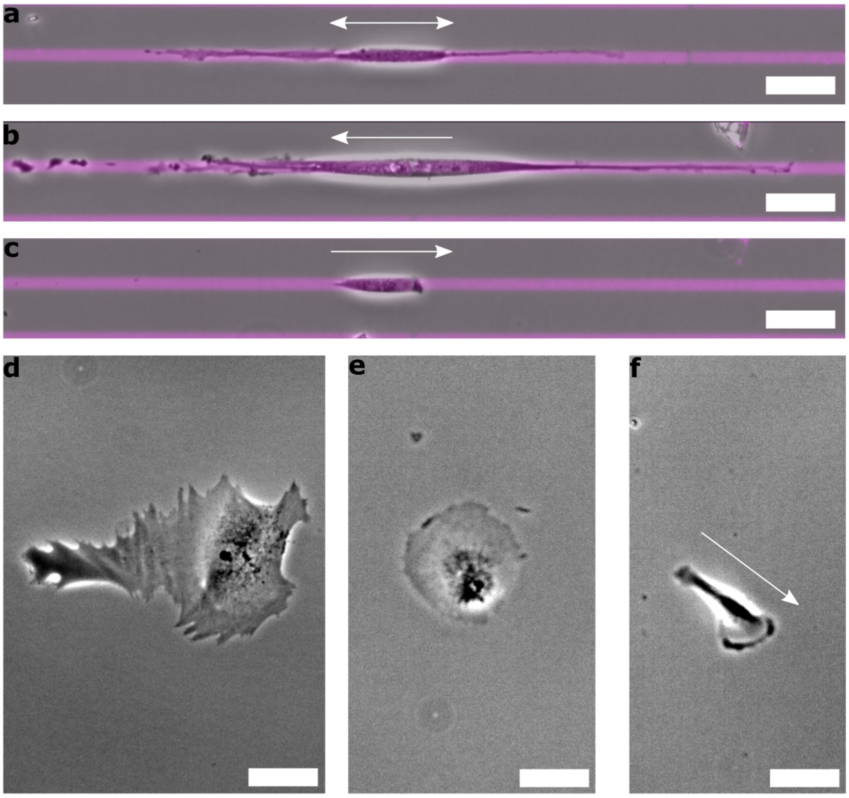

Figure 2.8: Pericyte morphology on 1D infinite lines and 2D surfaces. Bright-field images using phase contrast of: **a**, undecided spreading pericyte on infinite lines (magenta). **b**, Polarised spreading pericyte and in **c**, short directed PC. **d,e,f** Representative morphology of pericytes in 2D, with spreading PC (**d**), circular PC (**e**) and short directed PC (**f**). The white arrows indicate the direction in which the cells move. Scale bars = $50\ \mu$m.

The average cell length over time (Figure 2.9.a) shows that the majority of PCs display a length between 50 and $350\ \mu$m, with a median of $206\ \mu$m. This is of the same order of magnitude as in vivo capillary pericytes, whose length can vary between $\sim 50\ \mu$m and $\sim 250\ \mu$m [2]. In addition to the length, which is comparable to in vivo pericytes, the area is also similar to in vivo values. A characteristic feature of pericytes is that they usually do not cover the entire vessel surface [2]. In fact, PCs on capillaries have an average vessel coverage of $\sim 51\%$ to $\sim 72\%$. In our experiment, vessel coverage is calculated as the area of the cell divided by the rectangular area corresponding to the length of the cell times the width of the micropattern. Figure 2.9.b shows that the average coverage is $69.3 \pm 12.5\%$.

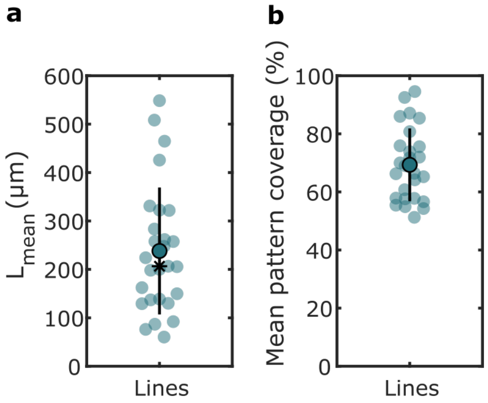

Figure 2.9: Pericyte length and coverage on infinite lines are similar to in vivo values. **a**, Average cell length over 24 hours (L_{mean}) on infinite lines. The coloured dot with a black outline represents the mean $L_{mean} = 235$ μm and the star the median $L_{median} = 206$ μm. **b**, Average PC coverage of micropatterns. The coloured dot with a black outline represents the mean 69.3%. Each coloured dot represents a cell. Error bars indicate STD. $n_{cell} = 27$ and at least three different experiments are used.

2.3.1.3 Pericyte migration on infinite lines can be modelled as Brownian motion with dry friction

The extreme heterogeneity of migration behaviours described above may appear discouraging to find any type of universal rules to describe pericyte migration. In spite of the difficulty of such a task, in the following, we will propose some elements of theoretical interpretation of the observed pericyte migration behaviour, which must be understood as an empirical description. The first parameter to look at to gain insight into the behaviour of confined PCs, based on trajectories is cell speed. We calculate the average centroid speed (V_{mean}) of PCs over time and compare it to the average PC length (L_{mean}). Figure 2.10 shows a negative correlation between PC speed and length over the whole population ensemble. Thus, short PCs of $L_{mean} \sim 100$ μm have an average speed $V_{mean} \sim 60-80$ μm/h, while longer PCs of $L_{mean} \sim 250$ μm exhibit a smaller average speed of $V_{mean} \sim 50$ μm/h. This tendency is consistent with previous observations for single-cell migration on 1D micropatterned lines [46]. However, our measured PC speeds are larger than those reported for other cell types. Indeed, our measured speed ranges from 20 to 90 μm/h, whereas previous results as The first World Cell Race obtained speeds between 6 and 60 μm/h for comparable cell length and similar setup [45, 46]. This shows that our cells are highly motile despite their length.

Let us next derive a mathematical interpretation compatible with the observed relationship between speed and length. As we discussed in the introduction of this chapter (section 2.1), the Ornstein-Uhlenbeck process (OU, simple persistent random walk) is often used to describe cells in 2D [55, 56]. The OU process can be described by the following Langevin equation [57, 58] :

$$\frac{dv}{dt} = -\beta v + \gamma(t), \tag{2.3}$$

where $-\beta v$ is the viscous friction term (or damping) that comes from adhesion between the cell and the substrate and which is proportional to the velocity v. The other term on the right-hand side, $\gamma(t)$ corresponds to a Gaussian white noise term and can be assimilated to the metabolic activity of the cell. To see if we can use the OU process to model our observed cell migration, we first look at the mean square displacement (MSD, section 2.2.4.3 equation 2.2) of the PCs to see if it can be correctly described by the OU model. The OU model is characterised by MSD, $< \Delta y(\tau)^2 > \sim \tau^2$ at short timescale which corresponds to ballistic motion and for long timescale a diffusive behaviour is observed with $< \Delta y(\tau)^2 > \sim \tau$ with the transition between regimes is the so-called persistence time [58]. We emphasise here that τ is not the time of the experiment but rather the time difference between two data points. Thus, the MSD for a given τ is obtained as an average over all pairs of data points along the experiment that are separated by a time interval τ. We can see on the log-log plot (Figure 2.11) of the MSD that at short timescale (up to $5h30$) for the average MSD, $< \Delta y(\tau)^2 > \sim \tau^{1.6}$ which corresponds to super-diffusive behaviour. In contrast, at long time scale ($\tau > 6h$) diffusive motion is observed with $< \Delta y(\tau)^2 > \sim \tau^{0.9}$. Note that for $\tau > 21h$, a slope of $\approx \tau^{1.8}$ is observed, which can be due to the fact that at very large τ there are fewer data points and, therefore, no conclusions can be drawn from this section of the plot.

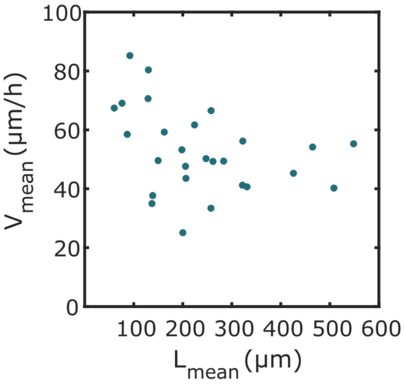

Figure 2.10: Inverse relationship between average pericyte speed and length. Average speed (V_{mean}) of pericytes on infinite lines decreases as average PC length (L_{mean}) increases. Each dot represents one cell. n_{cell} = 27 and at least three experiments are used.

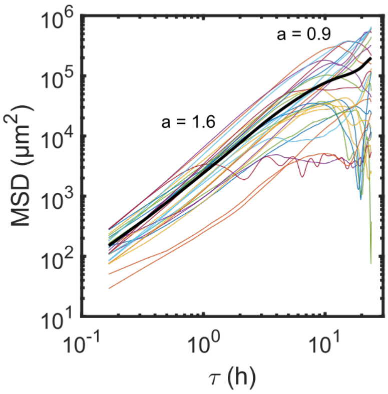

Figure 2.11: MSD of pericytes migrating on infinite lines over time in log-log representation. The black line is the average MSD with a slope of $a = 1.6$ at short time scale which represents super-diffusive motion and a slope of $a \approx 1$ at long time scale, which is typical for random motion. n_{cell} = 27 and at least three experiments are used.

The observed MSD thus appears in reasonable agreement with the long-time regime of the OU process but in imperfect agreement at the short-time regime. To further compare the OU description to our experiments, we examine the probability distribution of the instantaneous centroid speed (p). We study the probability distribution of the absolute value of the velocity. For an OU process, the velocity probability distribution should follow a Gaussian distribution with $p \sim Ae^{-2rv^{\gamma}}$ and $\gamma = 2$ [58]. However, our experimental data (Figure 2.12.a) rather follow an exponential decay. This is made clear by plotting the data on a log-log scale, which is well described by an exponential probability distribution $p \sim 2re^{-2rv}$ ($\gamma = 1$) rather than by a Gaussian ($\gamma = 2$) (Figure 2.12.b). We therefore discard the OU process to describe our data. Such an exponential distribution of the speed has been reported in other studies, such as that of Christensen et al. [62], who explained the exponential tails observed in the velocity distributions of several cell types by assuming that cell-substrate friction is better described as solid (Coulomb) friction compared to viscous friction. Therefore, we propose characterising pericyte motion as Brownian motion with dry friction, as conceptualised by De Gennes [63]. This type of motion is governed by the generalised Langevin equation:

$$\frac{dv}{dt} = -\beta v - sgn(v)\Delta + \gamma(t) \tag{2.4}$$

Here, we assume that dry friction is dominant over viscous friction, thus neglecting the corresponding term:

$$\frac{dv}{dt} = -sgn(v)\Delta + \gamma(t) \tag{2.5}$$

with $sgn(v)$ the sign of the velocity, Δ the magnitude of the dry friction force and $\gamma(t)$ the noise term. Note that, unlike viscous friction, dry friction is independent of the velocity magnitude. From equation 2.5 the following probability distribution of velocities is obtained:

$$p(|v_x| = v) = 2re^{-2r|v|} \tag{2.6}$$

where $r = \Delta/(2K)$ and K characterises the random noise correlation, $\langle\gamma(t_1)\gamma(t_2)\rangle = K\delta(t_1 - t_2)$, which can be interpreted as a measure of the metabolic agitation of the cell. Equation 2.6 is of the form $p \sim e^{-2rv}$ and it satisfactorily describes our experimental data with the fitting parameter value r = 0.009 h/μm (Figure 2.12.c).

It is important to recall that, in order to use instantaneous speed as a variable, it is important to ensure that it is correctly defined and does not depend on the time interval used [64]. In our case we chose 10 minutes as the time interval and then analysed the same data with larger intervals of 20 and 30 minutes. We can see in Figure A.2.a that there is a small variation between the speeds defined with an interval of 10, 20 or 30 minutes, which raises the question as to whether our cells exhibit a ballistic regime over a certain time scale, which could be either the smallest time scale or an intermediate one. However, we can see from Figure A.2.b that the distribution of instantaneous speed follows the same exponential decay for the three time intervals (10, 20 and 30). This observation, together with the moderate speed sensitivity to the choice of time interval, suggests that conclusions regarding the choice of model are robust. A shorter time interval could be tested in the future to further investigate this part.

This model predicts a relationship between cell speed and length. According to the model, the average cell velocity can be written as [63]:

$$v \sim \sqrt{\langle v^2 \rangle} = \frac{1}{2r} = \frac{K}{\Delta} \tag{2.7}$$

From this result, we proceed to obtain a prediction of the speed-length relationship. We hypothesise that K is a constant independent of cell shape that characterises the average behaviour of the whole population and that the friction parameter Δ is proportional to the cell-substrate contact area, i.e., $\Delta = C_\Delta Le$, with C_Δ a constant, L the cell length and e the cell width, which we assume equal to the pattern width, $e \approx W_p$. These hypotheses lead to the following relationship:

$$vL = \frac{K}{C_\Delta W_p} \Rightarrow v = \frac{B}{L} \tag{2.8}$$

where we define the constant $B = K/(C_\Delta W_p)$. We test this prediction by comparing it with our experimental data. From Figure 2.12.d we observe that equation 2.8 is able to describe the qualitative tendency of our data reasonably well. To produce the theoretical fit in the figure, we do not choose the value of B to optimise the fit. Rather, we estimate the value of B from the global mean values of the cell speed and cell length obtained respectively as average and median over the entire population, $B \approx \overline{v}\overline{L}$, with $\overline{v} = 1/(2r)$, $r = 0.009$ h/μm derived in Figure 2.12, and $\overline{L} = 206$ μm obtained in Figure 2.9.a. This results in an estimate of the constant, $B \approx 1.1x10^4$ μm^2/h, which yields the theoretical prediction in Figure 2.12.d, which provides a reasonable qualitative description of the experimental tendency. From the model prediction, we can see in Figure 2.12.d that the longer the cell, the lower the speed (the higher the friction), and that the slope asymptotically decreases to 0 μm/h for very long cells. For cells longer than 400 μm we can observe an average speed of $V_{mean} \sim 40$ μm/h, while the model predicts that the speed would continue to decrease with increasing cell length. There are only four experimental measurements in this regime, so more experiments should be done to draw conclusions about this difference.

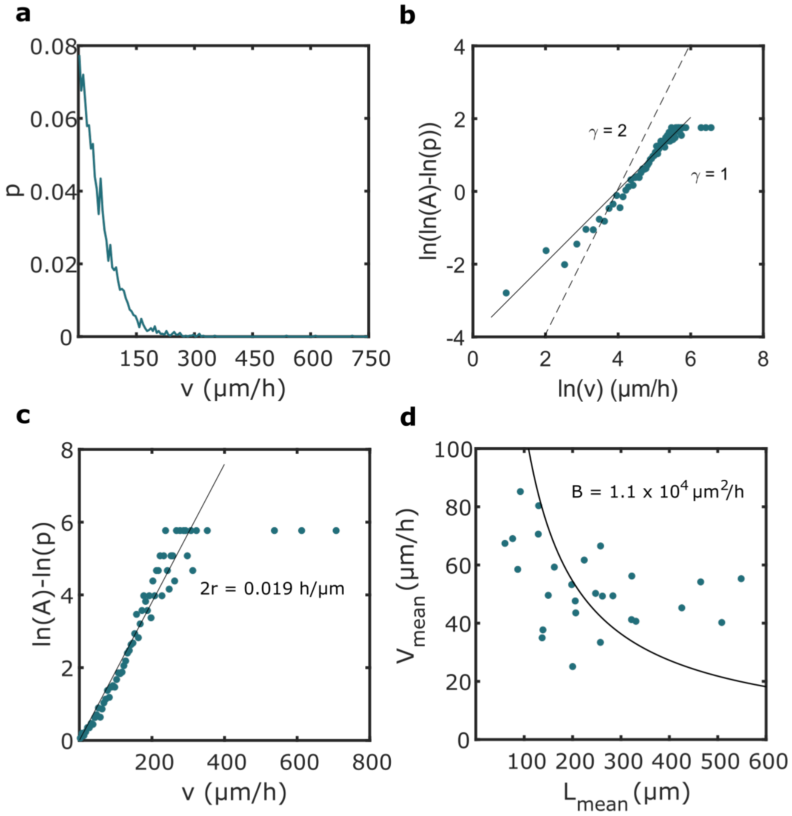

Figure 2.12: Exponential decay of the speed distribution of pericytes on infinite lines. **a**, The speed probability distribution over the cell population shows a non-Gaussian shape and points toward an exponential decay. **b**, Data from (**a**) are replotted in log scale to find the optimal fit. A fit of the expression $p \sim Ae^{-2rv^{\gamma}}$ shows that the best fit corresponds to $\gamma = 1$ (exponential dependence) rather than $\gamma = 2$ (Gaussian). The constant *A* on the y-axis corresponds to the experimental probability of having a speed of zero. **c**, The same data as in (**b**) are used to find the value $2r$ for $p \sim Ae^{-2rv}$. From that value, we can calculate the ratio between agitation K and dry friction Δ which corresponds to $1/r$. The constant *A* on the y-axis corresponds to the experimental probability of having a speed of zero. **d**, Relationship between the average speed V_{mean} and average length L_{mean} of the PCs over 24 hours. The black curve corresponds to the model prediction: $v = B/L$. The value of B is obtained with the value of r. $n_{cell} = 27$ and at least three experiments are used.

In this section, we have seen that PCs display similar morphological parameters in our in vitro setup as in vivo and that their trajectories can be theoretically described as a Brownian motion with dry friction. Indeed, it provides a good description of the characteristics of pericyte migration: length-speed relationship and probability distribution of speed. In the following section, we will investigate the behaviour of PCs on longitudinally confined micropatterns (constrained micropatterns).

2.3.2 Pericyte motility on constrained micropatterns

2.3.2.1 Pericyte morphology on constrained micropatterns

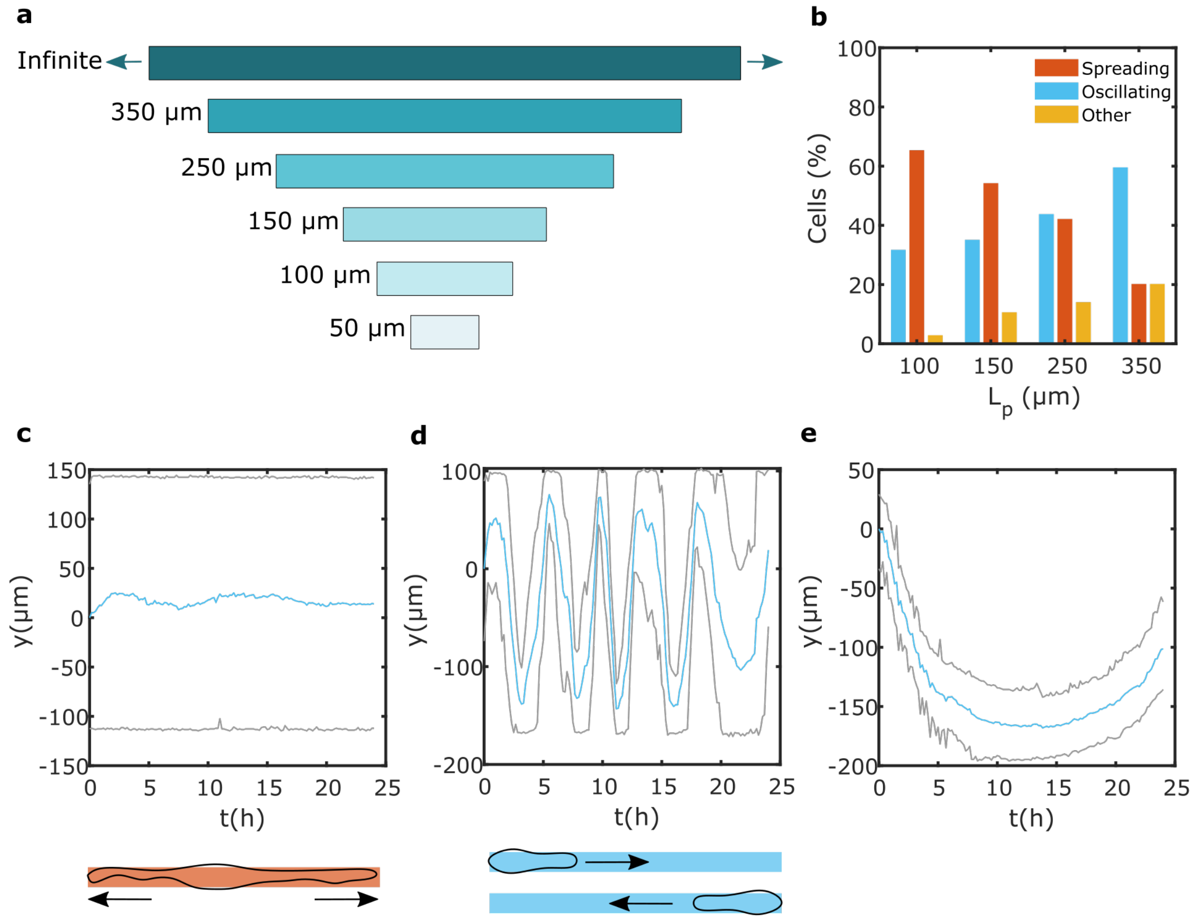

Figure 2.13: Pericytes either spread or oscillate on micropatterns. **a**, Geometry of micropatterns; the length of the adhesive rectangles L_p varies from 50 to 350 μm and the width is set to $W_p = 10$ μm. Adhesive rectangles are surrounded with Pll-g-PEG where cells cannot adhere. **b**, Histogram of the different PC behaviours observed over time on constrained micropatterns. **c,d,e** Typical kymographs of pericyte trajectories over time on $L_p = 250$ μm micropatterns. The Cyan line represents the centroid of the cell and the grey lines the extremities of the cell. **c**, Spreading pericyte, (**d**) oscillating pericyte and (**e**) an example of a pericyte that displays another type of trajectory, here directed motion. Other examples of trajectories observed in **c,d,e** can be found in the appendix A.4. $n_{100} = 104$, $n_{150} = 188$, $n_{250} = 121$ and $n_{350} = 99$ with at least three different experiments for each geometry.

We have seen in the introduction to this chapter (section 2.1) that in vivo PCs are organised as a cellular chain along the microvessel and do not overlap because they exhibit contact inhibition and are thus constrained to a certain area [27]. To observe pericytes in a constrained environment, we add non-adhesive gaps to the infinite lines using PLL-g-PEG, thus creating rectangular areas where the cell can be trapped (constrained micropatterns). Five different lengths (L_p) are tested to study the effect of constriction: 350, 250, 150, 100 and 50 μm. The micropattern width is kept constant at 10 μm (Figure 2.13.a). The lengths of the micropatterns are chosen on the basis of the range of PC length previously measured in section 2.3.1.2, Figure 2.9.a. As with migration on infinite lines, PCs trajectories are recorded with bright-field microscopy for 24 hours, with an acquisition every 10 minutes. Note that in this section, not all trajectories span over 24 hours. In fact, the size of the non-adhesive gaps ranges from 5 to 30 μm and therefore a number of cells can cross the gap over the 24 hours of observation, in spite of which we still include their trajectory before gap crossing in this study of cell dynamics. Other than their duration, the trajectories of cells that cross before 24 hours and those that do not, are statistically indistinguishable (we would not be able to predict the occurrence of crossing from the cell's initial trajectory). The phenomenon of gap crossing is the object of a separate study, presented in section 2.3.3.

Like for PCs on infinite lines, we observe different PC behaviours on constrained micropatterns, which we classify as 'spreading', 'oscillating' and 'other' based on cell kymographs and bright-field movies (Figure 2.13.b).

- 'Spreading' pericytes correspond to those which elongate over the entire length of the micropattern for the majority of the tracking as illustrated in Figure 2.13.c.
- In contrast with infinite lines, the majority of short pericytes exhibit oscillatory motion (Figure 2.13.d), which can be explained by the constrained geometry of the micropatterns. We observe running phases with directed motion similar to PCs on infinite lines. When such PCs reach the end of a micropattern, they reverse their polarity and run to the other side, thus generating an oscillatory behaviour. The period of oscillation is not constant over 24 h and across cells.
- Cells that either experience both behaviours with approximately equivalent distribution or show only directed motion without reorientation are classified as 'other' (Figure 2.13.e).

Here, we do not quantify cell features for L_p = 50 μm, as it is difficult to analyse the cells due to the increase in brightness in the centre of the cell (appendix A.3, Figure A.4). Qualitatively, we see that nearly all pericytes on 50 μm long micropatterns are too constrained to oscillate, thus they are classified as spreading. Figure 2.13.b shows that the longer the micropatterns ($L_p = 350$ μm), the more PCs oscillate (59.4%), and conversely, the shorter the micropatterns ($L_p = 100$ μm), the more cells spread out (65.4%). These observations are expected, indeed we saw in section 2.3.1.2 that on infinite lines PCs have a median length of 206 μm therefore, on shorter micropatterns a majority of cells will be trapped and considered as spreading whereas, for longer micropatterns that are above the median pericyte length, the cell will oscillate more as it will be harder for them to reach the length of the micropattern. This last aspect could also explain why the category 'other' also increases with micropattern length.

2.3.2.2 Applicability of the Brownian model to describe pericyte motility on constrained micropatterns

We then calculate the instantaneous cell centroid speed, mean centroid speed and mean cell length to see if pericyte motility on constrained micropatterns can be described by the Brownian motion with dry friction model. Figure 2.14 shows that PCs on micropatterns of 350 and 250 μm have similar speed distributions to those on infinite lines, with the distribution for 350 μm almost identical to that on infinite lines. However, for even more constrained micropatterns the slope of the distribution is steeper and the probability of having an instantaneous speed between $0-5$ μm/h (first bin) is much higher. For example, for L_p = 350 μm, $p = 0.08$ whereas, for L_p = 150 μm and L_p = 100 μm, $p = 0.17$ and $p = 0.25$ respectively. As shown in Figure 2.13.b, this could be explained by the fact that on shorter micropatterns, a greater number of pericytes spread over the entire length of the micropattern and that these cells are too constrained and almost non-motile. We observe a crossover at $v = 20$ μm/h, above which the inverse tendency is observed and it is the probability distribution of infinite lines that is the highest and that of L_p = 100 μm the lowest. From this graph, we deduce that the motility of PCs on short micropatterns diverges from that on infinite lines. Figures 2.15.a,b show that the distributions for 150 and 100 μm remain reasonably fitted with $\gamma = 1$; however not by the value of $2r = 0.019$ h/μm obtained for infinite lines. The validity of $\gamma = 1$ shows that a description of Brownian motion with dry friction remains plausible, but the fact that r varies indicates that cell dynamics are modified by the longitudinal constraint of the micropattern.

We hypothesise that this difference can be due to the elongated cells that are too constrained and thus nearly non-motile, especially for L_p = 150 and 100 μm micropatterns that have a size that is smaller than the median length of PCs on infinite lines (Figure 2.13.b). To verify this hypothesis, we remove spreading PCs from the analysis of the four constrained micropatterns, and compute the probability distribution of speed for PCs that are either oscillating or classified as 'other'. We see in Figure 2.15.d,e, that overall, the reanalysis excluding spreading PCs provides a better agreement between the data from constrained patterns and that from infinite lines. Indeed, the probability of having $v = [0-5]$ μm/h is now equivalent to the one of lines for $L_p = 250$ and 150 μm ($p = 0.08$) and decreased for $L_p = 100$ μm ($p = 0.13$). However, we observe that the agreement becomes slightly worse for the L_p = 350 micropatterns. This shows that spreading PCs on L_p = 350 micropatterns behave as on infinite lines and that by removing them we bias the comparison since we keep all cells in the analysis of infinite lines. The analysis could be improved by tracking the motion of the cell nucleus, in order to quantify the internal fluctuations of the soma in spreading cells.

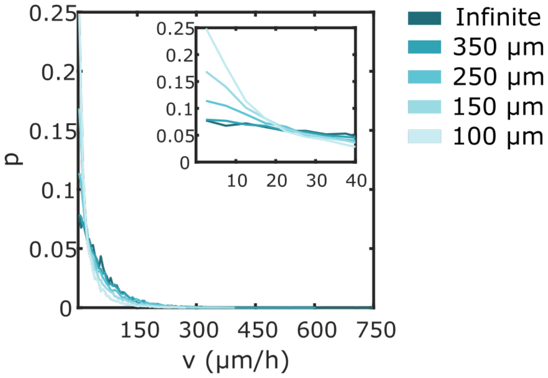

Figure 2.14: Probability distribution of speed on constrained micropatterns. Inset: corresponds to the zoom on the curves from 0 to 40 μm/h. n_{100} = 104, n_{150} = 188, n_{250} = 121, n_{350} = 99 and n_{lines} = 27 with at least three different experiments for each geometry.

Finally, as with infinite lines, we consider the relationship between average cell speed and average cell length. We see from Figure 2.15.c that if we look at all the cells, the data from L_p = 350 μm are relatively well fitted, but less so for 250, 150 and 100 μm. However, we observe the same tendency as for the infinite lines, with a negative correlation between cell speed and cell length. Contrary to PCs on infinite lines, the cell speed for micropatterns quickly decreases close to 0 μm/h. This corresponds to spreading PCs that are similar in length to the micropattern length and are therefore trapped. Since fewer cells can reach a length of 250 or 350 μm, the minimum speed is higher than for L_p = 100 and 150 μm. If we remove the spreading PCs as in Figure 2.15.d and e, we can observe in Figure 2.15.f that cells with lower speeds are no longer present, which improves the agreement with the fit. However, for micropattern sizes $L_p = 150$ and 100 μm, the fit still does not agree well with the data. The reason for this discrepancy is that there are still short PCs with low speeds on these micropatterns. This could be explained by the fact that either running cells or oscillating cells have a shorter directed phase between the two opposite ends of the micropattern when compared to cells on micropatterns of sizes $L_p = 350$ and 250 μm, as discussed in a previous study by Zhou et al. [53]. As a result, there is a lower probability of observing high speed values, resulting in a lower average speed for cells of a given length.

In this section, we have seen that PCs on constrained micropatterns display two main types of trajectory, which we call spreading and oscillating. The likelihood of observing each behaviour depends on the level of constriction imposed by the micropattern length. As with infinite lines, Brownian motion with dry friction can describe PCs on constrained micropatterns reasonably well, with the exception of fully spread cells that are nearly non-motile, especially on highly constrained micropatterns. Better agreement with the model is restored if such fully spread cells are removed from the analysis. For the next section, we investigate the effect of the micropattern width on PC motility.

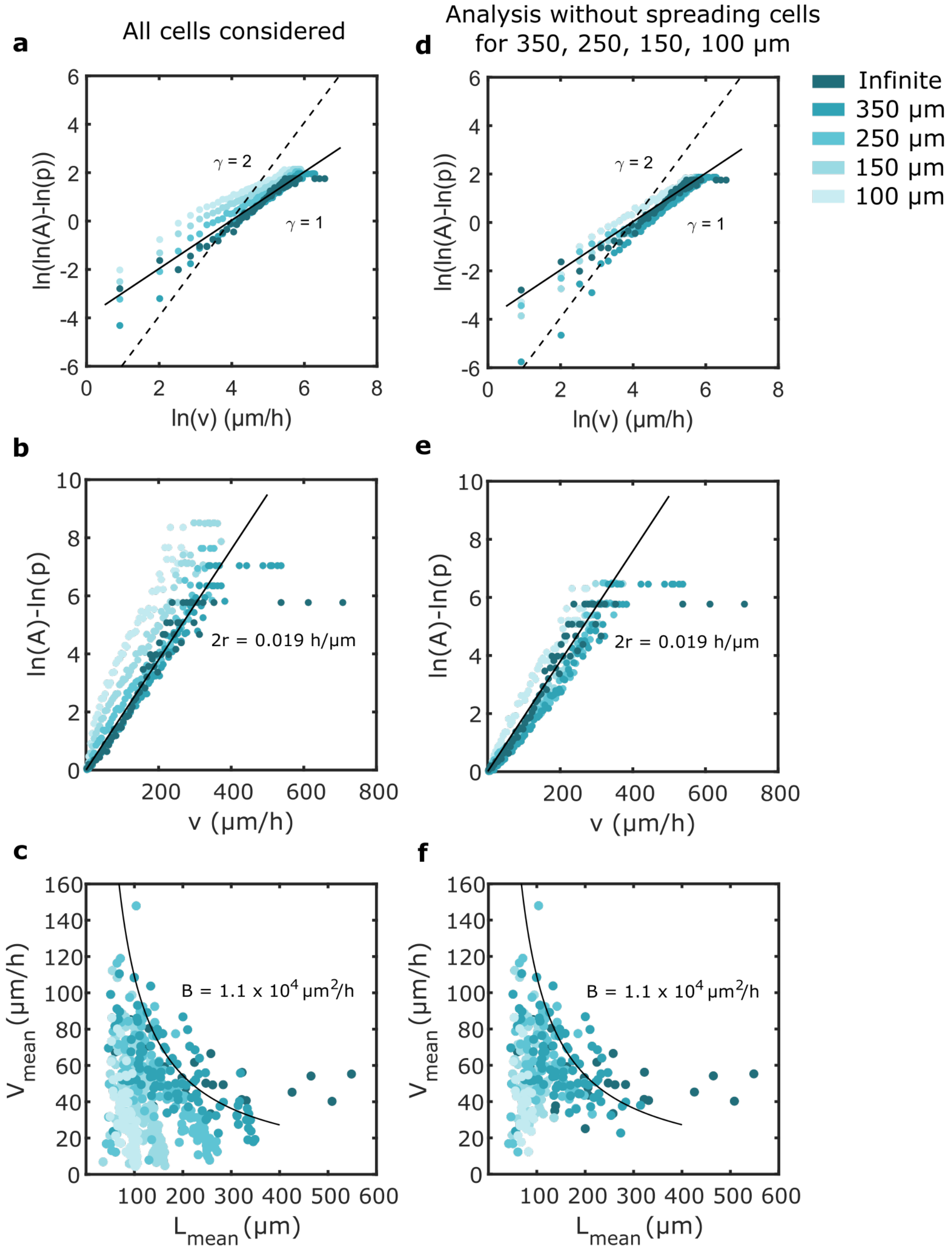

Figure 2.15: Fitting constrained data with the Brownian motion with dry friction model. **a**, Data from Figure 2.14 are reploted in log scale to see if data from micropatterns can be fitted with the same fit as infinite lines, $\gamma = 1$. **b**, The same data as in (**a**) are used to see if the fit with $2r = 0.019$ h/μm obtained for infinite lines remains reasonably valid. For (**a**) and (**b**), the constant *A* on the y-axis corresponds to the experimental probability of having a speed of zero. **c**, Relationship between the average speed V_{mean} and average length L_{mean} of PCs over 24 hours on both infinite lines and constrained micropatterns. The black curve corresponds to the model prediction, $v = B/L$, using the value of B obtained for infinite lines. $n_{100} = 104$, $n_{150} = 188$, $n_{250} = 121$, $n_{350} = 99$ and $n_{lines} = 27$ with at least three different experiments for each geometry. **d,e,f**, Same graph as **a,b,c** but after removing spreading cells for micropatterns $L_p = 350$, 150 and 100 μm.

2.3.2.3 Constrained motility: effect of micropattern width

In this section, we will explore the effect of micropattern width on PC migration. In our model, we hypothesise that the magnitude of dry friction (Δ) is proportional to the cell-substrate contact area (LW_p). Therefore, the value of the constant B, equal to the product of the cell speed and length ($vL = B$) is expected to decrease when the micropattern width is increased, whereas the constant r that characterises the speed probability distribution is expected to increase. To verify these predictions, we compare the average cell speed and the speed probability distribution on constrained micropatterns of L_p = 150 μm, width W_p = 10 μm and L_p = 150 μm , width W_p = 20 μm . Before discussing the results, it is important to note that this is exploratory work and that the experiments were carried out before analysing the cells on micropatterns of 250 and 350 μm; therefore, it would be more accurate to repeat the following experiments and analysis using micropatterns of 350 μm or infinite lines as the model fits these conditions better and we would not have the bias of cells that are too constrained. Here, we present our preliminary analysis for micropatterns of L_p = 150 μm to explain the reasoning and what could be improved.

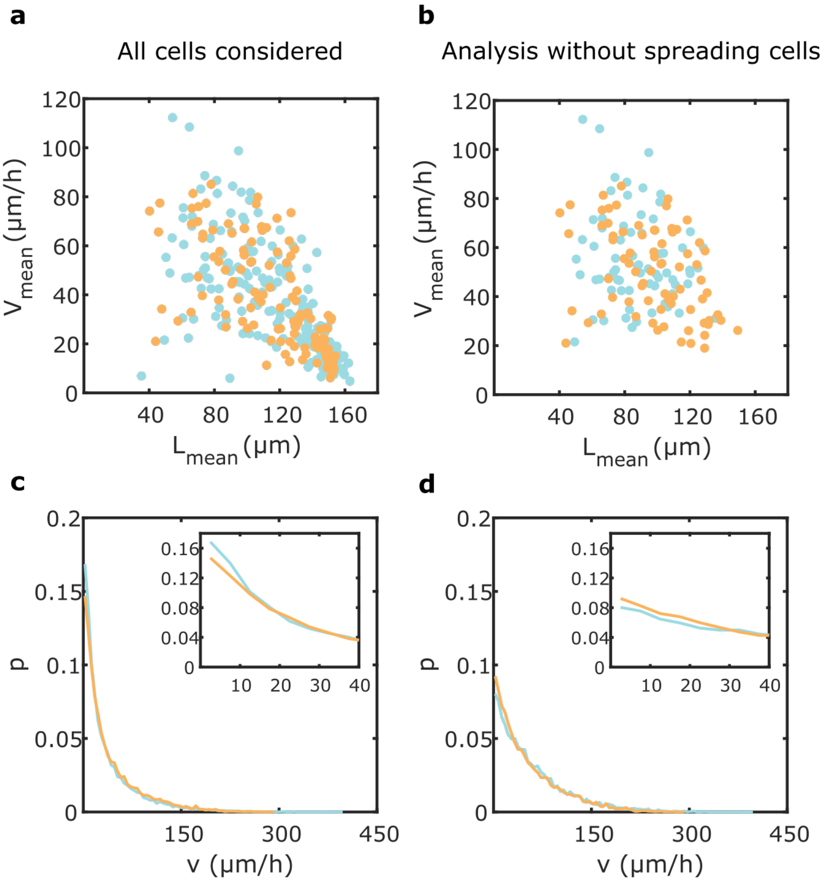

Figure 2.16: Micropattern width does not affect pericyte speed. **a**, Relationship between the average speed V_{mean} and average length L_{mean} of PCs over 24 hours. Cyan dots represent data for micropatterns with L_p = 150 μm and W_p = 10 μm and orange dots for L_p = 150 μm and W_p = 20 μm. **b**, Same graph as in (**a**) but without spreading cells in the analysis. Speed probability distribution with all the data (**c**) and without spreading cells (**d**). n_{10} = 188, n_{20} = 120 with at least three different experiments.

Figure 2.16.a shows the relationship between average cell speed and cell length. We can see that both widths tested (W_p = 10 μm and 20 μm) yield similar speed-length relationships. Furthermore, the probability distribution of the instantaneous speed is similar for both conditions (Figure 2.16.c). As in the previous section 2.3.2.1, we also remove the spreading cells for comparison and obtain similar results as when all data points are considered (Figure 2.16.b,d). These results are surprising as, according to the model, the average cell speed is expected to decrease by a factor of two as the micropattern width increases by a factor of two, due to the expected increase of substrate friction. However, no significant difference is experimentally observed. To ensure that there is indeed a difference in cell width between the two conditions, we measure PC area with the actin staining (phalloidin) of the cells. Figure 2.17.a shows that the area of PCs at W_p = 20 μm is larger

than for PCs on W_p = 10 μm and that if we normalise by the length of the corresponding cell, we obtain an average cell width e = 14.8 ± 2.7 μm for micropatterns with W_p = 20 μm and e = 8.2 ± 1.5 μm for micropatterns with W_p = 10 μm (Figure 2.17.c). However, we can see that they keep similar lengths (Figure 2.17.b). This shows that PCs do adapt to the width of their micropattern by laterally spreading and therefore, we should observe a difference in speed according to equation 2.8.

The predictions of the model are thus in apparent conflict with these preliminary data, based on the assumption that cell-substrate friction is proportional to cell area, which is in turn simply calculated as the product of cell length by pattern width. Therefore, these assumptions require further investigation. One reason that could explain the discrepancy between the model and experiments is that friction is not determined by the total cell area, but rather by focal adhesion (FA) area. Focal adhesions are complexes of proteins that link the actin fibres to the substrate. They play a crucial role in mesenchymal cell migration, and it has been shown in the literature that cell speed is correlated with adhesion area [47, 51]. Here, we analyse fixed PCs after imaging and stain them with phalloidin (F-actin) and paxillin (FA). In Figure 2.18 we can observe staining images of the actin organisation for the two different micropatterns widths, 10 and 20 μm. As expected for these micropattern widths, actin fibres are longitudinally aligned with the micropattern (Figure 2.18.b, e) [65]. Focal adhesions appear to be concentrated at the periphery of the cells and thus at the edges of the adhesive areas, similar to what is observed in other micropattern studies [50]. Note that the bright dots in the centre of the cells are not considered as active FAs (might be FAs that disassemble in the cell body [66]) and are removed with our algorithms, in which a size and circularity thresholds are used (section 2.2.4.4). Figure 2.19.a shows that the total area of FAs increases with cell length and micropattern width. Note that the difference between the total focal adhesion area for micropatterns W_p = 10 and 20 μm is only significant for cell lengths between 100 and 150 μm with $p_{value} = 0.0047$. The increase in the number of FA compared to the cell length that we can observe in Figure 2.19.a is coherent with our model as we have show that longer cells are subject larger friction leading to smaller speed. We also compare the density of FAs (total area of FA divided by cell area), and observe in Figure 2.19.b that both micropattern widths have similar FA density. Overall we can note that despite the increase of FA area as a function of micropattern width this increase is slower than as a function of cell length (Figure 2.19.a). This, therefore, suggests a weaker than linear effect of width on focal adhesion area and thus on friction. This observation provides a first explanation of the absence of speed difference observed between different micropattern widths and suggests an improvement of our theoretical description where substrate friction depends on FA area, rather than total cell area.

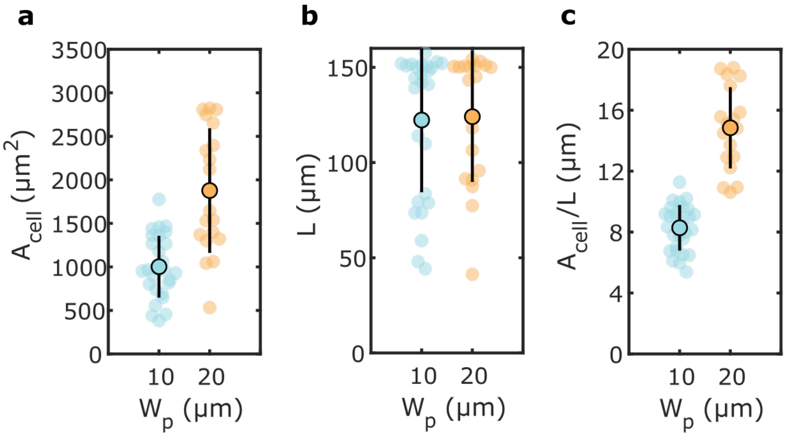

Figure 2.17: Pericyte characteristics as a function of micropattern width. a, PC area as a function of micropattern width $W_p = 10$ μm in cyan and $W_p = 20$ μm in orange; for both geometries the pattern length is $L_p = 150$ μm. **b**, Length of pericytes as a function of micropattern width. **c**, Area divided by length to represent the width of pericytes as a function of micropattern width. Both the area and length of PCs are obtained from phalloidin staining. Error bars correspond to STD. $n_{10} = 28$, $n_{20} = 19$ and at least two different experiments are used.

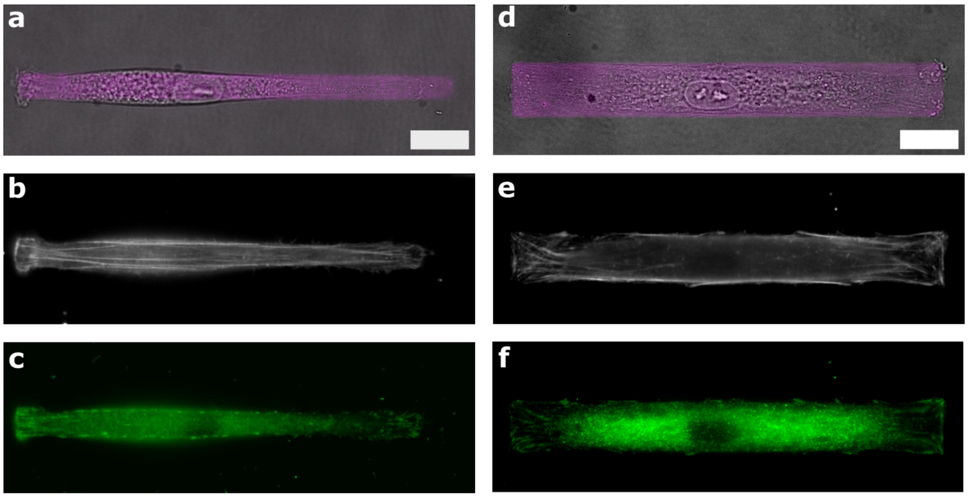

Figure 2.18: Fluorescent images of constrained pericytes. In **a,b,c** the cell is constrained on a rectangle of $L_p = 150$ μm and $W_p = 10$ μm. Whereas, in **d,e,f**, the cell is contained on a rectangle twice as wide, $L_p = 150$ μm and $W_p = 20$ μm. Micropatterns are shown in magenta (fluorescent fibrinogen mixed with fibronectin). Cells are fixed and stained with F-actin with phalloidin (shown in white) and focal adhesions with paxillin (green). Images are acquired with a water immersion objective of 40x. Scale bars = 20 μm.

It is difficult to draw final conclusions from our results. Indeed, the fact that the quantification is based on severely constrained micropatterns could bias the results, as we saw that the speed of the PCs can be impaired by the length of the micropattern. In addition, the use of fixed images does not allow access to FA dynamics. Note that not all the FAs play the same role, indeed as a function of their maturation FA can promote migration and other substrate remodelling [66, 67]. Therefore, for a more complete analysis, it would be more relevant to differentiate FA by size to compare PCs on infinite lines of different widths and to link total FA area or number with cell speed.

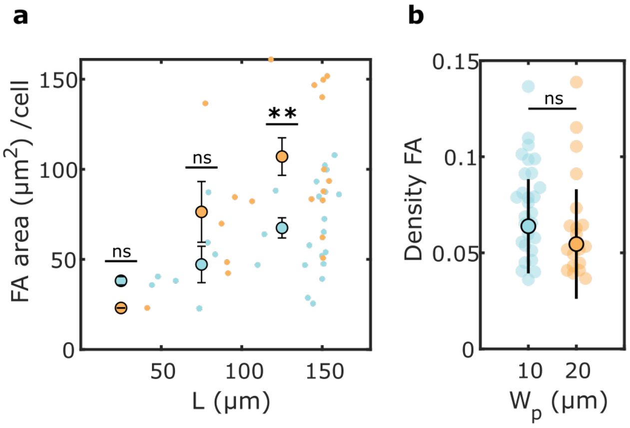

Figure 2.19: Pericyte total focal adhesion area as a function of micropattern width. **a**, Total focal adhesion (FA) area as a function of cell length (L) for PCs on 150 μm long and 10 μm wide micropatterns in cyan and 150 μm long and 20 μm wide micropatterns in orange. Data are averaged by length and standard error is shown. **b**, FA density corresponding to the total FA area divided by the cell area. Error bars indicate STD. $n_{10} = 28$, $n_{20} = 19$ at least two different experiments are used. Non parametric test Wilcoxon rank-sum, * $p_{value} \leq 0.05$, ** $p_{value} \leq 0.005$.

2.3.3 Non-adhesive gap crossing

In this last section, we study how pericytes cross non-adhesive gaps (Figure 2.20.b). There are two motivations for this study. First, we have seen that in vivo pericytes are organised as a chain of cells along the microvessel and exhibit contact inhibition. Berthiaume et al. (2018) [27] showed that in the absence of a neighbouring cell, the PCs surrounding the cell extend their processes to cover the denuded vessel wall. Investigating how pericytes cross non-adhesive gaps after being constrained could mimic this situation. In addition, the use of non-adhesive gaps allows us to study pericyte migration on non-homogeneous substrates. Normally, cells do not encounter such homogeneous substrates as continuous lines in vivo and, as explained in the general Introduction (section 1.1.2.1) this is also the case for PCs. It has been observed that the basement membrane is mainly composed of laminin, interspersed with fibronectin spots to which PCs have a preferential adhesion [32].

In our setup, gaps are made of Pll-g-PEG as previously explained and their size is based on the maximum extension of PC processes in vivo. PCs continuously sample their environment with their processes. Under healthy conditions, the process length reaches at least $5\ \mu$m, and some cells can reach a maximum extension of $20\ \mu$m. Therefore, for our assay, we choose gaps ranging from 5 to $30\ \mu$m (Figure 2.20.a) [27]. We investigate the effect of both micropattern length and width on the crossing of gaps.

2.3.3.1 Frequency of gap crossing exponentially decreases with gap length

First, we investigate the threshold value of gap length (l_g) for pericytes to cross. To this end, we quantify the probability of crossing for different micropattern geometries and gap sizes. To move to the next adhesive micropattern, PCs must extend a process longer than the gap and form an adhesion to the next micropattern to generate force and thus the motion of the cell [50]. As we can see in Figure 2.20.c,d for all the different micropattern lengths and widths we observe that for a length of non-adhesive gap $l_g = 5\ \mu$m almost all PCs are able to cross over the duration of the experiment (24 hours). However, on longer gaps of $10-20\ \mu$m, PCs often fail to cross the gaps, a tendency that increases with gap size. Finally, for $30\ \mu$m gaps, cells are no longer able to cross and cannot migrate to the next micropattern. Figure 2.20.c,d suggests an exponential decay of the percentage of PCs that cross with increasing gap size. Gaps of $20\ \mu$m long seem to be the upper limit that PCs are able to cross in this configuration. From Figure 2.20.c we observe no significant micropattern length effect, although results for 350 and $50\ \mu$m micropatterns long indicate a somewhat smaller percentage of crossings than for intermediate micropattern lengths. For the $350\ \mu$m size, these observations could be explained by the fact that cells have to migrate over a longer distance before encountering a gap. For $50\ \mu$m patterns, we hypothesise that cells might be too constrained, which may affect their behaviour and impair gap crossing. Note that the number of cells analysed for each condition is summarised in Table 2.1.

For larger micropattern widths, $W_p = 20\ \mu$m, we observe similar results as for $W_p = 10\ \mu$m (Figure 2.20.d). For gaps of $l_g = 10\ \mu$m there is a weakly significant difference between the two pattern widths with a $p_{value} = 0.06$. This difference can be explained by the variability of the experiments.

We first try to rationalise our observations as follows. Let us make the hypothesis that the maximum length (l_{max}) of the protrusion and thus the maximum gap length the cells can cross can be estimated by the product of its initial speed times the velocity persistence time ($l_{max} = V_{\mathrm{p}}t$). We assume that the initial speed of a protrusion scales as the typical migration speed observed for our cells (V_{mean}). To obtain the velocity persistence time (t), we fit the velocity autocorrelation function (VACF). Figures and details about the reasoning are described in appendix A.5. From our measurements we find that l_{max} increases with the micropattern length, $18\ \mu$m for $L_p = 150\ \mu$m and $55\ \mu$m for $L_p = 350\ \mu$m, which is not in accordance with what is observed from our data as the maximum gap length PCs can cross is $20\ \mu$m and this is independent of the microppatern length. We can therefore conclude that our hypothesis does not work. The maximum length a cell can cross might depend on the actin network and its ability to polymerise across the non-adhesive gap [48]. It might also depend on the cell type. Indeed the literature has reported that fibroblasts can cross gaps of $27\ \mu$m, whereas human umbilical cord vascular endothelial cells (HUVECs) cannot cross gaps of $10\ \mu$m [48, 50]. Note that we observe similar results in our preliminary experiments with HUVECs on micropatterns of $150\ \mu$m length and $10\ \mu$m size. Indeed, for one experiment HUVECs are only able to cross gaps of $5\ \mu$m, ($n_{cross}/n_{total} = 13/13$), whereas for gaps of

10 μm as for gaps of 30 μm none of the cells cross ($n_{cross}/n_{total} = 0/26$ and $n_{cross}/n_{total} = 0/21$ respectively). These results are preliminary and further experiments will be necessary to confirm our observations.

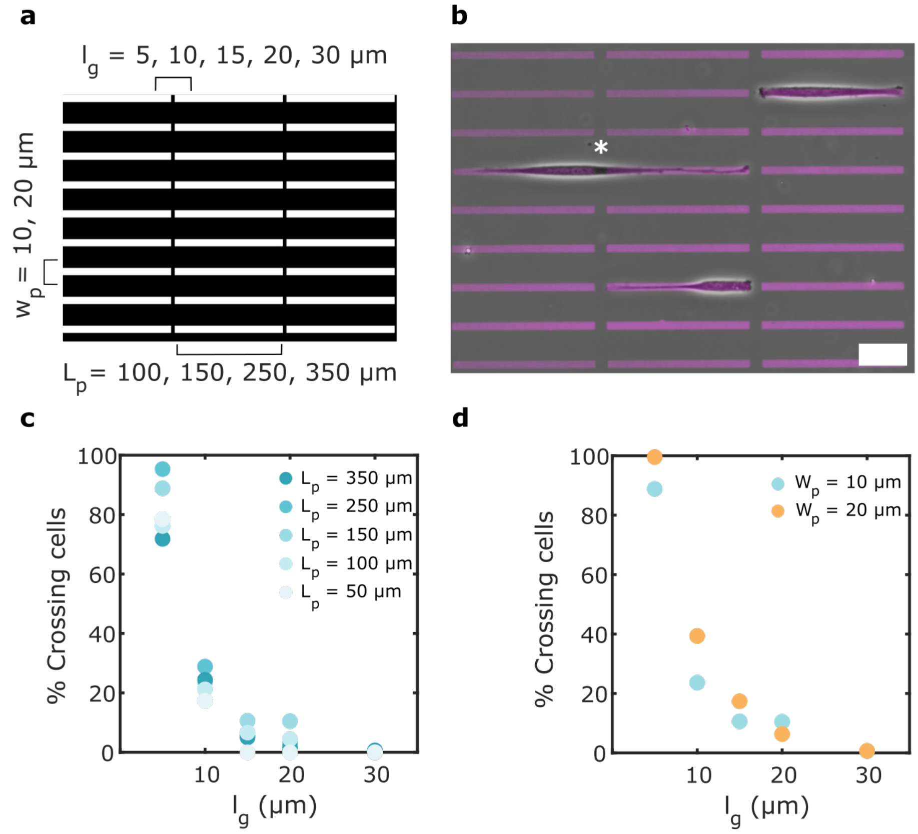

Figure 2.20: Pericyte cross decreases with gap length. a, Geometry of micropatterns with non-adhesive gaps (black). The length of the adhesive rectangles L_p varies from 50 to 350 μm for the width $W_p = 10$ μm. Two different widths W_p = 10 or 20 μm are studied for $L_p = 150$ μm. Transverse gaps are set at 30 μm and longitudinal gaps vary from 5 to 30 μm. **b**, Pericytes seeded on fibronectin micropatterns (magenta) of $Lp = 150$ μm times $W_p = 10$ μm separated by longitudinal gaps of $l_g = 10$ μm. The white asterisk indicates a PC crossing. Scale bar = 50 μm. **c**,**d**, Average probability of crossing over 24 hours as a function of gap length l_g for different micropattern geometries: (**c**) $L_p = 350$, 250, 150, 100 and 50 μm and $W_p = 10$ μm, (**d**) $L_p = 150$ μm and $W_p = 10$ and 20 μm. Note that percentages for gap $l_g = 10$ μm are almost significantly different with a $p_{value} = 0.06$ according to the analysis with Non-parametric test Wilcoxon rank-sum. The number of cells used for each analysis is summarised in Table 2.1.

We then establish a probabilistic model for the protrusions to reach the neighbouring pattern. In the previous paragraph, we saw that the probability of crossing is not linked to the protrusion speed. Therefore we use the probability of crossing an energetic barrier (the non-adhesive gap) where the probability of crossing follows an exponential distribution, which we can write as follows:

$$p_{\text{cross}} \sim e\left\{-\frac{l_g}{l_0}\right\} \rightarrow p_{\text{cross}}(l_g) = \begin{cases} 1 \ \text{if}\, l_g \leq l_0 \\ \exp(1-\frac{l_g}{l_0}) \ \text{if}\, l_g > l_0, \end{cases} \tag{2.9}$$

where l_g is the length of the gap and l_0 corresponds to the longest gap that cells always cross in practice and can be treated as a fitting parameter.

We observe in Figures 2.21 that the fit is in good agreement with the experiments for $l_0 = 4$ μm and $l_0 = 5$ μm for micropatterns with $W_p = 10$ μm and $W_p = 20$ μm respectively. These results are consistent with our experimental observations, as 5 μm is the largest gap size for which we observe that almost all the cells cross.

L_p x W_p	gap 5 µm	gap 10 µm	gap 15 µm	gap 20 µm	gap 30 µm
50 x 10	44/66	14/77	0/17	0/11	0/49
100 x 10	36/49	13/58	3/59	2/37	0/36
150 x 10	78/90	44/149	18/147	20/172	1/96
150 x 20	136/137	95/253	21/108	7/110	1/126
250 x 10	31/33	36/138	4/65	4/102	0/59
350 x 10	29/46	16/85	3/43	1/41	1/61

Table 2.1: Number (nb) of cells that cross for each micropattern geometry and each gap size in 24 hours: nb of cross/nb total. At least two experiments are conducted for each condition.

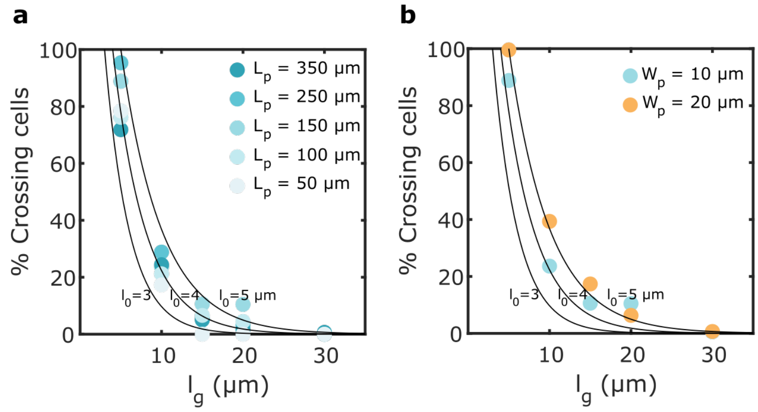

Figure 2.21: The probability of crossing follows an exponential distribution. a, Average probability of crossing as a function of gap length l_g for patterns of different lengths L_p and constant width W_p = 10 μm. **b**, Average probability of crossing as a function of gap length for micropatterns of constant length L_p = 150 μm and different widths: W_p = 10, 20 μm. Data are fitted with equation 2.9 and with $l_0 = 3$, 4 or 5 μm (black lines).

Taken together, the results from this section show that PC crossing exponentially decreases with gap length and that 4 μm is the minimal size pericyte can systematically cross and 20 μm the maximum length they can cross. However, it is independent of micropatterns length and width.

2.3.3.2 Pericyte behaviours during and after the cross

To explore the behaviour of PCs after the cross, we first quantify the speed and length of cells that cross over the 24 hours, rather than just before the cross. Note that for this section, we only consider micropatterns of 350, 250, 150 and 100 μm long and 10 μm wide. We can see in Figure 2.22 that the average speed of cells on micropatterns is higher for a given cell length than what we observed in section 2.3.2 and that the behaviour on infinite lines is almost recovered even for highly constrained micropatterns. Therefore, the equation $v = B/L$ with $B = 1.1x10^4$ μm^2/h fits the data satisfactorily after the cross.

We then look at the morphology of PCs during the cross and try to compare it to in vivo PC migration. Pericytes exhibit two main types of migration in vivo, crawling and escaping [25]. With our setup, we are in a similar configuration as for crawling. Note that this section discusses exploratory work; moreover, the discussion is qualitative since it is based on a categorisation by hand. As previously explained, we mainly observe spreading pericytes and oscillating pericytes on constrained micropatterns (before the cross). Figure 2.23.a shows the percentage of crossings as a function of cell behaviour and micropattern length for W_p = 10 μm. It appears that in general spreading cells have a tendency to cross more. We attempt to classify the crossings between cells that are either 'running' or 'elongating': we call running cells when we do not see any apparent protrusions (note that they might be there) and it seems that the cell crosses nearly as a whole (Figure 2.23.c). Usually, cells are short for this case. Whereas, the other crossing mechanism shown in Figure 2.23.d denotes the case where an apparent thin protrusion (filopodium) is observed followed by adhesion to the next micropattern, the protrusion grows (becomes larger) and then the rest of the cell follows. The latter process is much slower compared to the running cells. This mechanism is less visible for gaps of $5\ \mu$m as the gap is shorter. Note that sometimes cells will end up not crossing despite an exploration of the neighbouring micropattern. Figure 2.23.b, shows that in general PCs will elongate to cross, which is consistent with results from Figure 2.23.a. PCs that elongate display a migration process that is comparable to what has been observed previously in vivo with elongation of the forward process followed by a translation of the rest of the cell [29]. However, in our case, the translation of the rest of the cell is slower.

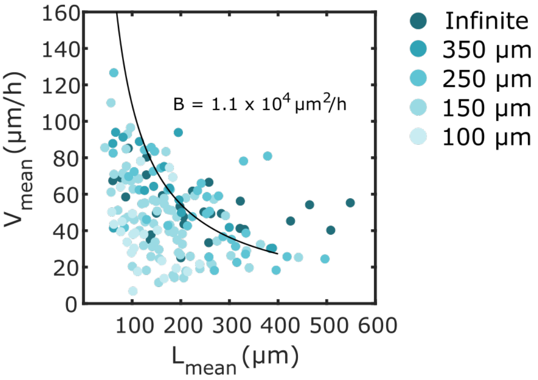

Figure 2.22: Crossing pericytes recover pericyte behavior similar to those on infinite lines. Relationship between the average speed V_{mean} and average length L_{mean} of cells that cross over the 24 hours of experiment. The data for the infinite lines are added in duck blue. The black curve corresponds to the model prediction $v = B/L$. $n_{lines} = 27$, $n_{100} = 23$, $n_{150} = 71$, $n_{250} = 36$ and $n_{350} = 15$ at least two different experiments for each geometry is used.

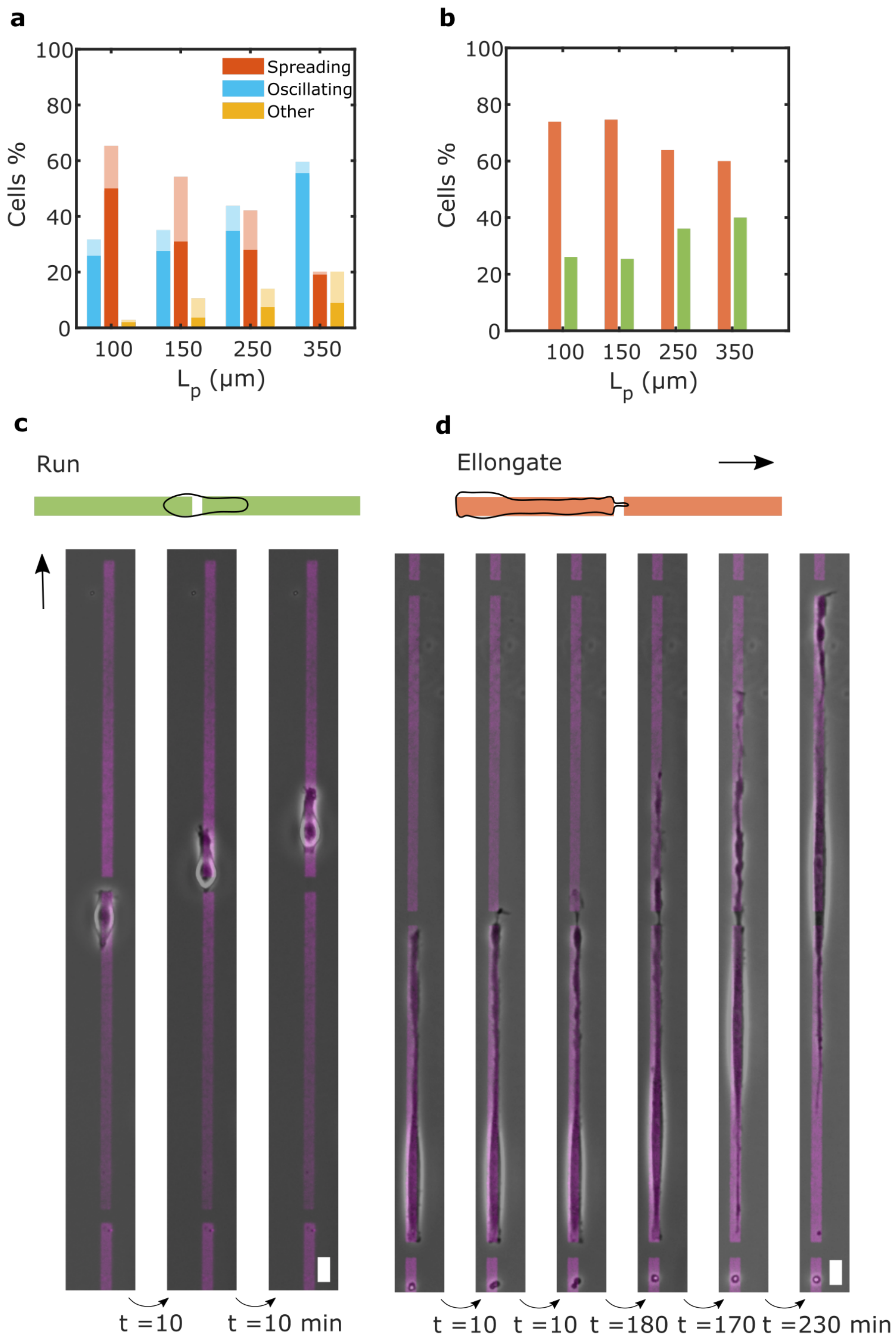

Figure 2.23: Qualitative analysis of gap crossing. **a**, As in Figure 2.13.b, histogram of the different PC behaviours observed over time on constrained micropatterns before the cross. Light areas correspond to the percentage of crossing cells per category. **b**, Percentage of PCs that cross either by running or elongating a protrusion to the next micropattern. **c,d**, Timelapse sequence of a pericyte that crosses a gap of $10\ \mu$m. Respectively (**c**) shows a cell that is running and (**d**) shows a cell that elongates a protrusion to cross. Scale bars = $10\ \mu$m.

2.4 Discussion and conclusion

2.4.1 Pericyte migration: impact of confinement

From this chapter, we can see that micropatterns with an infinite line geometry are a versatile tool that is well suited to studying pericyte (PC) migration, such as crawling. First, the confinement of infinite lines mimics the in vivo confinement that PCs experience in vivo when surrounding small blood vessels, a feature that is absent in traditional 2D migration assays. We focus our analysis on infinite lines of 10 μm, which mimic PC confinement of a capillary of 4 μm diameter. Our 1D migration setup simplifies the analysis of different parameters such as PC centroid speed or PC length as a function of time without the need for staining or complex imaging protocols, unlike 3D migration assays. Our results show that PCs display different migration behaviours; namely short PCs, spreading PCs and PCs with a behaviour that could be compared to stick and slip motion (that we call alternating) [46]. We observe that pericytes on infinite lines exhibit morphological parameters similar to in vivo pericytes on capillaries, such as their length and the partial coverage of the available surface [2]. Another parameter that could be explored is the height of the nucleus. Indeed one key morphological parameter of PCs is their protruding cell body [2]. We would expect that nucleus height will increase with confinement as observed for other cell types [47].

To our knowledge, there are no in vivo studies quantifying pericyte migration parameters such as speed. Therefore, it is difficult to conclude whether the obtained speeds are representative of the in vivo situation. However, the average PC speeds we obtained are comparable to the few in vitro quantifications on 2D glass surfaces in the literature. Indeed, we have an average PC speed between 35 and 100 μm/h and these other studies have reported speeds between 30 and 240 μm/h or 21 and 100 μm/h [38, 39]. Note that 2D assays do not use fibronectin. By taking the analysis a step further and looking at the relation between PC speed and length we find that our results are similar to the literature for other cell types on infinite lines [46], as we find a negative correlation between the cell speed and length.

Cell migration in 2D and 1D assays is usually described by the Ornstein-Uhlenbeck (OU) process, which corresponds to continuous random motion [55, 68]. However, the experimentally quantified mean square displacement (MSD) of PCs on infinite lines shows a superdiffusive behaviour over short time scales instead of the expected ballistic motion [58]. In addition, the speed probability distribution does not follow a Gaussian distribution as expected for the OU process but rather an exponential decay. We therefore model PC motility as a Brownian motion with dry friction, whose speed distribution follows a negative exponential [62]. This is in contrast to other models that account for viscous friction rather than for dry friction [50]. Note that little is known about the cell-substrate dissipation process. Here we first assume that the coefficient of friction is proportional to the cell-substrate contact area. The model gives a prediction of the speed-length relationship that fits our data reasonably well. To validate our hypothesis regarding the friction coefficient further experimental work on wider infinite lines should be performed.

2.4.2 Pericyte motility on constrained micropatterns

2.4.2.1 Impact of micropattern length

We next add non-adhesive gaps intercalated along the infinite lines to mimic the longitudinal confinement that PCs experience in vivo, where they form cellular chains along small blood vessels and display contact inhibition with their neighbours. Different microppatern lengths are explored ranging from 50 to 350 μm. At first, only the trajectories of cells before they cross a gap are analysed. Compared to infinite lines, PCs mainly display spreading or oscillating trajectories. The oscillations are due to the edges of the micropattern that force the cell to repolarise. The shorter the micropattern, the more PCs spread, as they are too constrained to oscillate. On the contrary, the longer the micropattern, the more PCs oscillate.

We show that the motility of PCs on long micropatterns can also be modelled as Brownian motion with dry friction. However, to fit the observed behaviour of PCs on shorter micropatterns (150 and 100 μm) we need to adjust the model parameters, which are otherwise universally valid for larger patterns as well as for infinite lines. We hypothesise that this difference is due to the higher proportion of spreading cells and thus almost immobile cells on shorter micropatterns. We therefore remove these cells from the analysis and show that the data are better fitted by the model using the parameter values deduced for infinite lines. There is still a difference with PCs on infinite lines and this can be explained by the fact that oscillating PCs on short micropatterns have shorter running phases than on longer micropatterns resulting in lower averaged speed [53]. In the future, it would be interesting to explore whether, for cells that spread, tracking the nucleus or the protrusions might provide additional information. Indeed, analysis of the nucleus could reveal an internal fluctuation that could provide additional information about the internal energy of the cell. In the introduction to this chapter, we saw that pericytes are constantly probing their environment with their processes, so tracking the position of pericyte processes as a function of micropatterns could provide more information about what is happening at the edges of the micropatterns, a dynamics of particular importance for the mechanism of cell crossing to a neighboring micropattern.

2.4.2.2 Impact of the micropattern width

In our exploratory study on the effect of micropattern width, we aim to verify one of the predictions of our model, according to which the coefficient of friction depends on both the length and width of the cell, and therefore velocity should decrease with micropattern width. Here we focus on micropattern of $150\ \mu$m length and compare two widths, 10 and $20\ \mu$m. We obtain surprising results, as the average speed-length relationship is similar for both geometries, as is the probability speed distribution. It is important to note that a more robust comparison would be to compare PC migration on infinite lines of different widths, as in the constrained micropattern the length of the micropattern can bias the cell trajectories and we have shown certain limitations in the ability of the model to describe PC behaviour on short micropatterns.

One promising way to understand this apparent contradiction is the analysis of focal adhesions (FA). Our hypothesis here is that cell-substrate friction does not simply depend on the total cell area but rather on the density and distribution of FAs. We see that the total area of focal adhesion is similar for cells of comparable length across both pattern widths. However, the longer the cells, the greater the total area of focal adhesion. We therefore assume that dry friction is proportional to the contact area of the focal adhesions rather than the total area of the cell as we had initially predicted. Further analysis would be required to draw conclusions.

2.4.3 How pericytes cross non-adhesive gaps

We then study how pericytes cross longitudinal non-adhesive gaps made of poly-L-lysine-grafted-poly(ethylene glycol) (PLL-g-PEG). Investigating how cells react to a chemical barrier is interesting as in vivo cells in general, and PCs in particular, do not migrate on uniform substrates. Indeed, it has been shown that pericytes prefer to adhere to fibronectin over laminin. We find that PCs are able to cross gaps of $5\ \mu$m almost systematically and that the frequency of crossing decreases exponentially as gap length increases. We observe that $20\ \mu$m is the maximum gap length that PCs are able to cross. To cross non-adhesive gaps, cells need to extend protrusions which are longer than the gap size, and we expect from the literature and preliminary observations with endothelial cells that the threshold length may vary with cell type and the ability of the cell to protrude in the non-adhesive gap [48, 50, 54]. Our findings are also comparable to in vivo observations, as in healthy conditions, PC protrusions can extend from 5 to $20\ \mu$m. Note that micropattern length and width do not seem to impact the frequency of crossing. We present a mathematical description to gain insight into the mechanistic origin of the threshold length for gap crossing and give a distribution of the probability of crossing gaps of different lengths.

Finally, we study PC behaviour during and after the cross. When considering the whole cell trajectory instead of only the portion before the cross, we observe that infinite line migration is nearly recovered for cells that cross. From our qualitative study, we note that spreading pericytes are the ones that cross the most compared to oscillating ones and that they retrieve similar behaviours as observed in vivo migration. Indeed, their migration consists of extending a protrusion followed by translocation of the rest of the cell. Indeed, in vivo, observations of pericytes in zebrafish show that migrating PCs first extend their leading process over a dozen micrometres and then translate the rest of the cell in a rapid manner.

Chapter 3

The microfibre force probe: fabrication, characterisation and applications

3.1 Introduction

3.1.1 In vitro tools to measure forces exerted by cells

To date, there are several methods for measuring the mechanical forces exerted by cells on their environment. As shown in Figure 3.1, we can divide such methods into three main categories [69]. The first ones, known as ’deformation-based techniques’, are probably the simplest. They consist of measuring forces qualitatively by observing the deformation of the substrate without relating it to any quantified values. For example, cells are embedded within a block of collagen and a reduction in diameter is observed (Figure 3.1). Although these deformation-based methods are simple to perform, quantitative techniques have since been developed that allow measurements with higher temporal and spatial resolution.

The second category corresponds to the use of pillars, ‘Tissue pillars and Micropillars’. Pillars of known stiffness are fabricated and can be used to measure forces exerted by a single cell or tissues (Figure 3.1). The deflection of each column is tracked and the force is then calculated using beam theory. The advantage of this technique over the previous one is that it is quantitative. However, the microfabrication process can be complicated and the fact that the cells are constrained on the micropillars (specific topography) can influence cell adhesion and thus forces.

Finally, traction force microscopy (TFM), which is also a quantitative method, uses fluorescent markers added to the substrate (silicon, polyacrylamide). For 2D TFM, cells are seeded on the hydrogel and the positions of the fluorescent beads are recorded during tension and after cell lysis. Tensile forces are calculated by measuring the displacement field and knowing the mechanical properties of the gel. 2D TFM has become a standard technique in many laboratories for characterising cell forces, it is a precise technique and easily tunable (change in substrate stiffness). However, it is limited because it can only measure tangential shear forces and not normal shear forces. 3D TFM has been developed to characterise both force components. It is mainly used to quantify the mechanical interactions between cells and their matrix. While 3D TFM is more accurate, it is also more computationally demanding.

A common limitation of most of these previous techniques is that they do not consider the curvature that cells experience in their physiological environment (organs, vessels, cell interactions) and, for 2D techniques, they only measure shear forces [70].

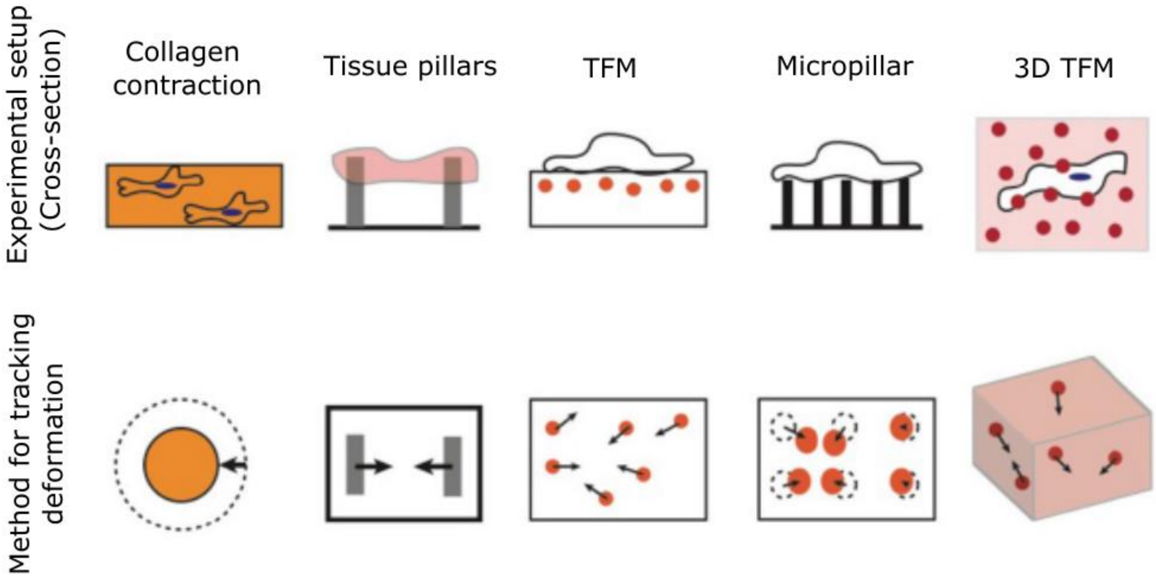

Figure 3.1: Common methods to measure forces exerted by cells. Adapted from Polacheck et al. [69].

3.1.2 Quantification of mural cell forces

Such limitations are also found in studies that investigate pericyte (PC) and smooth muscle cell (SMC) mechanics. Indeed, the main method to date to measure PC forces is called 'silicone wrinkle assay', which consists of seeding pericytes on a substrate and counting the wrinkles each cell makes (Figure 3.2.a) [71, 72, 73]. This technique is most of the time qualitative, and moreover, it can be biased as it leads to phenotype loss [25, 74]. Recent studies have used other techniques to measure PC forces: for example, Neuhaus et al. [75] used a commercially available electrical impedance system (Figure 3.2.b) to study PC contractility in response to vasoconstrictive peptides and PC relaxation in response to vasodilator compounds. They also applied chemical ischaemic solutions and observed significant PC contraction. The impedance system gives different impedance values in response to changes in the contact area between the cells and the substrate. Another study measured PC forces using polydimethylsiloxane (PDMS) micropillar arrays coated with fibronectin at the top, as shown in Figure 3.2.c. They showed that PCs apply forces to fibronectin deposits and can sense variations in substrate mechanical properties by changing the forces they apply, their spreading area and the size of focal adhesions [32]. However, these techniques still do not take into account the curvature of the PC environment and do not measure compressive forces.

SMCs have received significantly more attention than PCs, and their mechanics have mostly been characterised using 2D TFM. For instance, Sazonova et al. [76] used TFM to investigate the effect of stiffness and coating on individual SMC behaviour to better understand how SMCs react during arteriosclerosis. Petit et al. 2019 [77] used TFM to characterise an individual SMC basal tone. Studies have also measured SMC forces in both healthy and perturbed states. For instance, Petit et al. 2021 [78] compared SMC traction forces from healthy human aortas and aortic aneurysms. Hall et al. [22] used the nanonet force microscopy [1] to quantify the force exerted by a single SMC and compare the force between healthy and cells exposed to oxidative stress as for instance in aneurysmal disease. The fibres used in nanonet force microscopy are in the range of 250 nm to 1000 nm diameter to mimic the fibrous aspect of the extracellular matrix.

---

[1] The nanonet force microscopy is a suspended fibre-based force measurement platform.

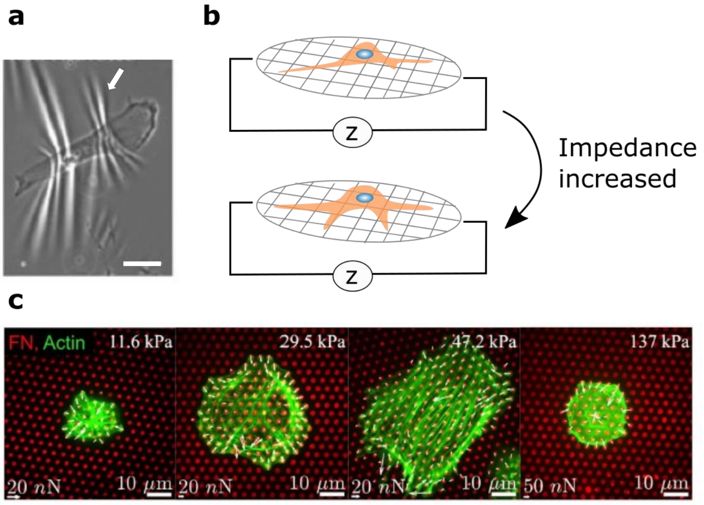

Figure 3.2: In vitro systems to measure pericyte forces. **a**, A pericyte wrinkling a silicon surface. The white arrow indicates one of the wrinkles. Scale bar = $50\ \mu$m, adapted from Durham et al. [71] **b**, Electrical impedance system, the impedance increases as the cell contact area or the number of cells increases. Inspired by Neuhaus et al. [75]. **c**, Pericytes on PDMS micropillar arrays of different stiffness, cell area and forces vary with substrate stiffness. White arrows indicate force magnitudes. Scale bar = $10\ \mu$m, adapted from Iendaltseva [32].

3.1.3 Quantification of normal cell forces using spherical microgels

To overcome the limitations just mentioned, some recent studies have started to use non-planar geometries [70, 79, 80]. For example, Vorselen et al. [70] recently developed stress cell sensors that can accurately calculate both shear and normal stresses (Figure 3.3). They illustrated their new technique by studying, for example, the forces exerted by macrophages during phagocytosis. To mimic the target, they produced and functionalised hydrogel microparticles with a size ($4 - 15\ \mu$m) and stiffness (Young's moduli: $E = 0.3$ to 10 kPa) comparable to cells or bacteria. Similar particle-based force-sensing strategies have also been developed to study cell interactions both in vivo and in vitro [79, 81]. For instance, Mohagheghian et al. fabricated alginate microparticles with a diameter range of 15-30 μm and Young's modulus between 1.4 and 3.36 kPa to measure compressive forces within melanoma cell colonies or zebrafish embryos. Recognising the importance of non-planar geometry, we hypothesised that a more reliable measurement of mural cell mechanical forces might be obtained if the cells are placed on a cylindrical substrate to mimic the shape of microvessels. To test this hypothesis, we developed soft micrometric fibres that could be used as force sensors for mural cells.

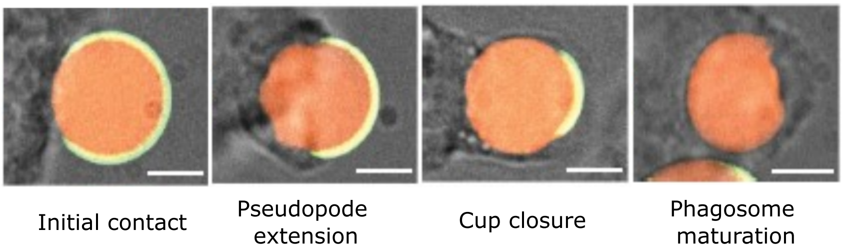

Initial contact

Pseudopode extension

Cup closure

Phagosome maturation

Figure 3.3: Microbeads force sensors. Confocal images (z-slices) of poly-AAm-co-AAc microparticles (DAAM-particles, in orange) undergoing phagocytosis. Scale bars = $5\ \mu$m. Adapted from Vorselen et al. [70].

3.1.4 Requirements to quantify compressive mural cell forces

Our system aims to measure compressive (normal) forces exerted by mural cells as illustrated in Figure 3.4. Note that here we initially focus on orthogonal compressive forces exerted by either SMCs or PCs that nearly or completely encircle the vessel, but other mechanisms have been hypothesised on how PCs exert forces on blood vessels like tangential forces [25]. To measure compressive forces, different requirements need to be met. The microfibres should be bio-compatible and allow cell growth. To mimic the geometry of small blood vessels such as capillaries or arterioles, fibres should be of small diameter, in the range of 5 to 30 μm [13]. It is important that the microfibres are transparent and with a refractive index close to the one of the cell medium to have good quality images with the microscope. Finally, microfibres should be soft enough to allow the measurement of forces exerted by mural cells. A simple approximation can be done to estimate the stiffness that needs to be targeted using the following formula:

$$\Delta r = \frac{F}{2\pi l E} \tag{3.1}$$

With Δr the change of radius of the microfibre, F the force exerted by the cell, l the average length of the cell and E the Young's Modulus of the hydrogel. From previous in vitro studies, pericytes are able to exert forces in the $0.01 - 1.5$ μN range and SMCs in the range of $0.01 - 10$ μN [22, 32, 74, 76, 77, 78]. The resolution of a microscope is usually around 1 μm and the length of the mural cells can range from 50 μm for SMCs to 200 μm for PCs. Therefore, with $l \approx 100$ μm, we can estimate that Young's modulus has to be in the range of 0.015 to 15 kPa.

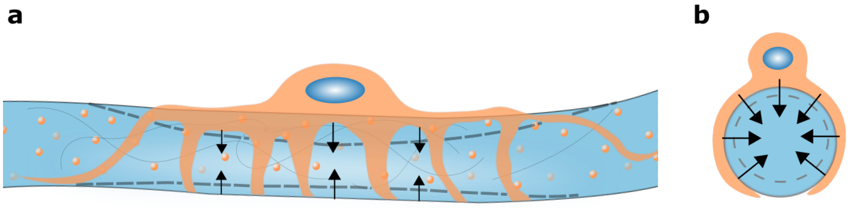

Figure 3.4: Normal forces exerted by pericytes. **a**, Schematic of a hydrogel microfibre deformation by normal forces exerted by a pericyte. **b**, Corresponding cross-section.

3.1.5 Hydrogel microfibres

An important area of applications for the hydrogel microfibres is the biomedical field [82]. They have been used for tissue engineering as scaffolds, for drug delivery, and to study cell migration or the effects of curvature on cell alignment [83]. In the last decade, hydrogel fibres have been produced by different techniques, including microfluidic spinning. This allows a wide variety of fibres with different sizes, shapes, porosities, or mechanical properties to be produced at high throughput without the need for complex, expensive equipment or facilities. To produce fibres in a microfluidic channel, two phases (continuous and dispersed) are used to create a coaxial flow. Then, the central fluid is solidified using various techniques [82]. Note that additional fluid streams could be used to produce hollow fibres, for example. The most common channel geometries used to produce fibres are coaxial and flow-focusing geometries (Figure 3.5) [82]. Coaxial channels are made using two glass capillaries where a smaller glass capillary with a tapered tip is inserted into a larger one (Figure 3.5.a). This technique requires a high level of skill, as the alignment of the capillaries requires precision and can be time-consuming [83]. In addition, the parameters (e.g. flow rates) have to be adjusted for each new channel, as it is difficult to obtain exactly the same diameter of the tapered tip each time. The other commonly used geometry is flow-focusing, characterised by the intersection of two channels forming a cross (Figure 3.5.b). Usually, flow-focusing channels are made by casting liquid PDMS on a custom mold. As it is always the same mold that is used for a specific channel geometry, parameters do not need to be adjusted each time. Among solidification techniques, the most common ones are photopolymerisation, ionic crosslinking, and solvent exchange [83].

Photopolymerisation uses ultraviolet (UV) to crosslink the dispersed phase that contains photoinitiator (PI). Radicals are produced from the reaction between UV and PI, they then react with monomers of the solutions to form polymers. Typical oligomer solutions are poly(ethylene glycol) diacrylate (PEG-DA), poly(ethylene glycol) dimethacrylate (PEGDMA), methacrylamide-modified gelatin (GelMA) or 1,6-hexanediol diacrylate (HDDA)

[83, 84]. Photopolymerisation has the advantage of being a fast and stable process. These materials are usually not biodegradable. Ionic crosslinking is a widely used technique for solidification of biological polymers. This process involves the cross-linking of pre-polymer chains using multivalent ions or small ionised molecules. The most used oligomer solution is sodium alginate. It reacts with $Ca2^+$ ions, that diffuse from the $CaCl_2$ sheath fluid. Other pairs can be used, for instance, chitosan with nontoxic sodium triphosphate pentabasic (STPP) or sodium tripolyphosphate (STP), or poly (acide lactique-co-glycolique) (PLGA) with glycerin [83, 84]. Usually, they are biocompatible however they also are biodegradable, which could be a limitation for our application.

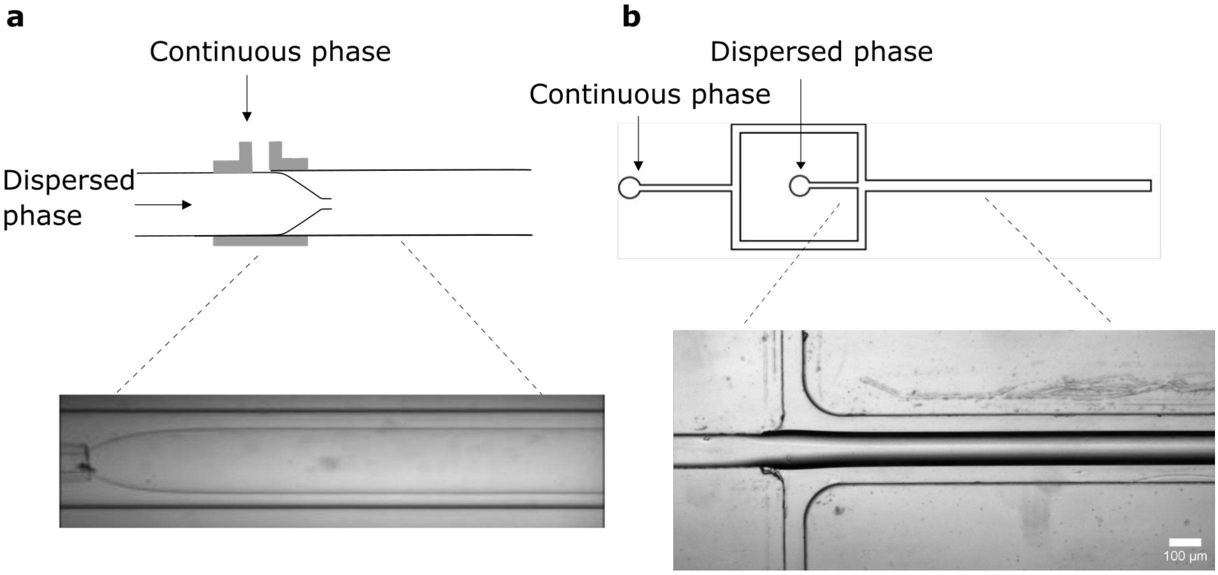

Figure 3.5: Coaxial and flow-focusing devices. **a**, Top: schematic of a coaxial microfluidic device. The connector to insert the continuous phase and hold glass capillaries together is shown in grey. Bottom: bright-field microscopy image of coaxial microfluidic device adapted from Guillot et al. [85]. **b**, Schematic of a flow-focusing microfluidic device (top) with bright-field microscopy image of one of our PDMS channels (bottom). Scale bar = 100 μm.

Solvent exchange is another method used for crosslinking. It consists of a sheath fluid containing the precipitating agent, which reacts with the central fluid, which contains the solvent. Materials include poly(lactic acid-glycolic acid) (PLGA), polymethyl methacrylate (PMMA), polycaprolactone (PCL) or collagen [83, 84]. There is a wide range of available materials whose nature dictates the mechanical properties of the resulting hydrogel, unlike photopolymerisation or ionic cross-linking, where mechanical properties can be tuned during fabrication.

3.1.6 PEG-DA hydrogels

As explained in the previous subsection, there is a wide variety of materials available to produce hydrogel microfibres. In this work, PEG-DA hydrogel is chosen. The properties of the PEG-based hydrogel are highly tunable, with Young's moduli that can range from 100 Pa to 10 MPa [86]. The gel's mechanical properties can be controlled by changing the number of acrylate groups, the UV light properties, the amount of PI or the amount of solvent. Water and PEG can be used as solvents, the advantage of PEG is that it does not reduce the viscosity of the solution and does not react with UV light as it lacks the acrylate groups. PEG-based hydrogels are highly stable over time and non-toxic. In addition, they can be functionalised to allow cell adhesion, usually with RGD (arginine-glycine-aspartic acid) [87, 88].

Due to their numerous applications, PEG-DA microfibres have been widely used and characterised over the last decade [86]. For example, Duprat et al. [86] developed a microfluidic method to directly measure the mechanical properties of PEG-DA microfibres upon their fabrication. By analysing the deformation of the gel beam under controlled flow, Young's modulus of the microfibre is determined. In parallel, they carried out a fairly complete quantification of the effect of different parameters on Young's modulus. However, their microfibres are produced using a stop-flow microscope-based projection photolithography process (where there is no flow and a mask is used), which does not involve the same parameters as jet polymerisation, in addition, the resulting microfibres are flat and not round. Pr. Howard Stone's group has extensively studied PEG-DA microfibres produced by continuous-flow gelation (jet polimerisation) [89, 90, 91, 92]. For instance, they investigated the effect of various parameters such as flow rates and PI content on the shape of the microfibres, more specifically, their waviness [90]. In a more recent study, they investigated the critical conditions for fibre formation, the different production regimes, fibre stiffness and fibre length [92]. Note that the latter study did not quantify the stiffness of the gel. Other studies have explored how to produce complex-shaped microfibres and characterise them, like hollow fibres or fibres with grooves [93, 94, 95]. Whereas the majority of these studies produce microfibres that are in a range close to the one targeted, 30-200 μm diameter, usually the produced fibres are stiffer than what is required for our application, with values in the range of ≈ 100 kPa to ≈ 10 MPa when quantified [86, 91, 95, 96]. In addition, few studies have so far managed to culture cells on soft PEG-DA fibres of small diameter. We have built our cell culture protocol upon the work of Kruger et al. [88], who developed a method to generate biocompatible PEG-DA based fibres of tunable stiffness and diameter ($D_{min} = 8$ μm and $E_{min} = 5.5$ kPa).

3.1.7 Chapter outline

The aim of this project is to fabricate soft micrometric fibres as substrates for mural cells to measure the mechanical forces they exert. For this purpose, we adapt a microfluidic platform already developed at LadHyX by Prof. Camille Duprat, which produces stiff PEG-DA 575 hydrogel fibres of large diameter (400 μm) using a flow-focusing geometry. This chapter describes the manufacturing process of uniform, thin, soft, biocompatible microfibres. It defines guidelines to produce a specific type of microfibres and to quantitatively characterise the mechanical properties of the resulting microfibres, such as their stiffness. In parallel, microbeads are produced and their mechanical properties are compared with those of microfibres. In the second part of the chapter, microfibres are cultured with mural cells and the effect of curvature on cell organisation is quantified. Finally, an approximative model is used to quantify the forces exerted by mural cells.

3.2 Materials and methods

3.2.1 Experimental setup to produce microgels

3.2.1.1 Microfluidic design and assembly

In this work, we use a technique which consists of creating microgels directly in situ using a two-phase flow microfluidic chip. A flow-focusing geometry is used, with either a rectangular or a square cross-section. The microfluidic chip is made using a micromachined brass mold. To make the channel, polydimethylsiloxane (PDMS, Sylgard 184, Corning) and curing agent are used at a $10:1$ ratio. Once mixed and degassed the preparation is cast onto the mold and cured. After that, the chip is cut out from the mold and the two inlets are made using a 1 μm diameter puncher. Channels are then washed with ethanol (EtOH) and plasma bonded to glass slides (Plasma cleaner, PDC-002-CE). As plasma makes our microchannels hydrophilic we then wait for at least three days before using the chips to ensure hydrophobicity. As we use mineral oil as a continuous phase and our dispersed phase is aqueous it is important to ensure hydrophobicity of our microchannel to avoid waiting of the dispersed phase and thus mixing with the continuous phase.

3.2.1.2 Microgel fabrication protocol

To fabricate microgels, we use a 40x long working distance objective mounted on an inverted microscope (Nikon Eclipse Ti) equipped with a UV light source (Intensilight, C-HGFI, Nikon) and an external computer-controlled shutter (LAMBDA SC, Sutter instrument) to control the illumination time. The channel is fixed on a Petri dish, using UV-sensitive glue (NOA81, EPOTECNY) to recover the microgels. The channel has two inlets, one for the continuous phase and the other one for the dispersed phase (Figure 3.6). Two syringe pumps (Nemesys, Cetoni) are used to control the flow rates of both the dispersed phase and the continuous phase.

Note that the dispersed phase syringe is covered with aluminium foil to avoid polymerisation of the solution. To produce microfibres, the continuous phase focuses and sheathes the dispersed phase forming a cylindrical jet. Once the jet is stable, a UV light with an external shutter (100 ms on, 200 ms off) is used to crosslink the dispersed phase and form microfibres. To produce microspheres, droplets are generated instead of a jet. Microgels are then recovered in EtOH 99%. To remove the oil and non-polymerized residues, microgels are purified by centrifugation and subsequent solvent exchange in ethanol at 7100 rpm for 3 minutes (Centrifuge 5430R, Eppendorf). Microgels are then resuspended in Milli-Q water (MQ water) in low binding tubes (1.5 ml LoBind, Eppendorf) and centrifuge three times (3500 rpm, 3 minutes, Centrifuge1-14, Sigma) to replace EtOH. Finally, microgels are stored in MQ water in low binding tube wrapped with aluminium foil to protect them from light. During the fabrication, microscope images are taken to measure either the jet diameter or droplet speed and the resulting microgel dimensions.

3.2.1.3 Microgel diameter measurements

Microgel diameters are measured from bright-field images at either 40x or 10x. Measurements are made manually using either the *Straight Line* tool from ImageJ for microfibres or *Oval Selections* for microspheres. We also estimate the measurement error by measuring different images three times on three different days and quantifying the error. If the measurement error is smaller than the standard deviation of our population it is not taken into account, otherwise it is shown in the graphs.

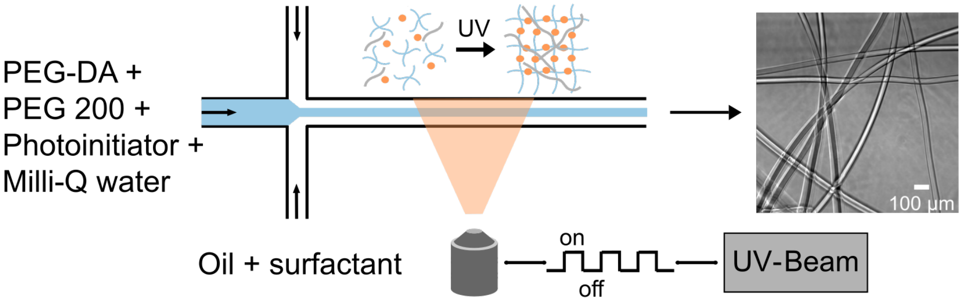

Figure 3.6: Experimental setup to produce microgels. Dispersed phase (mixture of oligomer, solvent and photoinitiator, shown in blue) ensheathed by the continuous phase (oil with surfactant, shown in white) flows in a flow-focusing microchip. The ratio of the two flow rates dictates the diameter of the jet/droplets. A pulsed UV spot polymerises the jet/droplets and produces microgels. Scale bar = 100 μm.

3.2.1.4 Dispersed and continuous phase solution

For the dispersed phase, we use different photosensitive preparations composed of the three following elements:

- Oligomer: 30% (v/v) of Poly(ethylene glycol) diacrylate (PEG-DA, Aldrich) . We try both PEG-DA with a molecular weight $Mw = 575$ g/mol and PEG-DA with $Mw = 700$ g/mol. Most of the experiments are performed using PEG-DA 700.
- Photoinitiator (PI): 10% (v/v) (Darocur 1173, 2-hydroxy-2-methylpropiophenone, Aldrich).
- Solvent: 60% (v/v) composed of 30% Milli-Q water and 30% of Poly(ethylene glycol) (PEG $Mw = 200$ g/mol, Aldrich).

Note that as we will see in section 3.3.1.2 we also vary one time the concentration of both the PEG-DA and solvent to see the impact on the production of a stable jet.

To quantify the deformation of microfibres in future cell experiments, we add to the photosensitive solution fluorescent beads of 500 nm diameter (Fluoresbrite YG Microspheres - Polysciences). We try various concentrations of beads to determine the optimal concentration. We aim to have a sufficient number of beads without encountering aggregation, and it appears that a starting concentration of 0.62% (v/v) is suitable.

For the continuous phase, two types of oils are tested:

- Fluorinated oil (FC-40, 3M Fluorinert) and 2% (w/w) of surfactant (157FSH, DuPont Krytox).
- Light mineral oil (Sigma) and either 3.5% or 30% (w/w) of Span80 (Sigma-Aldrich) as a surfactant.

Note that when using FC-40 as a continuous phase, the channel is made hydrophobic by injecting a coating (NOVEC 1700, 3M Company, St Paul MN) into the channel and baking at $110°$C for three times 30 min.

3.2.2 Density, viscosity and interfacial tension measurements

The viscosity (μ, mPa.s) is measured with a viscosimeter (ViscoQC 300, Anton Paar) using the manual mode and a measuring cup of 6.4 ml (CC18, Anton Paar). Interfacial tensions between continuous and dispersed phases are measured at the Solid States Physics Laboratory (LPS, Orsay) using the rising drop method with a tensiometer (Le Tracker, Teclis). A few complementary measurements were done at LadHyX with a homemade technique and a Matlab code from Prof. Camille Duprat using the pendant drop method. In the rising drop method, a curved capillary attached to a syringe is used to form the drop in a controlled manner [97]. The fluid with the lowest density is used to form the drop and the one with the largest inside the container (for the pendant drop method, it is the contrary). The densities (ρ, g/ml) of the continuous and dispersed phases are obtained using an analytical scale to measure the mass and a graduated cylinder for the volume. The densities of the different continuous phases used are summarised in the appendix B.1 in Table B.1 and those of the dispersed phases in Table B.2. To increase the contrast between the two solutions when measuring the interfacial tensions, a low quantity of Nil Red is mixed with the liquid in the drop (a control is performed to ensure that it does not impact the interfacial tension). The drop's profile is then analysed using the software WDROP and the interfacial tension is obtained using a model based on the Young-Laplace equation.

3.2.3 Exposure time and jet/droplet speed measurement

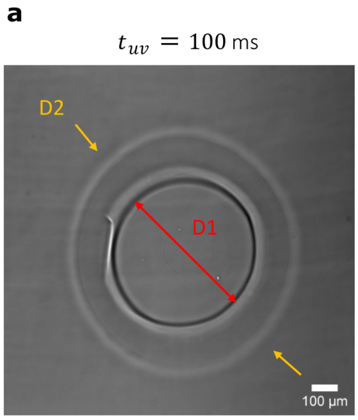

b

D1 (µm)	D2(µm)
546.7	916.4
550.7	876.3
550	870.4
565.1	832.9
551.3	859.9

Figure 3.7: UV spot size measurement. a, Bright-field image of UV light spot formed using a 40x objective at $t_{uv} = 100$ ms. The photosensitive solution used is 30% (v/v) PEG-DA 700 + 30% (v/v) PEG 200 + 30 % (v/v) MQ water + 10 % (v/v) PI. Scale bar = 100 μm. **b**, Diameter values measured for several replicates.

The average jet speed U_{jet} can be calculated by dividing the dispersed phase flow rate Q_d by the cross-sectional area of the jet. To calculate the area, we manually measure by drawing a line across the jet width with ImageJ *line* tool and from the 3D reconstruction of the microfibres (section 3.3.2) we assume that the cross-section of the jet is round. Note that for the jet diameter measurement, to ensure the quality of our measurements, the error of measurement is estimated. Different images are measured three times on three different days and the error is quantified. As the measurement error is smaller than the standard deviation of our measurements, it is not taken into account. The exposure time is calculated using the area of the UV light spot. To measure this parameter, a thin film of the typical photosensitive solution is pipetted on a glass slide glued to a Petri dish (to ensure the same working distance as in the setup) and illuminated during $t_{on} = 100$ ms (Figure 3.7.a).

Measurements of the largest diameter of the UV spot are presented in Figure 3.7.b, with average UV spot $D_1 = 552,8 \pm 7.1$ μm and $D_2 = 871.2 \pm 30.3$ μm.

3.2.4 Mechanical characterisation

3.2.4.1 Atomic force microscopy

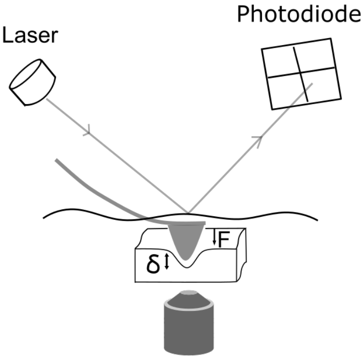

Figure 3.8: Simplified illustration of an AFM setup. The cantilever applies a compressive force F on the sample and indents the sample of a distance δ. This indentation causes the cantilever to bend and the bending is monitored by shining a laser light on the back of the reflective cantilever. The light is reflected on the photodiode. Inspired from Gavara et al. [98].

To measure the Young's modulus of our microgels, atomic force microscopy (AFM) measurements are performed in Quantitative Imaging (QI) mode, using a Nanowizard 4XP BioAFM (JPK/Bruker) at the Leducq Imaging Platform with Dr. Joni Frederick from the LadHyX (Figure 3.8). For sample immobilisation, we coat the bottom of a Petri dish with a thin layer of PDMS to make them hydrophobic, and then a drop of microgels resuspended in MQ water is added onto the PDMS. To produce the thin layer of PDMS a spin coater is used (SPIN150i-NPP, SPS). As the PDMS is hydrophobic, non-wetting water is manually removed by tilting the Petri dish and only microgels remain attached to the PDMS. We then carefully refill the Petri dish with pericyte medium for the AFM measurements to be close to conditions that are compatible with cells and to reduce adhesion between the AFM tip and the microgels, thanks to the presence of albumin in the serum added to the culture medium. Note that, for microspheres (section 3.3.3.3) we perform AFM measurements in PBS as the cell medium detaches the microspheres from the substrate. For soft microgels (between 0.5 kPa and 50 kPa), AFM experiments are performed with a conical tip of a spring constant $k = 0.1$ N/m (QP BIOAC CI10 CB2, Nanosensors). For stiffer microgels (between 100 kPa and 1500 kPa), a conical tip with a spring constant $k = 0.3$ N/m (QP BIOAC CI10 CB1, Nanosensors) is used. The cantilevers are calibrated by the thermal noise method before each experiment [99]. The Poisson's ratio was assumed equal to 0.5. For each measurement, at least 100 nanoindentations are performed over an area of a few micrometres in the centre of the microgel. In the QI mode, the user can select the setpoint [2] (nN), the Z-length [3] (nm), pixel time (ms) and pixel ratio $(4:1)$. To choose the most appropriate setpoint, successive setpoints are tried until a plateau is reached for the Young's modulus. For soft microgels, 1.2, 1.6 and 2 nN are tested, and 1.6 nN is kept with Z-length ranging from $3000-4000$ nm and a pixel time from 160 to 180 ms. For stiffer microgels, the setpoint is at 8 nN, Z-length at 4000 nm and pixel time between 100 and 160 ms. Young's moduli are then calculated by fitting the approach phase of the force-distance curves (Figure 3.9) with the Sneddon model (Hertz model for a conical probe) [100, 101]:

$$F = \frac{E}{1-\nu^2} \frac{2tan\alpha}{\pi} \delta^2,$$

---

[2] Setpoint is the maximal force applied to the sample.

[3] The Z-length is the vertical range of the piezo/indenter.

with F the applied force, E the Young's modulus, ν the Poisson's ratio, α half-angle of the probe $(15°)$ and δ the sample penetration depth. The applied force is obtained from the deflection of the probe while indenting (x) and the spring constant of the probe (k) using Hooke's law: $F = kx$ [102].

The average Young's modulus of each nanoindentation map is used as our final result. All the analyses are done using the data processing software Nanowizard 4 SPM [99].

It is important to note that, looking at Figure 3.9 we can see that the approach and retract curve do not overlap, which is normally the case [98]. We hypothesise that this difference could be due to drift on the cantilever as the measurements are in liquid and the speed is quite high ($\sim$50 µm/s). Further experiments at lower speeds would be required to see if the gap between the two curves is reduced. The fact that there is no sudden bump in the retraction curve and that the two baselines are parallel over the z-length shows that this difference is unlikely to be due to the adhesion. This and the fact that the fit is made on the approach curve ensure that the Hertz model can be used as a first simple model. If in the future this difference is found to be due to adhesion, then a more appropriate model such as the Johnson-Kendall-Roberts model could be used [103].

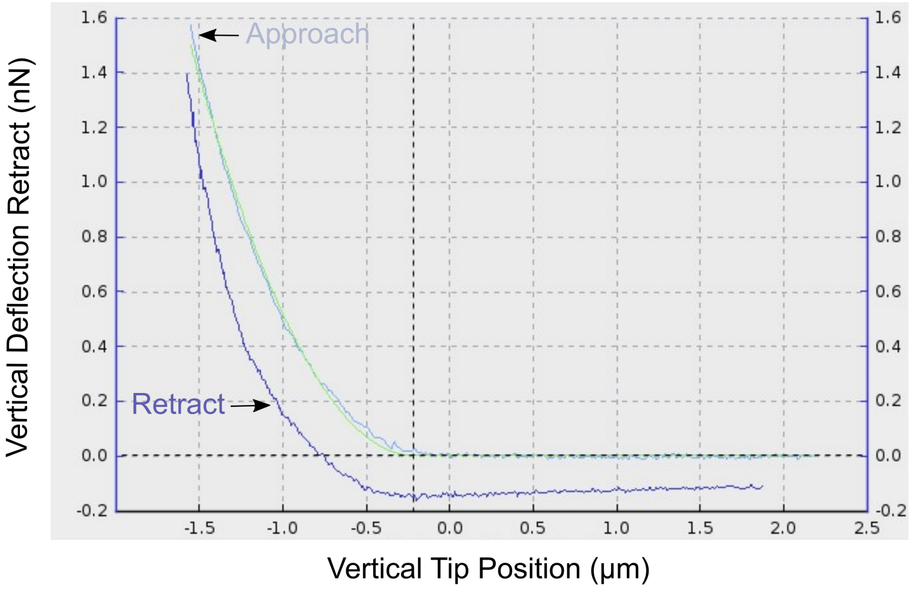

Figure 3.9: Typical force distance curve with AFM obtained for microfibre of $60\ \mu$m diameter produced with flow rates $Q_d = 10\ \mu$L/min and $Q_d = 40\ \mu$L/min. The green line is the fit of the approach curve applied to obtain the Young's modulus. The graph is obtained with the software Nanowizard 4 SPM.

3.2.4.2 Microindentation

Microindentation is also used to measure the Young's moduli of our microgels. We mostly use it for the microspheres, but we also tested one time for the microfibres. Measurements are performed with Prof. Julien Husson (LadHyX) as previously described by him in the Methods in Molecular Biology book series [104]. In short, microgels are resuspended in cell medium in a fluorodish previously treated with 0.1 mg/mL poly-L-lysine-grafted-poly(ethylene glycol) (Pll-g-PEG, PLL(20)-g[3.5]-PEG(2), SuSoS) to prevent microgels from attaching to the surface. Microgels are then held using an aspirating micropipette with a tip diameter $\approx$ 35 µm and pressed with a microindentor, consisting of a flexible micropipette with a glass bead fused at its tip. A microindentor of bending stiffness either $k = 184$ nN/μm or 276 nN/μm and a bead at its tip of diameter $D = 50\ \mu$m and $D = 40\ \mu$m respectively are used for microspheres. Bending stiffness of $k = 12.3$ nN/μm m and a diameter $D = 24\ \mu$m is used for microfibres. The position of the microindentor is set with a piezoelectric translation stage and the position of the microindenter's tip is monitored using the intensity profile on the image acquired by the camera. The applied force F is related to the deflection of the probe into the gel, $F = k[(d-z)-(d_0-z_0)]$, with k the spring constant of the microindentor and $d-z$ the deflection distance between the tip and the top during the measurement and $d_0 - z_0$ the initial deflection distance before the measurement. The applied force is gradually increased until it reaches a maximum set at 2500 nN. A schematic of the setup is shown in Figure 3.10.a. The applied force F, the deflection distance $d-z$ and the time t are extracted using a custom-written Matlab code.

To determine the Young's modulus, the classical Hertz equation between two spheres is used [105]:

$$F = \frac{4}{3}\frac{E}{1-\nu^2}R^{1/2}\delta^{3/2},$$

where F is the contact force between microgel and microindentor (applied force), E the Young's modulus, ν the Poisson's ratio (0.5), R the effective radius and δ the indentation depth.

The value of E is determined by fitting the force indentation curve using Excel's non-linear Generalized Reduced Gradient (GRG) solver (Figure 3.10.b).

The, effective radius is determined with the microgel radius $R_{microgel}$ and the microindentor radius R_{probe} : $R = 1/(1/R_{probe} + 1/R_{microgel}))$. The microindentor is not totally spherical; therefore its radius is: $R_{probe} = 1/average(1/R_1, 1/R_2)$ = $2/(1/R_1 + 1/R_2)$. For microfibre measurements, the microfibre's effective radius corresponds to $R_{microfibre} = 1/average(1/R_{radial}, 1/R_{longitudinal}) = 2/(1/R_{radial} + 0)$, as $R_{longitudinal}$ is infinite. For the microspheres the radii are measured by fitting a circle on ImageJ, and for the microfibre, its diameter is used.

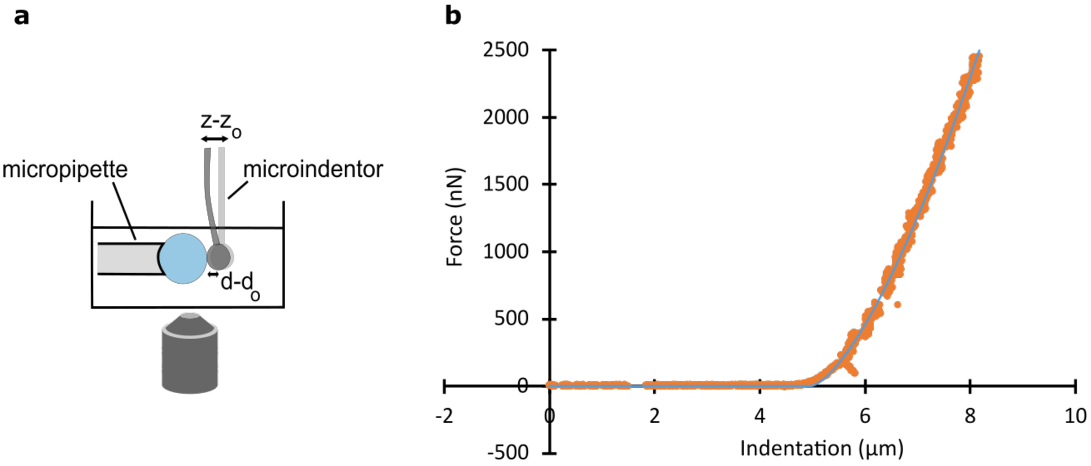

Figure 3.10: Microindentation setup and typical force-indentation curve. a, Illustration of the microindentation method. The microindentor indents the microsphere (light blue) and the initial position of microindentor is shown in light grey. z_o and d_o show respectively the initial position of the base and tip of the microindentor and the new positions as z and d. Adapted from Guillou et al. [106]. **b**, Typical force-indentation curve obtained for $S_{0.2/3.5}$ microsphere indentation. The blue line is the fit applied to obtain the Young's modulus. The fit is calculated using Excel's non-linear *GRG solver*.

3.2.4.3 Determination of volumetric shrinking ratio of microgels

To understand the mesh organisation of our different microgels, shrinking experiments are performed. Microgels are resuspended in MQ water in fluorodishes that were previously treated with 0.1 mg/mL Pll-g-PEG to avoid adhesion of the microgels on the surface. First, microgels are immersed in MQ water and a 10x objective is used to measure the diameter and a 2x to measure the length (Plan UW 2x/0.06, Nikon). Then Milli-Q water is replaced with 100% Glycerol (56-81-5, Fisher BioReagents BP2294). Glycerol will have an osmotic effect and the water inside the microgel will leak out, leading to microgel shrinkage. After 15 min in the glycerol bath, the resulting microgel size is measured. We also measure once after 24 hours to ensure that shrinking no longer evolves. First, to ensure that the shrinkage response is isotropic, dimensional shrinking ratios of both the length DSR_l and diameter DSR_d of microfibres are calculated [107] :

$$DSR_l = 100\,\frac{L_g - L_w}{L_w}$$
$$DSR_d = 100\,\frac{D_g - D_w}{D_w}$$

Where D_g and L_g are, respectively the diameter and length of microfibre after 15 minutes in glycerol and D_w and L_w are the initial diameter and length in Milli-Q water.

Then, the shrinking ratio Q is calculated as follows:

$$Q_{microfibre} = \frac{V_{water}}{V_{glycerol}} = \frac{D^2_{water}\,L_{water}}{D^2_{glycerol}\,L_{glycerol}}$$
$$Q_{microsphere} = \frac{V_{water}}{V_{glycerol}} = \frac{D^3_{water}}{D^3_{glycerol}},$$

with V the volume and D the diameter of the microgel. As microfibres are transparent, the contrast, especially in MQ water is low and automatic detection is difficult to perform. Therefore, all measurements are done manually using ImageJ. For each condition, at least five microgels are measured and the experiment is replicated three times. As for diameter measurements, to ensure the quality of our measurements, the error of measurement is estimated. As the measurement error is smaller than the standard deviation of our measurements, it is not taken into account.

3.2.5 Cell culture protocol

3.2.5.1 microfibre coating

To promote cell adhesion, microfibres are functionalised using Gly-Arg-Gly-Asp-Ser-Pro-Cys (GRGDSPC, Bachem, 25 mg/mL), 20 μl of RGD is added to the microfibres dispersed in ~ 480 μl phosphate buffered saline (1X PBS) and shaken overnight at 300 rpm. After coupling, the microfibre suspension is washed three times with PBS by centrifugation (3500 rpm, 3 minutes, Centrifuge1-14, Sigma). The microfibres are then resuspended in a fresh cell culture medium.

3.2.5.2 Cell culture

For our experiments, we use primary human brain vascular pericytes (PCs), human smooth muscle cells (HAOSMCs) and bovine smooth muscle cells (BAOSMCs). Both PCs (SienCell) and HAOSMCs (Cell Applications) are first thawed and then resuspended in the recommended medium (respectively, Medium-phenol red free, SienCell, 1201-PRF-SC, Human SMC Growth Medium, 095311-500, Tebubio, and Bovine SMC Growth Medium, 821K-500, Cell Applications). Cells are then cultured in 5 ml culture flask at 37℃ and 5 vol% CO_2, the medium is changed every two days for PCs and BAOSMCs and every day for HAOSMCs. When they are confluent, cells are detached using 10% (500 μl) of trypsine (Tryple express, Gibco) for 3 min in the incubator. Note that for PCs, approximately 80% confluency is used instead of full confluency to avoid influencing cell function or phenotype [38]. For PCs, cells are used between passages 2 and 5 and for HAOSMCs and BAOSMCs between passages 4 and 7. To promote cell adhesion, PC culture flasks are coated with Poly-L-Lysine (0.01%, Sigma Aldrich), whereas AOSMC culture flasks are coated with fibronectin (F1141, Sigma Aldrich) at 50 μg/ml for one hour. For the experiments, functionalised fibres are pipetted in Pll-g-PEG (0.1 mg/ml, PLL(20)-g[3.5]-PEG(2), SuSoS) coated fluorodish (WFD3510) and then 2 ml of cell suspension is added. The Pll-g-PEG is used to avoid microfibres sticking to the bottom of the fluorodish. A high density of cells is used to ensure coating of the microfibres, respectively $60000-80000$ cell/ml for AOSMCs and 25000 cell/ml for PCs. The samples are then cultivated at 37°C and 5 vol% CO_2 for 3 hours to 4 days.

3.2.6 Microfibre embedding

Microfibres are difficult to handle due to their size, fragility and transparency. To avoid aspirating all of them during staining and to immobilise them during imaging, we try different protocols to embed them.

3.2.6.1 Fibrinogen microfibre embedding

This protocol is inspired by Eglinger et al. [108]. When confluency is reached, microfibres covered with cells are carefully decanted in a low bind tube of 1.5 ml. Then we carefully replace the medium with 200 μL of fibrinogen resuspended in PBS at 2.5 mg/ml. Note that the fibrinogen solution is filtered with 0.45 μm filter (16555-K, Minisart). In parallel, aliquots of dissolved thrombin at 50 U/ml in PBS are thawed. Then 20 μL of thrombin is quickly but carefully mixed with 150 μL of fibrinogen/microfibres. We then let the gel solidify for 5 minutes at room temperature before adding cell medium. It is important to note that we cannot wait for more than one hour after this procedure before fixing the sample. Indeed, we observe that cells start to detach and migrate in the gel after approximately one hour.

3.2.6.2 Agarose microfibre embedding

To avoid the migration of cells in the gel, we try an inert gel. Indeed, this could allow us to culture our cells in the gel for several days. For that, we immerse 200 μL of the sample in 200 μL of 0.8% low melting agarose (Invitrogen), resulting in a gel of 0.4% agarose. Agarose is prepared at 0.8% by dissolving it in Milli-Q water for 2 hours at 70°C, we let it cool down before use. The percentage of agarose was chosen based on the literature to generate minimal stress on our cells [109].

3.2.7 Imaging procedure

3.2.7.1 Imaging protocol

Cells are fixed after 3 hours to 3 days of culture by treating them with 4% paraformaldehyde solution (28908, Thermo Fisher) for 15 minutes, then they are permeabilised by treating them with PBS + Triton-X-100 0.1% for 15 minutes. Nuclei are stained with DAPI, $1/200000$ μL (D9542, Aldrich), F-actin with phalloïdin Alexa Fluor 488 $1/200$ μL (A12379, Thermo Fisher). Once stained, cells are imaged using an inverted semi-confocal microscope (CREST,TI-DH, Nikon), either with a 20x (CFI Plan Apochromat Lambda 20x, Nikon) or a 40x water-immersion objective (N40XLWD-NIR, Nikon), as well as a confocal microscope (Leica, Laboratory for optics and biosciences, École polytechnique) with a 40x water-immersion or a 64x glycerol objective.

3.2.7.2 Imaging procedure to analyse cell organisation

To quantify the cell organisation on microfibres, both the actin network and the orientation of the nuclei are studied. For this purpose, a confocal z-stack of the phalloidin and DAPI signal is analysed (40x or 64x). A region of interest (ROI) is selected where the microfibre is straight in the z-direction. The microfibre is then tilted to align its axial direction parallel to the y direction (Figure 3.11.b,c,d). A normal projection of half of the microfibre is then made using the plugin *Stack Focuser* from ImageJ (Figure 3.11.b) [110]. A correction is then applied to this projection to account for the distortion that makes cells on the side of the microfibre appear thinner and more axially aligned than the cells at the top of the cylinder. A custom-written Matlab code is used to apply the correction in the horizontal direction (x) to the normal projection (Figure 3.11.a). The following formulas are used:

$$x_{\mathrm{f}} = \begin{cases} R\, cos^{-1}\left(\dfrac{R-x_{\mathrm{i}}}{R}\right) & \text{if } x_{\mathrm{i}} \leq R, \\ R\left[\pi - cos^{-1}\left(\dfrac{x_{\mathrm{i}}-R}{R}\right)\right] & \text{if } x_{\mathrm{i}} > R, \end{cases}$$

where x_{i} and x_{f} are respectively the horizontal coordinates before and after the correction. The radius of the fibre R is measured as half of the width of the fibre in the image. The origin $(0,0)$ is set to the upper right corner of the image. Once the correction has been applied, a larger image with black slots is obtained (Figure 3.11.c). To correct this, all black pixels in the image are replaced with the average intensity of their six neighbours. The *Unsharp mask filter* and *Despeckle* commands from ImageJ are then used to improve the image quality (Figure 3.11.d). The orientation distribution of actin is then extracted using the *Orientation J* plugin in ImageJ (Figure 3.11.e) [110]. Next, the orientation of the nuclei is extracted by fitting ellipses to each nucleus and measuring the angle between the major axis of the ellipse and the image direction. Note that for actin, *OrientationJ* measures the orientation of pixels in an image, whereas for nuclei, we measure the orientation of each nucleus. The data are then processed in Matlab. The probability distribution is plotted in the range -90 to 90°. To compare HAOSMCs and BAOSMCs, the weighted arithmetic mean of all probability distributions measured for each ROI is used.

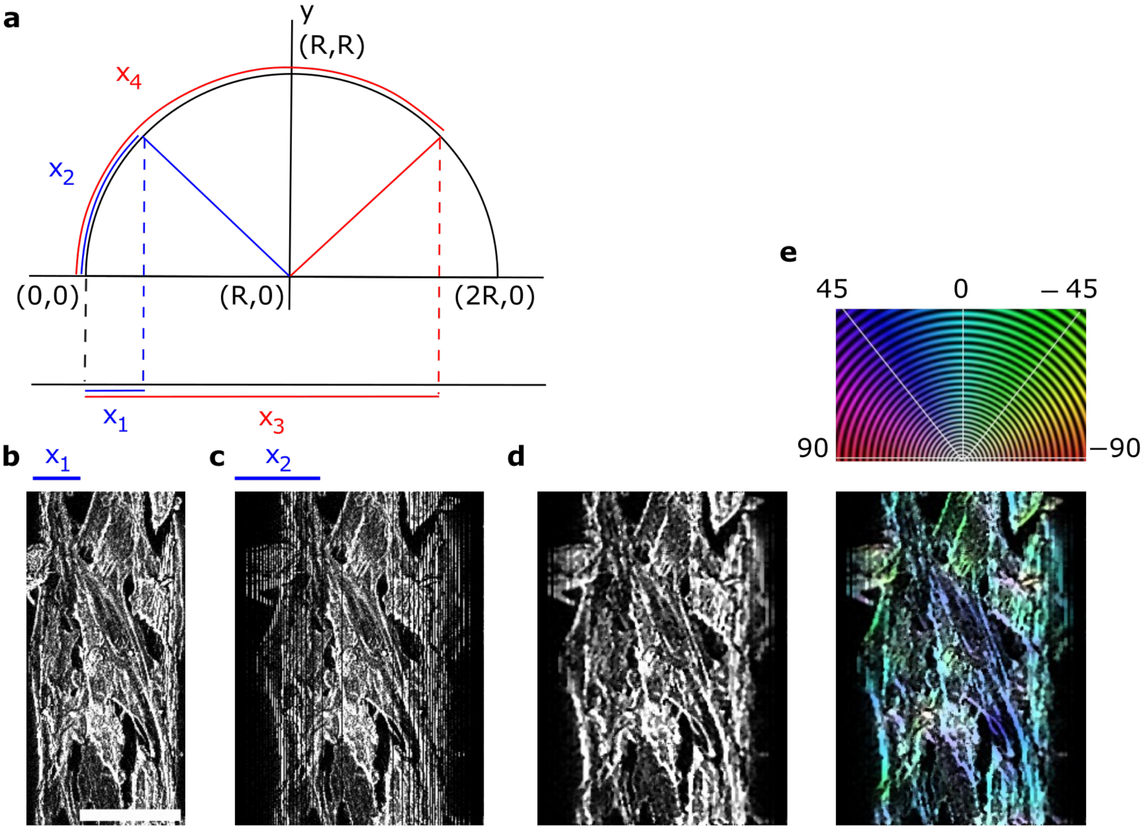

Figure 3.11: Image analysis procedure to quantify actin orientation. **a**, Sketch of the correction applied to the normal projection, where R is the radius of the microfibre, and x_1 and x_3 are the initial horizontal coordinates and x_2 and x_4 are the final horizontal coordinates. **b**, Normal projection of the actin filaments on the microfibre using *Stack Focuser* ImageJ plugin. **c**, Corresponding Matlab-produced stretched image of the actin on the microfibre. **d**, Black pixels of (**c**) are corrected to the intensity of their six neighbours and *Unsharp mask* and *Despeckle* ImageJ commands are applied to improve the image quality. **e**, Actin filaments are colour-coded for fibre orientation, using *Orientation J* plugin. The colour wheel indicates the colours associated with directions. Scale bar = $50\ \mu$m.

3.2.8 Quantification of cell forces

As a first approximation, cell forces are estimated from bright-field images of $\sim 30\ \mu$m diameter microfibres with cells. The DAPI signal is checked to ensure that there is only one cell and not two if there is any doubt in the bright-field image. The following parameters are manually measured using ImageJ's segmented line or angle tool: the length of the microfibre under consideration ($2L$), the diameter of the microfibre (D), the tilt angle (θ_0), the maximum deflection of the microfibre due to cell force (d).

3.2.9 Statistical analysis

The statistical tests used in this chapter are either parametric when the population follows a normal distribution or non-parametric when the data sets are too small and do not follow a normal distribution. The two-sample Student's t-test is used to compare two populations when they follow a normal distribution. If populations have equal variances, Matlab function *ttest2* is used and if they have different variances, *ttest2(x,y,'Vartype','unequal')* is used. For non-parametric tests, a signed test is used to compare a population with a given value; the Wilcoxon rank sum test is used to compare two conditions; and the Kruskal-Wallis test is used for more than two conditions. The Matlab functions *signrank*, *ranksum* and *kruskalwallis* functions are used respectively.

3.3 Results

3.3.1 Exploration of the different parameters to produce the desired microfibres

3.3.1.1 Phenomena of interest for microfibre design

As explained in the introduction, we want to produce homogeneous, straight microfibres with a round uniform cross-section and small diameter that are soft enough to be deformed. This is achieved by using a poly(ethylene glycol) diacrylate (PEG-DA) based solution which is polymerised under ultraviolet (UV) light. To produce the microfibres, a two-phase flow, flow-focusing microchannel is chosen. This makes it possible to produce a jet of tunable diameter with a circular cross-section [92]. Once a stable jet is produced, it is cross-linked using UV light to fabricate microfibres.

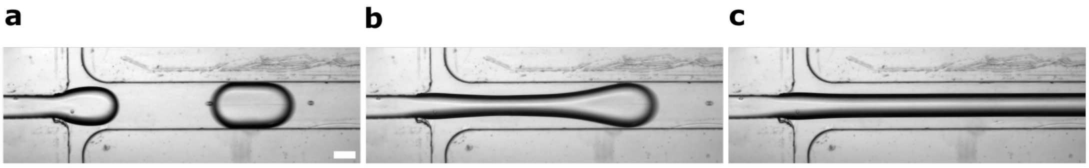

Figure 3.12: Flow regimes in a flow-flocusing channel. a, Dripping regime. **b**, Jetting regime. **c**, Threading regime. Scale bar = $100\ \mu$m.

In a two-phase flow system, different flow regimes can be observed. The three main ones are (i) the dripping regime, where droplets form, (ii) the jetting regime, where the jet breaks into droplets after a certain length (iii) and the threading regime (stable co-flow), where a continuous jet is produced [82, 111]. In the dripping regime (Figure 3.12.a), the dispersed phase enters the two-phase junction and directly breaks up into droplets. Droplets are generated due to instabilities (interfacial capillary forces) at the interface between the dispersed and the continuous phases [82]. In the jetting regime (Figure 3.12.b), the dispersed phase forms a jet of a certain length (l) before breaking into droplets. If the length of the jet is small, then this regime can also be used to fabricate microspheres (section 3.3.3.3) [111]. Whereas, when it is long we use it to fabricate microfibres. Finally, the threading regime (Figure 3.12.c) corresponds to a stable jet that does not break. A stable jet is formed when interface perturbations vanish and stabilising forces as shear stresses and fluid inertia are increased [82]. The transition between jetting and threading depends on the decided cut-off distance, for instance Cubaud and Mason [111] stated that the jetting regime is when $l < 20h$ with h the channel height and threading is when $l > 20h$. In our case, we state the threading is for $l \approx$ channel length.

Two main dimensionless numbers characterise jet stability: the capillary number (Ca) and the Weber number (We) [82]. The Ca number compares viscous forces and interfacial tension (forces that act at the liquid-gas or liquid-liquid interface). The Weber number is the ratio between inertia forces and interfacial tension. In microfluidic systems, where length scales are in the micrometric range, inertial forces are negligible compared to interfacial tension, thus the transition between dripping and jetting is essentially controlled by the Ca number.

Following Kruger et al. [88], we can write two capillary numbers for the continuous (Ca_c) and dispersed phases (Ca_d), respectively :

$$Ca_c = \frac{\mu_c\, U_c}{\gamma} = \frac{\mu_c\, Q_c}{\gamma\, c^2} \tag{3.2}$$

$$Ca_d = \frac{\mu_d\, U_d}{\gamma} = \frac{\mu_d\, Q_d}{\gamma\, c^2} \tag{3.3}$$

with $c = \sqrt{hw}$ where h is the height of the channel and w the width, U_i the section-averaged flow speed ($i = c,d$ for the continuous and dispersed phases), μ_i the viscosity of each phase and γ the interfacial tension between the two phases. We rewrite Ca as a function of the flow rates Q_i by taking the speeds as an average over the whole channel cross-section ($U_i = Q_i/(hw)$).

According to the literature for a flow-focusing geometry, the transition from dripping to jetting regime occurs for the lines, $Ca_c \sim 10^{-3}$ and $Ca_d \sim 10^{-1}$ [82, 111]. Threading regime can be found for $Ca_c > 10^{-2}$ and $Ca_d > 2$ x 10^{-1} approximately [82, 111].

It would be naive to think that all we need to do is to maximise the Ca numbers to produce a stable jet and thus our desired microfibres (section 3.3.1.2). In fact, when choosing our parameters, we have to bear in mind that we want to produce straight, uniform and homogeneous microfibres. This means that we have to impose certain conditions on the flow rate of the jet, the composition of the oligomer solution, the intensity of the UV light and the channel dimensions. This will be discussed in more detail in section 3.3.1.5. The production of thin microfibres requires small channels and small flow ratios (Q_d/Q_c), which will be explained in more detail in section 3.3.1.4. However, we hypothesised that the minimal size of the channel can be limited by the hydraulic resistance, this will be explored in section 3.3.1.5. Finally, as we want to produce soft microfibres, we will need to adjust the time under UV light (or jet speed), the intensity of the UV light or the composition of the solution. Note that this last point will be treated in section 3.3.3.

As we can see, there are several conditions that need to be met to produce the desired microfibres, and some of which impose opposite, competing requirements. It is, therefore, necessary to find an optimal combination at the intersection of all these requirements. To limit the extent of the exploration in this work, the intensity of the UV light as well as the amount of photoinitiator (PI) will be fixed.

3.3.1.2 Parameters studied to produce a stable jet

The first step in our exploration seeks the critical frontiers in the Ca_c-Ca_d diagram that separates the dripping, jetting and threading regimes. According to the literature we need to increase the Ca numbers to get a stable jet [82]. As we have seen with equations 3.3 and 3.2, there are several parameters that can be tuned, the flow rates (dispersed, Q_d and continuous, Q_c), the cross-section of the channel (height, h and width, w) or the composition of the solutions (interfacial tension, γ, viscosity, μ). In this exploration, we will vary the Ca numbers by varying the flow rates, whereas the other parameters (channel geometry, solution composition) will be fixed at set values to study their effect.

Let us first consider the effect of the channel geometry. For this analysis, the dispersed phase is set to 30% (v/v) PEG-DA 575, 30% (v/v) Milli-Q (MQ) water, 30% (v/v) PEG 200 and 10% (v/v) PI and continuous phase to Fluorinated oil (FC-40) and 2% (w/w) Krytox (surfactant). The different tested dimensions are summarised in Table 3.1. Note that when reducing the dimensions, we must also vary the flow rates. Indeed, our aim is to produce thin, uniform and homogeneous microfibres and the more the cross-section is reduced, the higher the jet speed is for the same flow rate. If the jet is too fast, microfibres may not be produced, as the jet will not have the time to polymerise [92]. For this reason, the flow rate must be adjusted. Therefore, the channel dimensions in our exploration seem to only have a limited effect on the formation of a stable jet, whereas we will see in more detail that it is important to consider it for jet solidification (section 3.3.2).

height (µm)	width (µm)	Length (mm)
200	400	11.3
200	300	11.3
130	200	18.6
110	150	14.9
60	100	11.3

Table 3.1: Channel geometry. Tested channel cross-sections (section 3.3.1.2). Here, the length is the distance between the cross intersection of the channel and the end of the channel. Note that for this analysis, the dispersed phase is fixed to 30% (v/v) PEG-DA 575, 30% (v/v) MQ water, 30% (v/v) PEG 200 and 10% (v/v) PI and continuous phase to FC-40 and 2% (w/w) Krytox.

Dispersed phase composition (v/v)	μ_d (mPa/s)	γ (mN/m)	μ_d/γ (s/m)
90% PEG-DA 575 + 0% PEG 200 + 0% MQ water + 10% PI	46.4 ± 0.06	7.4 ± 0.4	6.3
30% PEG-DA 575 + 50% PEG 200 + 10% MQ water + 10% PI	37.4 ± 0.6	5.8 ± 0.3	6.5
30% PEG-DA 575 + 30% PEG 200 + 30% MQ water +10% PI	21 ± 3	5.4 ± 0.3	3.9
50% PEG6DA 575 + 20% PEG 200 + 20% MQ water + 10% PI	27.4 ± 0.4	6.4 ± 0.2	4.3
15% PEG-DA 575 + 45% PEG 200 + 30% MQ water + 10% PI	16.4 ± 0.06	4.5 ± 0.2	3.7
30% PEG-DA 700 + 30% PEG 200 + 30% MQ water +10% PI	27.9 ± 0.1	6.4 ± 0.03	4.4

Table 3.2: Viscosities µ and interfacial tensions γ , of the different dispersed phase composition tested in section 3.3.1.2. Interfacial tension is measured with FC-40 + 2% Krytox as a continuous phase. For all solutions the pendant drop technique is used to measure interfacial tensions, except for the solutions indicated in bold where the rising drop technique is used. Dispersed phase compositions in bold are the ones where only PEG-DA molecular weight changes. For each measurement $n \geqslant 3$, and standard deviation of the mean (STD) is calculated.

Another parameter that can be changed is the composition of the solutions. Two quantities are involved in this parameter, the viscosity and the interfacial tension. To increase the Ca numbers, the interfacial tension must be reduced and the viscosity increased. For the dispersed phase, as explained above, the PI concentration is kept constant (10 % (v/v)). Different compositions of the dispersed phase as well as PEG-DA with two different molecular weights (575 g/mol and 700 g/mol) are tested and summarised in Table 3.2. We can see that the difference in the μ_d/γ ratio between different conditions is small and therefore does not affect the Ca_d value much. However, according to the literature, the amount of solvent is one of the parameters that affects the mechanical properties of the gel. The higher the amount of solvent, the lower the stiffness of the gel [96]. Note that the solution starts becoming biphasic at more than 50% water. The choice of PEG-DA type is also important for the stiffness of the gel. PEG-DA with a higher molar mass will give softer gels [112]. However, at average molar masses above 700 g/mol the polymer is no longer liquid at 25°C. PEG-DA 700 is the one with the highest average molar mass that remains liquid at 25°C [112]. In addition, the difference in the μ_d/γ ratio between PEG-DA 575 and 700 is small (Table 3.2).

Finally, the composition of the continuous phase can be varied. Three solutions are tested: FC-40 with 2% (w/w) Krytox (FC-40), mineral oil with 3.5% (w/w) Span80 (Span80_3.5) and mineral oil with 30% (w/w) Span80 (Span80_30). Figure 3.13.a.b shows that the continuous phase with the highest viscosity is mineral oil with 30% Span80, which also has the lowest interfacial tension. Table 3.3 shows that for Span80_30 the ratio μ_c/γ is more than 150 times higher than for FC-40, which maximises the Ca_c number. In addition, the Ca_d number also increases as the interfacial tension decreases. For example, for a dispersed phase with 30% (v/v) PEG-DA 700, 30% (v/v) MQ water, 30% (v/v) PEG 200 and 10% (v/v) PI, the ratio will be more than 20 times higher with Span80_30 than with FC-40 (Table 3.3).

From our investigation, it appears that for our system the composition of the continuous phase is the parameter that will increase the Ca numbers the most, while varying the cross-section of the channel mainly serves to control the fibre diameter and stiffness, as we will discuss later in more detail.

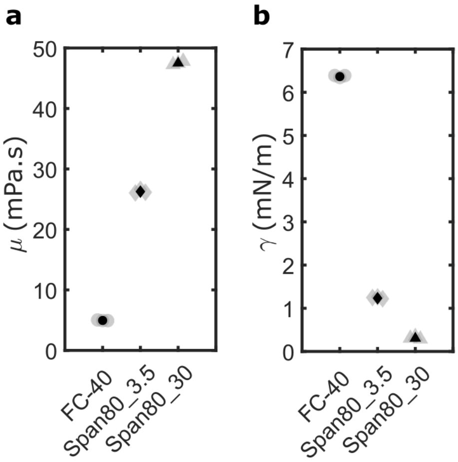

Figure 3.13: Viscosities and interfacial tensions of the tested continuous phases a, Viscosity (μ_i) of three different mixtures used as continuous phase, FC-40 + 2% Krytox, mineral oil + 3.5% Span80 and mineral oil + 30% Span80. **b**, Corresponding interfacial tensions. The measurements are performed at the LPS (at the University of Orsay) using the rising drop method. Nil red is added to the solution to increase contrast. The dispersed phase used to quantify the interfacial tensions is composed of 30% (v/v) PEG-DA 700, 30% (v/v) MQ water, 30% (v/v) PEG 200 and 10% (v/v) PI. Black dots correspond to the mean value and error bars correspond to STD. At least three measurements are carried out for each solution (grey dots).

Continuous phase composition	Name	μ_d/γ (s/m)	μ_c/γ (s/m)
FC-40 + 2% Krytox	FC-40	4.4	0.8
mineral oil + 3.5% Span80	Span80_3.5	22.7	21.4
mineral oil + 30% Span80	Span80_30	92.2	156.7

Table 3.3: Dispersed phase (μ_d) and continuous phase (μ_c) viscositiy and interfacial tension (γ) ratios as a function of continuous phase composition. For the ratio μ_d/γ, the dispersed phase composition used is: 30% (v/v) PEG-DA 700, 30% (v/v) MQ water, 30% (v/v) PEG 200 and 10% (v/v) PI.

3.3.1.3 Effect of the capillary numbers on the jet formation

The general Ca_c - Ca_d phase diagram, combining all the conditions obtained for the different tested parameters, is shown in Figure 3.14. We can see that a stable jet (threading regime) is obtained as the Ca numbers of the dispersed and continuous phases are increased and that the threshold lines are close to $Ca_d = 10^{-1}$ and $Ca_c = 10^{-2}$ a conclusion that is consistent with the literature on microfluidic flow-focusing [82, 111]. Two regions of the phase diagram can be distinguished depending on the value of Ca_c. For $Ca_c < 10^{-1}$, the transition between the dripping and threading regimes depends on Ca_c. Indeed, we can see in the phase diagram that the critical value of Ca_d where the transition occurs increases with Ca_c. Thus, for example, for $Ca_c \sim 3$ x 10^{-3} the threading regime is obtained for $Ca_d \sim 2$ x 10^{-2}, whereas for $Ca_c \sim 3$ x 10^{-2} the threading regime is obtained for $Ca_d \sim 10^{-1}$. In the second region, for $Ca_c > 10^{-1}$ the transition between dripping and threading seems to be independent of Ca_c and occurs around $Ca_d \sim 10^{-1}$. Note that we can observe differences between our phase diagram and the literature. Indeed, the transition between dripping and jetting regime occurs for $Ca_d \sim 3$ x 10^{-2} and $Ca_c \sim 10^{-3}$ however, in the literature for these capillary numbers, it is dripping regime that is obtained [82, 111]. These differences may be due to the different ways in which the flow regimes are defined, indeed we have seen that we use a different threshold length to define the jetting regime [111, 113]. It may also be due to the different solutions used. For example, Cubaud and Mason used a viscosity ratio $\frac{\mu_d}{\mu_c} = 264$ whereas we use $\frac{\mu_d}{\mu_c} = 0.6 - 5.8$.

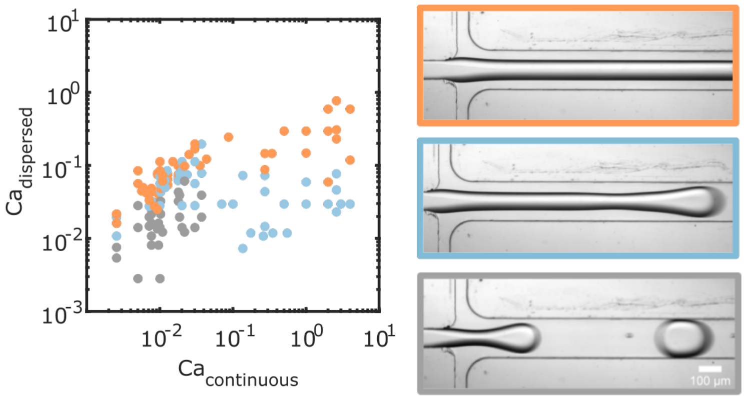

Figure 3.14: Capillary number-based phase diagram of the different flow regimes obtained for different explored channel dimensions, solution compositions and flow rates. Observed flow regimes are, threading (orange), jetting (cyan) and dripping (grey). Scale bar = $100\ \mu$m.

3.3.1.4 Production of a thin jet

Following our phase diagram (Figure 3.14) to be certain to produce a stable jet (threading regime) in our system, we need to have $Ca_d \sim 10^{-1}$ and $Ca_c \sim 10^{-2}$. Once a stable jet is obtained, the jet diameter must be adjusted to be close to small blood vessel diameters ($5-30\ \mu$m) [2]. To achieve this, either the flow rate ratio or the cross-section of the channel can be adjusted. We first decide to vary the flow rate between the inner and outer phases, keeping all other parameters constant.

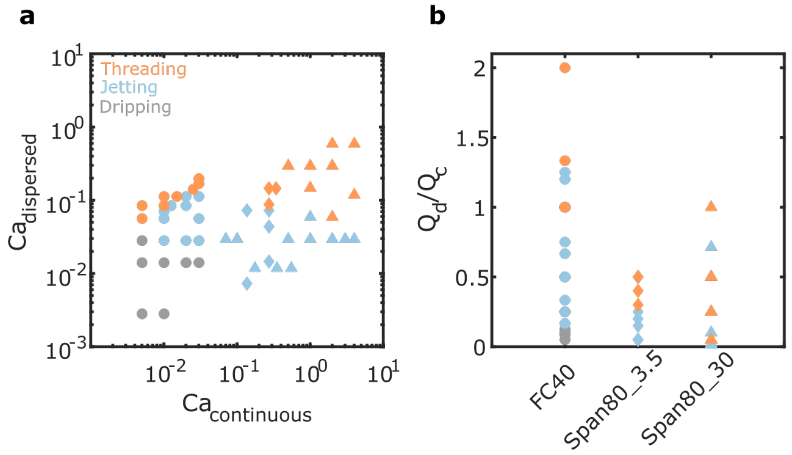

Figure 3.15: Impact of the continuous phase composition on capillary numbers. **a**, Phase diagram summarising Ca numbers for three different continuous phases and various flow rates. FC-40 with 2% of Krytox (circles), mineral oil with 3.5% of Span80 (diamonds) and mineral oil and 30% of Span80 (triangles). **b**, Corresponding flow rate ratios explored for the corresponding continuous phase composition. The dispersed phase composition is set to: 30% PEG-DA 700, 30% MQ water, 30% PEG 200 and 10% PI and channel cross-section: 200 x $130\ \mu m^2$. Observed flow patterns are, threading (orange), jetting (cyan) and dripping (grey).

According to the literature on PEG-DA fibres, we can produce fibres of $40\ \mu$m diameter with a channel of $w = 200\ \mu$m and $h = 135\ \mu$m, thus we decide to start with a similar cross-section ($h = 130\ \mu$m and $w = 200\ \mu$m) [92]. From our observations in section 3.3.1.2, we set the dispersed phase solution to 30% PEG-DA 700, 30% MQ water, 30% PEG 200 and 10% PI. Note that the composition of the solution could be optimised in the future. For the continuous phase, Figure 3.15.a shows that for these parameters threading regime can be achieved for all the three solutions that were tested. However, Figure 3.15.b shows that the minimal flow rate ratio required for threading to occur, is much smaller for Span80_30 (Q_d/Q_c = 0.05) than for FC-40 (Q_d/Q_c = 1), thus allowing us to stay in the jetting or threading regime for smaller jet diameters. Therefore, we first use mineral oil with Span80_30 as the continuous phase.

The tested flow rates are summarised in Table 3.4. From now on, each flow condition will be referred to by the notation F_{Q_d/Q_c}. As shown in Figure 3.16 (cyan), we are able to produce a minimal jet diameter of 27.7 ± 1.6 μm in a reproducible manner. However, if we want to produce smaller microfibres, we end up in the jetting regime, where the jet becomes too unstable. It is important to note that microfibres can be produced in the jetting regime as long as the jet breaks up far enough from the polymerisation spot, avoiding destabilisation of the jet while it is polymerising.

To further reduce the jet diameter to 10 μm, a smaller channel cross-section is required. From the literature, the minimum jet diameter that can be achieved for a given geometry is about ten times smaller than the channel cross-section [88]. Therefore, we decide to use a channel with a square cross-section of $h = 100$ μm. The results are shown in Figure 3.16 in duck blue and we can observe that the minimal diameter is $D_{jet} = 8.6 \pm 0.3$ μm. In this case, we are in the jetting regime, but the jet breaks far enough to produce microfibres in a reproducible manner.

Name (F_{Q_d/Q_c})	Q_d (μl/min)	Q_C (μl/min)	Q_d/Q_c	Channel cross section h x w (μm^2)
$F_{0.15/10}$	0.15	10	0.015	100 x 100
$F_{0.3/10}$	0.3	10	0.03	100 x 100
$F_{1/10}$	1	10	0.1	100 x 100
$F_{1.5/10}$	1.5	10	0.15	100 x 100
$F_{1/20}$	1	20	0.05	130 x 200
$F_{2/40}$	2	40	0.05	130 x 200
$F_{1.6/6.4}$	1.6	6.4	0.25	130 x 200
$F_{5/20}$	5	20	0.25	130 x 200
$F_{10/40}$	10	40	0.25	130 x 200
$F_{10/20}$	10	20	0.5	130 x 200
$F_{15/20}$	15	20	0.75	130 x 200

Table 3.4: Summary of tested flow rate ratios with 30% Span80 as continuous phase to produce a thin jet.

It was demonstrated by Cubaud and Mason [111], for a square flow-focusing geometry, that the jet diameter can be estimated from the following relationship :

$$D = h \left(\frac{Q_d}{2Q_c} \right)^{1/2} \tag{3.4}$$

with D the jet diameter, h the height (here, equal to the width) of the channel and Q_d and Q_c respectively the dispersed and continuous flow rate. This relationship is derived by assuming the continuity of velocity at the interface of the two fluids and continuity of shear stress [114]. It was assumed that the jet is a small cylinder in a circular tube $D_{jet} < 0.8h$. We can follow the same reasoning but for our rectangular channel and replace h with $\sqrt{hw}$ to obtain the following relationship:

$$D_{jet} = \left(\frac{hw\, Q_d}{2Q_c} \right)^{1/2} \tag{3.5}$$

Dashed lines in Figure 3.16 show the corresponding theoretical estimate for both the rectangular and square channels. It predicts pretty well jet diameters for the square channel and for small jet diameters in the rectangular channel. However, it is less exact for large jet diameters ($D_{jet} > 80\ \mu m$) in the rectangular channel. This can be due to the fact that the relationship is only valid for $D_{jet} < 0.8h$ [111]. This theoretical estimate could help us in the future to reasonably predict, for a fixed channel cross-section, the expected jet diameter for a given flow rate ratio. Knowing the corresponding Ca, we can then estimate if we are in either the jetting or threading regime.

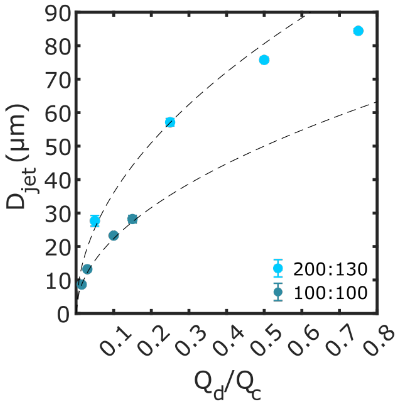

Figure 3.16: Jet diameter vs flow rate ratio using 30% Span80 and mineral oil. Jet diameter D_{jet} as a function of flow rate ratio Q_d/Q_c for a channel with $200\ \mu$m width and $130\ \mu$m height (cyan) and a channel with a square cross-section $100x100\ \mu m^2$ (duck blue). The dashed line represents the fit of the relationship between jet diameter and flow rate ratio using equations 3.4, 3.5). Error bars correspond to STD and dots to the mean. For channel $200x130$: $n_{0.75} = 3$, $n_{0.5} = 5$, $n_{0.25} = 25$, $n_{0.05} = 20$. For channel $100x100$: $n_{0.15} = 3$, $n_{0.1} = 2$, $n_{0.03} = 6$, $n_{0.015} = 4$, n represents the number of jets and is based on at least two different sets of experiments carried out on different days.

As previously explained, the threading regime can also be obtained with FC-40 and Krytox as a continuous phase. Figure 3.17 shows the jet diameter as a function of flow rate ratios for two channel dimensions. We can see that the minimal jet diameter is for both geometries much larger than $30\ \mu$m. Indeed, we cannot further decrease the flow rate ratio, as we are already in the jetting regime for most data points and decreasing further the dispersed phase flow rate will lead to the dripping regime. Therefore, for the rest of the experiments we will use mineral oil with 30% Span80 as the continuous phase.

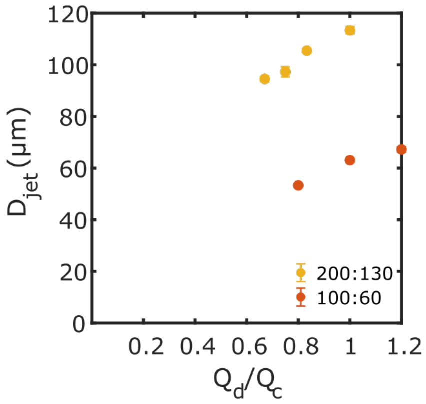

Figure 3.17: Jet diameter vs flow rate ratio, using FC-40 with 2% Krytox. Jet diameter D_{jet} as a function of flow rate ratio Q_d/Q_c for two channel cross-sections: $200x130\ \mu m^2$ (yellow) and $100x60\ \mu m^2$ (red). Error bars correspond STD, and dots are the means. For channel $200x130$: $n_1 = 3$, $n_{0.83} = 3$, $n_{0.75} = 3$, $n_{0.66} = 3$. For channel $100x60$: $n_{1.2} = 3$, $n_1 = 3$, $n_{0.8} = 3$, n represents the number of jets.

3.3.1.5 Other constraints to be taken into account when producing microfibres

As previously explained in section 3.3.1.1 at least two other parameters have to be taken into account: the resistance of the channel and the uniformity of the microfibres (as we aim to produce straight round microfibres).

Let us first discuss channel hydraulic resistance. At the beginning of the project, a channel of square cross-section $30\ \mu$m was tested. However, un-plug of the inlet of the continuous phase has been observed for the flow rate of Q_c = $10\ \mu$L/min. We therefore hypothesised that a limiting factor could be the hydraulic resistance of the channel, which would preclude the use of a too narrow channel. To verify this hypothesis, we can estimate the hydraulic resistance (R) of the channel and see for different flow rates the corresponding difference of pressure (ΔP). As the continuous phase is the more viscous phase (in our case), we can assume that the principal resistance is R_c. Here, the geometry of the channel will be assumed to be a tube of length L and a square cross-section. The continuous phase is set to: mineral oil + 30% Span80 (as it is the more viscous one that was tested). The resistance for a rectangular channel is therefore [115]:

$$R_c = \frac{12\mu_c L}{1 - 0.63\dfrac{h}{w}} \frac{1}{h^3 w} \tag{3.6}$$

With μ_c the viscosity of the continuous phase, h the height of the channel and w the width. By analogy to Ohm's law for electric circuits the relationship between ΔP and Q_c is: $Q_c = \Delta P / R_c$.

For channel (1) of $h = 30\ \mu$m and $L \approx 17$ mm, $R_c = 3.2$ x 10^{16} Pa.s.m^{-3} whereas, for channel (2) of $h = 100\ \mu$m and $L = 25$ mm (like the one that is used in section 3.3.1.4) $R_c = 3.9$ x 10^{14} Pa.s.m^{-3}. For a flow rate of $Q_c = 10\ \mu$L/min the corresponding pressures are $P_1 = 53.9$ bar and $P_2 = 0.64$ bar. The pressure for the second channel is more than fifty times smaller than the one for the first channel. Note that the Nemesis syringe pump that we use has a maximal pressure of 10 bar. As P_1 is larger than 10 bar, the syringe pump was not able to handle it and this might be why an unplug of the inlet was observed. However, for small channel of $h = 30\ \mu$m, (even with a longer length like we use now $L \approx 25$ mm) jetting can still be obtained for smaller flow rates. For instance, for $Q_c = 1\ \mu$L/min and $Q_d = 0.1\ \mu$L/min ($Ca_c = 2.9$ and $Ca_d = 0.17$) which corresponds to a $P = 7.9$ bar and would give according to equation 3.4 a jet diameter of $d = 6.7\ \mu$m. We can therefore state that hydraulic resistance can be a limiting factor if the flow rates are not adapted and a ΔP = 10 bar is exceeded.

Another parameter that has to be taken into account is the uniformity of the microfibres. Indeed, we want to produce relatively straight, uniform microfibres of round cross-sections. The uniformity of the microfibres depends on the dispersed phase composition, the intensity of the UV light, the size of the UV spot, the oxygen content, and the speed of the jet [92]. Here, the three first parameters are fixed, and the oxygen concentration is assumed to be relatively constant from one experiment to another. The only remaining parameter is the jet speed. If the jet speed is too important, the jet will not have the time to polymerise properly and will form non-uniform microfibres with semi-polymerized blobs or even no microfibre for too high speed [92]. Slutzky et al. [92] estimated that for $U_{jet} = 40 - 100\ \mu$m/ms, non-uniform or no microfibre could be observed for a similar range of parameters as ours. We therefore, hypothesise that jet speed should be smaller than $100\ \mu$m/ms. This will be further explored in section 3.3.2.

Once uniform microfibres are produced, another parameter that is important is the distance between the UV spot and the end of the channel. Indeed, this parameter will impact the waviness of the microfibre. The shorter the distance is, the wavier the microfibre is, for all other parameters kept constant. From experiments, the total length of the channel is set to $L \approx 25$ mm (with the distance between the cross-section and the end of the channel equal to 18.6 mm) to have enough distance between the UV spot and the end of the channel (15 mm). This phenomenon will be explored in more detail in section 3.3.3.

3.3.1.6 Recommended parameters for the production of thin, uniform microfibres

Our exploration enables us to prescribe guidelines to produce straight, uniform microfibres from approximately 10 to $80\ \mu$m diameter. Note that at this stage, the rigidity of the microfibres has not been explored yet. The results are summarised in Table 3.5. From our exploration, we can state that the limiting parameters are the following:

- The capillary numbers, $Ca_c \geqslant 0.1$ and $Ca_d \geqslant 0.1$, ensure to be in the threading regime and create thin jets.
- The jet speed $Umax_{jet} = 0.1$ m/s, to ensure that uniform microfibres are produced. Note that this might be decreased for lower PEG-DA % or PI%, lower intensity of the UV light and/or smaller size of the UV spot [92].
- The length of the channel $Lmin \sim 25$ mm, that we preconize to obtain straight microfibres.
- The range of diameters of the jet, $Dmin_{jet}$ and $Dmax_{jet}$ that depends on the application.
- The maximal pressure $Pmax = 10^6$ Pa, imposed by the syringe pump, which is important not to exceed.

From these parameters and the governing equations, the other parameters can be estimated. Note that either rectangular or square channels can be used and that the maximal jet diameter that can be produced will be set by the smallest side of the channel (height or width). The pressure should be estimated using equation 3.6, not to exceed 10 bar.

Parameter to determine	Governing equation
rectangular $A_r = hw \ (m^2)$	$Dmin_{jet} \approx \frac{\sqrt{hw}}{6}$
square $A_s = h^2 \ (m^2)$	$Dmin_{jet} \approx \frac{h^2}{10},$
$Q_d \ (m^3/\text{s})$	$Q_d \leqslant \frac{Umax_{jet} \ \pi D_{jet}^2}{4}$
$Q_c \ (m^3/\text{s})$	$Q_c = \frac{hw \ Q_d}{2D_{jet}^2}$
U_c (m/s)	$U_c = \frac{Q_c}{hw}$
$\frac{\mu_d}{\gamma}$ (s/m)	$\frac{\mu_d}{\gamma} \geqslant \frac{Ca_d}{U_d}$
$\frac{\mu_c}{\gamma}$ (s/m)	$\frac{\mu_c}{\gamma} \geqslant \frac{Ca_c}{U_c}$

Table 3.5: Summary of the parameters to produce the desired microfibres. A is the cross-sectional area of the rectangular or square channel, respectively A_r and A_s. It is determined from our previous observation in subsection 3.3.1.4. The maximal dispersed phase flow rate is Q_d and can be estimated using the threshold jet speed $Umax_{jet}$ and the continuity equation. The maximal continuous phase flow rate Q_c, can be estimated using the equation 3.4 or 3.5 [111]. Same as for Q_d, the continuous phase maximal speed U_c can be estimated from the continuity equation. Finally, the minimal ratio viscosity/interfacial tension is determined using the definition of the capillary number for flow-focusing geometry (equation 3.2) [88].

.

Possible parameters to produce a jet diameter between 10 and 80 μm are summarised in Table 3.6. For this example, the square relation is used to determine the channel cross-section (A_s). According to the conditions, the height of the channel needs to be between 100 and 80 μm. Here we perform the calculation for h = 100 μm. As we can see in Table 3.6, either Span80_30 or Span80_3.5 could be used as continuous phase and all the dispersed phase solutions that are tested in section 3.3.1.2 could be used.

For the rest of the project, we decide to use the following parameters: channel height of 130 μm with a width of 200 μm to produce microfibres from 30 to 80 μm or channel with $h = w = 100$ μm for 10 μm microfibres. A dispersed phase solution with 30% PEG-DA 700, 30% MQ water, 30% PEG 200 and 10% PI, and mineral oil with 30% Span80 as the continuous phase. However, as previously observed other sets of parameters can be used.

	$Dmin_{jet} = 10$ μ m	$Dmax_{jet} = 80$ μ m
A_s (m^2)	$A_s \leqslant 10^{-8}$ with $h \geqslant 80$	
Q_d (m^3/s)	7.8 x 10^{-12} (0.5 μL/min)	5 x 10^{-10} (30 μL/min)
Q_c (m^3/s)	3.9 x 10^{-10} (23.5 μL/min)	1.6 x 10^{-9} (93.6 μL/min)
U_c (m/s)	0.04	0.2
μ_d/γ (s/m)	1	1
μ_c/γ (s/m)	2.6	0.6

Table 3.6: Parameters to produce microfibres of 10 to 80 µm diameter. Here, the calculations are based on equations in Table 3.5 and limiting factors. A channel height $h = 100$ μm is used in the calculations.

3.3.2 From jet to microfibre

Once we have obtained the desired jet diameter and a stable jet, we use a pulsed UV light to polymerise the jet and fabricate microfibres of a few millimetres in length. In short, the PI reacts with the UV light to form radicals that react with the acrylate groups of the oligomer to form reactive alkyl monomer radicals. This is the initiation step. The radical then reacts with the monomers to propagate chain formation. The reaction is complete when the radical species react with each other to form neutral species. For polymerisation to proceed, most of the oxygen must be consumed. In fact, oxygen will react with radicals and inhibit polymerisation. Therefore, the propagation rate must be equal to or greater than the rate of oxygen inhibition [92, 116]. According to the literature, the fibre production will depend on the oxygen concentration, the intensity of the UV light (more or less photons can be sent), the speed of the jet and photoinitiator concentration [92]. Therefore, it is not because we have a stable jet that we will obtain uniform microfibres. Indeed, there are three different regimes of fibre production [92]: a first regime, where no fibres are produced, a second regime, where produced fibres are not uniform and with semi-polymerised blob, and a third regime, where uniform fibres are produced.

In section 3.3.1.5 we gave guidelines on the maximal jet speed not to exceed from the literature, in this paragraph, we investigate what is the optimal range of speed for our system. Different flow rates are tried with the channel of 200 μm width and 130 μm height to see for which flow rates and thus jet speed (U_{jet}) the different regimes happen. Similar regimes as Slutsky et al. [92] are observed. For instance, for jets of $D_{jet} \approx 57$ μm, uniform microfibres are produced for flow rates up to $Q_d = 20$ μL/min and $Q_c = 80$ μL/min (Figure 3.18.b) which corresponds to $U_{jet} \approx 130$ $\mu m/ms$. However, these microfibres are no longer straight. Indeed, above $Q_d = 10$ μL/min and $Q_c = 40$ μL/min ($U_{jet} \approx 65$ μm/ms) generated microfibres (Figure 3.18.a) are too wavy (the reason of this phenomenon will be discussed in detail in section 3.3.3.1). For larger flow rates of $Q_d = 24$ μL/min and $Q_c = 96$ μL/min microfibres no longer have the shape of the jet and their diameter is much larger (Figure 3.18.c), this regime could be apparent to the 'transitional regime' described by Slutzky et al. [92], however compare to them our fibres seem uniform with no semi-polymerised blobs or discontinuities. For flow rates of $Q_d = 30$ μL/min and $Q_c = 120$ μL/min microfibres are no longer produced, which corresponds to $U_{jet} \approx 196$ μm/ms. To produce uniform straight microfibre of a diameter similar to the jet in our system, it is therefore better not to exceed $U_{jet} \approx 65$ μm/ms.

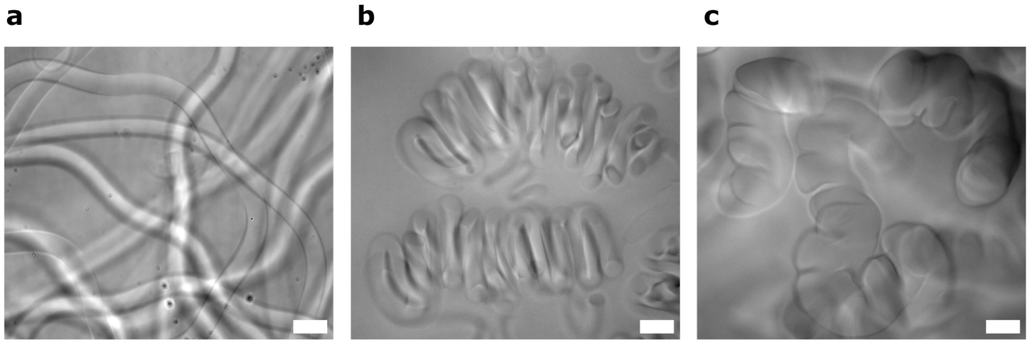

Figure 3.18: Impact of jet speed on the shape of microfibres. a, b, c, Representative bright-field images (10x) of ≈ 60 μm microfibres. From left to right, the flow rates of both dispersed and continuous phases are increased in a manner to keep the Q_d/Q_c ratio constant. Respectively, microfibres produced from a $U_{jet} \approx 65$ μm/ms, $U_{jet} \approx 130$ μm/ms, and $U_{jet} \approx 157$ μm/ms. Scale bars = 50 μm.

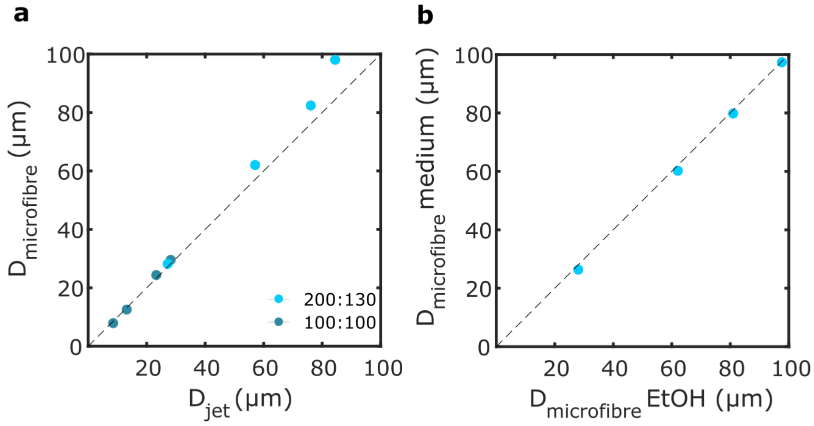

Figure 3.19: Comparison between jet diameter and microfibre diameter. a, Microfibre diameters of the jets produced in Figure 3.16. The microfibres are produced either with channel cross-section: 200 x 130 μm^2 or 100 x 100 μm^2. Dashed line is the linear fit $y = x$. For channel 200 x 130: $nj_{0.75} = 3$ and $nf_{0.75} = 11$, $nj_{0.5} = 2$ and $nf_{0.5} = 12$, $nj_{0.25} = 9$ and $nf_{0.25} = 37$. For channel 100 x 100: $nj_{0.15} = 3$ and $nf_{0.15} = 12$, $nj_{0.1} = 2$ and $nf_{0.1} = 8$, $nj_{0.03} = 4$ and $nf_{0.03} = 13$, $nj_{0.015} = 3$ and $nf_{0.015} = 9$. **b**, Comparison of microfibre diameter in EtOH before washing and 24 h later in medium after washing steps. Only microfibres for 200 x 130 μm^2 cross-section are measured. Dashed line is the linear fit $y = x$. $nj_{0.75} = 3$ and $nf_{0.75} = 5$, $nj_{0.5} = 6$ and $nf_{0.5} = 6$, $nj_{0.25} = 9$ and $nf_{0.25} = 11$, $nj_{0.05} = 8$ and $nf_{0.05} = 11$. The "n" represents the number of microfibres or jets and comes from at least two different batches for (**a**) and one batch for (**b**). Error bars (STD) are not shown as they are smaller than the dots (mean).

After producing microfibres, the first step is to ensure that microfibre diameters correspond to jet diameters. Figure 3.19.a compares jet diameter with the corresponding microfibre diameter. Here, microfibre diameter is directly measured after its production in an EtOH bath. We can see a correlation of microfibre diameter with their jet diameter (dashed line). However, the ratio of jet to microfibre diameters decreases for bigger microfibres. From the literature, this could be explained by the competition between swelling and oxygen inhibition. The polymerisation process of PEG-DA is inhibited by oxygen diffusion in the chip leading to a thin layer of non-polymerized gel [92, 116]. On the contrary, swelling is the process that will increase the diameter of the gel. For our experimental conditions, we can estimate that the penetration of oxygen from the outside into the jet is small. Indeed, from Slutzky et al. [92] we can estimate the maximal diffusion length $\sqrt{Dt}$ with D the diffusivity of oxygen in the oligomer solution $D \sim 10^{-10}$ $m^2.s^{-1}$ and $t_{uv} = L/U_{jet}$. For our setup, we measured a maximal average UV spot diameter of $L_{ave} = 871.2 \pm 30.3$ μm. For the slowest jet speed ($U_{jet} = 10.4 \pm 0.2$ μm/ms), the oxygen diffuses over approximately 3 μm into a 60 μm diameter microfibre. As the ratio $D_{microfibre}/D_{jet}$ is not constant and slightly increases there are probably other parameters to take into account in addition of swelling. In our case, as we focus on small diameters (< 60 μm), we did not investigate this difference further. Figure 3.19.b shows the difference in diameters of microfibres in EtOH and 24h after cleaning in the medium. We can see that they have the same diameter, and no swelling is observed after the production. Note that in Figure 3.19.a.b, some conditions have the same jet diameter and flow rate ratio but different flow rates and thus, jet speed. To verify if this difference leads to different microfibres, we measure both the jet and microfibre diameters and compare them. Figure 3.20 shows that for both flow rate ratios, Q_d/Q_c = 0.25 (triangles, $F_{1.6/6.4}$, $F_{5/20}$, $F_{10/40}$) and Q_d/Q_c = 0.05 (circles, $F_{1/20}$, $F_{2/40}$), microfibre diameter is independent of jet speed. We will see in section 3.3.3 that while jet speed in this range does not influence fibre diameter, it may change its mechanical properties. Figure 3.21 shows representative bright-field images of fibres that can be obtain with either channel 200 x 130 μm^2 (**a,b**) or channel 100 x 100 μm^2 (**c,d**).

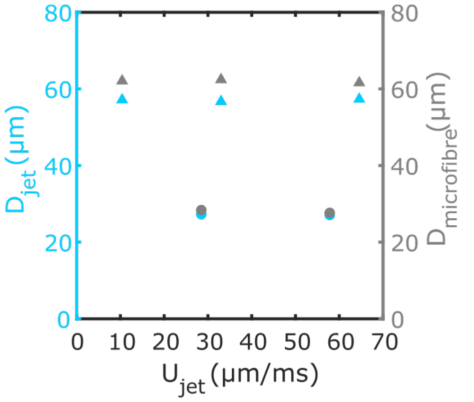

Figure 3.20: Jet speed has no effect on jet and microfibre diameter. Jet (cyan) and corresponding microfibre diameters (grey) for two different flow rate ratios, $Q_d/Q_c = 0.25$ (triangles, $F_{1.6/6.4}$, $F_{5/20}$, $F_{10/40}$) and $Q_d/Q_c = 0.05$ (circles, $F_{1/20}$, $F_{2/40}$) but with different jet speeds, U_{jet}. For $F_{1.6/6.4}$: $nj = 3$ and $nf = 13$, for $F_{5/20}$: $nj = 3$ and $nf = 11$, for $F_{10/40}$: $nj = 3$ and $nf = 13$, for $F_{1/20}$: $nj = 3$ and $nf = 4$, for $F_{2/40}$: $nj = 3$ and $nf = 10$. The "n" represents the number of microfibres or jets and comes from at least three different batches. Error bars (STD) are not shown as they are smaller than the dots (mean).

To ensure a circular cross-section and to later track the deformation of microfibres due to cell forces, fluorescent nanoparticles (500 nm in diameter) can be embedded in microfibres. 3D reconstruction of a microfibre using confocal microscopy shows uniform distribution and no aggregation for large microfibres (Figure 3.22.a). However, in thinner microfibres, the distribution of nanoparticles becomes non-uniform 3.22.b). In this case, dye-like Rhodamine might be used instead.

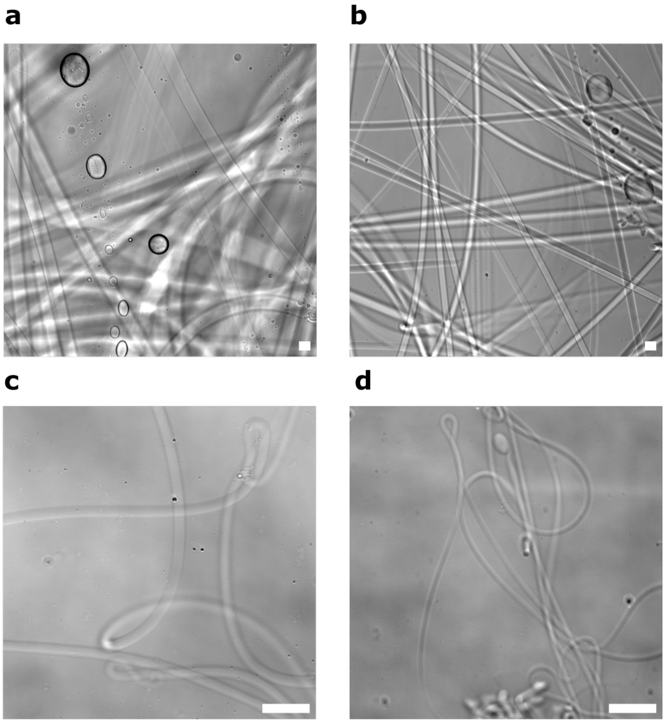

Figure 3.21: Microfibres produced in different conditions. a,b, Representative bright-field images (10x) of $\approx 60\ \mu$m and $\approx 30\ \mu$m microfibres, respectively $F_{5/20}$ and $F_{1/20}$. Channel dimensions are $w = 200\ \mu$m and $h = 130\ \mu$m. **c,d**, Representative bright-field images (40x) of $\approx 12\ \mu$m and $\approx 8.5\ \mu$m microfibres, respectively $F_{0.3/10}$ and $F_{0.15/10}$. A square cross-sectioned channel is used $h = 100\ \mu$m. Scale bars = $50\ \mu$m.

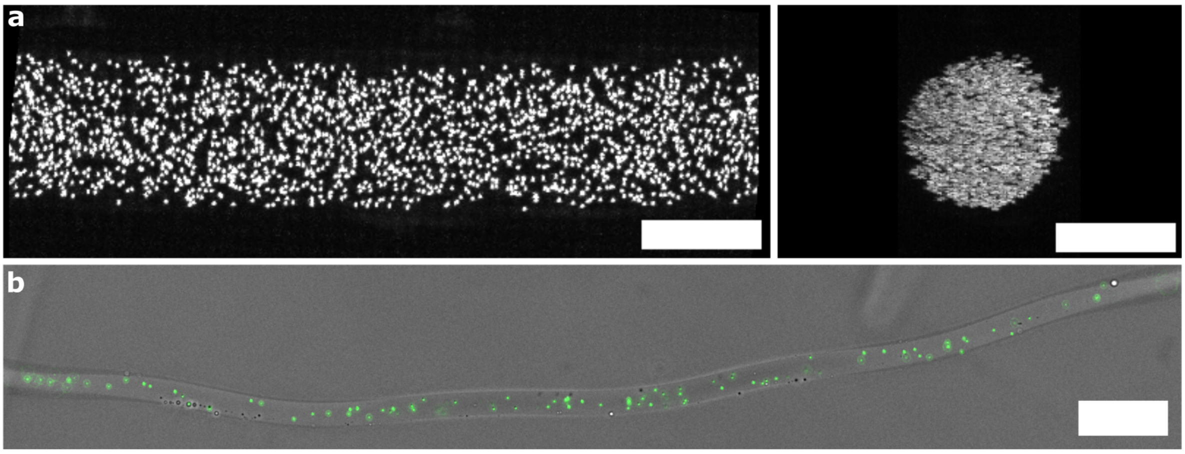

Figure 3.22: Microfibre with embedded nanoparticles. a, Three-dimensional reconstruction of a $F_{5/20}$ microfibre with embedded 500 nm fluorescent beads, with the image on the right corresponding to the cross-section of the fibre. A confocal microscope with 40X water objective is used. Scale bars = $50\ \mu$m. **b**, Thin microfibre ($F_{0.3/10}$) composite image of bright-field and fluorescent nanoparticles (green). A fluorescence microscope with a 20x objective is used. Scale bar = $50\ \mu$m.

3.3.3 Microfibre stiffness

The second objective of this chapter is to create microgels within a stiffness range that would allow the measurement of forces exerted by mural cells. To achieve this, it is necessary to characterise the mechanical properties of the microgels. In this section, we will begin with a qualitative observation, followed by using either atomic force microscopy (AFM) or microindentation to measure Young's modulus (E). Our initial focus will be on characterising microfibres with diameters of ≈ 30 ($F_{1/20}$, $F_{2/40}$) and ≈ 60 μm ($F_{5/20}$, $F_{10/40}$). These dimensions were chosen rather than the thinnest microfibres because they are easier to handle while remaining in the target size range (for instance, for smooth muscle cells, SMCs).

3.3.3.1 Qualitative characterisation of fibre stiffness

Once produced, we note that not all our conditions lead to straight microfibres. Indeed, some of our microfibres are wavy. This phenomenon was already studied by Nunes et al. 2013 [90] for a similar setup as ours. The reason why some microfibres can have this wavy shape is due to the large opening at the end of the channel. In our case, the end of the channel directly leads to an ethanol bath ($180°$ opening). From the study, the jet that is polymerising can buckle due to axial compressive stress at the end of the channel from a decrease in the flow speed. Once the microfibre is outside the channel, it will quickly finish its polymerisation and therefore stay in this wavy shape.

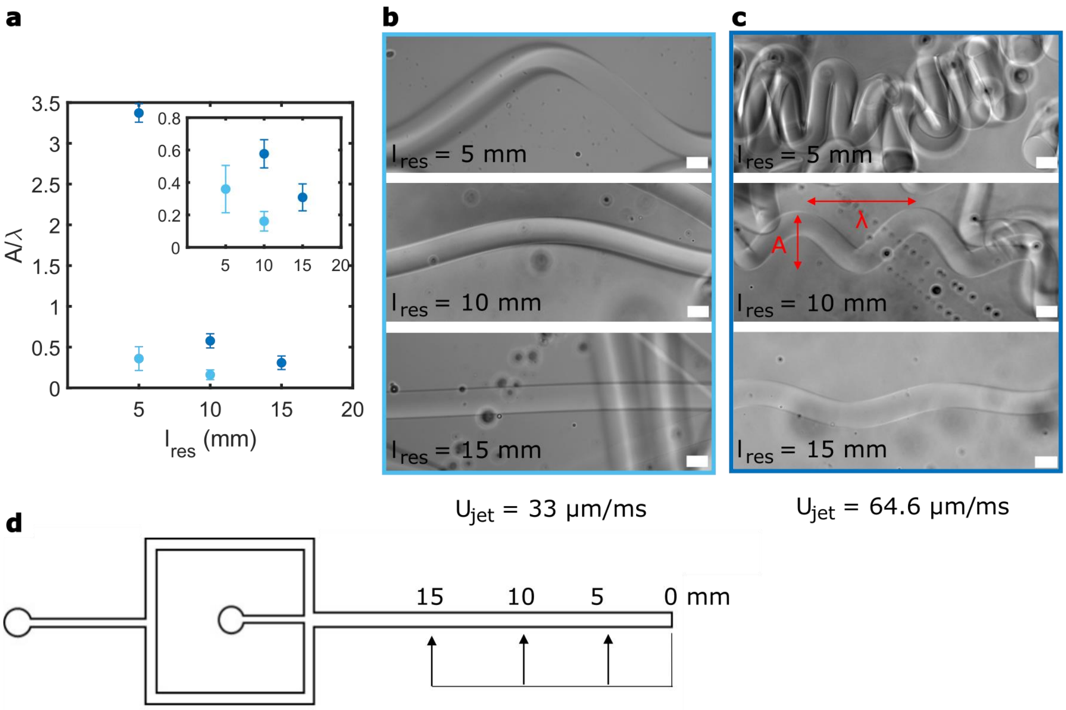

Figure 3.23: Microfibre morphology as a function of jet speed and UV spot position in the channel. a, Amplitude (A)/wavelength (λ) ratio as a function of l_{res} the distance from the UV spot to the channel end. Fibres of ≈ 60 μm diameter with two different jet speeds are analysed, $F_{5/20}$ ($U_{jet} = 33$ μ m/ms, $t_{UV} = 26.4$ ms cyan) and $F_{10/40}$ ($U_{jet} = 64.6$ mu m/ms, $t_{UV} = 13.5$ ms, navy blue). Note that for $l_{res} = 15$ mm and $U_{jet} = 33$ μm/ms the ratio $A/\lambda = 0$, as corresponding microfibres are straight. Dots represent the mean and error bars are the STD and for each condition, three to four measurements are done. **b.c**, Corresponding bright-field images of microfibres after polymerisation, at different l_{res}. Scale bars = 50 μm. **d**, Illustration of the microchip with the different UV spot positions indicated by arrows.

Nunes et al. 2013 [90] demonstrated that the degree of waviness can vary with the composition of the solutions, the intensity of the UV light, the jet speed and the distance between the UV spot and the end of the channel (l_{res}). To quantify it, they calculated the ratio of the amplitude (A) over the wavelength (λ). The smaller the ratio is, the straighter the microfibre is. In our case, the goal is not to investigate the effect of different parameters on waviness but to obtain straight enough microfibres to enable cell culture and measurements. For this purpose, three different l_{res} (Figure 3.23.d) are tested for two jet speeds ($U_{jet} = 33 \pm 0.3$ and 64.6 ± 1.3 μm/ms). Figure 3.23.a shows similar results as in Nunes et al. 2013 [90] study. The longer l_{res} is the straighter the microfibres are and for a given l_{res}, microfibres with larger jet speed will be more wavy. Using Figure 3.23.b.c to give us an idea of what A/λ ratio represents, we can state that $l_{res} = 15$ mm seems sufficient to give time to the jet to nearly fully polymerise before the end of the channel allowing to fabricate rather straight microfibres.

Looking at our different conditions and this change in the degree of waviness already gives us an insight into which microfibre will be the softest one. Indeed, for a given transversal applied force the degree of deformation of a 1D beam is linked to its Young's modulus by the Euler-Bernoulli equation, where the deflection of the beam is inversely proportional to the Young's modulus [117]. Therefore, for a given l_{res} the wavier the microfibre, the softer it is.

3.3.3.2 Mechanical characterisation with atomic force microscopy

From the literature, we know that to modulate PEG-DA microgel stiffness, we can vary experimental conditions such as UV light intensity, jet speed or dispersed phase composition [86]. We have seen in Figure 3.23 that, for given UV exposure conditions, the jet speed and therefore the time under UV light can impact the Young's modulus. Thus, we will first investigate the impact of this parameter. It has been shown by Duprat et al. [86] that, for a given PEG-DA gel composition, the Young's modulus of PEG-DA microgel increases exponentially with exposure time (or decreases exponentially with jet speed) until it reaches a plateau:

$$E_{max} = \frac{3\rho RT}{M_n} \tag{3.7}$$

with R the ideal gas constant, T the temperature (in Kelvin), ρ the density, and M_n the number average molecular weight. This relationship was demonstrated for microgel composed of 90% PEG-DA 575 and 10% PI and created with a mask at zero flow rate. In our case, microgels are created from continuous flow gelation, and we only have 30% of PEG-DA 700. Thus, a question is whether this relationship is applicable and what region of the curve corresponds to our experimental conditions.

To measure the Young's modulus, as explained, we used atomic force microscopy. AFM is a technique that uses a cantilever with a certain tip geometry and stiffness to indent a sample. A force is applied to the sample while the cantilever position and deflection are tracked [98]. These measurements are then converted into a force versus displacement curve where a fit is then performed on the approaching curve (section 3.2.4.1). We performed all our measurements with a conical probe and in cell medium to be close to the conditions cells will experience on microfibres. We assume PEG-DA as an isotropic and elastic material and thus use the Hertz model for a conical tip (Sneddon model) to extract the Young's modulus [100, 101]. When performing AFM measurements it is important to be careful to avoid certain sources of bias. For instance, it is important to ensure that the support does not impact the measurement. Usually, the effect of the substrate is negligible if the indentation depth is less than 10% of the sample [103]. With a sharp tip, we need to ensure that we are not penetrating the gel instead of indenting it. The choice of the spring constant k is also important, for gels between 1 and 10 kPa a value of $k = 0.1 - 0.3$ N/m can be used [103]. Finally, we first assume a Poisson's ratio of 0.5 (incompressible material).

As previously explained, we first focus on the influence of exposure time/jet speed on various samples. We vary the speed between 10.4 ± 0.2 and 64.6 ± 1.3 μm/ms corresponding to an exposure time ranging from 13.5 ± 0.5 and 83.8 ± 3.3 ms. Simultaneously, we also vary the diameter of the microfibres, we both test ≈ 30 and ≈ 60 μm microfibre diameters. A summary of the different microfibre is shown in appendix B.2 Figure B.1. From Figure 3.24 we can see that the time under UV light has an important impact on the Young's modulus. As observed by Duprat et al. [86] the Young's modulus seems to increase exponentially when the exposure time increases. Unlike Duprat et al. [86] we do not observe a plateau with an E_{max}, probably due to the fact that our minimal jet speed corresponds to a maximal exposure time of only 84 ms. From Cappello et al. 2019 [96] we can estimate from measurement on similar samples (30% PEG-DA 700 + 60 % PEG 1000 and MQ water (ratio $2:1$ in volume) + 10% PI) that $E_{max} \approx 400$ kPa is indeed higher than our maximal observed E. The majority of our samples fall within the lower part of the curve where an increase in the exposure time is nearly proportional to an increase in the Young's modulus. For instance, for ≈ 60 μm microfibres (Figure 3.24, cyan dots), increasing the exposure time from 13.5 ± 0.5 to 26.4 ± 0.9 ms leads to increasing the Young's modulus by a factor of two. The graph suggests that the microfibre diameter also affects the Young's modulus, with a tendency to increase it. However, on this last point, further investigation is required since we only tested for two different diameters, exposure times are not precisely the same for both diameters, and there is an important variability of E for the ≈ 30 μm microfibres at 15.1 ± 0.6 ms.

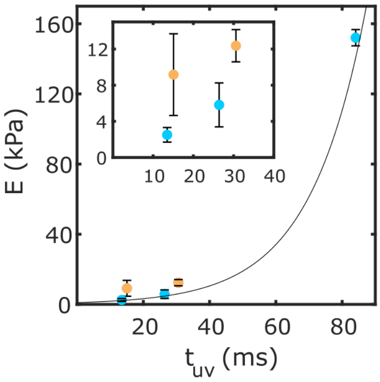

Figure 3.24: AFM measurements: Young's modulus increases exponentially with exposure time. Evolution of Young's modulus (E) of microfibres with 30 μm (orange, $F_{1/20}$, $F_{2/40}$) and 60 μm (cyan, $F_{1.6/6.4}$, $F_{5/20}$, $F_{10/40}$) diameters as a function of time under UV light (t_{UV}). For each condition, three different batches are measured. For each batch, three microfibres are measured at three different locations. One measurement is at least 100 curves. For the exposure time calculation, the speed is determined from the mean of three jet diameters. Error bars are the STD. The red line corresponds to an exponential fit.

Our results show that we can produce ≈ 60 μm microfibres with Young's moduli as low as $E_{min} = 2.5 \pm 0.8$ kPa and ≈ 30 μm microfibres with $E_{min} = 9.2 \pm 4.5$ kPa. These results are promising for our objective of measuring cell forces, as our fibre rigidity is comparable to that of substrates previously used to perform such measurements. Indeed, it was reported that PCs in 2D exert forces in the range of $0.035 - 0.04$ μN for substrate rigidity of ≈ 12 kPa [32] and that SMCs exert forces of $\approx 0 - 20$ μN for substrate rigidity ranging from $4 - 12$ kPa [76, 77, 78]. As we are in a 3D system, forces might be different than on a 2D substrate. Therefore, we will need to investigate if our microfibres are soft enough to observe a deformation. We also try to produce microfibres at even larger speeds, to make them softer. However, they are too wavy which would make the cell culture difficult. Also, according to the fitting curve in Figure 3.24 it would be challenging to decrease the Young's modulus further as it seems that we already are close to the minimal value for those conditions. A possibility could be to change the composition of the dispersed phase (i.e.: % PI or % PEG-DA).

To verify the accuracy of our estimates of E, we decide to look at the sensitivity of our values to the value of Poisson's ratio, which we first assumed to be 0.5. However, Cappello et al. 2020 [118] showed that the Poisson's ratio decreases with the amount of solvent. Indeed, PEG-DA 700 + 10% PI with 0% of solvent will have a Poisson's ratio of 0.5, but the Poisson's ratio will decrease to 0.25 when using 50% of water and to 0.16 when using 50% of solvent with PEG 1000-water ($2:1$ in volume). While these compositions are not exactly the same as ours, Capello et al.'s results can inform us of the range of values of the Poisson's ratio. Thus, we decided to recompute our data with a Poisson's ratio of 0.2 instead of 0.5. This drastic change of Poisson's ratio leads to a moderate rise of 28% for the value of E, which shifts the range of our Young's modulus to $3.21 - 196.45$ kPa. In conclusion, our results are fairly insensitive to the Poisson's ratio, and we estimate values of E_{min} below 10 kPa independently of the assumed value of the Poisson's ratio.

AFM-based indentation is a local measurement of the stiffness, which may limit the relevance of these results, as the estimated E is based on a length scale much smaller than that sampled by a cell. For this reason, we decide to compare our measurements with another, more macroscopic technique available at LadHyX: microindentation measurements, which we perform with Prof. Julien Husson.

3.3.3.3 Mechanical characterisation with microindentation

The microindentation technique consists of indenting a usually spherical sample (e.g. cell, microsphere) with a spherical bead fixed to the tip of a cantilever of known mechanical properties (stiffness, diameter). In short, the sample is held with a micropipette by exerting an aspiration pressure, while a microindentor indents the sample. In parallel, bright-field microscopy is used to visualise the sample and determine the deflection of the microindentor (section 3.2.4.2) [104]. Classical Hertz model between two spheres is then used to determine the Young's modulus [105].

In our case, our samples are microfibres which are not locally spherical and not easy to grab with a micropipette, and therefore they are not easy to characterise with this technique. We therefore, hypothesise that microspheres fabricated in similar conditions (solution composition, channel cross-section, UV intensity, diameter and exposure time) would possess a similar stiffness, which could more easily be measured. We saw in the phase diagram in Figure 3.14 (section 3.3.1.3) that optimal production of microspheres with our setup occurs in the dripping regime, therefore using FC-40 and Krytox as a continuous phase. Here, as we want to compare our results with microfibres, we decide to keep mineral oil plus 30% Span80 as a continuous phase and decrease the flow rates in order to be in the jetting regime and thus produce droplets. Note that this choice of continuous phase is not optimal for producing droplets as the Ca numbers are rather high. To decrease Ca numbers as much as possible the flow rates need to be decreased to be in the jetting regime, as no dripping regime is observed for this continuous phase (Table 3.7).

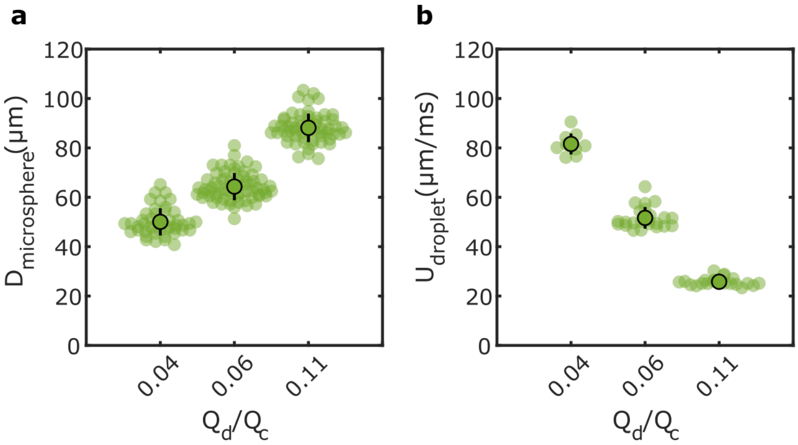

Figure 3.25: Microsphere diameter and speed as a function of flow rate ratio. a, Microsphere diameters ($D_{microsphere}$) as a function of flow rate ratios. $n_{0.04} = 46$, $n_{0.06} = 67$, $n_{0.11} = 60$. **b**, Droplet speeds ($U_{droplet}$) as a function of flow rate ratios. $n_{0.04} = 10$, $n_{0.06} = 23$, $n_{0.11} = 21$. Error bars indicate STD. For each condition, at least two different batches are measured.

Name	Qd (μL/min)	Qc (μL/min)	Qd/Qc	h x w (μm^2)	D (μm)	t_{UV} (ms)
$S_{0.2/1.75}$	0.2	1.75	0.11	130 x 200	88.1	33.8
$S_{0.2/3.5}$	0.2	3.5	0.06	130 x 200	64.3	16.9
$S_{0.2/5.5}$	0.2	5.5	0.04	130 x 200	50	10.7

Table 3.7: Parameters used to produce microspheres. Data come from Figure 3.25. D is the average microsphere diameter, and t_{UV} the average UV exposure time obtained with the droplet speeds and the size of the UV spot (871.2 μm).

As shown in Figure 3.25.a.b microspheres of diameter between 50 ± 5.5 and 88 ± 5.7 μm with corresponding speeds of 81.6 ± 4.2 and 25.8 ± 1.7 μm/ms are produced. Note that we only vary Q_c. We can see that the higher Q_c, the smaller the microspheres and the higher their speed. We thus fabricate three different types of microspheres with distinct speeds and diameters to be in the range of our microfibre diameter and speed. Microsphere diameters after polymerisation approximately correspond to liquid droplet diameters before polymerisation. We could not measure the condition with Q_c = 5.5 μl/min ($S_{0.2/5.5}$) as their speed was too fast to acquire droplet diameter. Once produced and cleaned, we immersed the microspheres in a medium and microindented them.

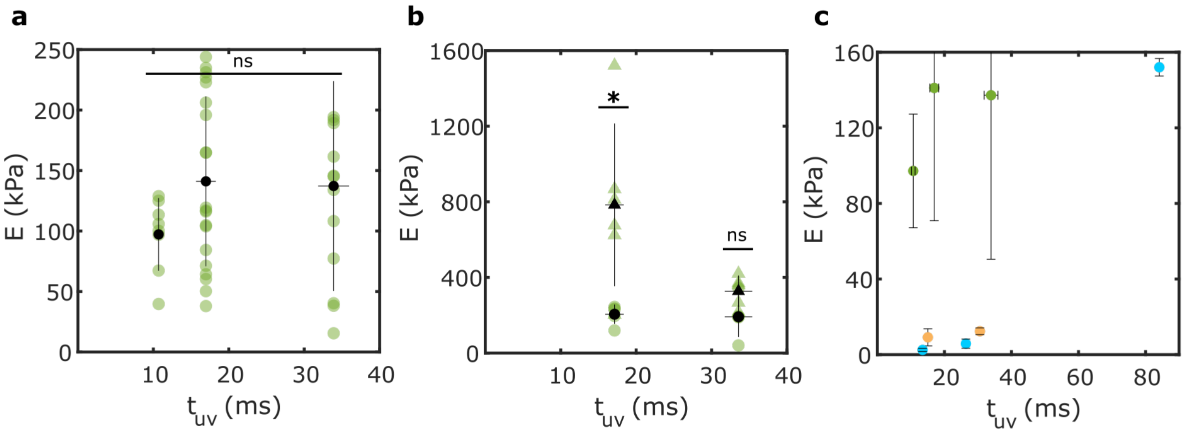

Figure 3.26: Young's modulus of microspheres is larger than that of microfibres using microindentation and AFM. a, Young's modulus (E) microspheres as a function of exposure time (t_{uv}), using microindentation. From left to right, $S_{0.2/5.5}$, $S_{0.2/3.5}$ and $S_{0.2/1.75}$. For each condition and batch $n_{microsphere} \geqslant 5$, at least two batchs are used for $S_{0.2/1.75}$ and $S_{0.2/3.5}$ however, only one batch is used for $S_{0.2/5.5}$. One-way ANOVA, * $p_{value} \leq 0.05$. **b**, Comparison of Young's modulus of microspheres ($S_{0.2/3.5}$ and $S_{0.2/1.75}$) with microindentation (circles) and AFM (triangles) as a function of exposure time. For each condition and each technique $n_{microsphere} \geqslant 5$ and one batch is used. Two-sample t-test, * $p_{value} \leq 0.05$. **c**, Evolution of Young's modulus as a function of exposure time. Cyan and orange symbols correspond respectively to microfibres of 60 and 30 μm diameter measured with AFM. Green symbols correspond to microspheres measured with microindentation. This graph is a summary of Figure 3.24 and graph (**a**). For all three graphs, error bars indicate STD. For the average exposure time calculation, $n_{dropplet} = 7-23$.

Figure 3.26.a shows Young's modulus obtained for the different types of microspheres. Surprisingly, the Young's modulus of microspheres is in general much higher than that of microfibres of similar size and exposure time. Indeed, for exposure time lower than 40 ms, microfibres have on average a Young's modulus between 2.5 ± 0.8 and 12.4 ± 1.7 kPa, compared to microspheres that have an average Young's modulus between 97.2 ± 30 and 141 ± 70.2 kPa. Note that, for microspheres of average $t_{uv} = 16.9 \pm 1.6$ and 33.8 ± 2.5 ms the Young's modulus is close to the one of microfibres with $t_{uv} = 83.8 \pm 3.3$ ms ($E = 152 \pm 4.6$ kPa). In addition, we can observe that there is no significant difference between the Young's modulus of the microspheres and their exposure time as observed for the microfibres. Overall, these results suggest that the relationship between the Young's modulus and dispersed phase speed is different for microspheres. For similar exposure times, the resulting Young's moduli of microfibres and microspheres are quite different, with microspheres having a higher Young's modulus. It is important to note that here, both the diameter and the speed are changed at the same time. Thus, further experiments would be required to distinguish the influence of these two parameters.

To see if the measured difference in Young's modulus between microspheres and microfibres is not due to the different techniques used (AFM for microfibres and microindentation for microspheres), we compare obtained Young's moduli for two types of microspheres ($S_{0.2/1.75}$ and $S_{0.2/3.5}$) with AFM and microindentation. The Figure 3.26.b shows the comparisons between the two techniques. Both techniques are consistent as they give larger Young's moduli than that of microfibres. However, AFM measures systematically higher Young's moduli than microindentation. For microspheres $S_{0.2/1.75}$, E_{AFM} is 1.7 time bigger and for $S_{0.2/3.5}$ E_{AFM} is 3.5 times bigger. This reasonable difference could be explained by the difference in probe geometry. According to the literature, sharp tips can overestimate the Youngs' modulus compared to spherical ones [119, 120]. Batch variability could also be the reason why there is a difference between the two techniques.

Overall, this comparison shows us that AFM and microindentation give reasonably comparable results. We thus reject our initial hypothesis that microfibres and microspheres produced from jets with the same diameter and speed would have similar mechanical properties. On the contrary, their Young's moduli are significantly different as summarised in Figure 3.26.c with microspheres in green and microfibres in orange and cyan.

In addition, we perform preliminary additional verification where we indented soft microfibres ($F_{10/40}$, Figure 3.27.a). As we can see in Figure 3.27.b we obtain an average Young's modulus of 0.7 ± 0.1 kPa compared to 2.5 ± 0.8 kPa with AFM. Again there is a moderate overestimation with AFM. However, the results are consistent with those obtained for microspheres, showing that AFM is a relevant technique to measure microfibre Young's modulus. Note that further measurements should be done to confirm our observations.

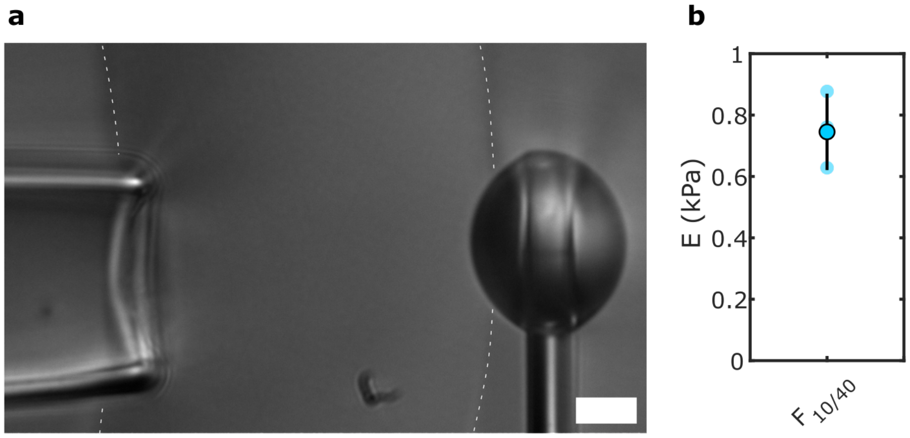

Figure 3.27: Microfibre Young's modulus measured by microindentation. a, Bright-field image of a microfibre during microindentation. Dashed white lines show the edges of the microfibre. Scale bar = $10\ \mu$m. **b**, Young's modulus (E) of $F_{10/40}$ microfibres obtained with microindentation. Each data point is the average of 3 indentations at $2-3$ different locations along a microfibre ($n=3$). The error bar corresponds to the STD.

3.3.4 Comparison between microfibre and microsphere architectures

These results push us to a diversion of our main task, i.e., fabricating thin and soft microfibres to measure forces exerted by mural cells. We are interested in understanding why microspheres and microfibres fabricated with similar parameters possess significantly different Young's moduli. Our motivations are two-fold. We have seen in the introduction that microspheres can be used as 3D substrates to measure cell forces [70]. Thus, a better understanding of the network organisation of PEG-DA microspheres could help us to target optimal parameters. In addition, understanding the root of this difference would increase our knowledge of the architecture and mechanical properties of PEG-DA microfibres. Indeed, several published studies present mechanical characterisations of PEG-DA fibres produced with similar conditions to ours. However, to our knowledge, very few have quantified Young's modulus and correlated all the different parameters [88, 92].

The difference in stiffness between microspheres and microfibres might result from a difference in cross-linked chain organisation. Microspheres could have a tighter mesh than microfibres. Studies usually measure the swelling behaviour of microgels to later quantify the swelling ratio and link it to the Young's modulus and the mesh size [80, 121]. Instead of measuring the swelling behaviour, we measure the contrary, the shrinking behaviour. Here, from our observations, we suppose that PEG-DA is not permeable to glycerol thus, an osmotic pressure will be generated due to a more important concentration of water inside the microgel. Microgels are immersed in pure glycerol to achieve deflation through osmosis. This drives water out of the microgel and results in shrunk microgels. The first step is to ensure that microgel shrinking is isotropic. For microspheres, this can be verified visually, while for microfibres it requires measurement of both their length and diameter. For that, we calculate the dimensional shrinking ratio of the length (DSR_l) and diameter (DSR_d) of microfibres as explained in section 3.2.4.3 [107].

In Figure 3.28.a we can see that DSR_l and DSR_d are similar with a maximal difference of 33% for $F_{10/40}$ microfibres. Thus, we can assume that microfibre shrinkage is isotropic. The shrinking behaviour of our microgels can thus be quantified by calculating the ratio of volumes 3.2.4.3. Figure 3.28.b shows that the shrinking ratio decreases with UV light exposure time for microfibres. The value for microfibres $F_{1/20}$ (orange marker) has a shrinking ratio larger than $F_{5/20}$ microfibres. However, the contrary is expected. Indeed, as they are stiffer, it is expected that they will shrink less. This can be due to the difference in diameters of the microfibres. Also, it is difficult to clearly determine the position of the ends of microfibres, which can have impacted the length measurement. Compared to microfibres, microsphere shrinking seems independent of the speed of the droplets nor the size, similar to what is observed for E measurements. Figure 3.28.c puts $V_{water}/V_{glycerol}$ ratio and E in relation and shows that E decreases when $V_{water}/V_{glycerol}$ ratio increases. From the literature, we know that the swelling ratio is linked to the mesh size and to the Young's modulus [80, 121]. The Young's modulus decreases when the mesh size increases. From this information we can therefore conclude that microspheres and microfibres do not have the same mesh size, which can explain the observed difference in Young's moduli. Further measurements and experiments should be performed to confirm our observations and further understand these differences.

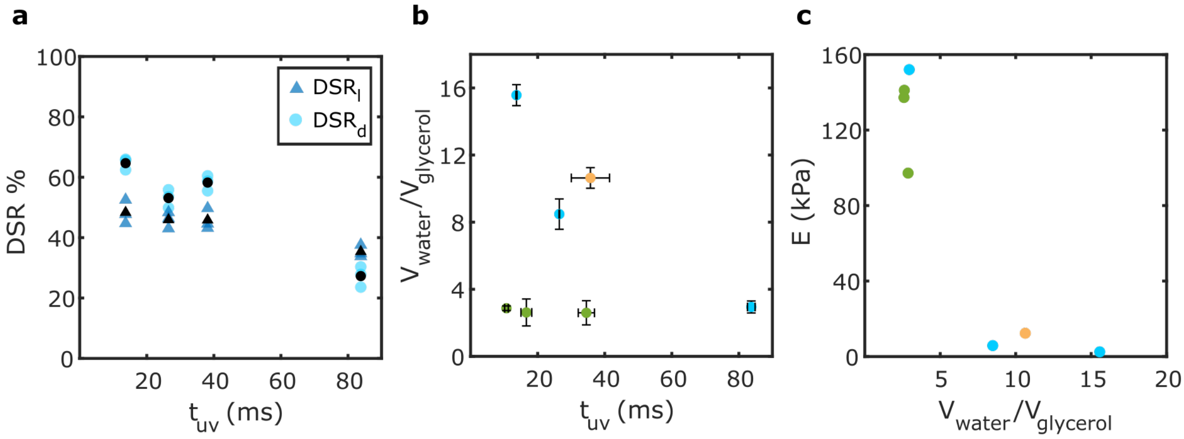

Figure 3.28: Shrinking behaviour of microgels.a, Dimensional shrinking ratio of microfibre length (DSR_l) and diameter (DSR_d) as a function of UV exposure time. Two diameters are tested 30 ($F_{1/20}$) and 60 μm, and for 60 μm three different jet speeds are investigated ($F_{1.6/6.4}$, $F_{5/20}$, $F_{10/40}$). **b**, Evolution of volume shrinking ratio ($V_{water}/V_{glycerol}$) for microfibres (cyan and orange) and microspheres (green) as a function of exposure time. For (**a**) and (**b**), error bars indicate STD. Each experiment is replicated three times and for each replicate $n_{microgel} \geq 5$. **c**, Young's modulus of microfibres (cyan and orange) and microspheres (green) as a function of volume shrinking ratio.

Name	Diameter (μm)	E (kPa)	Q_d (μL/min)	Q_c (μL/min)	Shape
$D60\_E6$	62.4 ± 0.7	5.8 ± 2.4	5	20	straight
$D60\_E2$	61.6 ± 0.7	2.5 ± 0.8	10	40	wavy
$D30\_E12$	28.7 ± 0.6	12.4 ± 1.8	1	20	straight
$D30\_E9$	27.7 ± 0.8	9.2 ± 4.5	2	40	straight
$D13$	12.6 ± 0.6	–	0.3	10	straight

Table 3.8: Microfibres used for cell analysis. The diameter of the microfibres is estimated from the data used in Figure 3.19. Young's modulus is the one measured using AFM and a Poisson's ratio of 0.5, and the term shape refers to Figure 3.23. $D13$ microfibres are not mechanically characterised therefore $'-'$ is indicated for E.

In the following sections, we will use microfibres of ≈ 60 μm, ≈ 30 μm and ≈ 12 μm of different stiffness for cell analysis. For ease of reading they will be refereed by their approximate diameter and Young's modulus as

$D60\_E6$, $D60\_E2$, $D30\_E12$, $D30\_E9$ and $D13$, their detailed properties are summarised in Table 3.8.

3.3.5 Cell seeding on microfibres

Unlike collagen or fibrin, PEG-DA is a synthetic hydrogel and therefore does not naturally promote cell adhesion. To overcome this problem, synthetic hydrogels must be functionalised using various strategies, such as incorporating proteins like fibronectin, mixing with natural hydrogels (collagen, chitosan), or attaching peptides to promote cell adhesion [32, 84, 88]. We started by naively using fibronectin, a protein commonly used to functionalise glass slides, which did not lead to efficient adhesion. Since PEG-DA is resistant to protein absorption, fibronectin did not adhere properly to the microfibres [87]. Next, we tried functionalisation with the cell adhesive RGD (arginine-glycine-aspartic acid) extracellular matrix peptide.

There are different types of RGD and different ways to incorporate them. RGD incorporation usually requires long protocols and expertise where laboratories design RGD peptides and then assemble them with PEG-DA before hydrogel polymerisation. In our case, we want to post-functionalise our microfibres. Therefore, we follow the protocol of Kruger et al [88]. The advantage of the RGD derivative (GRGDS-PC) they use is that it contains a thiol group which covalently binds to the remaining free acrylate groups of the microfibres. RGD is diluted and mixed with microfibres in PBS overnight. The microfibres are then washed and resuspended in medium containing cells. Note that this protocol has several limitations that should be addressed in the future. Controlling the quality, uniformity and reproducibility of the coating would require the use of fluorescently labeled antibodies. In addition, a possible effect of RGD concentration on cell behaviour should be investigated.

To test whether our functionalised microfibres lead to cell adhesion and spreading, we culture human brain vascular pericytes (PCs), human aortic smooth muscle cells (HAOSMCs) or bovine aortic smooth muscle cells (BAOSMCs). We try to culture aortic smooth muscle cells (AOSMCs) on ≈ 60 and $\approx 30\ \mu$m diameter microfibres (denoted $D60\_E6$, $D60\_E2$ and $D30\_E12$, $D30\_E9$ respectively). Because in vivo PCs are located on smaller vessels like capillaries ($5-8\ \mu$m) or pre-capillary arterioles ($10\ \mu$m), we try to culture them on ≈ 30 ($D30\_E12$, $D30\_E9$) and $\approx 12\ \mu$m ($D13$) microfibres [2]. Figure 3.29 and Figure 3.30.a.b.c show that all three cell types successfully adhere to microfibres of 60 and $30\ \mu$m . However, on $12\ \mu$m , PCs are able to adhere within an hour of seeding but are unable to spread properly, resulting in deformation of the microfibres and aggregation of microfibres and cells in a few hours (Figure 3.30.d). Microfibre deformation is also observed on $30\ \mu$m microfibres after 3 h (Figure 3.30.a.b.c) and aggregations after 6 h.

One of the major challenges in this project is to attach the microfibres to a support that allows the cells to spread freely on the microfibres without complete microfibre aggregation. This is also necessary to allow long image acquisition without sample drift and to facilitate fixation and staining procedures. The difficulty lies in the thin (less than $100\ \mu$m), fragile and transparent nature of the microfibres, which also require constant immersion in a solution, making them difficult to manipulate with tweezers or glue. To overcome this problem, we try to embed microfibres in a soft fibrin gel to prevent any effect on cell behaviour. The microfibres are first mixed with cells to allow them to attach, and then the sample is resuspended in fibrin solution. Thrombin is added to polymerise the gel, which takes five minutes at room temperature. Fibrin gel, being a natural gel, causes cells to migrate within the gel after approximately one hour, making long-term cell culture difficult.

As an alternative to fibrin, we try low-melting agarose at 0.4%. Like fibrin, agarose is soft enough not to affect the cells, and its synthetic nature prevents cells from detaching from the microfibres. However, aggregation of thin microfibres still occurs and cells appear to grow more slowly. Therefore, further investigation will be necessary to avoid thin microfibres aggregation.

As previously explained, cell growth remains a challenge on microfibres with diameters smaller than $30\ \mu$m, as aggregation of microfibres is observed after only a few hours. For this reason, we decided to first focus on AOSMCs instead of PCs. Indeed, AOSMCs are located in vivo on larger vessels, $30\ \mu$m for arterioles up to a few millimetres for arteries [13, 77]. Here, as we are interested in microvasculature we will use microfibres of either $60\ \mu$m or $30\ \mu$m diameter (Table 3.8). As a final protocol, cells are resuspended with functionalised microfibres and allowed to grow freely for a few hours up to several days. Note that for $30\ \mu$m diameters, samples are fixed after 3 h to avoid complete aggregation. Prior to fixation and staining, either agarose or fibrin is used to immobilise the microfibres.

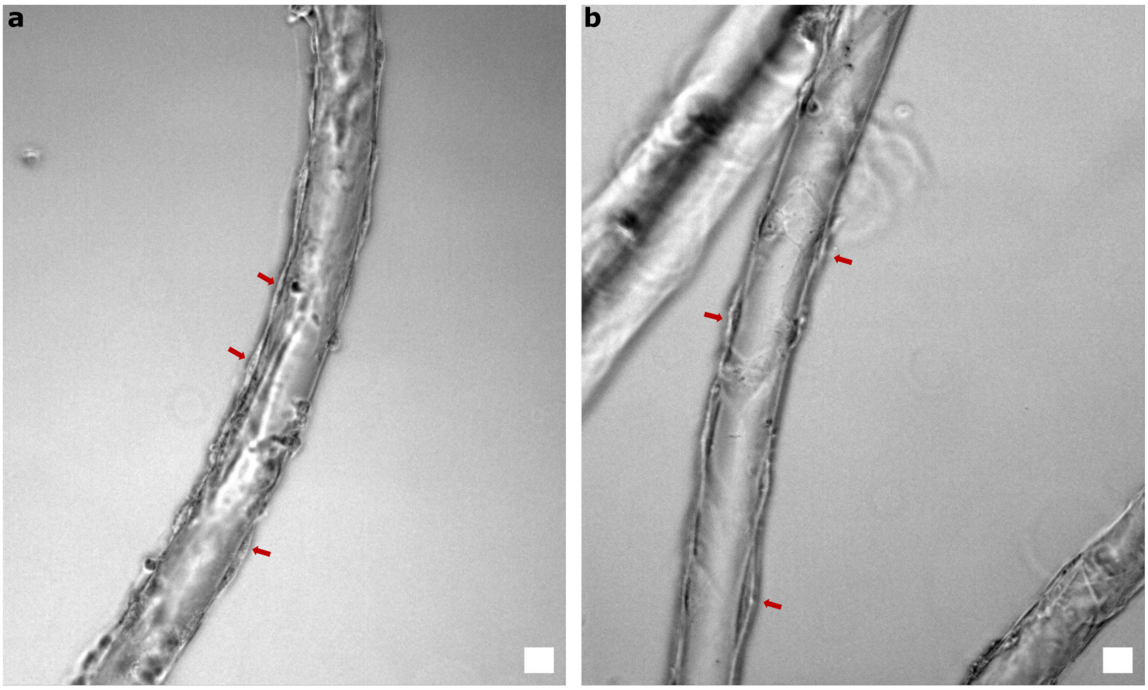

Figure 3.29: Microfibres with cultured BAOSMCs and HAOSMCs a, Bright-field image of BAOSMCs on $60\ \mu$m microfibre ($D60\_E6$) after 48 h of culture. **b**, Bright-field image of HAOSMCs on $60\ \mu$m microfibre ($D60\_E6$) after 48 h of culture. The cells are confluent or near confluent and can be seen as small bumps along the microfibres indicated by red arrows. Scale bars = $30\ \mu$m, a 10x objective is used.

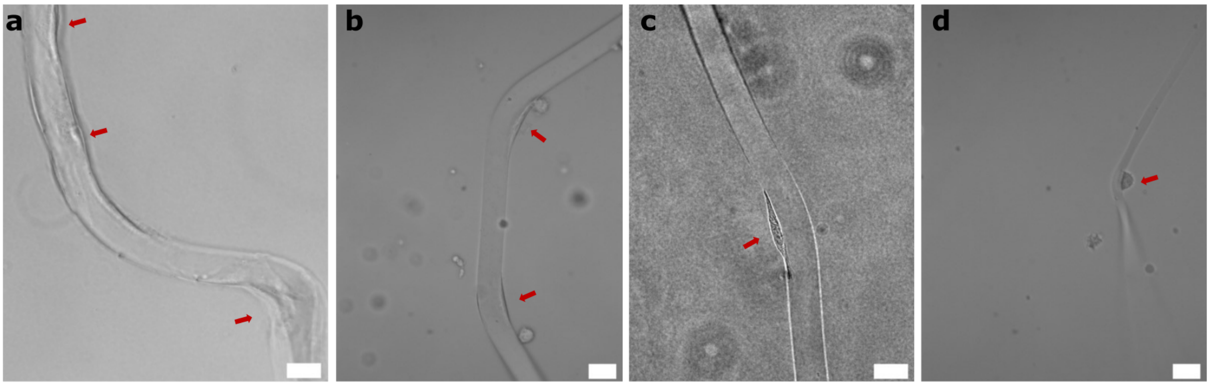

Figure 3.30: Thin microfibres cultured with BAOSMCs and HAOSMCs. a, Bright-field image of BAOSMCs on $30\ \mu$m microfibre ($D30\_E12$) after ≈ 3 h of culture. Some parts of the microfibre are out of the focus plane. **b**, Bright-field image of HAOSMCs on $30\ \mu$m microfibre ($D60\_E6$) after ≈ 3 h of culture. **c**, Bright-field image of PCs on $30\ \mu$m microfibres ($D60 - E6$) after ≈ 3 h of culture. **d**, Bright-field image of PCs on $12\ \mu$m microfibre ($D13$) after ≈ 3 h of culture. Scale bars = $30\ \mu$m, 20X objective is used. Cells are indicated with red arrows.

3.3.6 AOSMCs organisation on soft microfibres

SMCs possess contractile capabilities that enable them to regulate blood flow [22]. Depending on their location within the vascular system, they can organise themselves in multiple layers surrounding large vessels such as the aorta (25 mm diameter) and arteries (4 mm diameter) or in a single layer around smaller vessels like arterioles ($\approx 30\ \mu$m diameter) [13]. In all cases, their alignment is either circumferential or in helical patterns

[122]. The forces they exert are primarily directed in a circumferential manner [77]. Given that we are examining microfibres measuring 30 and $60\ \mu$m, we are approaching a situation similar to arterioles where a single layer of cells is present. In this section, we will study the organisation of AOSMCs on soft ($\approx 2-12$ kPa) and thin microfibres (30 and $60\ \mu$m). This investigation is crucial for subsequently measuring compressive forces.

Several studies have investigated the effect of curvature on the alignment of SMC monolayers [122, 123]. The curvature at a given point along a surface is characterised by the principal curvatures, k_1 and k_2, which respectively correspond to the maximum and minimum principal curvatures. They measure the maximum and minimum bending of a surface at this point [124]. The principal curvatures are related to the principal radii of curvature, R_1 and R_2, by $k_1 = 1/R_1$ and $k_2 = 1/R_2$. The sign of Gaussian curvature $K = k_1 k_2 = \frac{1}{R_1 R_2}$ is often used to describe the general shape of the surface [125]. Surfaces with $K = 0$ Gaussian curvature are either flat surfaces or cylinders, $k_2 = 0$ (Figure 3.31.a). When $K > 0$, the shape resembles that of a bowl, with principal curvatures in the same direction. On the other hand, if $K < 0$, we have a saddle shape with principal curvatures that have opposite signs (Figure 3.31.b).

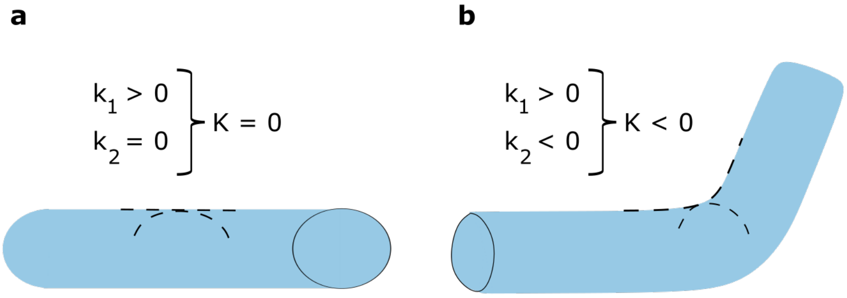

Figure 3.31: Gaussian curvature of microfibres. **a**, Gaussian curvature (K) of a straight microfibre like $D60-E6$. The dashed lines indicate k_1 and k_2 the principal curvatures. **b**, Gaussian curvature of wavy microfibres ($D60-E2$), at the bend, the local curvature is negative. The dashed lines indicate k_1 and k_2 the principal curvatures.

AOSMCs have been shown to behave consistently on convex surfaces, such as fibres or half cylinders, with radii ranging from 200 to $40\ \mu$m [122]. On these surfaces, AOSMCs predominantly align along the direction k_2, forming an angle of approximately $10°$. This angle tends to increase when the curvature decreases or when cells are isolated [122, 123]. Conversely, on concave surfaces, it has been observed that airway SMCs align circumferentially [123]. Notably, all these observations were made on stiff substrates, including glass capillaries or polydimethylsiloxane (PDMS) with a stiffness of 3 MPa. The stiffness of the substrate can influence cell behaviour and the actin cytoskeleton, suggesting that it may also impact how cells respond to curvature. Here we investigate whether the stiffness of the substrate can alter the axial orientation of AOSMCs on convex surfaces.

We will first focus on $60\ \mu$m microfibres. To study the organisation of AOSMCs, either BAOSMCs or HAOSMCs are cultured on $D60\_E6$ and $D60\_E2$ microfibres for 2 to 4 days. Usually, a monolayer is obtained for BAOSMCs. In the case of HAOSMCs, cells take longer to reach confluence in culture flasks (1 to 2 weeks) and require fibronectin coating to improve cell growth. Therefore, after 2 to 4 days they usually are less confluent on microfibres. Microfibres are then embedded in agarose or fibrin gel as previously described and stained with phalloidin and DAPI to visualise actin filaments and nuclei respectively. 3D scans are performed using a confocal microscope with a 40x or 63x objective. Briefly, to assess the orientation of actin and nuclei, a scan of half of the microfibre is projected onto the same plane and then the image is stretched. This stretching allows the position of each element to be corrected based on its location on the half microfibres, giving more accurate distances and angles than a simple normal projection. After stretching, the alignment with the longitudinal axis of the microfibres is measured, either with the *OrientationJ* plugin for actin filaments or with the *Analyse particle* tool from ImageJ for nuclei [110]. A value of $0°$ indicates that the cell is perfectly aligned with the longitudinal axis of the microfibre, and a value of -90 or $90°$ indicates that the cell is circumferentially aligned with the microfibre.

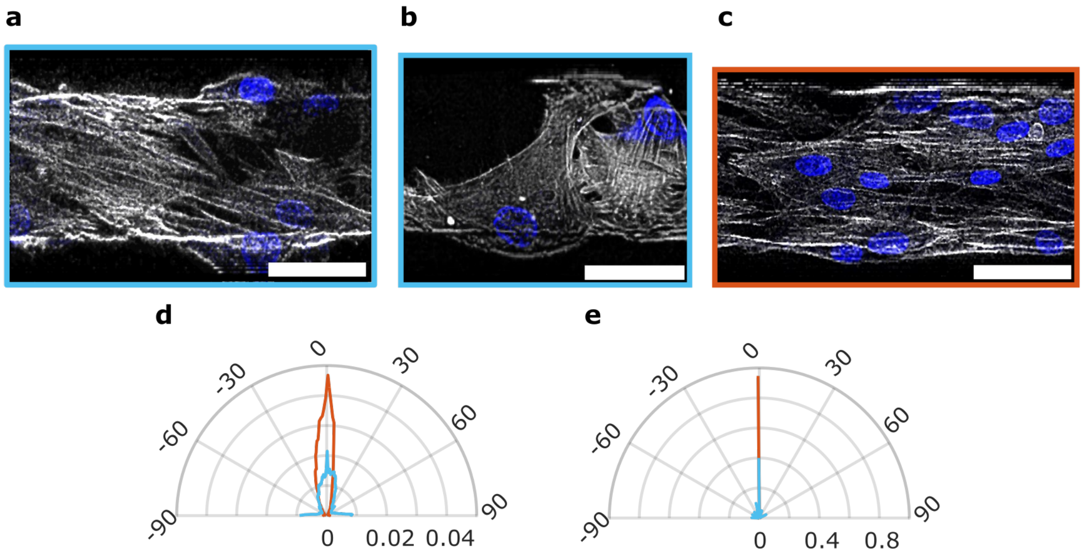

Figure 3.32: Actin and nuclei orientation of AOSMCs on 60 µm microfibres. a.b, Representative corrected projection of HAOSMCs on $D60\_E6$ microfibre. Image (**b**) shows that HAOSMCs can have circumferential actin filaments. Nuclei are stained with DAPI (blue), and phalloidin staining for F-actin is shown in white. All images are acquired with a 63x glycerol objective using confocal microscopy, scale bars = 50 μm. **c**, Representative corrected projection of BAOSMCs on $D60\_E6$ microfibre. **d**, Polar plot showing the probability distribution of actin orientation (pixel orientation in the ROI) of BAOSMCs in orange and HAOSMCs in cyan. An angle of $0°$ means that they are aligned with the longitudinal axis of the microfibre. **e**, Polar plot showing the probability distribution of the orientation of nuclei in orange BAOSMCs and cyan HAOSMCs. For BAOSMCs, $n_{fibre} = 8$, $n_{cell} = 131$, for HAOSMCs, $n_{fibre} = 7$, $n_{cell} = 20$ and at least two independent experiments are analysed.

The results show that on $D60\_E6$ microfibres, BAOSMCs are strongly aligned in the axial direction (Figure 3.32.c). Both their nuclei and actin filaments show an angle of almost $0°$ with the k_2 direction of the microfibre (Figure 3.32.d.e). HAOSMCs are also aligned longitudinally with the microfibres (Figure 3.32.d.e). However, they are less aligned than BAOSMCs. Indeed, the probability (P) of having actin filaments oriented at an angle of $|10|°$ to the microfibre (axial direction) is about $P_{10} = 0.6$ for BAOSMCs, while for HAOSMCs it is $P_{10} = 0.3$. On the contrary, the probability of having an angle greater than or equal to $|60|°$, corresponding to the circumferential orientation, is greater for HAOSMCs ($P_{60} = 0.2$) than for BAOSMCs ($P_{60} = 0.05$). These observations are confirmed by the mean (μ) and standard deviation (σ) of the probability distributions. The means of the two distributions are close $\mu_{BAOSMCs} = -4.3$ and $\mu_{HAOSMCs} = 0.8$, but the standard deviation is larger for HAOSMCs $\sigma_{HAOSMCs} = 42.8$ than for BAOSMCs $\sigma_{BAOSMCs} = 22.7$, confirming that HAOSMCs are less axially aligned than BAOSMCs. Similar observations can be made for nuclei with $P_{10} = 1$ and $P_{60} = 0.01$ for BOASMCs and $P_{10} = 0.5$ and $P_{60} = 0.2$ for HAOSMCs. These observations can visually be confirmed in Figure 3.32.b where we can see that HAOSMCs have actin filaments that are circularly aligned with the microfibre. Here, HAOSMCs are less confluent than BAOSMCs and may be more aligned with the microfibre when fully confluent [122]. These results show that AOSMCs align in the axial direction on our microfibres as on stiff cylinders and that in this case stiffness does not seem to affect the alignment [122]. This could be explained by the fact that our microfibres have a large curvature and, according to the literature, cells will align in the direction that minimises the bending energy of their stress fibres, which here is the axial direction.

Compared to $D60\_E6$ microfibres, $D60\_E2$ microfibres are softer and do not have the same Gaussian curvature. Indeed, as we saw in section 3.3.3.1, $D60\_E2$ microfibres are naturally wavy due to axial compressive stress they experience during fabrication at the end of the channel. Therefore, they have areas with negative Gaussian curvature (Figure 3.31.b). The same protocol is used to study the straight part of the microfibres and a qualitative observation is made for the curved part of the microfibres. For BAOSMCs, Figure 3.33 shows that, as for $D60\_E6$, the cells are oriented in the local axial direction of the microfibres for both nuclei and actin filaments. With $P_{10} = 0.7$, $P_{60} = 0.01$, $\mu = 4.4$ and $\sigma = 14.2$ for actin fibres and $P_{10} = 0.7$, $P_{60} = 0.03$, $\mu = -1$ and $\sigma = 19.1$ for nuclei . Similar results to $D60\_E6$ microfibres are obtained for actin fibre orientation, however nuclei are less axially aligned. As we do not have a lot of samples, this would require further experiments to confirm the difference. Considering the saddle locations of the microfibres, we can observe in Figure 3.34.a that cells have a tendency to accumulate in these regions ($k_2 < 0$), as already described in the literature for other cell types [125]. Cells can also form bridges as we can see in Figure 3.34.b. As explained in the literature, cells in saddle regions avoid bending by lifting away from the surface rather than following it [125, 126].

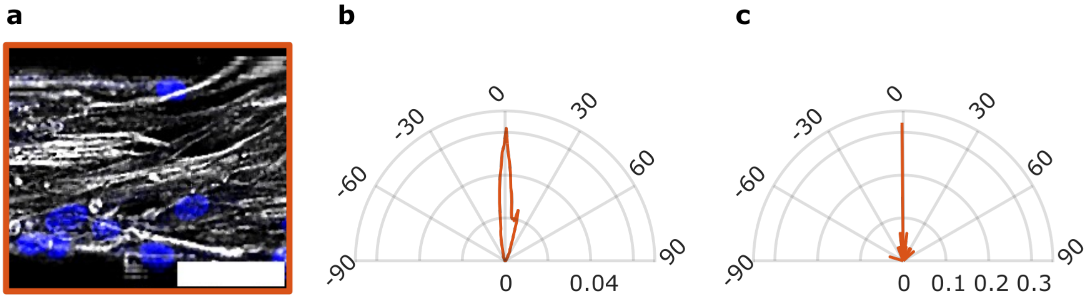

Figure 3.33: Actin and nuclei orientation of BAOSMCs on 60 µm wavy microfibres.a, Representative corrected projection of BAOSMCs on a straight segment of $D60\_E2$ microfibre. Nuclei are stained with DAPI (blue) and F-actin in white with phalloidin. All images are acquired with a 40x water objective using confocal microscopy, scale bar = 50 μm.**b.c** polar plot showing respectively the probability distribution of BAOSMCs actin and nuclei orientation (pixel orientation in the ROI) on $D60\_E2$ microfibre, $n_{fibre} = 2$, $n_{cell} = 31$, only one experiment is analysed.

Figure 3.34: BAOSMCs organisation on a saddle-like part of 60 µm microfibre.a, Single confocal image from a z-stack of BAOSMCs on a $D60\_E2$ microfibre. Nuclei are stained with DAPI in blue and F-actin in white with phalloidin. The white arrow indicates the accumulation of cells on the saddle-like part of the microfibre. A 40X water objective is used, scale bar = 50 μm. **b**, Bright-field image of BAOSMCs on 60 μm microfibre ($D60\_2$). The white arrow indicates the bridge formed by the cell. A 10x objective is used, scale bar = 50 μm.

For HAOSMCs we cannot obtain a confluent monolayer and therefore analyse the orientation. However, the phenomenon of bridging is also observed and cells appear to follow the sinusoidal direction of the microfibres (Figure 3.35). This needs to be further investigated in the future. This could be due to the low confluency of the cells but also to the fact that HAOSMCs are longer cells (≈ 150 μm) than BAOSMCs (≈ 50 μm) and may feel the waviness of the microfibres more.

On straight microfibres with a higher curvature, 30 μm diameter ($D30\_E12$), we cannot quantify the cell orientation. Indeed, as explained in section 3.3.5, aggregation of microfibres is observed after ≈ 6 h of culture.

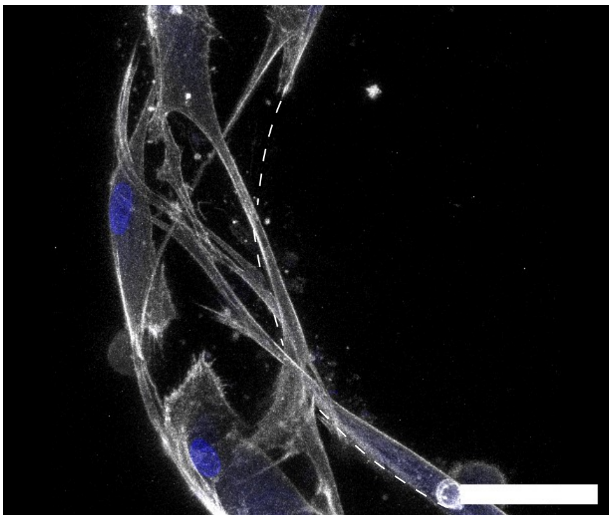

Figure 3.35: HAOSMCs behavior on 60 µm wavy microfibres. Three-dimensional reconstruction of HAOSMCs on a $D60\_E2$ microfibre. Nuclei are stained with DAPI (blue) and F-actin in white with phalloidin. The white dashed line indicates the internal curvature of the microfibre. Scale bar = $40\ \mu$m, a 65x glycerol objective is used in confocal microscopy.

In fact, after three hours, the cells begin to bend the microfibre in the axial direction. On the remaining unbent part, cells seem aligned in the axial direction of the microfibres.

The overall message of this section is that AOSMCs align in the axial direction of our soft microfibres and can form bridges on wavy microfibres. The behaviour of AOSMCs in our system differs from that in vivo, as we do not observe circumferentially aligned cells. Interestingly, AOSMCs can bend $30\ \mu$m straight microfibres in the axial direction. This observation suggests that the axial deformation of microfibres by the cells can be used to quantify cell forces, which we will study in the next section.

3.3.7 Bending of microfibres due to cell forces

Same as for cell organisation discussed above, this section presents exploratory work that would require confirmation and further quantification. As explained in section 3.3.6, AOSMCs align longitudinally on our microfibres. However, on $D60\_E2$ and $D30\_E12$, respectively 60 and $30\ \mu$m microfibres, we observe cell bridges and bending of the microfibres showing that cells exert traction forces on our microfibres. We will not investigate the case of $D60\_E2$ as the microfibres are naturally wavy and focus on $30\ \mu$m microfibres. As we can see in Figure 3.36.b.c.d both AOSMCs and PCs can bend $30\ \mu$m diameter microfibres after only a few hours. Figure 3.36.a shows that initially, the microfibres are straight and that their bending is due to the presence of cells.

To estimate the order of magnitude of the force exerted by our cells we perform a calculation based on the following assumptions:

- We consider that cells only exert point forces at their extremities (F) and that we can consider the problem as symmetric.
- We treat the microfibre as if it had a finite length ($2L$), thus treating the problem as independent from what happens outside the section we consider. For instance, we do not take into consideration the impact of close cells.
- We assume that the presence of the cell does not modify the mechanical behaviour of the microfibre (E and I remain unchanged).

- We assume that the microfibre behaves as a linear elastic material.
- We assume that the microfibre is thin enough to apply the calculation at the neutral axes and consider that its bending is proportional to the applied moment, corresponding to linear elasticity theory.

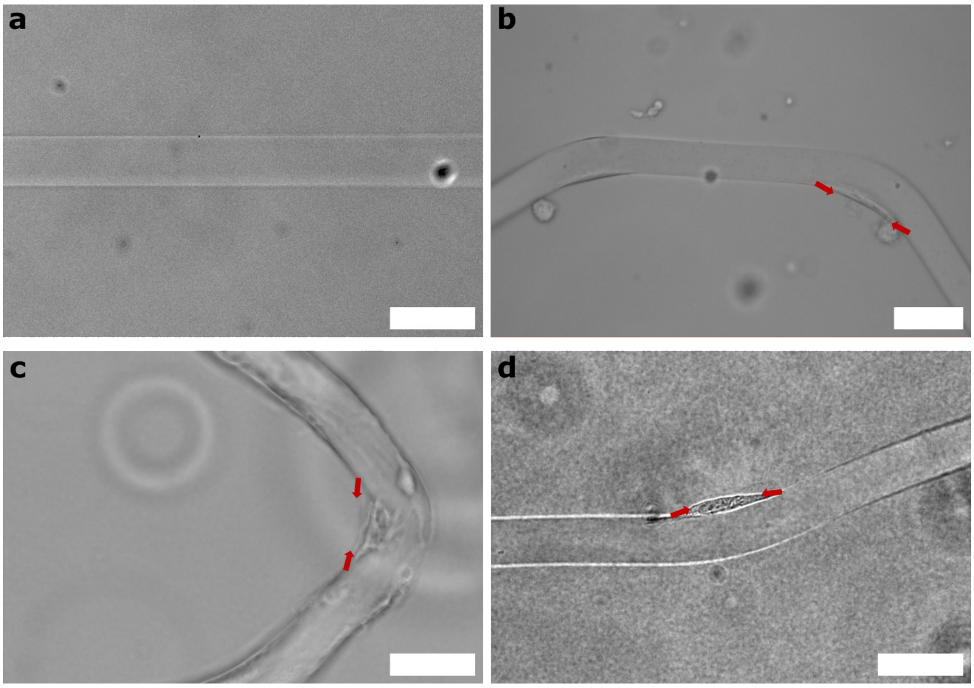

Figure 3.36: Microfibre deformation due to cell forces. a, Bright-field image of a $30\ \mu$m microfibre, $D30\_E12$ in MQ water. **b,c,d** Bright-field images of respectively HAOSMCs, BAOSMCs and PCs on $30\ \mu$m microfibres, $D30\_E12$ after ≈ 3 h of culture. Red arrows represent the direction of exerted forces. For all the images, a 20X objective is used, scale-bars = $50\ \mu$m.

Figure 3.37.a shows the configuration of our microfibre of length $2L$ and diameter D, subject to two equivalent opposite cell forces F. From our assumptions, the deflection of the microfibre along the x axes can be written as:

$$EI\frac{d\theta(l)}{dl} = -M(l), \tag{3.8}$$

with θ(l) the local tilt angle, $M(l)$ the local bending moment, l the curvilinear coordinate along the fibre, E the Young's modulus and I the second moment of area of our microfibre. The latter can be written as $I = \frac{\pi D^4}{64}$, with D the microfibre diameter. Following Shima. et al. [127] who solve a similar problem to ours, the moment can be written as $\frac{dM(l)}{dl} = Fsin(\theta(l))$ and equation 3.8 can be rewritten as :

$$\begin{aligned} \frac{d^2\theta(s)}{ds} &= \frac{FL^2}{EI}sin(\theta(s)) \\ s &= 1 - \frac{l}{L} \end{aligned} \tag{3.9}$$

Solving Equation 3.9 requires approximating the solution θ(s) using Maclaurin series up to at least the fourth order (as detailed in appendix B.3). To obtain an order of magnitude of the force, we can simplify the calculation by approximating $M(s)$ by a constant equal to the maximal bending moment, $M = Fd$, where d is the maximal deflection of our microfibre. Equation 3.9 becomes:

$$EI\frac{\theta_0}{L} = Fd \tag{3.10}$$

θ_0, d, L and D can be estimated manually from bright-field images of our microfibres with cells using ImageJ. And the average Young's modulus $E = 12.4$ kPa from the section 3.3.3 is used. We emphasise here, that the value of the force generated by the cell is known to depend on the stiffness and coating of the substrate, as well as the cell line [32, 76, 77]. Figure 3.37.b shows the approximated forces for three HAOSMCs, BAOSMCs and PCs. We can see that despite the small amount of data and the approximations the values appear consistent with each other, and the range of estimated forces $0.05 - 0.2$ μN is close to what is found in the literature. Indeed, using Traction Force Microscopy with HAOSMCs, forces of $0 - 10$ μN on substrates of $8 - 12$ kPa have been reported [76, 77, 78]. Another study on HAOSMCs using nanonet technology reported a value of $0.01 - 0.014$ μN [22]. Studies on PCs on micropillars have reported forces of $0.035 - 0.04$ μN on micropillars of 11.6 kPa and $0.01 - 0.015$ μN on micropillars of 29.5 kPa [32].

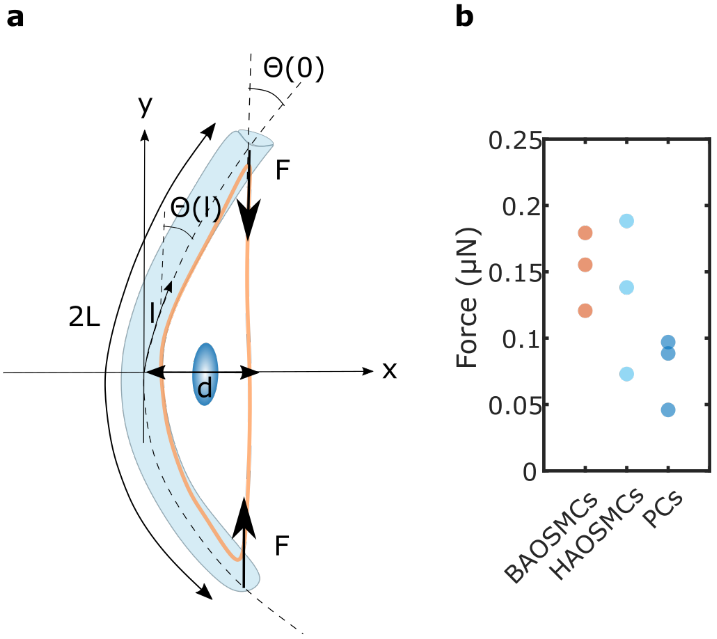

Figure 3.37: Forces exerted by mural cells, a simple approach. a, Geometry of a bending microfibre under cell forces. F are the concentrated forces exerted by the cell at its extremities. $2L$ is the length of the microfibre. $\theta(l)$ is the local tilt angle with $\theta(0)$ the tilt angle where the force is exerted. The maximal deflection of the microfibre is noted d. **b**, Calculated force using equation 3.10 for three cell types: BAOSMCs, HAOSMCs and PCs. For each cell type three cells are analysed.

3.4 Discussion and conclusion

3.4.1 Design of microfibres

In this chapter, we first establish guidelines for the production of uniform, circular poly(ethylene glycol) diacrylate (PEG-DA) microfibres of desired diameter using a two-phase flow and a flow-focusing geometry. The proposed guidelines result from a systematic analysis of the effect of varying the channel cross-section, the compositions of the oligomer and of the continuous phase solution, as well as the flow rates. It should be noted that although the effect of certain parameters has been discussed in the literature, to our knowledge, no previous study has systematically investigated the joint effect of all the cited parameters.

First, a phase diagram of capillary numbers (Ca) is constructed to characterise jet production and stability. Our phase diagram is consistent with previous studies for flow-focusing geometries. Indeed, we obtain similar Ca numbers for the transition between jetting and threading regimes, and we verify that the threading regime is obtained as Ca numbers are increased. We show that in our case, the composition of the continuous phase is the parameter that most influences the Ca numbers. We find that the optimal continuous phase is composed of mineral oil with Span80, as it both reduces the interfacial tension and increases the viscosity, resulting in a larger Ca_c and therefore allowing the threading regime to be maintained over a wider range of parameters (which for example allows producing thinner microfibres). While the use of mineral oil and Span80 for jet production has been proposed before, the previously proposed composition included hexadecane, a highly toxic substance, and a smaller amount of Span80 than we recommend, resulting in a higher interfacial tension than with our selected composition [89, 92].

We also show that the obtained jet diameter is controlled by the flow rate ratio and the channel cross-section. The dependence is well described by an adapted version of the theoretical estimate originally proposed by Cubaud and Mason [111]. In our system, the microfibre diameter corresponds to the jet diameter up to $60\ \mu$m. For larger jet diameters, microfibres with diameters larger than their jet diameter are observed. As our study focuses on the production of thin microfibres, we do not investigate this phenomenon further, which we hypothesise may be linked to microfibre swelling and a combination of other parameters such as jet speed, jet diameter, and solution composition. While unimportant for our intended application, this effect should be taken into account for the production of larger microfibres. We apply our protocol to successfully produce uniform, circular microfibres with diameters ranging from ≈ 8 to $\approx 60\ \mu$m, corresponding to the range of microvessel diameters.

3.4.2 Mechanical properties of microfibres

To quantify the deformation of the microfibres and thus measure the cell forces, quantification of the mechanical properties of the hydrogel is necessary. To obtain more information about the mechanical properties, the Young's modulus of the microfibres is determined by atomic force microscopy (AFM) with a conical probe. The Young's modulus is shown to increase exponentially with ultraviolet (UV) exposure time. It should be noted that similar observations were reported by Duprat et al. [86] for microfibres that were produced using a mask and without flow, unlike ours. In addition, the stiffness range studied by Duprat et al. is much higher. We also observe that the diameter of the microfibres could influence the stiffness, as different moduli are obtained for similar exposure times but different microfibre diameters, a preliminary observation that would deserve further investigation. Our choice of parameters yields microfibres down to 2.5 kPa, which is in the targeted range.

As AFM is a local measurement, microindentation is used as a more macroscopic measurement as well as to confirm the reliability of our measurements. Because the microindentation technique is optimised for a spherical sample, we fabricate PEG-DA microspheres of similar size and stiffness to microfibres to perform this comparison. To our surprise, we find that the Young's modulus of the microspheres is about 30 times greater than the one of corresponding microfibres having the same composition and similar UV exposure times. Same as for microfibres, increasing exposure time appears to increase microsphere stiffness. These results pushed us to divert from our main task and investigate the difference in Young's modulus. To our knowledge, we are the first to identify and investigate this phenomenon. Indeed, while earlier studies have quantified the Young's modulus of PEG-DA microspheres, few studies have quantified the mechanical properties of microfibres. We hypothesise that the difference in stiffness between microfibres and microspheres may arise from differences in the cross-linked chain organisation. To indirectly investigate this point, we experimentally determine the shrinkage ratio of the different microgels using glycerol. We observe that stiffer microsphere gels have a lower shrinkage ratio than softer microfibre ones, consistent with previous shrinkage studies [121]. These results yield support for the idea that the difference in stiffness between microspheres and microfibres can be attributed to a difference in network organisation (e.g. mesh size), which would also explain the observed difference in shrinkage rates. Additional research is needed to understand why the cross-link organisation is different. One reason that could explain such a difference is the internal flow in the droplet, which is different from that in a jet. Another explanation could be the restrained number of reactive species in a droplet compared to the very large pool of reactive species in a jet.

Our work provides a proof of concept that microindentation can be used to determine the Young's modulus of microfibres: we show that similar results to AFM are obtained. We note that the AFM estimate of the Young's modulus depends on the assumed value of the Poisson's ratio. Thus, to complete the mechanical characterisation of the microfibres, we investigate the sensitivity of the result to the value of the Poisson's ratio. First, PEG-DA is assumed to be incompressible ($\nu = 0.5$) and then a lower Poisson's ratio value from the literature [118] was tested ($\nu = 0.2$). The results show that the Young's modulus is fairly insensitive to the chosen value of the Poisson's ratio in the stiffness range of interest.

It is important to note that we cannot further reduce the Young's modulus of the microfibres by reducing the UV exposure time without losing the uniformity of the microfibres. Softer microfibres could theoretically be produced by reducing the amount of photoinitiator or PEG-DA. However, adjustments to the length of the channel may be necessary to ensure the uniformity of the microfibres and to avoid waviness. In the future, it would be interesting to study the effect of the functionalisation of the microfibre on the Young's modulus to obtain a more precise characterisation. Indeed, it has been observed that functionalisation can increase the stiffness of the gel [70, 80].

3.4.3 Impact of curvature on mural cell organisation

Microfibres in the arteriole diameter range ($D_{min} \approx 30\ \mu$m) are successfully functionalised with RGD (arginine-glycine-aspartic acid) and enable mural cell attachment and growth. As it is difficult to culture cells on thinner microfibres, in this thesis we focus on smooth muscle cells (SMCs), which in vivo are found in larger microvessels than pericytes (PCs) [2].

Cells usually respond to environmental changes, for instance, a change in stiffness, curvature, topography and functionalisation. It has been shown that Human aortic smooth muscle cells (HAOSMCs) cultured on glass capillaries of 80 to $400\ \mu$m diameter align in a direction parallel to the cylinder axis [122]. This alignment increases with increasing curvature (decreasing diameter) and with increasing cell confluency. We observe that both bovine aortic smooth muscle cells (BAOSMCs) and HAOSMCs align in the direction parallel to our microfibres when they are confluent or nearly confluent, even if HAOSMCs alignment with the microfibre is less aligned than that of BAOSMCs. Further measurements will be needed to draw conclusions and see if there is a significant difference in alignment between the two cell types or if this is due to other parameters. One parameter that could cause this difference in alignment between BAOSMCs and HAOSMCs could be the confluence of the cells. In fact, it has been shown that HAOSMCs tend to align less axially when isolated than when in monolayers [122]. Therefore, it would be necessary to redo experiments with both cell types at confluence. Our results show that substrate stiffness does not influence cell alignment as SMCs align parallel to the microfibre on soft microfibres, the same as observed in rigid ones [122]. It is important to note that the microfibre diameter in our study is smaller ($60\ \mu$m) than that of previous studies [122, 123]. According to the literature, the main reason why cells align longitudinally with microfibres of large curvature is the energy penalty of bending the stress fibres [122]. In fact, when aligned along the cylinder axis, the stress fibres do not need to bend and therefore, axial alignment is preferred. On microfibres with negative Gaussian curvature, we observe similar results to other cell types on similar geometries, with cells that accumulate in the saddle region and form bridges.

It has been shown that the use of Rho, a small GTPase that regulates F-actin assembly, enables HAOSMCs to circumferentially align with the glass capillaries [122]. It would be interesting to investigate if such behaviour can be replicated on soft microfibres, thus reproducing the in vivo orientation of SMCs. According to the literature, if contractility dominates over bending energy, stress fibres are predicted to align in a circular fashion. It would be interesting to investigate this phenomenon using, for example, Ca^{2+}, which is known to increase the contractility of SMCs [122].

On thinner microfibres, $D = 30\ \mu$m cell alignment is difficult to quantify as cells are able to deform the microfibres in the longitudinal direction, resulting in microfibre buckling. We make this observation not only for SMCs but also for PCs. Further experiments and maybe a change in the system (2D surfaces with different curvatures and stiffness) would be necessary to quantify the impact of curvature and stiffness on PC organisation [123, 125].

3.4.4 Microfibres as a force sensor

Our microfibres enable us to measure both SMC and PC forces. However, due to cell orientations aligned axially with the microfibres, we can measure traction forces that bend the microfibres, rather than compressive forces that would squeeze the fibres as initially intended. The measurements presented in the thesis, despite the small number of samples and the analysis using a simplified model, are consistent with the literature, in the range of 0.015-0.04 μN for pericytes and 0-12 μN for SMCs [22, 32, 76, 77, 78]. Forces generated by mural cells remain incompletely characterised and the system developed in this thesis appears promising to quantify traction forces in a much simpler way than existing approaches such as Traction Force Microscopy. Coupled with fluorescence microscopy, a more accurate model could be developed by linking the distribution and number of focal adhesions to the force measured. In addition, as with other systems, the effect of substrate stiffness could also be investigated. Finally, as discussed in the previous section, our system should allow measuring mural cell contractile forces if circumferential organisation observed in vivo can be reproduced.

Chapter 4

Conclusion and perspectives

4.1 Summary of the results

Pericytes (PCs) are present all over our body and have been reported to play a crucial role in health and disease: they are involved in the development of new blood vessels, in the maintenance of the blood-brain barrier, in the control of blood flow [5, 28, 34]. Moreover, their loss or dysfunction can for instance, contribute to the progression of diseases such as Alzheimer's disease or tumours [5, 7, 17]. Despite a growing interest over the past two decades, there are remaining debates about pericyte characterisation and functions among the scientific community [7]. This thesis focuses on two functions of pericytes: PC migration and contractility. To study these functions, we have developed in vitro tools that mimic geometrical aspects of the PC environment, such as confinement or curvature.

In chapter 2 we demonstrate that micropatterned lines which create confinements similar to those cells experience on microvessels are a versatile tool for studying pericyte migration. We successfully show that in vivo morphological features of pericytes, such as length and vessel coverage, can be accurately reproduced using 1D continuous lines (called infinite lines) compared to 2D assays. In addition, 1D line migration assay, by its configuration, allows easy access to large cellular data sets, including cell trajectories, shapes, and immunostainings, compared to 3D assays, where parameters are much more challenging to extract. When they migrate, PCs display an inverse relationship between average cell length and speed. To model PC migration, we hypothesise that migrating PCs can be described as particles undergoing Brownian motion with dry friction. We demonstrate good agreement between the model predictions and our experimental data for speed probability distribution and average cell length-speed relationship.

In vivo, pericytes arrange themselves in cellular chains along small blood vessels, exhibiting contact inhibition with neighbouring cells, resulting in longitudinal confinement [27]. To replicate this confinement, we introduce non-adhesive gaps into the infinite lines, creating constrained micropatterns of varying lengths corresponding to different longitudinal confinement levels. While our model effectively describes PC motility on longer micropatterns, it encounters limitations with shorter ones. This discrepancy can be attributed to the larger occurrence of fully spread cells on short patterns, which are thus constrained and prevented from migrating. If those spreading cells are removed from the analysis, we demonstrate that our model can reasonably describe pericyte motility.

According to our model, cell speed depends on the friction between the cell and the substrate, directly proportional to the cell's contact area. To validate this hypothesis, we increase the micropattern width by a factor of two. Surprisingly, cells on micropatterns twice as wide exhibit the same length-speed relationship as cells on thinner micropatterns, challenging our initial model's prediction of a width-dependent relationship based on the total cell spreading area. To refine this hypothesis, we investigate the area of focal adhesions (FAs), where we expect to find the dominant friction. Looking at the total area of focal adhesions, we can see that it is similar for cells of comparable length on both micropattern widths. However, as cells get longer, the total area of focal adhesions increases. Therefore, we hypothesise that dry friction is proportional to the contact area of focal adhesions rather than the total area of the cell, as we initially postulated.

In the final section of this chapter, we investigate pericytes' ability to cross non-adhesive gaps to gain insights into their behaviour on non-uniform substrates. Our observations reveal that pericytes can easily cross non-adhesive gaps of $5\ \mu$m. Still, for larger gap sizes, the probability of crossing decreases exponentially, with $20\ \mu$m representing the maximum length they can cross. We propose a probabilistic model based on the probability of crossing an energetic barrier to establish criteria for crossing, which correctly describes the experimentally observed probability distribution for crossing.

In the chapter 3, we extend our study to mural cells and aim to measure the compressive forces exerted by smooth muscle cells (SMCs) or pericytes. We take a systematic approach involving the design, fabrication and mechanical characterisation of poly(ethylene glycol) diacrylate (PEG-DA) microfibres tailored to replicate the curvature experienced by mural cells in their in vivo environment. We use a two-phase flow approach to fabricate the microfibres, utilising flow-focusing microchannels and photopolymerisation. By adjusting parameters such as flow rates, channel dimensions and solution compositions, we establish a phase diagram based on capillary numbers (Ca) to define which combination of parameters generates a stable jet. Our investigations show that for our setup, the continuous phase composition is the parameter that increases the Ca numbers the most, thereby facilitating stable jet formation, while variations in the channel cross-section primarily control the microfibre diameter and stiffness. As a result, we achieve reproducible production of microfibres in the range of 8 to $80\ \mu$m in diameter.

Mechanical characterisation of hydrogels is essential for accurate force determination. In this work, we use atomic force microscopy (AFM) to measure the Young's modulus (E) of our microfibres. To modulate the stiffness of the microfibres, we investigate the influence of UV exposure time, which correlates with the jet speed. Our results show an exponential relationship between UV exposure and Young's modulus, similar to that observed for microfibres fabricated using the stop-flow lithography technique [86]. By decreasing the exposure time, we reduce Young's modulus down to $E \approx 2.5$ kPa. We also observe an increase in Young's modulus with decreasing microfibre diameter that will need further experiments to be confirmed. To validate our measurements, we use microindentation and produce microspheres of similar diameter and UV exposure time. The comparative analysis between AFM and microindentation on microspheres shows reasonably similar results. However, we observe an important difference between the stiffness of microspheres and microfibres, which raises new questions about the effect of the shape and flow of the pre-gel on the stiffness of the microgel. The use of shrinkage measurements allows us to confirm this difference.

In the last part of chapter 3, we examine the behaviour of mural cells on microfibres of different diameters and stiffness. In vivo, SMCs are circumferentially aligned on the outer walls of blood vessels, and PCs have circumferentially aligned secondary processes [2, 122]. To observe compressive forces, a similar cell orientation as in vivo is necessary. For experimental reasons, we only quantify SMCs orientation. With $60\ \mu$m microfibres, we observe that SMCs in monolayers tend to align parallel to the direction of the microfibres (axially), preventing us from measuring compressive forces. However, we observe that both SMCs and PCs can bend straight microfibres of $30\ \mu$m diameter in the axial direction, suggesting a possibility to measure traction forces exerted by mural cells. To provide a first approximation of the traction forces exerted by SMCs or PCs on thin microfibres, simple approximation formulas based on beam theory are used to analyse the bending behaviour of our microfibres [128]. Despite the limited sample size and a simplified model for the analysis, our results are consistent with existing literature using other techniques [22, 32, 78].

This PhD implements two new experimental projects at the LadHyX. Due to the inherent limited time of a PhD, many unanswered questions remain. We will attempt to address some of them in the following sections, suggesting possible explorations and interpretations.

4.2 Perspectives

4.2.1 Probing pericyte dynamics: investigating lateral and longitudinal confinement

4.2.1.1 The impact of line width on pericyte shape and migration

From our analysis of PC migration on infinite lines of $10\ \mu$m in width, we observed that PCs can be modelled as particles undergoing Brownian motion with dry friction. In our model, we initially hypothesised that the magnitude of dry friction is proportional to the cell contact area. Therefore, for larger micropatterns, cell speed and length product is expected to decrease as width increases. Using constrained micropatterns of $20\ \mu$m wide, we observed that the length-speed relationship is the same as for $10\ \mu$m wide micropatterns, invalidating our hypothesis. From these observations and a first quantification of FAs, we hypothesised that dry friction depends on the total area of FAs. As previously mentioned (section 2.3.2), constrained micropatterns can bias the results as PCs are trapped. Indeed, our model could less accurately describe cells on highly constrained micropatterns of $100\ \mu$m and $150\ \mu$m long. Therefore, a more robust verification would be to use infinite lines of different widths. At the beginning of this thesis, we first started with micropatterns of 5, 10, 20 and $31\ \mu$m (Figure 4.1) to mimic the different confinement of the microvessels [2]. At that time, the cell density was too important, and we could not quantify the behaviour of PCs. Replicating these experiments would not only allow us to either confirm or refute our observations on constrained micropatterns, but it would also allow us to explore the behaviour of PCs at different degrees of lateral confinement and see if we can compare such behaviour with that of other PC subtypes observed in vivo: as mesh pericytes or pre-capillary pericytes. For example, it would be interesting to see if PC coverage increases and PC length decreases with the width of the infinite line [2].

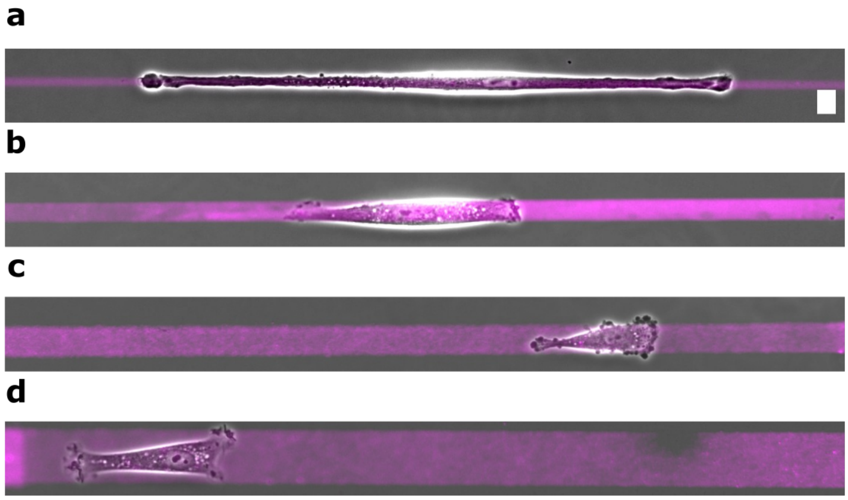

Figure 4.1: The impact of lateral confinement on pericytes. Bright-field images of pericytes migrating on infinite lines of different widths: (**a**), $5\ \mu$m, (**b**), $10\ \mu$m, (**c**), $20\ \mu$m and (**d**) $31\ \mu$m. Micropatterns are shown in magenta (fibronectin plus fibrinogen). Scale bar = $10\ \mu$m.

4.2.1.2 The impact of substrate non-uniformity on pericyte migration

To mimic the non-uniformity of substrate that PCs can encounter in vivo, we introduced non-adhesive gaps of different sizes and explored if PCs could cross these barriers. This work is limited to quantifying the probability of gap crossing. It would be interesting to correlate the position of the cell and its speed on the micropattern and see if we can note a change in the speed of the cell when crossing the gap. This could also help us to refine the model. A study of the front and rear and shorter time steps (1 or 5 minutes instead of 10 minutes) might be more appropriate for this analysis. Indeed, tracking the cell protrusions might give us information on the maximum gap size PCs can cross, and shorter time steps might help better capture variations in protrusion activity [50, 52].

The substrate that pericytes encounter in vivo consists of a laminin layer containing small fibronectin spots [33]. These fibronectin spots colocalise with FAs of both endothelial cells (ECs), which line the inside of blood vessels and pericytes [25, 32]. A recent in vitro study showed that PCs strongly prefer fibronectin spots to laminin to mediate adhesions [32]. Therefore, the next step towards a more physiological PC environment would be to replace non-adhesive gaps with laminin and study their behaviour. Does laminin have the same effect as non-adhesive gaps, and therefore, pericytes will not adhere to it, how would it impact cell speed? We postulate that PCs will avoid laminin gaps, bridging them without forming FAs or avoiding them by changing their direction. More complex micropattern geometries, such as lines of varying width coated with fibronectin spots surrounded by laminin, would also be interesting to use and study their effects on cell migration and morphology.

4.2.1.3 A potential platform to study escaping pericytes

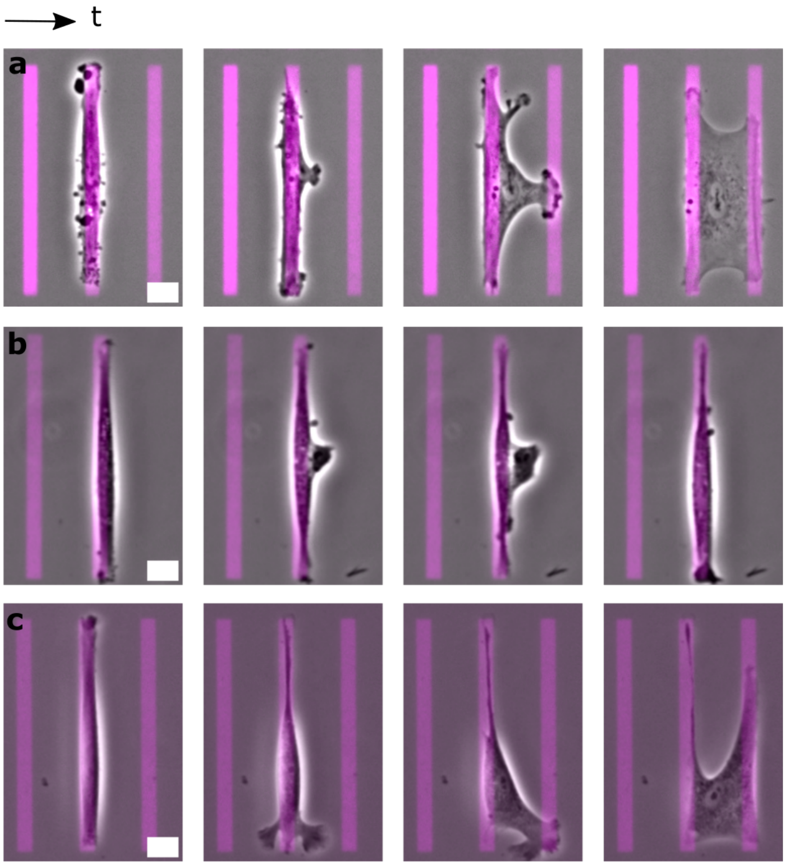

Figure 4.2: Pericyte escaping can be observed on constrained micropattern. Bright-filed images of pericytes that either extend a protrusion at their soma: (**a**), (**b**) or at their front (**c**) to explore their environment and potentially reach a micropattern and form a bridge. Micropatterns are shown in magenta (fibronectin plus fibrinogen). Scale bars = $20\ \mu$m.

In chapter 2, we focused on the crawling migration of PCs. However, PCs can also display another type of migration called escaping [25]. During escaping, pericytes retract their process, degrade the basement membrane, then form a protrusion at their soma like an antenna, and migrate to the surrounding tissue [25]. Studies have also reported the formation of bridges where pericytes connect to a neighbouring capillary with an antenna that they form or one of their process extremities [9, 30]. Usually, in vivo, pericyte escaping occurs in reaction to stressful situations or during angiogenesis [9, 28, 30]. As we can see in Figure 4.2 with our simple micropattern configuration, we observed a few pericytes able to form bridges with neighbouring micropatterns either by extending a protrusion from their soma (Figure 4.2.a) or by reaching it with their front protrusion (Figure 4.2.c) similarly to what is observed in vivo. Note that for this case, the transversal gap distance was $30\ \mu$m, a distance that PCs nearly never cross as a longitudinal gap, as shown in this thesis. We also started to use micropatterns separated by $10\ \mu$m and observed similar behaviour as for $30\ \mu$m. These observations show that our setup could also give a first quantification on pericyte escaping without complexifying the system to 3D.

4.2.1.4 Pericyte migration/behaviour on curved substrates

In vivo, pericytes migrate along microvessels with high curvature. In the literature, the curvature has been demonstrated to impact cell alignment, migration or internal organisation [122, 123, 125]. To investigate the impact of curvature on PC migration and morphology, preliminary tests are performed on tungsten wires of $10\ \mu$m diameter. The setup was first developed by Dr. Claire Dessalles at the LadHyX; it consists of a polydimethylsiloxane (PDMS) ring with an 8 mm diameter hole. Tungsten wires of different diameters $(4,7,\ 10$ or $50\ \mu$m) are attached to it using liquid PDMS, as shown in Figure 4.3.a. wires are then functionalised with fibronectin (as for micropatterns, section 2.2), and a drop of medium with suspended PCs is placed above it to let PCs adhere to the wires. A similar protocol as for micropatterns is then used to image PC migration using bright-field microscopy. As we can see in Figure 4.3.b, as tungsten wires are opaque, we can only see a part of the cells thus, as a first analysis, we use *MtrackJ* plugin with ImageJ to track the protruding part of the cells and obtain preliminary results on PC speed [129]. As for micropatterns, we avoid tracking cells that divide and cross each other. Figure 4.3.c shows that PCs on $10\ \mu$m wires display a similar speed range as on $10\ \mu$m infinite lines (section 2.3.1.3). Further experiments with Hoechst or live dye markers such as Cell Tracker will be necessary to help with the tracking or using different setups with glass capillaries or convex substrates [123, 130]. Note that we tried to use glass capillaries and a pipette puller to obtain desired diameters; however, glass capillaries are very fragile, and it is challenging to obtain a constant diameter over a few millimetres. Therefore, a system similar to Jin et al. [123] with convex PDMS surfaces may be another option, although obtaining a convex substrate of $10\ \mu$m diameter may be challenging. This setup could also allow us to study escaping migration (PC bridging); we are aware that a technique to control the distance between two wires will be necessary for such a study.

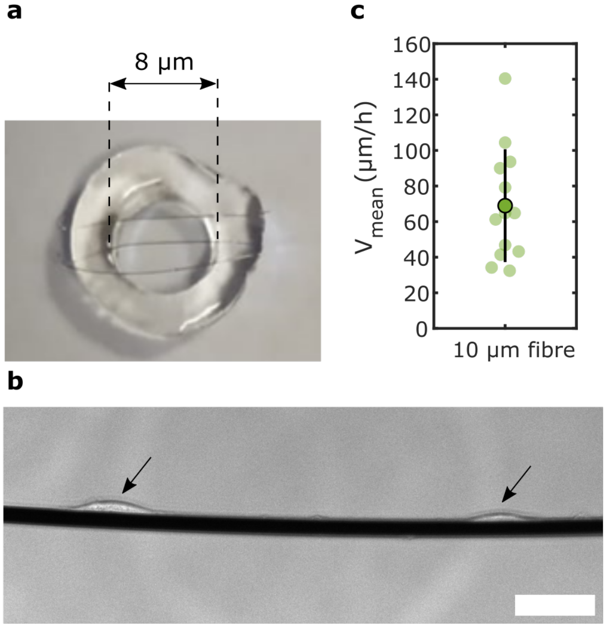

Figure 4.3: Pericyte migration on tungsten wires. a, Photograph of the experimental device, with a PDMS ring of a few millimetres height and a hole of 8 mm and tungsten wires attached to it. **b**, A bright-field image of pericytes on $10\ \mu$m diameter tungsten wires, black arrows indicate cell soma. Scale bar = $50\ \mu$m. **c**, Average cell speed over a few hours (V_{mean}) on $10\ \mu$m diameter tungsten wires. Error bars indicate the standard deviation of the mean (STD).

In addition to studying migration on tungsten wires, we also investigate the morphology of PCs on different rod diameters. As with micropatterns, we stained cells with phalloidin (F-actin) and Dapi (nucleus) and imaged them with fluorescent microscopy. Again, due to the opacity of tungsten wires, we can only image half of the cylinder. We can see in Figure 4.4.b that PCs on $10\ \mu$m wires can display an elongated shape as observed on similarly confined lines. Also, we observed that they could show protruding cell bodies as observed in vivo (Figure 4.4.b below). Conversely, pericytes on $50\ \mu$m diameter wires look more like cells on 2D surfaces with large areas and flat nuclei (Figure 4.4.a). As a first analysis, we manually measured the length of PCs using a *segmented line* tool from ImageJ; we can see from Figure 4.4.c that cells display similar characteristic lengths in both cases despite their different shapes as opposed to in vivo conditions where cells have their length that decreases as blood vessels diameter increases. Here, we suggest that intermediate diameters such as 20 or $30\ \mu$m would be more relevant to use as $50\ \mu$m might be too large for PCs as they behave as in 2D. Note that on thinner wires of 4 or $7\ \mu$m, we did not observe differences in PC morphology with respect to $10\ \mu$m wires. Further quantification will be necessary to draw conclusions.

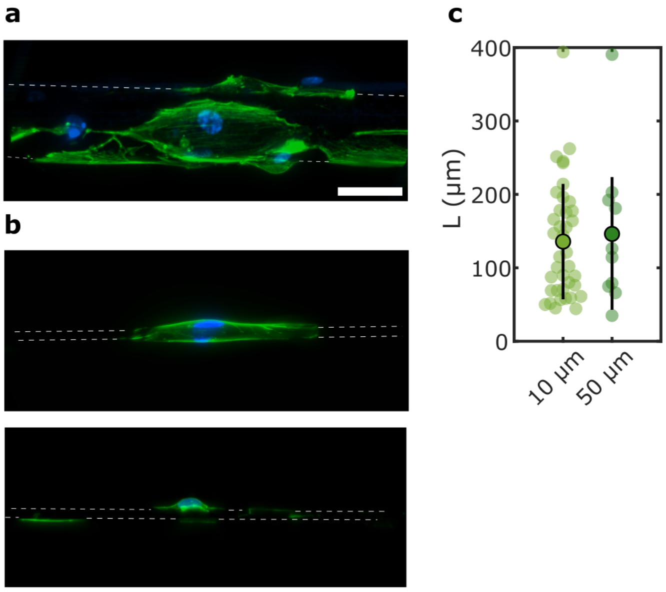

Figure 4.4: Impact of curvature on pericyte morphology. a,b, Representative three-dimensional reconstruction of pericytes on tungsten wires of respectively $50\ \mu$m and $10\ \mu$m diameter. Nuclei are stained with DAPI (blue) and F-actin with phalloidin (green), white dashed lines delimit the wires. **c**, Average pericyte length on 10 and $50\ \mu$m tungsten wires. Error bars indicate STD. Scale bar = $50\ \mu$m.

4.2.1.5 Discrimination from other cell types

We have seen in the general introduction (section 1) that PCs are difficult to identify due to their different morphologies across subtypes, biomarker expression, and origin across organs and microvascular beds [2, 5]. In addition, they share common features and markers with SMCs, they can differentiate in other cell types such as SMCs, fibroblasts, adipocytes, and osteoblasts [2, 7, 17, 131]. Micropatterns could be used to see if a difference between those cell types can be observed, allowing a simple way to distinguish them. For instance, preliminary results show a difference in endothelial cells' gap-crossing ability. Zhao et al. [39] used a 2D migration assay, among other techniques, to distinguish fibroblasts from pericytes; they observed that fibroblasts have higher speeds compared to pericytes.

4.2.1.6 Therapeutical applications

Live observation of pericytes in vivo is quite complex, and quantification based on in vivo studies is even more difficult. Pericyte migration can vary depending on the situation (angiogenesis or disease) and might differ across organs or PC subtypes. Our micropatterns allow us to study PC migration in a simple configuration that we have shown can reproduce some morphological parameters as in vivo PCs while providing access to numerous other parameters and a fairly large data set. In the future, this simple configuration could be used to study the impact of growth factors on PC migration, such as platelet-derived growth factor-BB (PDGF-BB) secreted by sprouting endothelial cells during angiogenesis [28]. It could also be used to investigate the impact of stress conditions corresponding to certain diseases, such as hyperglycemia in diabetes or to compare healthy PCs and deficient ones [9]. For instance, we hypothesise that under stress conditions, cells could cross longer gaps, as it is observed in vivo that protrusions can extend up to $60\ \mu$m in stressed PCs [27].

4.2.2 The microfibre force probe: fabrication, characterisation and applications

In chapter 3, we focus on the fabrication and mechanical characterisation of PEG-DA microfibres to then culture mural cells on them and measure the forces exerted by the cells. Knowledge of the relationship between fabrication parameters such as; UV light intensity, solution composition, flow rates and/or UV exposure times (jet speed) and the properties of the microfibres for continuous flow gelation fabrication is crucial for various applications [92]. However, some aspects, such as mechanical properties, are still relatively unexplored, and most studies on this topic remain qualitative. In section 4.2.2.1, we will focus on gel characterisation and then in sections 4.2.2.2 and 4.2.2.3 we will focus on cell applications.

4.2.2.1 Mechanical properties of PEG-DA microfibres using continuous flow gelation technique

We first decided to use atomic force microscopy (AFM) to quantify the Young's modulus (E) of our microfibres. We limited the study to the quantification of the effect of the UV time exposure (jet speed) on the E and observed a similar trend as what was observed in stop-flow gelation of microgel, namely that the Young's modulus increases exponentially with UV exposure time [86]. By only changing this parameter, we obtained microfibres of $60\ \mu$m diameter down to $E = 2.5$ kPa, which was soft enough for our application. Knowing that other parameters such as photoinitiator concentration, PEG-DA concentration, or UV light intensity can impact E, it would be interesting to explore how those parameters affect E and see if similar relationships as for stop-flow gelation are obtained. Being able to precisely characterise the mechanical properties of microgels is essential in various situations, such as in cell biology to quantify cell forces but also to understand the fluid-structure interactions like clogging of soft particles or the flow of deformable particles [86, 118]. In addition, the first set of measurements on thinner microfibres ($30\ \mu$m diameter) gave a larger E for similar UV exposure times than for larger microfibres. Further measurements on microfibres produced at different exposure times and on even thinner microfibres ($10\ \mu$m) will allow us to confirm or deny these observations.

In a similar trend to the effect of diameter on E, we also observed a difference between microspheres and microfibres of similar diameter and produced with similar UV exposure times. Shrinking experiments with pure glycerol confirm our observations. We hypothesise that the mesh size is different between microspheres and microfibres and that this is due to how crosslinking happens in droplets and jets. Scanning electron microscopy or cryo-scanning electron microscopy could allow us to measure the mesh size and compare the different produced microgels [132]. We hypothesise that the difference in flow between the droplets and jets could also impact the stiffness in the microgel, therefore Particle Image Velocimetry (PIV) could be used to compare the flow in the jets and the droplets. Stop-flow photo-polymerisation could also be used to measure the Young's modulus for the same exposure time, and composition but zero speed [86].

One limitation we encountered during our project is that our microfibres can be wavy once produced. In section 3.3.3.2 we quantified this phenomenon and observed as in the literature, that it depends on the distance from the UV light to the channel end and the flow rates [90]. We also observed that the more crimped the microfibre, the softer it was for the same UV light position. Supplementary measurements would be necessary to verify if the Young's modulus can be recovered from these observations. If proven doable, this would be a simple technique to obtain a first order of magnitude of E.

4.2.2.2 Can SMCs align circumferentially on microfibres and deform them?

In the second part of chapter 3, we focused on mural cell culture and organisation, as well as cell-exerted forces on PEG-DA microfibres. We observed that bovine aortic SMCs (BAOSMCs) in monolayer orient axially on $E \approx 6$ kPa microfibres of $60\ \mu$m diameter as SMCs do on larger rigid fibres [122, 123]. For human aortic SMCs (HAOSMCs), we obtained preliminary results showing that cells also orient axially but to a lesser extent compared to BAOSMCs. Further experiments with higher cell confluency would be necessary to conclude regarding the orientation of the HAOSMCs. The central hypothesis from the literature is that cells align axially to minimise the bending energy of actin stress fibres (SFs) [122]. An alternative hypothesis suggests that the orientation depends on both SF bending energy and contractility [122]. If the bending energy dominates, then cells will orient axially, whereas if contractility dominates, cells will orient circumferentially.

A study of how SMCs organise on stiffer ($\approx 15, 20$ kPa) and softer fibres (≈ 2 kPa) could help to conclude if there is a rigidity for which cell contractility dominates over bending energy. Note that if the microfibre is too soft, cells will exert less force [77]. We did produce microfibres of $E \approx 2.5$ kPa; however, they were wavy and thus, the local geometry impacted the orientation of the cells. To produce straight microfibres, longer microchannels are necessary.

It has been shown that activation of the Rho pathway, a GTPase involved in stress fibre formation, allows SMCs to orient themselves circumferentially on glass capillaries [122]. Medium starvation and the rho activator CNO3 were used to achieve this [122]. A future test would be to see if this also applies to soft microfibres and, if so, if we observe a deformation of the microfibre diameter. This would require nanobeads, as we first used, or rhodamine dye to help visualise the microfibre deformation.

4.2.2.3 Analysis of pericytes on soft and thin microfibres

We know from our experiments of PCs on stiff wires (tungsten or glass) that PCs can fully or partially wrap around $10\ \mu$m fibres. However, on soft fibres of $12\ \mu$m diameter, we could not observe PCs as they bend the microfibres too much and would not spread properly on them. One of the unresolved experimental challenges of this thesis was to find a way to hold the microfibres due to their fragility, size and transparency. This issue will need to be addressed to study PCs on thin microfibres.

Meanwhile, studies of PC migration on soft and curved substrates would be interesting to investigate the effect of substrate stiffness and curvature on PC behaviour. This could be done by attaching thin microfibres to the bottom of a Petri dish (as we do for AFM, for instance) and passivating the rest of the substrate [133].

Appendix A

Probing pericyte dynamics: supplementary information

A.1 Step by step micropattern fabrication: Alvéole

Materials

Reagents

- Dulbecco's Phosphate Buffered Saline (PBS)
- Milli-Q water (filtered)
- Photosensitive reagent PLPP (Alvéole)
- Pll-g-PEG, poly-L-lysine-grafted polyethylene glycol (SuSoS)
- Fibronectin (Sigma Aldrich)
- Fibrinogen 647 (Invitrogen)

Equipment

- FluoroDishes (WFD3523) or glass slides
- polydimethylsiloxane (PDMS) wells ($4\ \mu$m diameter, Alvéole)
- Plasma cleaner
- Cell culture hood with laminar flow
- Microscope with PRIMO system (Alvéole)

Softwares

- Leonardo software (Alvéole)
- Inkscape
- ImageJ

Procedure

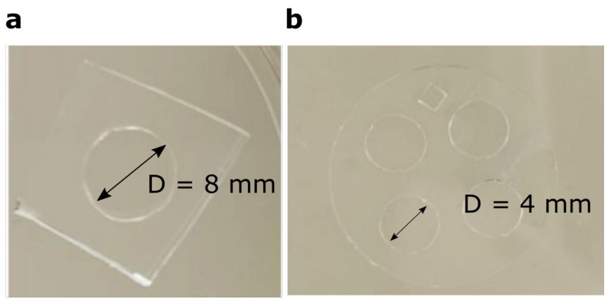

Figure A.1: PDMS wells for micropatterning. **a**, Photograph of a PDMS well of 8 μm diameter.**b**, Photograph of four PDMS wells of 4 μm diameter from Alvéole.

Prepare design of the micropatterns

- Step 1: Draw your desired micropattern in Inkscape by following the Alvéole tutorial video. (https://www.alveolelab.com/fr/tutoriels/dessiner-micropatterns-primo/), then save your drawing in PNG go to ImageJ: image, then 8 bit, and save it in Tiff.
  Note: To do your drawing, you have to know the objective magnification that you will use and the conversion from pixels to micrometres.

Sample preparation

- Step 2: Clean and plasma activate the surface you want to pattern for 45 seconds.
- Step 3: Add PDMS wells (Figure A.1) to hold your patterning solution and allow multiple conditions in parallel.
- Step 4 : Cover the surface with PLL-g-PEG to form a little dome (0.1 mg/ml). Using the Alvéole 4 circular wells, ≈ 20 μL/well is enough. If needed, you can dilute your Pll-g-Peg solution with PBS.
- Step 5: Leave your sample for 1 hour at room temperature. Do not let the sample dry.

Calibration of the microscope (while your sample is incubating with Pll-g-PEG)

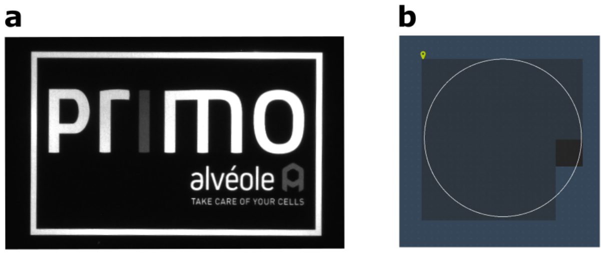

Figure A.2: Micropattern preparation with Leonardo software. **a**, Photograph of the calibration image obtained using a 10x objective and a coverslip with a yellow highlighter. The letters appear with sharp edges and different intensities. **b**, Photograph of a scan using the circle tool to obtain a bright-field image of your well.

- Step 6: Ensure that the microscope incubator is switched off. If it is on and the air inside the incubator is still hot, open the sliding windows and wait a while, otherwise your sample will evaporate very quickly. Switch on the various components of the setup in the following order: computer, microscope, camera, Primo (button on the back, then turn the key on the front and wait for the blue light) and open NIS.
- Step 7: Once in NIS, click on 'application' and then 'show Leonardo dialog box'.
- Step 8: Select in the NIS software the objective you want to use, and if there is a ring on your objective, make sure the ring is set to the adequate thickness of the surface. If you are using a coverslip or a

fluorodish, leave it on 0.17.

- Step 9: Verify that only the UV filter is ON in the Ti2Pad panel. Make sure the sample holder is properly placed. The evenness of the surface ensures a good patterning result.

- Step 10: Place a coverslip with some yellow (or green) highlighter on the holder, then go to the Leonardo window and click on 'Calibrate'.
  Note: The tube calibration should be set and if nobody changes it, it will remain correct.

- Step 11: Select the objective you want to use on the Leonardo interface, then click 'Next'.

- Step 12: To succeed in your calibration, you need to see the image in Figure A.2.a with sharp edges and a grey scale on the 'I' of Primo. To do that, change the exposure and laser level until you get an image that looks like Figure A.2.a. It is important that your DIA is off and that your Z is up. Zoom in so that you can check the sharpness properly and adjust the focus to see the different intensities and sharp letters of 'Take care of your cells'. Once you have an image that is good enough, press on 'Next' and then 'Pattern'.

Patterns

- Step 13: Thaw the aliquot of PLPP. Cover it to avoid light.

- Step 14: Rinse three time your sample with Milli-Q water (MQ). Be careful not to let dry your sample while doing this step.
  Note: If you are using multiple wells, we advise you to rinse one well at a time using the same volume that you used for Pll-g-PEG.

- Step 15: Remove the MQ water from your sample and add the PLPP. Be careful not to let the surface dry while doing this step and to add enough PLPP to avoid complete evaporation during patterning. Draw a little line with a marker on the coverslip close to your sample for the focus, then place your sample on the microscope stage.

- Step 16: Turn on the DIA on the NIS interface. To see your sample on the computer, you need to use the Leonardo window and not the NIS one. Then, find the edges of your sample well. Click on the location icon and set the size of the circular well or the rectangular area you want to scan. Then, check the scan box and click on 'Lock' to draw your well (Figure A.2.b). We advise you to do all the scanning areas before you do the focus to avoid too much stage movement.

- Step 17: To do the focus, go back to the line you draw in Step 15 and adjust the focus. You can also do the focus using dust in your wells.

- Step 18: Once the focus and scanning are done, select 'μPattern' in the Leonardo window to add your micropattern. Browse to your mask file, it must be either Tiff or PDF, and open it. If you need a larger pattern area, you can duplicate your design by clicking 'line', 'column' and 'space' to adjust your drawing. When you are happy with your design, click 'Lock' and repeat this step for each pattern you wish to add.

- Step 19: Set the 'dose' to the desired value. You may need to do some tests to adjust the dose. If you are using fluorescent PEG, the intensity will need to be higher. The pattern before the action will appear in orange. The colour varies with the light dose, from light orange to dark red. Check the duration of the patterning process at the bottom right of the screen. If it takes more than an hour, check that the sample is not evaporating.

- Step 20: Before clicking on 'Play', verify that your DIA is off (on the NIS window). While your pattern is being “burned”, your design will appear in blue. When the pattern is finished, your design will be green, from yellowish green to dark green, depending on the illumination dose.

Coating of the sample

- Step 21: Rinse PLPP with MQ water three times as for Pll-g-PEG. Do not let the sample dry, and avoid touching the surface otherwise, you might scratch your pattern.
- Step 22: This step can be performed under a laminar hood to avoid contamination. Add the coating solution you wish to use to your sample. In our case, it is fibronectin, use 50 μg/ml and leave for 15 minutes (cover your sample to avoid light). For direct visualisation of the patterns, add fibrinogen to the fibronectin solution.
- Step 23: Rinse the coating with PBS three times, and then you can add the cells or keep the micropattern in the fridge for 24 hours (protect your sample from light).

A.2 Impact of the time interval on the speed measurement

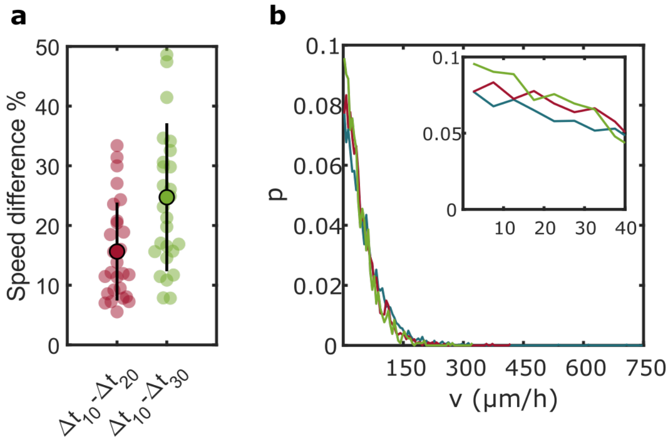

Figure A.3: Measurement of pericyte speed on infinite lines for different time intervals. a, Average speed difference between time intervals of 10 and 20 ($\Delta t_{10} - \Delta t_{20}$) in red and between time intervals 10 and 30 ($\Delta t_{10} - \Delta t_{30}$) in green. Each dot represents one cell and the ones with a black outline represent the mean. Error bars indicate the standard error of the mean (STD). **b**, The speed probability distribution over the cell population on infinite lines. The blue curve corresponds to a time interval of 10 minutes, the red to 20 minutes and the green to 30 minutes. The three distributions have the same exponential decay. n_{cell} = 27 and at least three different experiments are used.

A.3 Pericytes on 50 µm micropatterns

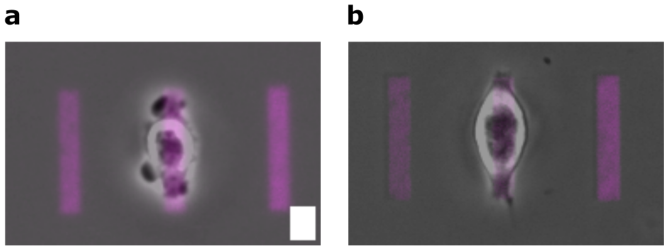

Figure A.4: Pericytes on 50 µm micropatterns are more difficult to binarise. a,b, Bright-field images of pericytes on 50 μm micropatterns (magenta), the two images come from different experiments. Scale bar = 10 μm.

A.4 Trajectories of pericytes on constrained micropatterns

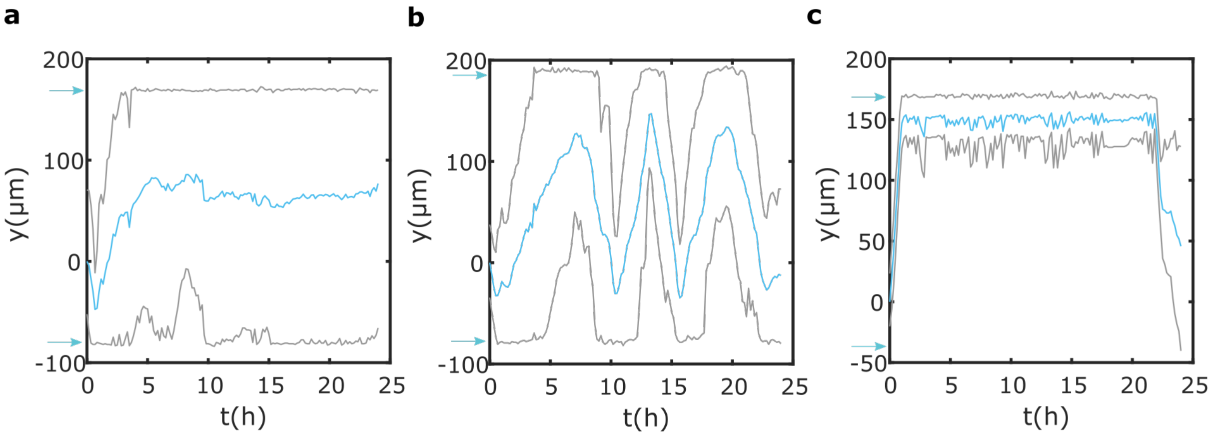

Figure A.5: Trajectories of pericytes on constrained micropatterns. Pericyte trajectories over time on an $L_p = 250$ μm micropattern. The Cyan line represents the centroid of the cell, and the grey lines the extremities of the cell. Cyan arrows indicate the extremities of the patterns. **a**, A kymograph of a spreading pericyte, (**b**) of an oscillating pericyte and (**c**) of a pericyte classified as 'other'.

A.5 Estimation of the maximum gap length crossed by pericytes

To obtain the velocity persistence time, we fit the velocity autocorrelation function (VACF) with an exponential fit $y = Ae^{-mt}$ and calculate the value of 't' for which $y = 0.2$. Here, we assume that 0.2 can be considered as a critical threshold above which the VACF is considered significant (Figure A.6.a,b,c). Note that other thresholds as 0.1, could have been considered. According to the proposed migration model, which describes PC migration as a Brownian motion with dry friction, the VACF should follow an exponential decay [62]. To calculate the persistence time, we plot the VACF of non-crossing cells on micropatterns $L_p = 350$, 250 and 150 μm. For micropatterns of $L_p = 150$ μm we only take the oscillating cells, as spreading cells are almost non-motile, which precludes them from being described by the model, as discussed in section 2.3.2. For $L_p = 100$ μm, even when considering only oscillating cells, we cannot fit the VACF with an exponential fit. This may be due to the fact that the cells are too constrained and, as shown previously, the model is less robust for smaller micropatterns. The fitting parameters and robustness, as well as the attenuation time, average speed and maximal length that PCs can cross, are summarised in Table A.1. We can see that the obtained attenuation times are similar however, it decreases with the micropattern length. We can see in Table A.1 that l_{max} range from $18 - 55$ μm which is larger than the maximum length PCs can cross, 20 μm that we observe for our data and in addition, dependent on the micropattern length. We can therefore conclude that our hypothesis does not work.

L_p (μm)	m	A	t (h)	V_{mean} (μm/h)	l_{max} (μm)
350	-0.96	0.52	1	55	54.97
250	-1.47	0.48	0.59	47,5	28.09
150	-4.71	0.94	0.33	56,4	18.55

Table A.1: Summary of the fitting parameters obtained from Figure A.6.a,b,c to calculate the attenuation time and obtain the maximal gap that PCs can cross.

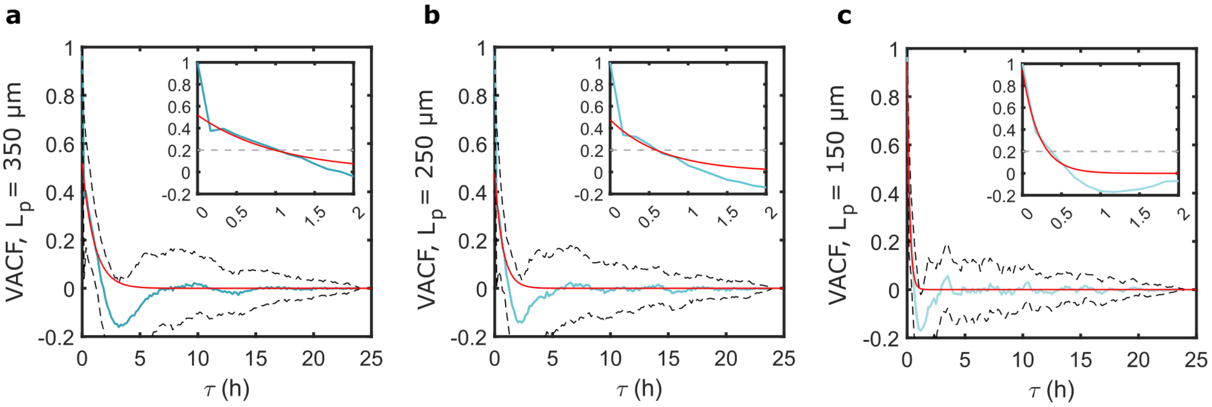

Figure A.6: Velocity autocorrelation plot. **a,b,c**, Average velocity autocorrelation function (VACF) for micropatterns $L_p = 350$ μm (**a**), $L_p = 250$ μm (**b**) and $L_p = 150$ μm (**c**). For all the micropatterns, the width is 10 μm and only PCs that do not cross are analysed. In addition, for $L_p = 150$ μm spreading cells are removed from the analysis. Dashed lines represent the standard deviation of the mean (STD). The red curves represent the exponential fits $y = Aexp(-mt)$, with fitting parameters that are summarised in Table A.1.

Appendix B

The microfibre force probe: supplementary information

B.1 Densities of continuous and dispersed phases

Continuous phase composition (v/v)	ρ (g/ml)
FC-40 + 2% Krytox	1.81
mineral oil + 3.5% Span80	0.78
mineral oil + 30% Span80	0.85

Table B.1: Density (ρ) of the different continuous phases used in chapter 3.

Dispersed phase composition (v/v)	ρ (g/ml)
90% PEG-DA 575 + 0% PEG 200 + 0% MQ water + 10% PI	1.12
30% PEG-DA 575 + 50% PEG 200 + 10% MQ water + 10% PI	1.15
30% PEG-DA 575 + 30% PEG 200 + 30% MQ water +10% PI	1.09
50% PEG6DA 575 + 20% PEG 200 + 20% MQ water + 10% PI	1.06
15% PEG-DA 575 + 45% PEG 200 + 30% MQ water + 10% PI	1.08
30% PEG-DA 700 + 30% PEG 200 + 30% MQ water +10% PI	1.06

Table B.2: Density (ρ) of the different dispersed phases used in chapter 3.

B.2 Microfibres used for atomic force microscopy measurements

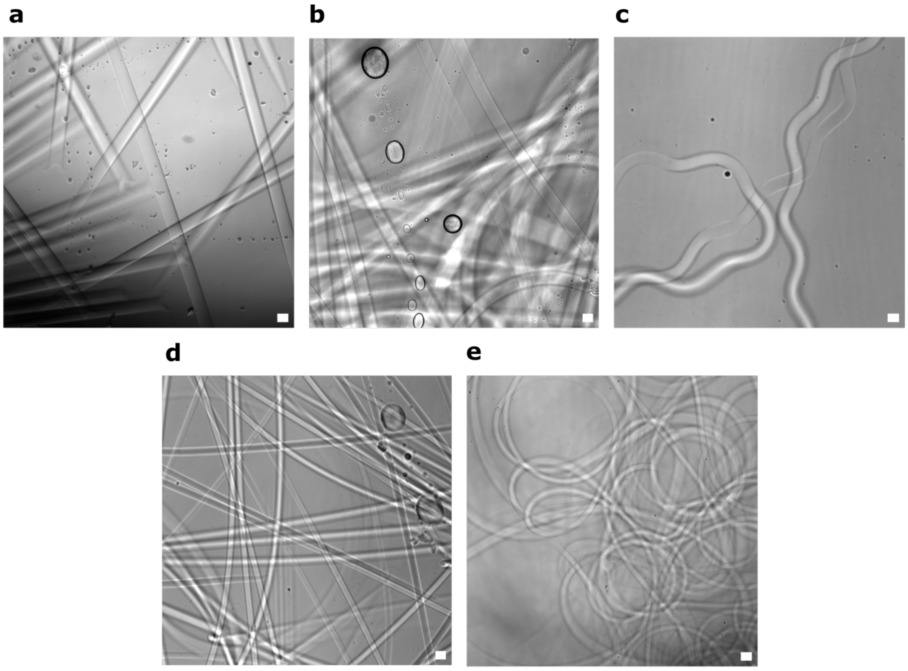

Figure B.1: Microfibres measured with atomic force microscopy. a,b,c, Representative bright-field images of ≈ 60 μm microfibres produced with different exposure times (t). **a**, Microfibres $F_{1.6/6.4}$ produced with $t = 83.8$ ms. **b**, Microfibres $F_{5/20}$ produced with $t = 26.4$ ms. **c**, Microfibres $F_{10/20}$ produced with $t = 13.5$ ms. **c,d**, Representative bright-field images of ≈ 30 μm microfibres. **d**, Microfibres $F_{1/20}$ produced with $t = 30.6$ ms. **b**, Microfibres $F_{2/40}$ produced with $t = 15.1$ ms. Scale bars = 50 μm.

B.3 Cell forces quantification: detailed calculation

In this section, we detail the model to quantify forces exerted by single mural cells. The following calculation is based on the work of Shima [127].

Figure 3.37.a from section 3.3.7 shows the configuration of our microfibre of length $2L$ and diameter D, subject to two equivalent opposite cell forces F. As explained, the deflection of the microfiber along the x axes can be written as:

$$EI\frac{d\theta(l)}{dl} = -M(l), \tag{B.1}$$

with l the curvilinear coordinate along the neutral axis of the fibre, $\theta(l)$ the local tilt angle, $M(l)$ the local bending moment, E the Young's modulus, and I the second moment of area of the microfibre, which can be written as $I = \frac{\pi D^4}{64}$. The moment can be written as $\frac{dM(l)}{dl} = Fsin(\theta(l))$ and the equation B.1 can be rewritten as :

$$\frac{d^2\theta(s)}{ds} = \frac{FL^2}{EI}sin(\theta(s))$$
$$s = 1 - \frac{l}{L},$$

with $\theta(s) = 0$ for $s = 1$ and $\dfrac{d\theta(s)}{ds} = 0$ for $s = 0$ that are the boundary conditions.

An approximate solution of this equation can be derived using Maclaurin series evaluated at $s = 0$:

$$\theta(s) = \theta_0 + s\theta_0^{'} + \frac{s^2\theta_0^{''}}{2!} + \frac{s^3\theta_0^3}{3!} + \frac{s^4\theta_0^4}{4!} + ... \tag{B.2}$$

$$\begin{aligned}
\theta_0^{'} &= 0 \\
\theta_0^{''} &= -\alpha\sin(\theta_0) \\
\theta_0^3 &= \frac{d(-\alpha\sin(\theta_0))}{ds} = -\alpha\cos(\theta_0)\theta_0^{'} = 0 \\
\theta_0^4 &= \frac{\alpha^2\sin(2\theta_0)}{2},
\end{aligned}$$

where for simplicity we write $\alpha = \dfrac{FL^2}{EI}$. The fifth order term will be equal to 0, and terms of 6^{th} and higher orders will have a very small contribution to the final solution. At $s = 1$ when $l = 0$, θ_0^k needs to satisfy :

$$\sum_{k=0}^{n} \frac{\theta_0^k}{k!} = 0. \tag{B.3}$$

Therefore, using the equation B.2 and B.3 we get the final equation :

$$\theta_0 - \frac{\alpha\sin(\theta_0)}{2} + \frac{\alpha^2\sin(2\theta_0)}{48} = 0, \tag{B.4}$$

where the parameters θ_0, L, and I can be determined from the microscopic images of our cell-deformed microfibres and the Young's modulus is the one measured in section 3.3.3.2 for microfibres $D30\_12$, $E = 12.4$ kPa. Note that similar force values are obtained as when using the equation 3.10.

Appendix C

Project as a visiting PhD student at the University of Manchester

C.1 Introduction

The process by which the flow of particles in a confined geometry is interrupted is called clogging. Clogging has been observed in many domains and at different scales. At our scale, pedestrians or animals can cause intermittent clogging, for example, when there is a panic situation, and many people try to leave a space through a single exit or in agriculture, when emptying a silo of dry particles [134] [135]. Clogging can also be observed in pipelines due to the formation of biofilms or the accumulation of particles [136] [137]. On a smaller scale, clogging often occurs in microchannels and can also occur in our blood vessels, for example during diseases [138] [139]. Clogging is not always negative and has found multiple applications, for example, particles of different sizes can be separated by clogging. It can also be used to distinguish diseased cells from healthy cells, for example in cancer [140] [141]. Clogging depends on different parameters such as the particle properties (stiffness, size), the geometry of the confined environment, the flow velocity and the volume fraction of the particles [136]. In the following sections, we will briefly review the different mechanisms that lead to the clogging of rigid and soft particles. We will focus on the clogging of spherical or nearly spherical particles.

C.1.1 Clogging of rigid particles

Three main mechanisms for clogging of rigid particles have been reported in the literature: sieving, bridging and aggregation [136]. The first two mechanisms are purely mechanical [137]. Sieving is the clogging of a single particle by a constriction whose width (W) is smaller to the diameter of the particle (D) (Figure C.1.a). Sieving can be employed in filtration processes or as a particle size selection mean [142]. If $W > D$ then sieving is no longer possible and bridging can occur.

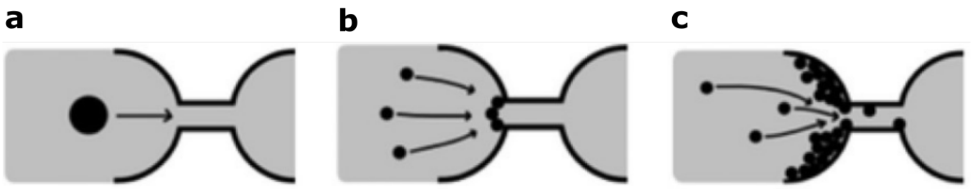

Figure C.1: The different clogging mechanisms at a constriction.(**a**) Sieving, (**b**) bridging and (**c**) aggregation. Adapted from Dressaire et al. [136].

Bridging corresponds to the formation of a particle bridge/arch across the confinement (Figure C.1.b). Note that it can also happen along the channel without the need for any confinement. Compared to sieving, which is fully deterministic, bridging is a stochastic process and can be transient as the bridge can be broken by flow oscillations [136]. According to the literature, bridging depends on the local volume fraction of particles (ϕ), flow rate (Q), the ratio W/D and particle properties [137, 143, 144]. Arch formation is more likely to occur if the volume fraction of particles near the confinement is high, leading to a jamming transition [136]. In fact, particles jam at a critical volume fraction above which they behave like a solid and cannot rearrange. Bridging has also been observed at a small volume fraction of particles. In their study, Marin et al. [143] observed that in a 2D microchannel clogging of a small volume fraction of non-adhesive polystyrene particles depends mainly on the ratio W/D. They reported that for $\phi = 20\%$ bridging is observed for $W/D < 3$ however, when W/D increases and is superior to 3, thus for wider constrictions, they did not observe bridging even for $\phi = 60\%$ which is close to the critical jamming volume fraction (Figure C.2). Note that the threshold of W/D for clogging is larger for a flow of dry particles. Agbangla et al. [137] showed that bridging at low particle concentrations also depends on flow rates and that increasing flow rates can increase the probability of arch formation.

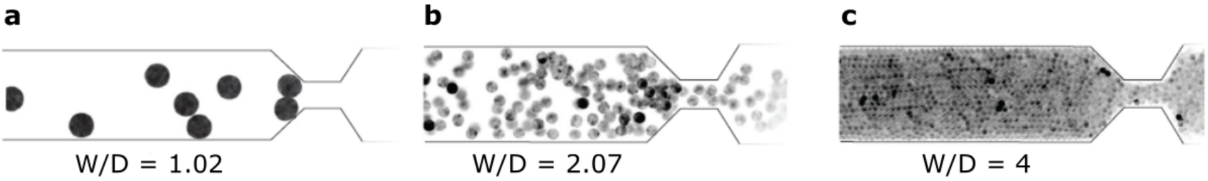

Figure C.2: Bridging depends on the ratio of constriction width over particle diameter. a,b A particle bridge is formed for a ratio of $W/d = 1.02$ and 2.07. **c**, For ratio $W/d = 4$, despite high particle concentration clogging does not happen. Adapted from Marin et al. [143].

The last mechanism of clogging is called aggregation, it corresponds to the accumulation of particles in the confinement (Figure C.1.c). Aggregation depends on the hydrodynamic and surface forces between particles and the wall of the channel [145, 146]. The three different mechanisms of clogging can happen individually or together. For instance, aggregation can lead to bridging [137].

C.1.2 Clogging of soft particles

The case of non-adhesive soft particles (droplets, soft microspheres, capsules) has been studied less than rigid particles in the literature and does not depend on the same parameters as for rigid particles, it is actually harder to clog deformable particles. To our knowledge, most of clogging observations for soft particles are due to sieving (Figure C.3,a,b) [136, 147, 148]. Compared to rigid particles, deformable ones can pass through constrictions smaller than their diameter. However, they might clog at one point. This depends on the difference of pressure across the channel, if it is smaller than the translocation pressure, $\Delta P < \Delta P_{max}$ then the particle will be trapped [149]. The threshold value can be estimated using the following power-law [149]:

$$\Delta P_{max} \propto E(\frac{D}{d_c})^{14/3} \tag{C.1}$$

With E the Young's modulus of the microgel, D the diameter of the microgel at rest and d_c the diameter of the channel. The power-law depends on the prefactor $K(\alpha)$ that takes into account the geometry of the microchannel and the tapering angle α as well.

Very few studies have reported clogging with bridging for deformable particles. Bielinski et al. [147] used numerical simulations to show that clogging of soft particles in quasi-2D microchannels depends on the particle rigidity calculated as $K = 1/Ca$ and W/D ratio. The capillary number Ca is calculated as $Ca = \frac{\rho \nu r \gamma}{k_s}$ with ρ the density, ν the kinematic viscosity, γ the shear rate at the wall and k_s the shear elastic modulus. They showed that bridging does not occur for highly deformable particles even for small W/D ratios and that particles with lower deformability ($K = 500$) may form an arch but only for $W/D < 1.5$. Experimental works will be necessary to validate those numerical observations. At a larger scale (mm), Hong et al. [148] studied the flow of soft hydrogels through a quasi-2D hopper. They demonstrated that clogging can be observed by varying the tilt angle of their chamber and therefore changing the gravity value. They observed an increase in clogging probability when gravity is decreased (Figure C.3.c). In contrast to the clogging of rigid particles, the clogging of deformable ones happens when flow velocity decreases.

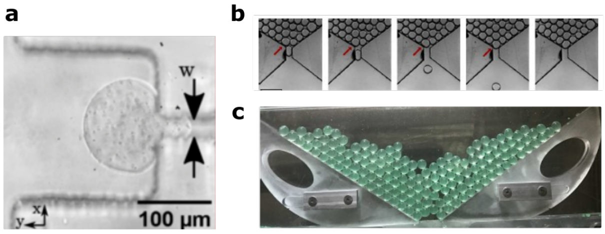

Figure C.3: Clogging of soft particles. **a**, Sieving of a soft (Poly(ethylene glycol) diacrylate) PEG-DA microgel trough a $25\ \mu$m constriction, adapted from Moore et al. [150]. **b**, Sieving of an oil droplet with a diameter of $370\ \mu$m trough a constriction of $300\ \mu$m. **c**, Bridging of soft hydrogel spheres in a quasi-2D chamber. (**b,c**) Adapted from Hong et al. [148].

Finally, very few studies have explored the clogging of a mixture of particles, soft and rigid. Alborzi et al. [151] observed that clogging is more likely to happen when the density of rigid particles is increased in a 2D hopper.

C.1.3 Examples of clogging in vivo

As previously mentioned, the study of clogging is important in a number of domains and one of them is health. Indeed, clogging has also been observed in vivo in diseased conditions, and therefore a better understanding of how biological elements such as cell clogs in diverse situations could help to detect diseases or develop treatments. For instance, Shelby et al. [139] used a polydimethylsiloxane (PDMS) 2D microchannel to compare infected red blood cells (RBCs) at different stages of malaria. When infected with the bacteria causing malaria, RBCs lose their ability to deform and can block small blood vessels such as capillaries. In their study, Shelby et al. demonstrated that with the progression of malaria, RBCs experience sieving for larger channel constrictions.

Another disease in which clogging is observed and of particular interest for this project is sickle cell disease. Sickle cell disease corresponds to the mutation of haemoglobin (HbS) which, under conditions of low oxygen pressure, leads to the polymerisation of the mutated haemoglobin and the formation of fibres [152] [138]. This change affects the morphology of RBCs, increases their adhesion to other cells and to the vascular bed and reduces their deformability. All this leads to a change in the rheology of the blood (increase in viscosity) and, in extreme cases, to a vaso-occlusive crisis (VOC) [153]. VOC corresponds to the blockage of blood vessels by RBCs, resulting in a reduction in the oxygen supply to the surrounding tissues. Since 2010, several studies have investigated RBC clogging using microfluidic channels where pressure is controlled and hypoxic conditions can be recapitulated [138, 154, 155]. In addition, microfluidic diagnostic platforms have been developed and drug screening has been carried out [153]. Despite this strong interest in sickle cell disease, the mechanisms behind VOC are still unclear [153].

C.1.4 Aim of the project and outline

In this introduction, we have seen that in general, the mechanisms behind clogging of soft particles or mixtures of deformable and rigid particles are still unclear. The project I joined for three months in the Physics of Fluids and Soft Matter group aims to better understand the clogging mechanism in sickle cell disease using PDMS capsules, which have been shown to be a good model for RBCs [156]. During these three months, I worked in tandem with a first-year PhD candidate Valeria Ciccone on her PhD project. After learning to fabricate capsules, we tested different microchannel geometries and developed a first experimental setup to study capsule clogging. In the following sections, I will present the main results we obtained and discuss the limitations we encountered.

C.2 Materials and methods

C.2.1 Capsule fabrication protocol

The deformable capsules that we use consist of a liquid core (glycerol) encapsulated in a PDMS membrane. They are prepared using the protocol described in Chen et al. [156]. Briefly, the capsules are prepared using a three-phase flow microfluidic channel consisting of three glass capillaries of circular cross-section arranged in a coaxial configuration. Figure C.4.b shows an illustration of the setup, with the three glass capillaries corresponding to the injection, collection and outer capillaries carrying the inner phase, the middle phase (PDMS) and the unpolymerised capsules, respectively. Prior to assembly, the injection glass capillary tube is pulled with a micropipette puller to narrow the capillary tip down to $D \approx 120\ \mu$m, then treated with Sigmacote (Sigma-Aldrich) to make it hydrophobic to obtain water-oil-water double emulsions. The outer capillary is cut to approximately 2 cm and for the collecting capillary a gas torch flame is used to constrict the tip of the capillary down to $D \approx 350\ \mu$m and to bend the capillary in the middle to $90°$ to facilitate the collection of the capsules. Both the outer and collecting capillaries are treated with plasma to make them hydrophilic. The injection and collection tubes are then aligned coaxially in the outer tube, and Teflon connectors and UV-curable glue are used to hold the glass capillaries together (Figure C.4.a). Once the microfluidic system is prepared to create a train of glycerol-coated droplets a pressure-driven flow controller (Elveflow Mk3+ 0–2 bar, Elvesys) is used to impose the flow of the inner and outer phase and the middle phase flow rate is imposed with a syringe pump (KD Scientific, Model 210). The membrane of the capsules is made of PDMS (Sylgard 184, Corning) and curing agent at a $40:1$ ratio, the inner and outer phases are the same to avoid osmotic effects and fixed to 64% glycerol + milli-Q water (MQ). The inner phase is dyed in red using Carminic acid (Sigma-Aldrich) at 0.1 wt% to help visualise the droplets in the microchannel and later the capsules. As demonstrated in Chen et al. [156] the diameter of the capsule is controlled by the ratio of flow rates: $\frac{Q_o}{Q_i + Q_m}$ and the capsule thickening is governed by the following formula :

$$\frac{2\delta}{d_o} = 1 - (1 + \frac{Q_m}{Q_i})^{-1/3} \tag{C.2}$$

with δ the thickness of the capsule membrane, d_o the total diameter of the capsule (including membrane), Q_o, Q_m and Q_i respectively the flow rate of the outer phase, middle and inner phase. In our case, all of the experiments are performed with capsules of $d_o \approx 350\ \mu$m and $\delta \approx 6.7\ \mu$m.

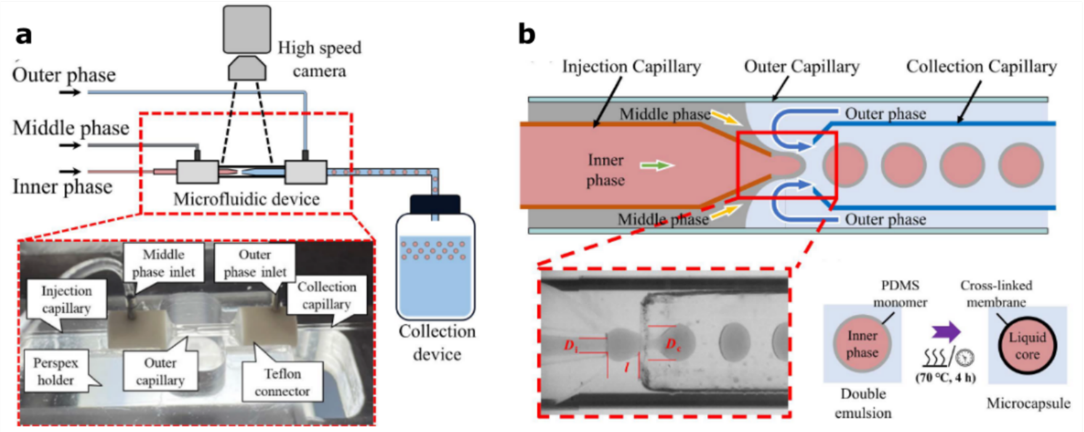

Figure C.4: Schematic diagrams of the setup for capsule fabrication. a, Three-phase coaxial microfluidic channel with the inset showing the image of the different elements of the microfluidic channel. **b**, Zoom on the microfluidic channel showing the formation of double emulsion droplets. The inner phase in pink corresponds to glycerol with MQ water and dye, the middle phase in grey corresponds to PDMS $40:1$ and the outer phase in light blue corresponds to glycerol with MQ water. The inset shows a bright-field image of the microfluidic channel. To the right of the inset is a diagram illustrating the final step in capsule fabrication, curing. Retrieved from Chen et al. [156].

After the double emulsion droplets have been collected, they are cured in the oven for 4 hours at $70°$ C (Figure C.4.b). Capsules are then stored in the previously used outer-phase solution and can be used for several months. Capsules can be deflated on demand using osmotic pressure allowing to change the surface to volume ratio of the capsule and mimicking RBCs properties [156]. As shown in Figure **??**.a, the storage solution of the 64% glycerol capsules is replaced by 100% glycerol, leading the water inside the capsule to flow out until the concentrations in water equilibrate and osmosis is reached. The resulting capsules are 36% deflated (Figure **??**.b).

C.2.2 Experimental setup

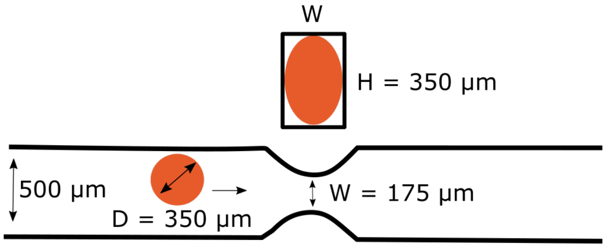

Figure C.5: Schematic of the channel geometry used for sieving analysis. Microfluidic PDMS channel with a constriction of 175 μm wide and 350 μm height. Capsules are indicated in orange and have a diameter of 350 μm and as we can see with the side view of the constriction, they do not fully clog the channel.

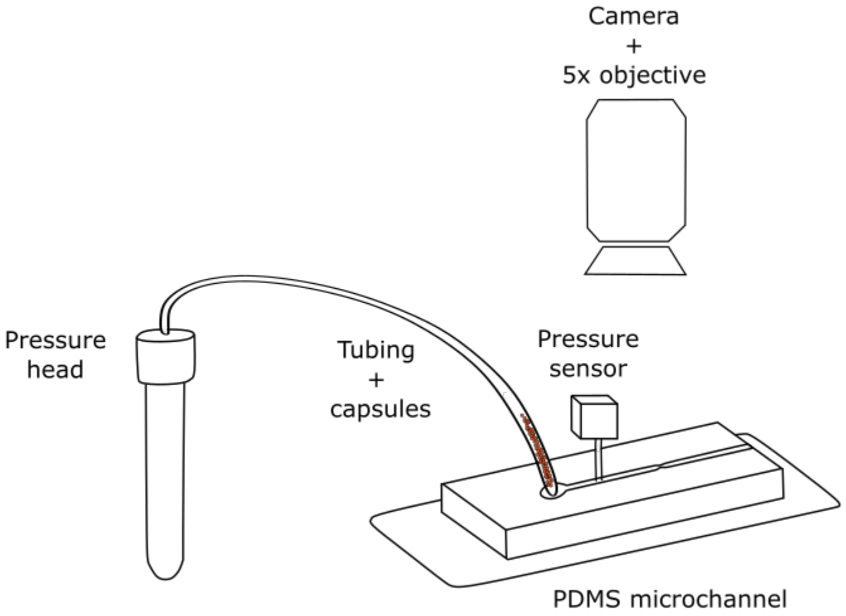

Figure C.6: Experimental setup used to study the flow of capsules. Pressure is applied using a pressure controller, capsules in orange are inserted into the tube and flowed into the PDMS channel with a constriction. A pressure sensor can be placed between the inlet and the constriction of the channel to measure and record the pressure inside the channel during the experiment. A camera is used to monitor the capsules as they flow through the constriction.

To observe the flow of capsules, a microfluidic chip with a constriction is made using a micromachined brass mold. The dimensions and geometry of the channel are summarised in Figure C.5. To make the channel, PDMS and curing agent are used at a $10:1$ ratio. After mixing and degassing, the preparation is cast onto the mold and cured. The PDMS is then cut out from the mold and an inlet is punctured using a 1.2 mm diameter puncher. A suspension of 64% PDMS capsules in 64% glycerol is flowed in the channel using a pressure-driven flow controller (Elveflow Mk3+ 0–2 bar, Elvesys) that imposes a positive pressure difference between the inlet and outlet of the channel. An inlet tube of ≈ 1 mm diameter is used. To analyse the capsules flowing through the channel a camera is used with a 5x objective. Capsules are recovered at the end of the experiment. A schematic of the experimental setup is shown in Figure C.6. Note that because of the presence of capsules upstream of the channel, which changes the resistance and thus the pressure drop, it is not straightforward to estimate the pressure drop across the channel. For this reason, for some of the experiments, we insert a pressure sensor (±1 PSI) close to the inlet of the microchannel (Figure C.6) to measure the pressure drop. The sensor is powered using a 9V battery and to recover the pressure values, the DC voltage output of the sensor is connected to an analog-to-digital converter and recorded on the computer using LabVIEW.

C.2.3 Analysis

Particle speed is obtained using *TrackMate* and a self-made macro in ImageJ which allows us to track the centroid of the capsule and graphs are obtained with code that was developed by Valeria Ciccone in Python [157].

C.3 Results

C.3.1 The red blood cell model

RBCs have a diameter between $6-8$ μm and a biconcave shape, they are highly deformable [158]. The capsules used in this project are much larger $D = 350$ μm and have a membrane thickness of 4% the radius of the capsule. Despite their large size, Chen et al. [156] showed that these capsules, once deflated by 36%, can match the reduced volume of RBCs and show similar deformation when flown through a glass capillary at a constant flow rate as RBCs over a similar range of Ca numbers. Because these capsules are highly tunable and can mimic RBCs, they are a good candidate to study the mechanism of clogging and compare it to VOC that happens during sickle cell disease.

C.3.2 Sieving of neutrally inflated capsules

Before studying the flow of deflated capsules, we first analyse the clogging conditions for neutrally inflated capsules and as a first step, investigate the sieving of these capsules with a ratio $W/D = 0.5$. Based on the literature, we decide to first impose a pressure gradient to flow the deformable capsules [136, 149]. We expect that a deformable capsule will sustain clogging by not building up pressure before the clog compared to an imposed flow rates [159]. In a typical experiment, a suspension of capsules is introduced into the inlet tube, which is then connected to the microchannel inlet. During this step, it is important to avoid generating bubbles because they can alter the flow. After the microchannel is connected to the inlet tube, a pressure gradient (ΔP) is thus applied to push the capsule suspension to flow through the microchannel. We first try with a low concentration of capsules in order to have only one capsule at a time at the constriction entry. Figure C.7 shows snapshots at different times of the experiment of a single capsule flowing through the constriction for different imposed pressure gradients ranging from $\Delta P = 10$ to 2 mbar. As explained in the introduction (section C.1) for soft microgels and imposed pressure gradient, when the local ΔP exceeds the translocation pressure ΔP_{max}, the capsule deforms and passes through the constriction. In our experiment, this is the case for imposed pressure gradient down to 3 mbar. However, if ΔP is too small, the capsule enters the constriction and may deform but does not pass through it as we can observe for $\Delta P = 2$ mbar in Figure C.7. In this case, the force imposed by the pressure gradient between the extremes of the capsule is not enough to deform it and force it through the constriction. Tracking of the capsules shows that the speed of the capsule when it is in the constriction is close to 0 μm/ms and that its speed is increased when exiting the constriction compared to the speed before the constriction (Figure C.8).

Based on these results, we can hypothesise that $\Delta P = 2$ mbar is the imposed pressure gradient at which these capsules will clog in this configuration. However, we observe that for the same imposed ΔP the time a capsule spends in the constriction can vary. Indeed, we can see that for the channel geometry and $\Delta P = 5$ mbar, the time in the constriction is different $t = 1.6$ s and $t = 6.8$ s which could impact the clogging threshold (respectively bottom and top graph in Figure C.8). This phenomenon can be explained by the fact that the pressure drop across the channel is influenced by the number of capsules upstream of the channel. Indeed, the capsules increase the resistance and so the pressure drop based on their number and distribution resulting in different local ΔP at the entry of the constriction.

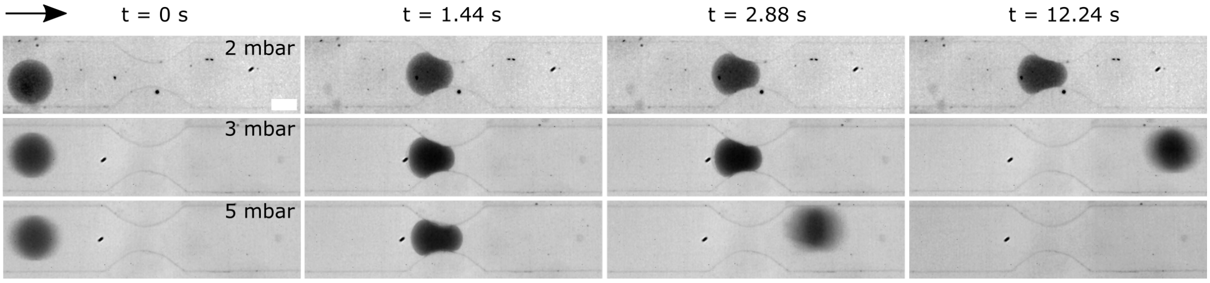

Figure C.7: Sieving of a single capsule. Bright-field images of capsules flowing through a channel with a constriction, capsule diameter ratio $W/D = 0.5$. Three different pressure gradients are imposed: $\Delta P = 2, 3$ and 5 mbar. For $\Delta P = 2$ mbar clogging is observed. Note that for $\Delta P = 3$ and 5 mbar capsule is blurred before and after the constriction because the exposure time used is too high for these two experiments. Scale bar = $200\ \mu$m.

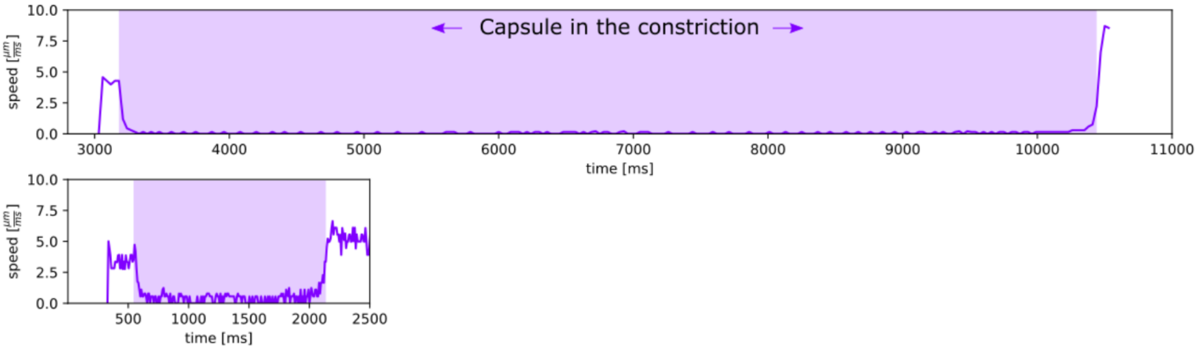

Figure C.8: Speed of a capsule as a function of time flowing through a channel with a constriction, capsule diameter ratio $W/D = 0.5$ and an imposed pressure gradient of $\Delta P = 5$ mbar. The constriction is indicated in magenta. Despite the same imposed ΔP the time in the constriction is different for the two experiments.

We then increase the volume fraction of capsules in the inlet tube. This time we observe clogging for higher imposed ΔP, as we can see in Figure C.9, clogging can be observed for $\Delta P = 3$ mbar and we also can observe it for $\Delta P = 5$ mbar. This confirmed our previous observations that clogging can occur for different imposed pressure gradients. Despite these pressure variations as a general trend, we observe that clogging is more likely to occur for a particle train as in Figure C.9 and could occur for a higher imposed pressure gradient. In Figure C.9 we can see that clogging does not occur immediately for the first capsule and that only a few capsules can pass through the constriction before clogging. We observe that while a capsule passes through the constriction it blocks the constriction and during this time capsules upstream of the constriction continue to move slowly, this is expected as the channel's cross-section is rectangular and therefore the capsule does not fully clog the constriction when passing through, compared to a circular cross-sectioned channel. The liquid continues to flow when the constriction is blocked, upstream capsules get closer to each other and the density of capsules can increase (as new capsules arrive), this locally increases the pressure drop and therefore may lead to clogging for the next capsule. When the capsule exits the constriction its speed increases as well as the speed of the other capsules which probably contributes to the packing of capsules upstream of the constriction. As for the previous section, it is difficult to compare experiments with each other due to the non-trivial effect of capsules upstream the constriction and therefore, to define a deterministic imposed pressure gradient at which clogging will happen.

To quantify the pressure drop at the entry of the constriction, we insert a pressure sensor inside the channel.

However connecting the pressure sensor can be complicated and often leads to the introduction of air bubbles that affect the control of experiments. In addition, we observe that the noise of the signal due to the moving capsules in the channel is larger than the pressure drop. Therefore, to obtain a quantitative analysis of the sieving phenomenon and, in the future, to compare the clogging of neutrally inflated capsules with deflated capsules, it is necessary to change the set-up configuration to remove the effect of upstream particles, either by monitoring the volume fraction of capsules upstream of the constriction and the capsule position or by trying to see if clogging could occur when imposing a constant flow rate.

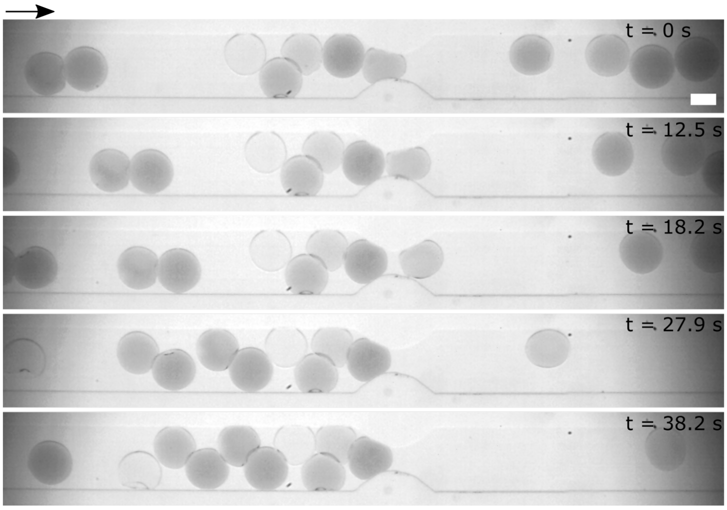

Figure C.9: Sieving of the capsule when increasing capsule density. Bright-field image of multiple capsules flowing through a channel with a constriction, capsule diameter ratio $W/D = 0.5$ and an imposed pressure gradient of $\Delta P = 5$ mbar. Scale bar = $200\ \mu$m.

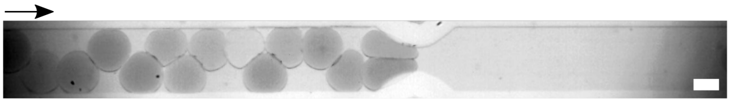

Figure C.10: Bridging of capsule. Bright-field image of two capsules forming a bridge with an imposed $\Delta P = 10$ mbar. Scale bar = $200\ \mu$m.

With this configuration, we can also observe clogging with two capsules at the same time $\Delta P = 10$ mbar, which corresponds to bridging (Figure C.10). However, as the microstate of two capsules entering the constriction at the same time is less likely than one capsule at a time, we did not observe it again during my stay. Changing the setup and a wider constriction might allow us to observe bridging more often.

C.4 Conclusion

During these three months, we mainly investigated the flow of capsules through constrictions smaller than their diameter ($W/D = 0.5$). With this configuration, we could observe the sieving of capsules as described in the literature for soft gels. We observed that the number and the density of capsules upstream of the constriction are key as they impact the pressure drop across the channel. As a consequence, from one experiment to another the imposed pressure gradient for clogging could vary. As a general trend, we observed that when flowing multiple capsules at the same time in the channel, clogging could happen for a higher imposed pressure gradient than when only one capsule is flowing through the channel. We observed that this setup was limited as we could not control the density of capsules in the inlet tube and it was difficult to increase the packing of capsules. In addition, by imposing the pressure gradient we could not control the pressure drop or the flow rate across the channel making the interpretation of the results more difficult. For a quantitative analysis, an improved setup is therefore required. For instance, efforts could be put into investigating how to measure the pressure drop inside the channel or experiments with an imposed flow rate could be performed or as Hong et al. [148] experiment using gravity could be tested. In the future, experiments with a larger W/D ratio could be performed to see if bridging can be obtained as well as experiments with deflated capsules to see the impact of morphological change and higher deformability on the clogging mechanism. Note that experiments with glass capillaries will also be interesting to see how capsules behave when the constriction is fully clogged. Finally, in the long term, it would be interesting to establish a phase diagram showing clogging as a function of different parameters such as rigidity, W/D ratio, flow rates, and volume fraction of particles.

List of Abbreviations

$CaCl_2$ calcium chloride.

α**-SMA** alpha smooth muscle actin.

$\alpha 4\beta 1$ fibronectin receptor integrin.

1D one-dimension.

2D two-dimension.

3D three-dimension.

Ab amyloid beta.

AFM atomic force microscopy.

ANOVA analysis of variance.

AOSMCs aortic smooth muscle cells.

BAOSMCs bovine aortic smooth muscle cells.

BBB blood brain barrier.

BM basement membrane.

BSA bovine serum albumine.

Ca capillary number.

CD13 alanyl (membrane) aminopeptidase.

CD31 platelet endothelial cell adhesion molecule 1(PECAM-1).

CO_2 carbon dioxide.

DAPi 4’,6-diamidino-2-phenylindole.

DMEM Dulbecco’s Modified Eagle Medium.

ECM extracellular matrix.

ECs endothelial Cells.

EtOH ethanol.

FA focal adhesions.
FC-40 fluorinated oil.

GelMA methacrylamide-modified gelatin.

HAOSMCs human aortic smooth muscle cells.
HbS haemoglobin.
HDDA 1,6-hexanediol diacrylate.
HUVECs human umbilical vein endothelial cells.

LSS loud sound-stimulated.

MCs mural cells.
MQ Milli-Q.
MSD mean square displacement.

NG2 Neural/glial antigen 2.

O_2 oxygen.
OU Ornstein Unlenberck.

PBS phosphate-buffered saline.
PCL polycaprolactone.
PCs pericytes.
PDGF-BB platelet-derived growth factor-BB.
PDGFRβ platelet derived growth factor receptor β.
PDMS polydimethylsiloxane.
PEG poly(ethylene glycol).
PEG 200 poly(ethylene glycol), average molecular weight 200.
PEG-DA poly(ethylene glycol) diacrylate.
PEG-DA 575 poly(ethylene glycol) diacrylate, average molecular weight 575.
PEG-DA 700 poly(ethylene glycol) diacrylate, average molecular weight 700.
PEGDMA poly(ethylene glycol) dimethacrylate.
PI photoinitiator.

PLGA poly(lactic acid-glycolic acid).

Pll-g-PEG poly-L-lysine-grafted-poly(ethylene glycol).

PLPP photosensitive reagent, Alvéole.

PMMA polymethyl methacrylate.

QI Quantitative Imaging.

RBC red blood cells.

RGD arginine-glycine-aspartic acid.

RNA ribonucleic acid.

ROI region of interest.

SMCs smooth muscle cells.

STD standard deviation of the mean.

STP sodium tripolyphosphate.

STPP sodium tripolyphosphate pentabasic.

TFM traction force microscopy.

UV ultraviolet.

VACF velocity autocorrelation function.

VOC vaso-occlusive crisis.

References

[1] A. Lin, N. J. Peiris, H. Dhaliwal, M. Hakim, W. Li, S. Ganesh, Y. Ramaswamy, S. Patel, and A. Misra, “Mural cells: Potential therapeutic targets to bridge cardiovascular disease and neurodegeneration,” *Cells*, vol. 10, pp. 1–25, 3 2021.

[2] R. I. Grant, D. A. Hartmann, R. G. Underly, A. A. Berthiaume, N. R. Bhat, and A. Y. Shih, “Organizational hierarchy and structural diversity of microvascular pericytes in adult mouse cortex,” *Journal of Cerebral Blood Flow and Metabolism*, vol. 39, pp. 411–425, 3 2019.

[3] F. Ran, W. Li, Y. Qin, T. Yu, Z. Liu, M. Zhou, C. Liu, T. Qiao, X. Li, R. G. Yousef, I. H. Eissa, and M. M. Khalifa, “Inhibition of vascular smooth muscle and cancer cell proliferation by new vegfr inhibitors and their immunomodulator effect: Design, synthesis, and biological evaluation,” *Oxidative Medicine and Cellular Longevity*, vol. 2021, 2021.

[4] H. Y. Tang, A. Q. Chen, H. Zhang, X. F. Gao, X. Q. Kong, and J. J. Zhang, “Vascular smooth muscle cells phenotypic switching in cardiovascular diseases,” *Cells*, vol. 11, 12 2022.

[5] D. Attwell, A. Mishra, C. N. Hall, F. M. O’Farrell, and T. Dalkara, “What is a pericyte?,” *Journal of Cerebral Blood Flow and Metabolism*, vol. 36, pp. 451–455, 2 2016.

[6] D. J. Beard, L. S. Brown, and B. A. Sutherland, “The rise of pericytes in neurovascular research,” *Journal of Cerebral Blood Flow and Metabolism*, vol. 40, pp. 2366–2373, 12 2020.

[7] L. S. Brown, C. G. Foster, J. M. Courtney, N. E. King, D. W. Howells, and B. A. Sutherland, “Pericytes and neurovascular function in the healthy and diseased brain,” *Frontiers in Cellular Neuroscience*, pp. 13–282, 5 2019.

[8] A. P. Hall, “Review of the pericyte during angiogenesis and its role in cancer and diabetic retinopathy.,” *Toxicologic pathology*, vol. 34, pp. 763–775, 2006.

[9] F. Pfister, Y. Feng, F. V. Hagen, S. Hoffmann, G. Molema, J. L. Hillebrands, M. Shani, U. Deutsch, and H. P. Hammes, “Pericyte migration: A novel mechanism of pericyte loss in experimental diabetic retinopathy,” *Diabetes*, vol. 57, pp. 2495–2502, 9 2008.

[10] P. Li and H. Fan, “Pericyte loss in diseases,” *Cells*, vol. 12, p. 1931, 8 2023.

[11] A. Armulik, G. Genové, and C. Betsholtz, “Pericytes: Developmental, physiological, and pathological perspectives, problems, and promises,” *Developmental Cell*, vol. 21, pp. 193–215, 2011.

[12] K. W. Zimmermann, “Der ieinere bau der bluteapillaren.,” *Z Anat Entwicklungsgesch*, vol. 68, p. 29–109, 1923.

[13] B. Müller, S. Lang, M. Dominietto, M. Rudin, G. Schulz, H. Deyhle, M. Germann, F. Pfeiffer, C. David, and T. Weitkamp, “High-resolution tomographic imaging of microvessels,” vol. 7078, p. 70780B, SPIE, 8 2008.

[14] D. A. Hartmann, R. G. Underly, R. I. Grant, A. N. Watson, V. Lindner, and A. Y. Shih, “Pericyte structure and distribution in the cerebral cortex revealed by high-resolution imaging of transgenic mice,” *Neurophotonics*, vol. 2, p. 041402, 5 2015.

[15] U. Lendahl, P. Nilsson, and C. Betsholtz, “Emerging links between cerebrovascular and neurodegenerative diseases—a special role for pericytes,” *EMBO reports*, vol. 20, pp. 1–18, 2019.

[16] A. A. Berthiaume, D. A. Hartmann, M. W. Majesky, N. R. Bhat, and A. Y. Shih, “Pericyte structural remodeling in cerebrovascular health and homeostasis,” *Frontiers in Aging Neuroscience*, vol. 10, p. 210, 7 2018.

[17] A. Holm, T. Heumann, and H. G. Augustin, “Microvascular mural cell organotypic heterogeneity and functional plasticity,” *Trends in Cell Biology*, vol. 28, pp. 302–316, 4 2018.

[18] R. A. Hill, L. Tong, P. Yuan, S. Murikinati, S. Gupta, and J. Grutzendler, “Regional blood flow in the normal and ischemic brain is controlled by arteriolar smooth muscle cell contractility and not by capillary pericytes,” *Neuron*, vol. 87, pp. 95–110, 7 2015.

[19] L. Borysova and K. A. Dora, “The three faces of pericytes,” *Journal of Physiology*, vol. 596, pp. 3453–3454, 8 2018.

[20] C. Rouget, “Mémoire sur le développement, la structure et les propriétés physiologiques des capillaires sanguins,” *Archives Physiol Normal Pathol*, vol. 5, pp. 603–61, 1873.

[21] M. T. Uemura, T. Maki, M. Ihara, V. M. Lee, and J. Q. Trojanowski, “Brain microvascular pericytes in vascular cognitive impairment and dementia,” *Frontiers in Aging Neuroscience*, vol. 12, 4 2020.

[22] A. Hall, P. Chan, K. Sheets, M. Apperson, C. Delaughter, T. G. Gleason, J. A. Phillippi, and A. Nain, “Nanonet force microscopy for measuring forces in single smooth muscle cells of the human aorta,” *Molecular Biology of the Cell*, vol. 28, pp. 1894–1900, 7 2017.

[23] M. Vanlandewijck, L. He, M. A. Mäe, J. Andrae, K. Ando, F. D. Gaudio, K. Nahar, T. Lebouvier, B. Laviña, L. Gouveia, Y. Sun, E. Raschperger, M. Räsänen, Y. Zarb, N. Mochizuki, A. Keller, U. Lendahl, and C. Betsholtz, “A molecular atlas of cell types and zonation in the brain vasculature,” *Nature*, vol. 554, pp. 475–480, 2 2018.

[24] D. E. Sims, “The pericyte a review,” *TISSUE CELL*, vol. 18, p. 174, 1986.

[25] C. A. Dessalles, A. Babataheri, and A. I. Barakat, “Pericyte mechanics and mechanobiology,” *Journal of Cell Science*, vol. 134, 3 2021.

[26] L. Borysova, S. Wray, D. A. Eisner, and T. Burdyga, “How calcium signals in myocytes and pericytes are integrated across in situ microvascular networks and control microvascular tone,” *Cell Calcium*, vol. 54, pp. 163–174, 2013.

[27] A. A. Berthiaume, R. I. Grant, K. P. McDowell, R. G. Underly, D. A. Hartmann, M. Levy, N. R. Bhat, and A. Y. Shih, “Dynamic remodeling of pericytes in vivo maintains capillary coverage in the adult mouse brain,” *Cell Reports*, vol. 22, pp. 8–16, 1 2018.

[28] L. B. Payne, J. Darden, A. D. Suarez-Martinez, H. Zhao, A. Hendricks, C. Hartland, D. Chong, E. J. Kushner, W. L. Murfee, and J. C. Chappell, “Pericyte migration and proliferation are tightly synchronized to endothelial cell sprouting dynamics,” *Integrative Biology*, vol. 13, pp. 31–43, 2 2021.

[29] K. Ando, S. Fukuhara, N. Izumi, H. Nakajima, H. Fukui, R. N. Kelsh, and N. Mochizuki, “Clarification of mural cell coverage of vascular endothelial cells by live imaging of zebrafish,” *Development (Cambridge)*, vol. 143, pp. 1328–1339, 4 2016.

[30] Z. Hou, X. Wang, J. Cai, J. Zhang, A. Hassan, M. Auer, and X. Shi, “Platelet-derived growth factor subunit b signaling promotes pericyte migration in response to loud sound in the cochlear stria vascularis,” *JARO - Journal of the Association for Research in Otolaryngology*, vol. 19, pp. 363–379, 8 2018.

[31] L. Díaz-Flores, R. Gutiérrez, J. F. Madrid, H. Varela, F. Valladares, E. Acosta, P. Martín-Vasallo, and J. Díaz-Flores, “Pericytes. morphofunction, interactions and pathology in a quiescent and activated mesenchymal cell niche,” *Histology and Histopathology*, vol. 24, pp. 909–969, 7 2009.

[32] O. Iendaltseva, V. V. Orlova, C. L. Mummery, E. H. Danen, and T. Schmidt, “Fibronectin patches as anchoring points for force sensing and transmission in human induced pluripotent stem cell-derived pericytes,” *Stem Cell Reports*, vol. 14, pp. 1107–1122, 6 2020.

[33] P. J. Courtoy and J. Boyles, “Fibronectin in the microvasculature: Localization in the pericyte-endothelial interstitium,” *Journal of ultrastructure research*, vol. 83, pp. 258–273, 1983.

[34] D. A. Hartmann, A. A. Berthiaume, R. I. Grant, S. A. Harrill, T. Koski, T. Tieu, K. P. McDowell, A. V. Faino, A. L. Kelly, and A. Y. Shih, “Brain capillary pericytes exert a substantial but slow influence on blood flow,” *Nature Neuroscience*, vol. 24, pp. 633–645, 5 2021.

[35] J. Rustenhoven, L. C. Smyth, D. Jansson, P. Schweder, M. Aalderink, E. L. Scotter, E. W. Mee, R. L. Faull, T. I. Park, and M. Dragunow, “Modelling physiological and pathological conditions to study pericyte biology in brain function and dysfunction,” *BMC Neuroscience*, vol. 19, p. 6, 2 2018.

[36] C. S. Casey, Y. Atagi, Y. Yamazaki, M. Shinohara, M. Tachibana, Y. Fu, G. Bu, and T. Kanekiyo, “Apolipoprotein e inhibits cerebrovascular pericyte mobility through a rhoa protein-mediated pathway,” *Journal of Biological Chemistry*, vol. 290, pp. 14208–14217, 5 2015.

[37] A. Grazioli, C. S. Alves, K. Konstantopoulos, and J. T. Yang, “Defective blood vessel development and pericyte/pvsmc distribution in α4 integrin-deficient mouse embryos,” *Developmental Biology*, vol. 293, pp. 165–177, 5 2006.

[38] L. S. Brown, N. E. King, J. M. Courtney, R. J. Gasperini, L. Foa, D. W. Howells, and B. A. Sutherland, “Brain pericytes in culture display diverse morphological and functional phenotypes,” *Cell Biology and Toxicology*, 2023.

[39] H. Zhao, J. Darden, and J. C. Chappell, “Establishment and characterization of an embryonic pericyte cell line,” *Microcirculation*, vol. 25, 7 2018.

[40] J. Kim, M. Chung, S. Kim, D. H. Jo, J. H. Kim, and N. L. Jeon, “Engineering of a biomimetic pericyte-covered 3d microvascular network,” *PLoS ONE*, vol. 10, 7 2015.

[41] E. Lee, H. Takahashi, J. Pauty, M. Kobayashi, K. Kato, M. Kabara, J. I. Kawabe, and Y. T. Matsunaga, “A 3d in vitro pericyte-supported microvessel model: Visualisation and quantitative characterisation of multistep angiogenesis,” *Journal of Materials Chemistry B*, vol. 6, pp. 1085–1094, 2018.

[42] J. J. Bravo-Cordero, M. A. Magalhaes, R. J. Eddy, L. Hodgson, and J. Condeelis, “Functions of cofilin in cell locomotion and invasion,” *Nature Reviews Molecular Cell Biology*, vol. 14, pp. 405–417, 7 2013.

[43] G. Reig, E. Pulgar, and M. L. Concha, “Cell migration: From tissue culture to embryos,” *Development (Cambridge)*, vol. 141, pp. 1999–2013, 2014.

[44] A. D. Doyle, F. W. Wang, K. Matsumoto, and K. M. Yamada, “One-dimensional topography underlies three-dimensional fi brillar cell migration,” *Journal of Cell Biology*, vol. 184, pp. 481–490, 2 2009.

[45] P. Maiuri, E. Terriac, P. Paul-Gilloteaux, T. Vignaud, K. McNally, J. Onuffer, K. Thurn, P. A. Nguyen, N. Georgoulia, D. Soong, A. Jayo, N. Beil, J. Beneke, J. C. H. Lim, C. P.-Y. Sim, Y.-S. Chu, W. participants, A. Jiménez-Dalmaroni, J.-F. Joanny, J.-P. Thiery, H. Erfle, M. Parsons, T. J. Mitchison, W. A. Lim, A.-M. Lennon-Duménil, M. Piel, and M. Théry, “the first wolrd cell race,” *Current biology*, vol. 22, pp. R673–R675, 2012.

[46] K. Hennig, I. Wang, P. Moreau, L. Valon, S. Debeco, M. Coppey, Y. A. Miroshnikova, C. Albiges-Rizo, C. Favard, R. Voituriez, and M. Balland, “Stick-slip dynamics of cell adhesion triggers spontaneous symmetry breaking and directional migration of mesenchymal cells on one-dimensional lines,” *Science advances*, vol. 6, 2020.

[47] D. Mohammed, G. Charras, E. Vercruysse, M. Versaevel, J. Lantoine, L. Alaimo, C. Bruyère, M. Luciano, K. Glinel, G. Delhaye, O. Théodoly, and S. Gabriele, “Substrate area confinement is a key determinant of cell velocity in collective migration,” *Nature Physics*, vol. 15, pp. 858–866, 8 2019.

[48] D. Garbett, A. Bisaria, C. Yang, D. G. McCarthy, A. Hayer, W. E. Moerner, T. M. Svitkina, and T. Meyer, “T-plastin reinforces membrane protrusions to bridge matrix gaps during cell migration,” *Nature Communications*, vol. 11, 12 2020.

[49] D. B. Brückner, A. Fink, C. Schreiber, P. J. Röttgermann, J. O. Rädler, and C. P. Broedersz, “Stochastic nonlinear dynamics of confined cell migration in two-state systems,” *Nature Physics*, vol. 15, pp. 595–601, 6 2019.

[50] D. Caballero, R. Voituriez, and D. Riveline, “Protrusion fluctuations direct cell motion,” *Biophysical Journal*, vol. 107, pp. 34–42, 7 2014.

[51] S. L. Vecchio, R. Thiagarajan, D. Caballero, V. Vigon, L. Navoret, R. Voituriez, and D. Riveline, “Collective dynamics of focal adhesions regulate direction of cell motion,” *Cell Systems*, vol. 10, pp. 535–542.e4, 6 2020.

[52] C. Schreiber, B. Amiri, J. C. J. Heyn, J. O. R. Adler, and M. Falcke, “On the adhesion-velocity relation and length adaptation of motile cells on stepped fibronectin lanes,” *Proceedings of the National Academy of Sciences of the United States of America*, vol. 118, 2021.

[53] F. Zhou, S. A. Schaffer, C. Schreiber, F. J. Segerer, A. Goychuk, E. Frey, and J. O. Rädler, “Quasi-periodic migration of single cells on short microlanes,” *PLoS ONE*, vol. 15, 4 2020.

[54] C. Schreiber, F. J. Segerer, E. Wagner, A. Roidl, and J. O. Rädler, “Ring-shaped microlanes and chemical barriers as a platform for probing single-cell migration,” *Scientific Reports*, vol. 6, 5 2016.

[55] M. H. Gail and C. W. Boone, “The locomotion of mouse fibroblasts in tissue culture,” *Biophysical Journal*, vol. 10, pp. 980–993, 1970.

[56] C. L. Stokes, D. A. Lauffenburger, and S. K. Williams, “Migration of individual microvessel endothelial cells: stochastic model and parameter measurement,” *Journal of cell science*, vol. 99, pp. 419–430, 1991.

[57] Ornstein and LS, “On the brownian motion,” *Huygens Institute - Royal Netherlands Academy of Arts and Sciences (KNAW)*, vol. Proceedings 21, pp. 96–108, 1919.

[58] G. E. Uhlenbeck and L. S. Ornstein, “On the theory of the broknian motion,” *Physical Review*, vol. 36, pp. 823–841, 1930.

[59] J. d’Alessandro, A. Barbier-Chebbah, V. Cellerin, O. Benichou, R. M. Mège, R. Voituriez, and B. Ladoux, “Cell migration guided by long-lived spatial memory,” *Nature Communications*, vol. 12, 12 2021.

[60] I. Arganda-Carreras, V. Kaynig, C. Rueden, K. W. Eliceiri, J. Schindelin, A. Cardona, and H. S. Seung, “Trainable weka segmentation: A machine learning tool for microscopy pixel classification,” *Bioinformatics*, vol. 33, pp. 2424–2426, 8 2017.

[61] C. F. Natale, J. Lafaurie-Janvore, M. Ventre, A. Babataheri, and A. I. Barakat, “Focal adhesion clustering drives endothelial cell morphology on patterned surfaces,” *Journal of the Royal Society Interface*, vol. 16, 2019.

[62] A. Christensen, A. K. V. West, L. Wullkopf, J. T. Erler, L. B. Oddershede, and J. Mathiesen, “Friction-limited cell motility in confluent monolayer tissue,” *Physical Biology*, vol. 15, 7 2018.

[63] P. G. D. Gennes, “Brownian motion with dry friction,” *Journal of Statistical Physics*, vol. 119, pp. 953–962, 6 2005.

[64] G. L. Thomas, I. Fortuna, G. C. Perrone, J. A. Glazier, J. M. Belmonte, and R. M. de Almeida, “Parameterizing cell movement when the instantaneous cell migration velocity is ill-defined,” *Physica A: Statistical Mechanics and its Applications*, vol. 550, 7 2020.

[65] A. B. Buskermolen, T. Ristori, D. Mostert, M. C. van Turnhout, S. S. Shishvan, S. Loerakker, N. A. Kurniawan, V. S. Deshpande, and C. V. Bouten, “Cellular contact guidance emerges from gap avoidance,” *Cell Reports Physical Science*, vol. 1, 5 2020.

[66] M. L. Gardel, I. C. Schneider, Y. Aratyn-Schaus, and C. M. Waterman, “Mechanical integration of actin and adhesion dynamics in cell migration,” *Annual Review of Cell and Developmental Biology*, vol. 26, pp. 315–333, 11 2010.

[67] D. H. Kim and D. Wirtz, “Focal adhesion size uniquely predicts cell migration,” *FASEB Journal*, vol. 27, pp. 1351–1361, 4 2013.

[68] G. A. Dunn and A. F. Brown, “A unified approach to analysing cell motility,” *Cell Science*, pp. 81–102, 1987.

[69] W. J. Polacheck and C. S. Chen, “Measuring cell-generated forces: A guide to the available tools,” 5 2016.

[70] D. Vorselen, Y. Wang, M. M. de Jesus, P. K. Shah, M. J. Footer, M. Huse, W. Cai, and J. A. Theriot, “Microparticle traction force microscopy reveals subcellular force exertion patterns in immune cell–target interactions,” *Nature Communications*, vol. 11, 12 2020.

[71] J. T. Durham, H. K. Surks, B. M. Dulmovits, and I. M. Herman, “Pericyte contractility controls endothelial cell cycle progression and sprouting: Insights into angiogenic switch mechanics,” *American Journal of Physiology - Cell Physiology*, vol. 307, pp. C878–C892, 2014.

[72] A. S. Pellowe, M. Sauler, Y. Hou, J. Merola, R. Liu, B. Calderon, H. M. Lauridsen, M. R. Harris, L. Leng, Y. Zhang, P. V. Tilstam, J. S. Pober, R. Bucala, P. J. Lee, and A. L. Gonzalez, “Endothelial cell-secreted mif reduces pericyte contractility and enhances neutrophil extravasation,” *FASEB Journal*, vol. 33, pp. 2171–2186, 2019.

[73] M. Kotecki, A. S. Zeiger, K. J. V. Vliet, and I. M. Herman, “Calpain- and talin-dependent control of microvascular pericyte contractility and cellular stiffness,” *Microvascular Research*, vol. 80, pp. 339–348, 12 2010.

[74] S. Lee, A. Zeiger, J. M. Maloney, M. Kotecki, K. J. V. Vliet, and I. M. Herman, “Pericyte actomyosin-mediated contraction at the cell-material interface can modulate the microvascular niche,” *Journal of Physics Condensed Matter*, vol. 22, 2010.

[75] A. A. Neuhaus, Y. Couch, B. A. Sutherland, and A. M. Buchan, “Novel method to study pericyte contractility and responses to ischaemia in vitro using electrical impedance,” *Journal of Cerebral Blood Flow and Metabolism*, vol. 37, pp. 2013–2024, 2017.

[76] O. V. Sazonova, B. C. Isenberg, J. Herrmann, K. L. Lee, A. Purwada, A. D. Valentine, J. A. Buczek-Thomas, J. Y. Wong, and M. A. Nugent, “Extracellular matrix presentation modulates vascular smooth muscle cell mechanotransduction,” *Matrix Biology*, vol. 41, pp. 36–43, 1 2015.

[77] C. Petit, A. Guignandon, S. Avril, P. Claudie, G. Alain, and A. Stéphane, “Traction force measurements of human aortic smooth muscle cells reveal a motor-clutch behavior,” *Traction Force Measurements of Human Aortic Smooth Muscle Cells Reveal a Motor-Clutch Behavior. Molecular and Cellular Biomechanics*, p. 10, 2019.

[78] C. Petit, A. A. K. Yousefi, O. B. Moussa, J. B. Michel, A. Guignandon, and S. Avril, “Regulation of smc traction forces in human aortic thoracic aneurysms,” *Biomechanics and Modeling in Mechanobiology*, vol. 20, pp. 717–731, 4 2021.

[79] E. Mohagheghian, J. Luo, J. Chen, G. Chaudhary, J. Chen, J. Sun, R. H. Ewoldt, and N. Wang, “Quantifying compressive forces between living cell layers and within tissues using elastic round microgels,” *Nature Communications*, vol. 9, 2018.

[80] S. Girardo, N. Träber, K. Wagner, G. Cojoc, C. Herold, R. Goswami, R. Schlüßler, S. Abuhattum, A. Taubenberger, F. Reichel, D. Mokbel, M. Herbig, M. Schürmann, P. Müller, T. Heida, A. Jacobi, E. Ulbricht, J. Thiele, C. Werner, and J. Guck, “Standardized microgel beads as elastic cell mechanical probes,” *Journal of Materials Chemistry B*, vol. 6, pp. 6245–6261, 2018.

[81] N. Träber, K. Uhlmann, S. Girardo, G. Kesavan, K. Wagner, J. Friedrichs, R. Goswami, K. Bai, M. Brand, C. Werner, D. Balzani, and J. Guck, “Polyacrylamide bead sensors for in vivo quantification of cell-scale stress in zebrafish development,” *Scientific Reports*, vol. 9, 12 2019.

[82] J. K. Nunes, S. S. Tsai, J. Wan, and H. A. Stone, “Dripping and jetting in microfluidic multiphase flows applied to particle and fibre synthesis,” *Journal of Physics D: Applied Physics*, vol. 46, 2013.

[83] Y. Jun, E. Kang, S. Chae, and S. H. Lee, “Microfluidic spinning of micro- and nano-scale fibers for tissue engineering,” *Lab on a Chip*, vol. 14, pp. 2145–2160, 2014.

[84] X. Y. Du, Q. Li, G. Wu, and S. Chen, “Multifunctional micro/nanoscale fibers based on microfluidic spinning technology,” *Advanced Materials*, vol. 31, pp. 1–38, 2019.

[85] P. Guillot, A. Colin, and A. Ajdari, “Stability of a jet in confined pressure-driven biphasic flows at low reynolds number in various geometries,” *Physical Review E - Statistical, Nonlinear, and Soft Matter Physics*, vol. 78, 7 2008.

[86] C. Duprat, H. Berthet, J. S. Wexler, O. D. Roure, and A. Lindner, “Microfluidic in situ mechanical testing of photopolymerized gels,” *Lab on a Chip*, vol. 15, pp. 244–252, 1 2015.

[87] J. Zhu, P. He, L. Lin, D. R. Jones, and R. E. Marchant, “Biomimetic poly(ethylene glycol)-based hydrogels as scaffolds for inducing endothelial adhesion and capillary-like network formation,” *Biomacromolecules*, vol. 13, pp. 706–713, 3 2012.

[88] A. J. Krüger, O. Bakirman, L. P. Guerzoni, A. Jans, D. B. Gehlen, D. Rommel, T. Haraszti, A. J. Kuehne, and L. D. Laporte, “Compartmentalized jet polymerization as a high-resolution process to continuously produce anisometric microgel rods with adjustable size and stiffness,” *Advanced Materials*, vol. 31, 2019.

[89] J. K. Nunes, K. Sadlej, J. I. Tam, and H. A. Stone, “Control of the length of microfibers,” *Lab on a Chip*, vol. 12, pp. 2301–2304, 2012.

[90] J. K. Nunes, H. Constantin, and H. A. Stone, “Microfluidic tailoring of the two-dimensional morphology of crimped microfibers,” *Soft Matter*, vol. 9, pp. 4227–4235, 4 2013.

[91] A. Perazzo, J. K. Nunes, S. Guido, and H. A. Stone, “Flow-induced gelation of microfiber suspensions,” *Proceedings of the National Academy of Sciences of the United States of America*, vol. 114, pp. E8557–E8564, 10 2017.

[92] M. Slutzky, H. A. Stone, and J. K. Nunes, “A quantitative study of the effect of flow on the photopolymerization of fibers,” *Soft Matter*, vol. 15, pp. 9553–9564, 2019.

[93] S. S. Aykar, D. E. Reynolds, M. C. McNamara, and N. N. Hashemi, “Manufacturing of poly(ethylene glycol diacrylate)-based hollow microvessels using microfluidics,” *RSC Advances*, vol. 10, pp. 4095–4102, 2020.

[94] C. H. Choi, H. Yi, S. Hwang, D. A. Weitz, and C. S. Lee, “Microfluidic fabrication of complex-shaped microfibers by liquid template-aided multiphase microflow,” *Lab on a Chip*, vol. 11, pp. 1477–1483, 2011.

[95] F. Sharifi, B. B. Patel, M. C. Mcnamara, P. J. Meis, M. N. Roghair, M. Lu, R. Montazami, D. S. Sakaguchi, and N. N. Hashemi, “Photo-cross-linked poly(ethylene glycol) diacrylate hydrogels: Spherical microparticles to bow tie-shaped microfibers,” *ACS Appl. Mater. Interfaces*, vol. 11, pp. 18797–18807, 2019.

[96] J. Cappello, M. Bechert, C. Duprat, O. D. Roure, F. Gallaire, and A. Lindner, “Transport of flexible fibers in confined microchannels,” *Physical Review Fluids*, vol. 4, 3 2019.

[97] J. D. Berry, M. J. Neeson, R. R. Dagastine, D. Y. Chan, and R. F. Tabor, “Measurement of surface and interfacial tension using pendant drop tensiometry,” *Journal of Colloid and Interface Science*, vol. 454, pp. 226–237, 9 2015.

[98] N. Gavara, “A beginner’s guide to atomic force microscopy probing for cell mechanics,” *Microscopy Research and Technique*, vol. 80, pp. 75–84, 1 2017.

[99] jpk-tech-force-spectroscopy.14 2, “Nanowizard ® afm user manual version 4.2,” 2012.

[100] I. N. Sneddon, “The relation between load and penetration in the axisymmetric boussinesq problem for a punch of arbitrary profilet,” *International Journal of Engineering Science*, vol. 3, pp. 47–57, 1965.

[101] J. I. AG, “Determining the elastic modulus of biological samples using atomic force microscopy.”

[102] J. I. AG, “A pratical guide for afm force spectroscopy and data analysis.”

[103] M. D. Norman, S. A. Ferreira, G. M. Jowett, L. Bozec, and E. Gentleman, “Measuring the elastic modulus of soft culture surfaces and three-dimensional hydrogels using atomic force microscopy,” *Nature Protocols*, vol. 16, pp. 2418–2449, 5 2021.

[104] J. Husson, *Measuring Cell Mechanical Properties Using Microindentation*, vol. 2600, pp. 3–23. Humana Press Inc., 2023.

[105] K. L. Johnson, *Contact Mechanics*. Cambridge University Press, 1985.

[106] L. Guillou, A. Babataheri, P. H. Puech, A. I. Barakat, and J. Husson, “Dynamic monitoring of cell mechanical properties using profile microindentation,” *Scientific Reports*, vol. 6, 2 2016.

[107] K. Hou, H. Wang, Y. Lin, S. Chen, S. Yang, Y. Cheng, B. S. Hsiao, and M. Zhu, “Large scale production of continuous hydrogel fibers with anisotropic swelling behavior by dynamic-crosslinking-spinning,” *Macromolecular Rapid Communications*, vol. 37, pp. 1795–1801, 11 2016.

[108] J. Eglinger, H. Karsjens, and E. Lammert, “Quantitative assessment of angiogenesis and pericyte coverage in human cell-derived vascular sprouts,” *Inflammation and Regeneration*, vol. 37, 1 2017.

[109] A. Trushko, I. D. Meglio, A. Merzouki, C. Blanch-Mercader, S. Abuhattum, J. Guck, K. Alessandri, P. Nassoy, K. Kruse, B. Chopard, and A. Roux, “Buckling of an epithelium growing under spherical confinement,” *Developmental Cell*, vol. 54, pp. 655–668.e6, 9 2020.

[110] Z. Püspöki, M. Storath, D. Sage, and M. Unser, “Transforms and operators for directional bioimage analysis: A survey,” *Advances in Anatomy Embryology and Cell Biology*, vol. 219, pp. 69–93, 2016.

[111] T. Cubaud and T. G. Mason, “Capillary threads and viscous droplets in square microchannels,” *Physics of Fluids*, vol. 20, 2008.

[112] C. Jean, “Dynamics of freely transported fibers in confined viscous flows role of shape and flexibility,” 2020.

[113] A. Kamnerdsook, E. Juntasaro, N. Khemthongcharoen, M. Chanasakulniyom, W. Sripumkhai, P. Pattamang, C. Promptmas, N. Atthi, and W. Jeamsaksiri, “On classification of water-in-oil and oil-in-water droplet generation regimes in flow-focusing microfluidic devices,” *Colloids and Interfaces*, vol. 7, 3 2023.

[114] C. Qing, V. A. L, S. K.R, and P. A. K, “Instability due to viscosity stratification,” *The Canadian Journal of Chemical Engineering*, vol. 81, 2003.

[115] H. Bruus, *Theoretical Microfluidics*. Oxford University Press, 2008.

[116] K. Krutkramelis, B. Xia, and J. Oakey, “Monodisperse polyethylene glycol diacrylate hydrogel microsphere formation by oxygen-controlled photopolymerization in a microfluidic device,” *Lab on a Chip*, vol. 16, pp. 1457–1465, 4 2016.

[117] M. P. Paidoussis, *Fluid-structure interactions: slender structures and axial flow*, vol. 1. academic press ed., 1998.

[118] J. Cappello, V. d’Herbemont, A. Lindner, and O. du Roure, “Microfluidic in-situ measurement of poisson’s ratio of hydrogels,” *Micromachines*, vol. 11, 3 2020.

[119] A. R. Harris and G. T. Charras, “Experimental validation of atomic force microscopy-based cell elasticity measurements,” *Nanotechnology*, vol. 22, 8 2011.

[120] P. H. Wu, D. R. B. Aroush, A. Asnacios, W. C. Chen, M. E. Dokukin, B. L. Doss, P. Durand-Smet, A. Ekpenyong, J. Guck, N. V. Guz, P. A. Janmey, J. S. Lee, N. M. Moore, A. Ott, Y. C. Poh, R. Ros, M. Sander, I. Sokolov, J. R. Staunton, N. Wang, G. Whyte, and D. Wirtz, “A comparison of methods to assess cell mechanical properties,” *Nature Methods*, vol. 15, pp. 491–498, 6 2018.

[121] K. I. Hoshino, T. Nakajima, T. Matsuda, T. Sakai, and J. P. Gong, “Network elasticity of a model hydrogel as a function of swelling ratio: From shrinking to extreme swelling states,” *Soft Matter*, vol. 14, pp. 9693–9701, 2018.

[122] N. D. Bade, R. D. Kamien, R. K. Assoian, and K. J. Stebe, “Curvature and rho activation differentially control the alignment of cells and stress fibers,” *Science Advances*, vol. 3, 2017.

[123] Y. Jin, L. Liu, P. Yu, F. Lin, X. Shi, J. Guo, B. Che, Y. Duan, J. Li, Y. Pan, M. Luo, and L. Deng, “Emergent differential organization of airway smooth muscle cells on concave and convex tubular surface,” *Frontiers in Molecular Biosciences*, vol. 8, 9 2021.

[124] B. Schamberger, R. Ziege, K. Anselme, M. B. Amar, M. Bykowski, A. P. Castro, A. Cipitria, R. A. Coles, R. Dimova, M. Eder, S. Ehrig, L. M. Escudero, M. E. Evans, P. R. Fernandes, P. Fratzl, L. Geris, N. Gierlinger, E. Hannezo, A. Iglič, J. J. Kirkensgaard, P. Kollmannsberger, Łucja Kowalewska, N. A. Kurniawan, I. Papantoniou, L. Pieuchot, T. H. Pires, L. D. Renner, A. O. Sageman-Furnas, G. E. Schröder-Turk, A. Sengupta, V. R. Sharma, A. Tagua, C. Tomba, X. Trepat, S. L. Waters, E. F. Yeo, A. Roschger, C. M. Bidan, and J. W. Dunlop, “Curvature in biological systems: Its quantification, emergence, and implications across the scales,” *Advanced Materials*, vol. 35, 3 2023.

[125] S. J. Callens, D. Fan, I. A. van Hengel, M. Minneboo, P. J. Díaz-Payno, M. M. Stevens, L. E. Fratila-Apachitei, and A. A. Zadpoor, “Emergent collective organization of bone cells in complex curvature fields,” *Nature Communications*, vol. 14, 12 2023.

[126] N. D. Bade, T. Xu, R. D. Kamien, R. K. Assoian, and K. J. Stebe, “Gaussian curvature directs stress fiber orientation and cell migration,” *Biophysical Journal*, vol. 114, pp. 1467–1476, 3 2018.

[127] H. Shima, “Simple approximate formulas for postbuckling deflection of heavy elastic columns,” *Applied Sciences (Switzerland)*, vol. 10, pp. 1–10, 10 2020.

[128] S. Sharma, J. C. Hill, J. A. Phillippi, and A. S. Nain, “Fiber diameter and architecture direct three-dimensional assembly of pericytes into spheroids,” *bioRxiv*, 2022.

[129] E. Meijering, O. Dzyubachyk, and I. Smal, “Methods for cell and particle tracking,” *Methods in enzymology,*, vol. 504, pp. 183–200, 2012.

[130] H. G. Yevick, G. Duclos, I. Bonnet, and P. Silberzan, “Architecture and migration of an epithelium on a cylindrical wire,” *Proceedings of the National Academy of Sciences of the United States of America*, vol. 112, pp. 5944–5949, 5 2015.

[131] S. Zhu, M. Chen, Y. Ying, Q. Wu, Z. Huang, W. Ni, X. Wang, H. Xu, S. Bennett, J. Xiao, and J. Xu, “Versatile subtypes of pericytes and their roles in spinal cord injury repair, bone development and repair,” *Bone Research*, vol. 10, 12 2022.

[132] M. Alaa Eddine, A. Carvalho, M. Schmutz, T. Salez, S. de Chateauneuf-Randon, B. Bresson, S. Belbekhouche, and C. Monteux, “Sieving and clogging in peg–pegda hydrogel membranes,” *Langmuir*, vol. 42, p. 15085–15094, 9 2023.

[133] D. Zhang, Y. Sheng, N. Piano, T. Jakuszeit, E. J. Cozens, L. Dong, A. K. Buell, A. Pollet, I. M. Lei, W. Wang, E. Terentjev, and Y. Y. S. Huang, “Cancer cell migration on straight, wavy, loop and grid microfibre patterns,” *Biofabrication*, vol. 14, 4 2022.

[134] D. Helbing, I. Farkas, and T. Vicsek, “Simulating dynamical feature of escape panic,” *Nature*, vol. 407, pp. 487–490, 2000.

[135] C. Mankoc, A. Garcimartín, I. Zuriguel, D. Maza, and L. A. Pugnaloni, “Role of vibrations in the jamming and unjamming of grains discharging from a silo,” *Phys. Rev. E*, vol. 80, p. 011309, Jul 2009.

[136] E. Dressaire and A. Sauret, “Clogging of microfluidic systems,” *Soft Matter*, vol. 13, pp. 37–48, 2017.

[137] G. C. Agbangla, Éric Climent, and P. Bacchin, “Experimental investigation of pore clogging by microparticles: Evidence for a critical flux density of particle yielding arches and deposits,” *Separation and Purification Technology*, vol. 101, pp. 42–48, 11 2012.

[138] J. M. Higgins, D. T. Eddington, S. N. Bhatia, and L. Mahadevan, “Sickle cell vasoocclusion and rescue in a microfluidic device,” *Proceedings of the National Academy of Sciences of the United States of America*, vol. 104, pp. 20496–20500, 2007.

[139] J. P. Shelby, J. White, K. Ganesan, P. K. Rathod, and D. T. Chiu, “A microfluidic model for single-cell capillary obstruction by plasmodium falciparum-infected erythrocytes,” *Proceedings of the National Academy of Sciences of the United States of America*, vol. 100, pp. 14618–14622, 2003.

[140] L. Pang, S. Shen, C. Ma, T. Ma, R. Zhang, C. Tian, L. Zhao, W. Liu, and J. Wang, “Deformability and size-based cancer cell separation using an integrated microfluidic device,” *Analyst*, vol. 140, pp. 7335–7346, 11 2015.

[141] M. Aghaamoo, Z. Zhang, X. Chen, and J. Xu, “Deformability-based circulating tumor cell separation with conical-shaped microfilters: Concept, optimization, and design criteria,” *Biomicrofluidics*, vol. 9, 5 2015.

[142] H. Wei, B. H. Chueh, H. Wu, E. W. Hall, C. W. Li, R. Schirhagl, J. M. Lin, and R. N. Zare, “Particle sorting using a porous membrane in a microfluidic device,” *Lab on a Chip*, vol. 11, pp. 238–245, 1 2011.

[143] A. Marin, H. Lhuissier, M. Rossi, and C. J. Kähler, “Clogging in constricted suspension flows,” *Physical Review E*, vol. 97, 2 2018.

[144] M. Souzy, I. Zuriguel, and A. Marin, “Transition from clogging to continuous flow in constricted particle suspensions,” *Physical Review E*, vol. 101, 6 2020.

[145] W. Guo, H. H. Ngo, and J. Li, “A mini-review on membrane fouling,” *Bioresource Technology*, vol. 122, pp. 27–34, 10 2012.

[146] P. Bacchin, A. Marty, P. Duru, M. Meireles, and P. Aimar, “Colloidal surface interactions and membrane fouling: Investigations at pore scale,” *Advances in Colloid and Interface Science*, vol. 164, pp. 2–11, 2011.

[147] C. Bielinski, O. Aouane, J. Harting, and B. Kaoui, “Squeezing multiple soft particles into a constriction: Transition to clogging,” *Phys. Rev. E*, vol. 104, p. 065101, Dec 2021.

[148] X. Hong, M. Kohne, M. Morrell, H. Wang, and E. R. Weeks, “Clogging of soft particles in two-dimensional hoppers,” *Physical Review E*, vol. 96, 12 2017.

[149] Y. Li, O. S. Sarlyer, A. Ramachandran, S. Panyukov, M. Rubinstein, and E. Kumacheva, “Universal behavior of hydrogels confined to narrow capillaries,” *Scientific Reports*, vol. 5, 11 2015.

[150] C. P. Moore, J. Husson, A. Boudaoud, G. Amselem, and C. N. Baroud, “Clogging of a rectangular slit by a spherical soft particle,” *Phys. Rev. Lett.*, vol. 130, p. 064001, Feb 2023.

[151] S. Alborzi, D. Abrahamyan, and S. M. Hashmi, “Mixing particle softness in a two-dimensional hopper: Particle rigidity and friction enable variable arch geometry to cause clogging,” *Phys. Rev. E*, vol. 107, p. 024901, Feb 2023.

[152] D. K. Kaul, M. E. Fabry, P. Windisch, S. Baez, and R. L. Nagel, “Erythrocytes in sickle cell anemia are heterogeneous in their rheological and hemodynamic characteristics,” *Journal of Clinical Investigation*, vol. 72, pp. 22–31, 1983.

[153] A. Aich, Y. Lamarre, D. P. Sacomani, S. Kashima, D. T. Covas, and L. G. de la Torre, “Microfluidics in sickle cell disease research: State of the art and a perspective beyond the flow problem,” *Frontiers in Molecular Biosciences*, vol. 7, 3 2021.

[154] D. K. Wood, A. Soriano, L. Mahadevan, J. M. Higgins, and S. N. Bhatia, “A biophysical indicator of vaso-occlusive risk in sickle cell disease,” *Science Translational Medicine*, vol. 4, 2 2012.

[155] E. Loiseau, G. Massiera, S. Mendez, P. A. Martinez, and M. Abkarian, “Microfluidic study of enhanced deposition of sickle cells at acute corners,” *Biophysical Journal*, vol. 108, pp. 2623–2632, 6 2015.

[156] Q. Chen, N. Singh, K. Schirrmann, Q. Zhou, I. Chernyavsky, and A. Juel, “Robust fabrication of ultra-soft tunable pdms microcapsules as a biomimetic model for red blood cells,” *Soft Matter*, vol. 19, pp. 5197–5418, 2 2023.

[157] J. Y. Tinevez, N. Perry, J. Schindelin, G. M. Hoopes, G. D. Reynolds, E. Laplantine, S. Y. Bednarek, S. L. Shorte, and K. W. Eliceiri, “Trackmate: An open and extensible platform for single-particle tracking,” *Methods*, vol. 115, pp. 80–90, 2 2017.

[158] G. Tomaiuolo, “Biomechanical properties of red blood cells in health and disease towards microfluidics,” *Biomicrofluidics*, vol. 8, 9 2014.

[159] D. F. D. Nascimento, J. A. Avendaño, A. Mehl, M. J. Moura, M. S. Carvalho, and W. J. Duncanson, “Flow of tunable elastic microcapsules through constrictions,” *Scientific Reports*, vol. 7, 12 2017.

ECOLE
DOCTORALE

Titre : Génération de force et migration des cellules vasculaires sous contraintes géométriques

Mots clés : Mécanobiologie, Microfluidique, Hydrogels, Cellules murales, Contractilité, Motilité cellulaire

Résumé : Les vaisseaux sanguins sont constitués de différents types de cellules, dont les cellules endothéliales et les cellules murales. Les cellules endothéliales tapissent la paroi interne des vaisseaux, tandis que les cellules murales se trouvent à l'extérieur des vaisseaux sanguins. Le terme "cellules murales" englobe deux types de cellules : les cellules musculaires lisses vasculaires (CMLs), qui se trouvent autour des gros vaisseaux, et les péricytes (PCs), présentes autour des vaisseaux plus petits tels que les capillaires. Les péricytes jouent un rôle essentiel dans notre santé, renforçant mécaniquement les microvaisseaux, contrôlant le flux sanguin dans les microvaisseaux, et contribuant à l'angiogenèse. Leur dysfonctionnement, en revanche, est à l'origine de nombreuses maladies, telles que la maladie d'Alzheimer, la formation de tumeurs ou le diabète. En dépit de leur rôle important, des aspects tels que l'hétérogénéité et les fonctions des PCs restent encore à clarifier et font l'objet de divers débats scientifiques. Dans cette thèse, nous nous concentrons sur l'étude de deux fonctions essentielles des péricytes : leur migration et leur capacité à exercer des forces contractiles. Pour ce faire, nous avons développé deux outils in vitro qui reproduisent les contraintes géométriques que les péricytes rencontrent in vivo.

Pour caractériser la migration des péricytes, nous utilisons d'abord des micropatterns en forme de ligne pour imiter le confinement des microvaisseaux. Parallèlement, nous développons un modèle théorique simple pour rationaliser le comportement des cellules. Nous avons constaté qu'avec notre configuration 1D, nous pouvons retrouver certains des paramètres morphologiques des PCs in vivo. L'analyse de la migration des PCs révèle que la vitesse des cellules est négativement corrélée à leur longueur, et que leur migration peut être modélisée comme une particule soumise à un mouvement brownien 1D à friction sèche. Nous ajoutons ensuite des espaces non-adhérents de différentes tailles aux lignes, créant ainsi un substrat non-uniforme pour étudier la dynamique des PCs dans diverses configurations. Nous observons que la probabilité de franchissement des PCs diminue de manière exponentielle avec la taille de l'espace non-adhérent et est indépendante de la longueur des micropatterns.

La deuxième partie de cette thèse vise à mesurer les forces contractiles exercées par les cellules murales. Nous fabriquons des microfibres d'hydrogel suffisamment molles pour mesurer les forces des cellules murales et suffisamment fines pour imiter la courbure des microvaisseaux. Les fibres d'hydrogel sont produites dans des microcanaux à deux phases et solidifiées par photopolymérisation. Nous établissons d'abord des lignes directrices pour produire les fibres souhaitées puis, caractérisons quantitativement leurs propriétés mécaniques, telles que leur module de Young, à l'aide de la microscopie à force atomique. Nos résultats montrent une augmentation exponentielle du module d'Young avec le temps d'exposition aux UV et que la forme et le flux dans le pré-gel pourraient impacter les propriétés mécaniques. Après avoir obtenu des microfibres fines et d'une rigidité de quelques kilopascals, nous étudions l'effet de la courbure sur l'organisation des CMLs et observons que, comme sur les fibres rigides, elles s'alignent longitudinalement avec la fibre. Sur les fibres encore plus fines, les cellules murales plient les fibres, ce qui nous permet d'estimer les forces de traction exercées par les cellules.

Dans l'ensemble, cette thèse apporte des informations sur la migration des cellules murales ainsi que sur leur comportement sur des substrats courbés et mous. De plus, la caractérisation mécanique des fibres d'hydrogel peut servir à d'autres applications en biologie ou en interactions fluide-structure.

Title : Vascular cell migration and force generation under tailored geometrical constraints

Keywords : Mechanobiology, Microfluidic, Hydrogels, Mural cells, Contractility, Cellular motility

Abstract : Blood vessels are constituted of different cell types, including endothelial cells and mural cells. Endothelial cells form the vessel's inner wall, while mural cells line the outer endothelial tube. The term mural cell refers to two types of cells : vascular smooth muscle cells (SMCs), found on large vessels, and pericytes (PCs), found on smaller vessels such as capillaries. Pericytes play a crucial role in maintaining our health by regulating blood flow within the microcirculation, providing mechanical support to small blood vessels, and contributing to the formation of new blood vessels. Their dysfunction is involved in a number of diseases, such as Alzheimer's disease, tumour formation or diabetes. Despite the important role they play, the heterogeneity and functions of the pericyte are yet to be fully understood and remain subjects of ongoing debate. Clarifying these aspects is crucial for advancing our knowledge of vascular biology and its potential therapeutic applications. In this thesis, we study two essential pericyte functions, migration and contractility. We create two in vitro tools that mimic the geometrical constraints that pericytes experience in vivo.

To investigate pericyte migration, we first use micropatterned lines to mimic microvascular confinement. In parallel, we develop a minimal theoretical model to rationalise cell behaviour. We are able to reproduce some of the in vivo morphological parameters with our simple 1D system. The quantification of PC migration shows that cell speed and length are negatively correlated and that PC migration can be modelled as a particle undergoing 1D Brownian motion with dry friction. Then, we add non-adherent gaps of different sizes to the lines to create non-uniform substrates and study pericyte dynamics in different configurations. We observe that the pericyte crossing probability decreases exponentially with gap size and is independent of micropattern length.

The second part of this work aims to measure the contractile forces exerted by mural cells. We fabricate hydrogel microfibres that are soft enough to measure cell forces and thin enough to mimic the curvature of small blood vessels. The hydrogel microfibres are produced using a two-phase flow-focusing channel and photopolymerisation. We first define guidelines for producing the desired microfibres and then characterise their mechanical properties, such as their Young's modulus, using atomic force microscopy. Our results show an exponential increase of Young's modulus with UV exposure time and that the shape and flow of the pre-gel could have an impact on mechanical properties.

After successfully obtaining and functionalising thin microfibres of a few kilopascals, we study the effect of curvature on the organisation of SMC cytoskeleton and observe that as on stiff fibres, they align axially with the fibre. However, on even thinner fibre, mural cells bend the fibre, allowing us to estimate cell-exerted traction forces.

Overall, this thesis provides insight into vascular cell migration and behaviour on curved and soft substrates. In addition, the mechanical characterisation of hydrogel fibres can serve for other applications in biology or fluid-structure interactions.

Institut Polytechnique de Paris
91120 Palaiseau, France